Time-Resolved Pump-Probe Investigation of the Terahertz Quantum Cascade Laser

David Robert Bacon, MEng

Submitted in accordance with the requirements
for the degree of Doctor of Philosophy

University of Leeds

School of Electronic and Electrical Engineering

May 2017

The candidate confirms that the work submitted is his/her own, except where work which has formed part of jointly-authored publications has been included. The contribution of the candidate and the other authors to this work has been explicitly indicated below. The candidate confirms that appropriate credit has been given within the thesis where reference has been made to the work of others.

A number of publications have arisen from the work presented in this thesis:

Chapter 4

- **D. R. Bacon**, J. R. Freeman, R. A. Mohandas, L. Li, E. H. Linfield, A. G. Davies, and P. Dean. "Gain recovery time in a terahertz quantum cascade laser," *Appl. Phys. Lett.*, vol. *108*, no. *8*, p. *081104*, 20*16*.

The adapted time domain spectroscopy system used to collect the data was originally designed by Dr Joshua Freeman. Data collection was done so under his and Dr Paul Dean's supervision. My work for this publication included collecting, analysing and plotting the data for all of the figures. The one exception to this is the data fitting in fig.2 (lower inset) which was performed by Dr Joshua Freeman. After I wrote the first draft of the paper, it became a collaborative effort between all authors.

Chapter 3

- **D.R. Bacon**, A. D. Burnett, M. Swithenbank, C. Russell, L. Li, C. D. Wood, J. Cunningham, E. H. Linfield, A. G. Davies, P. Dean and J. R. Freeman. "Free-space terahertz radiation from a LT-GaAs-on-quartz large-area photoconductive emitter," *Opt. Express*, vol. *24*, no. *23*, pp. *26986–26997*, 20*16*.

My work for this publication began with the fabrication of all devices discussed in the text, with assistance from Matthew Swithenbank and Dr Christopher Russell. The time domain spectroscopy systems used to collect the data were originally designed by Dr Andrew Burnett and Dr Joshua Freeman. I collected, analysed and plotted the data of all figures. Stimulation

work shown in fig. 5 d) was performed by Dr Joshua Freeman. After I wrote the first draft of the paper, it became a collaborative effort between all authors.

This thesis is dedicated to my late auntie Rita

Acknowledgements

First and foremost I would like to thank my PhD and masters project supervisor Dr. Paul Dean, for both allowing me to continue with my studies at the University of Leeds, and provided me with continuous guidance and support throughout. As my co-supervisor, I would also like to express my sincere gratitude to Prof. Edmund Linfield, whose undergraduate module originally sparking my interest in the subject. Thanks are also due to Prof. Giles Davies and Prof. John Cunningham for their important comments and assistance given in supervision meetings.

I would like to extend a special thank you to Dr. Joshua Freeman, whose unwavering support and patience over the past 4 years has been absolutely vital for the progression of this project. His extensive knowledge of QCLs and photoconductive devices has proved a very important resource throughout this project, and his general attitude and enthusiasm for research has acted as an inspiration for my continued development. In the same vein, I would also like to express my sincere gratitude to Dr. Andrew Burnett, who has been a fountain of knowledge on the subject of time-domain spectroscopy throughout the project. Arguably more important than that though is the vital role he has played in helping me to maintain a perspective on what is important, especially during some of the more difficult days of my PhD.

For similar reasons, together with his extensive knowledge of QCLs and simulation software, I would like to thank Dr. Alex Valavanis. I would also like to thank Dr. Mark Rosamond and Dr. Chris Wood for keeping the cleanroom running smoothly and for assisting me with various fabrication techniques throughout the project, while at the same time delivering their own unique style of guidance and supervision. Work done in the cleanroom would not have been possible without the help of Geoff Butterworth, Dr. Li Chen, Jordan and Chris Day,

who have all either assisted in my cleanroom training or have helped maintain the cleanroom during the project. I am also grateful to Dr. Lianhe Li for supplying me with wafers of material.

I would like to thank all past and present occupants of the fourth floor student offices in the IMP for their companionship, including Dr. Iman Kundu, Dr. Nic Hunter, Dr. Siddhant Chowdhury, Dr. Divyang Mistry, Dong Rui, Dr. Viktor Doychinov, Nicholas Peters and Pierluigi Rubino. A special thanks must be expressed to my good friends Matthew Swithenbank, Nicholas Greenhall, Dr. Chris Russell, Dr. Jay Keeley and Dr. Reshma Mohandas, all of whom have supported me throughout my masters and PhD projects and are most responsible for me enjoying my time at Leeds. I would also like to thank Sue Hobson for her administrative help and support and all members of staff at the School of Electronic and Electrical Engineering.

I would like to thank those people who I have lived with or close to during this process including Nick, Nici, Jake, Adam, Matt, Cathryn and Megan. You have all made the limited time I have spent away from the university a pleasurable experience. Thanks are also due to my good friends Steven and Lowri, who have entertained me since the beginning of my undergraduate degree and have kept me sane throughout this process. Lastly, I would like to thank my family for all their help and support.

Abstract

The terahertz (THz) region of the electromagnetic spectrum remains relatively underdeveloped and unexploited. This is due to the lack of compact and high-power sources which are able to output radiation between 100 GHz and 10 THz. In this thesis two separate methods of generating THz radiation are considered; the quantum cascade laser (QCL) and the photoconductive (PC) emitter. THz-QCLs generate radiation through the intersubband transition of electrons within quantum wells. Electrons are then transported into the adjacent quantum well, where they are recycled. Alternatively, PC emitters generate THz radiation through the excitation, acceleration and recombination of electron-hole pairs in semiconducting material, leading to the emission of short pulse THz radiation.

In this work, the gain dynamics of two different designs of THz-QCL are investigated using well-established time domain spectroscopy (TDS) techniques. The gain recovery time of a bound-to-continuum (BTC) device, a property known to be responsible for the prevention of mode-locking in the laser, is recovered through use of THz-pump-THz-probe TDS. This was performed multiple times, both with and without anti-reflective coating applied to the QCL facets. This coating prevents the QCL from lasing. Furthermore, this approach was then used to investigate the carrier dynamics of a hybrid active region device, which yielded some interesting preliminary results.

To facilitate these measurements, a new form of quartz-mounted PC device was designed and fabricated. This entails removing the LT-GaAs active layer from its SI-GaAs growth substrate and bonding it directly to a layer of z-cut quartz. In emission, this device has been shown to produce significantly higher THz output fields, when compared to the previously

used PC devices. In addition to this, the use of an optically transparent substrate provides the ability to perform back-side illumination, which is shown to improve the output characteristics of the device. Furthermore, when used in detection, the newly fabricated devices have shown significantly increased sensitivity, when compared to other methods of detection.

Publications

The work presented in this thesis has been presented in the following publications and conference proceedings.

Peer-reviewed journals

- A . Valavanis, S. Chowdhury, A. D. Burnett, A. R. Clarkson, **D. R. Bacon**, S.P.Khanna, A. G. Davies, E. H. Linfield and P. Dean. "Diffuse-reflectance spectroscopy using a frequency-switchable terahertz quantum cascade laser," *IEEE Transactions on Terahertz Science and Technology*, vol. *6*, no. *2*, p. *341–347*, 20*16*.

- **D. R. Bacon**, J. R. Freeman, R. A. Mohandas, L. Li, E. H. Linfield, A. G. Davies, and P. Dean. "Gain recovery time in a terahertz quantum cascade laser," *Appl. Phys. Lett.*, vol. *108*, no. *8*, p. *081104*, 20*16*.

- **D. R. Bacon**, A. D. Burnett, M. Swithenbank, C. Russell, L. Li, C. D. Wood, J. Cunningham, E. H. Linfield, A. G. Davies, P. Dean and J. R. Freeman. "Free-space terahertz radiation from a LT-GaAs-on-quartz large-area photoconductive emitter," *Opt. Express*, vol. *24*, no. *23*, pp. *26986–26997*, 20*16*.

- A. Garufo, G. Carluccio, J. R. Freeman, **D. R. Bacon**, N. Llombart, E. H. Linfield, A. G. Davies and A. Neto. "Norton Equivalent Circuit for Photoconductive Antennas âĂŞ Part II: Experimental Validation," (Submitted to Transactions on Terahertz Science and Technology)

Conference proceedings

- **D. R. Bacon**, J. R. Freeman, R. A. Mohandas, L. Li, E. H. Linfield, A. G. Davies, and P. Dean, "Pump-Probe Gain Recovery Measurements in a Terahertz Quantum Cascade Laser," *UK Semiconductors*, 2016.

- **D. R. Bacon**, J. R. Freeman, R. A. Mohandas, L. Li, E. H. Linfield, A. G. Davies, and P. Dean, "Gain recovery time in a terahertz quantum cascade laser," *International Quantum Cascade Lasers School and Workshop (IQCLSW)*, 2016.

- **D. R. Bacon**, J. R. Freeman, R. A. Mohandas, L. Li, E. H. Linfield, A. G. Davies, and P. Dean, "Pump-probe measurements of gain in a terahertz quantum cascade laser," *The 41st International Conference on Infrared, Millimeter, and Terahertz Waves (IRMMW-THz)*, 2016.

- J. R. Freeman, **D. R. Bacon**, E. H. Linfield, A. Giles Davies, A. Garufo, G. Carluccio, N. Llombart and A. Neto, "Power measurements of photoconductive antennas and comparison with the power estimated by an equivalent circuit model approach," *The 41st International Conference on Infrared, Millimeter, and Terahertz Waves (IRMMW-THz)*, 2016.

- Garufo, G. Carluccio, J. R. Freeman, **D. R. Bacon**, N. Llombart, E. H. Linfield, A. Giles Davies and A. Neto, "Validation by Power Measurements of a Norton Equivalent Circuit Model for Photoconductive Antennas," *Proceedings of the Eleventh European Conference on Antennas and Propagation (EuCAP)*, 2017

- **D. R. Bacon**, A. D. Burnett, M. Swithenbank, C. Russell, L. Li, C. D. Wood, J. Cunningham, E. H. Linfield, A. G. Davies, P. Dean and J. R. Freeman. "Free-space terahertz radiation from a LT-GaAs-on-quartz large-area photoconductive emitter," *Optical Terahertz Science and Technology (OTST)*, 2017.

- **D. R. Bacon**, A. D. Burnett, M. Swithenbank, C. Russell, L. Li, C. D. Wood, J. Cunningham, E. H. Linfield, A. G. Davies, P. Dean and J. R. Freeman. "Investigation into Free-space terahertz radiation from a LT-GaAs-on-quartz large-area photoconductive emitter," *UKSemiconductors*, 2017.

- **D. R. Bacon**, A. D. Burnett, M. Swithenbank, C. Russell, L. Li, C. D. Wood, J. Cunningham, E. H. Linfield, A. G. Davies, P. Dean and J. R. Freeman. "Investigation into Free-space terahertz radiation from a LT-GaAs-on-quartz large-area photoconductive emitter," Accepted for presentation at *The 42nd International Conference on Infrared, Millimeter, and Terahertz Waves (IRMMW-THz)*, 2017.

Contents

List of Figures

List of Tables

List of acronyms

ARC	Anti-reflective coating
BSI	Backside-illumination
BTC	Bound-to-continuum
BWO	Backward wave oscillators
CSL	Chirped superlattice
CW	Continuous wave
DC	Direct current
DM	Double metal
EO	Electro-optic
FEL	Free electron laser
FFT	Fast Fourier transform
FIR	Far-infrared
FSI	Front-side-illumination
FTIR	Fourier transform infrared spectroscopy
FWHM	Full-width-half-maximum

GaAs	Gallium arsenide
GRT	Gain recovery time
I-V	Current-voltage
IR	Infrared
L-I	Light-current
L:He	Liquid helium
LIV	Light-current-voltage
LO	Longitudinal optic
LoG	LT-GaAs-on-SI-GaAs
LoQ	LT-GaAs-on-quartz
LOT	Lift-off-transfer
LT	Low-temperature grown
MBE	Molecular beam epitaxy
MIR	Mid-infrared
ND	Neutral density
NDR	Negative differential resistance
PC	Photoconductive
PCB	Printed circuit board
PPD	Pump-probe delay
PTFE	Polytetrafluoroethylene
QCL	Quantum cascade laser
QW	Quantum well

RP	Resonant phonon
RTD	Resonant tunnelling diode
SI	Semi-insulating
SI-SP	Semi-insulating surface plasmon
SNR	Signal-to-noise ratio
SOS	Silicon-on-sapphire
TDS	Time-domain spectroscopy
THz	Terahertz
TO	Transverse optical
UV	Ultraviolet

Chapter 1

Introduction

The terahertz (THz) frequency region of the electromagnetic spectrum is commonly defined as being between 300 GHz and 10 THz, situated between lower frequency microwaves and infrared (IR) radiation. This is graphically indicated in Figure 1.1. This frequency range has also been referred to as T-rays, far-infrared (FIR), sub milli-meter waves and the THz-gap, owing to the historic lack of sources and detection methods that operate at these frequencies. However, relevantly recent interest in this frequency region has lead to rapid development in this area and its application in a range of industrial sectors.

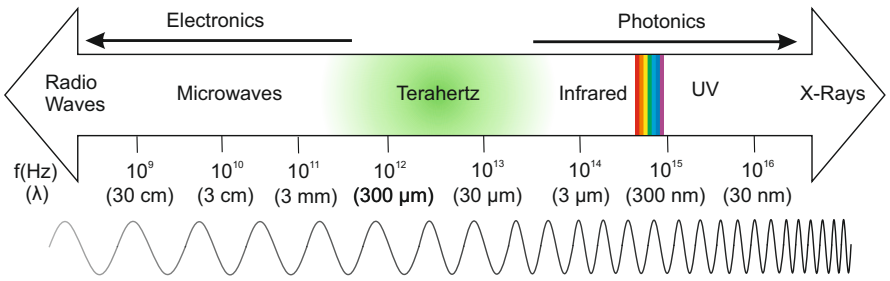

Figure 1.1: The electromagnetic spectrum highlighting the THz region in green. The 'rainbow' region of the spectrum represents visible light. This image is adapted from reference [1].

For example, the ability of THz radiation to pass through a range of nonpolar materials including fabrics, cardboard, plastics and paper packaging make it an ideal candidate for non-invasive inspection applications, for example in airport and postal security services [2]. It has been demonstrated as an effective technique for the non-destructive detection of concealed weapons, drugs and explosives [3,4]. This is aided by the fact that many polycrystalline mate-

rials, including drugs-of-abuse and explosive chemicals, exhibit characteristic spectral features in the THz region, owing to the excitation of both inter- and intra-molecular modes [5, 6]. THz radiation has also been used to probe electronic transitions of quantum dots [7, 8] and to manipulate quantum bits for computing applications [9]. Unlike X-rays, THz radiation is also non-ionising due to its smaller photon energy. This attribute, combined with its high absorption in water, make it an attractive prospect for use in medical applications, such as the detection of skin-cancer on human tissue [10]. This technique relies on the difference in water content between the effected and non-effected skin samples and has been demonstrated for both *in vivo* and *ex vivo* imaging at THz frequencies [11]. Furthermore, this has been used to detect the presence of breast [12] and colon cancer [13].

THz radiation has also proved of great interest to astronomers and meteorologists, as interstellar dust clouds also exhibit spectral artefacts in this region [14]. This data can reveal information about the composition of these clouds, as well as provide an incite into star formation within our galaxy [15,16]. Similar techniques have also been used to study variation in the earth's atmosphere and ozone layer over time, leading to climate change [17,18]. Other applications for THz radiation include high-frequency wireless communication [19, 20], the diagnosis of tooth decay through dental cavity imaging [21] and the non-destructive evaluation of paintings [22]. For a more detailed review on THz applications in a wide range of fields see references [14, 23–25].

1.1 Terahertz sources

The industrial impact of THz radiation has been limited by the lack of compact, high power sources operating in this frequency range. To attempt to bridge the 'THz-gap' the majority of techniques developed to date, broadly speaking, originate from the extension of two established areas. The first approach involves the up-conversion in frequency of signals generated through electronic means, such as gunn oscillators, Schottky diode multipliers and resonant tunnelling diodes (RTD). One example of these is a gallium arsenide (GaAs)-based planar Schottky diode that when cooled to 120 K has been demonstrated producing ~15 μW of output power at 1.7 THz [26]. Furthermore, the negative differential resistance (NDR) associated

with RTDs have been used to generate 23 μW at 342 GHz [27]. Unfortunately, these devices are limited to relatively low frequencies as capacitance and transit-time limitations result in high frequency roll-off [28]. Other sources which have shown much promise below 500 GHz include gyrotrons [29], backward wave oscillators (BWO) [30, 31] and free electron lasers (FEL) [32]. These all generate THz radiation by modulating, spinning or accelerating a beam of electrons inside an magnetic field. While these can provide a high-powered and tunable source of radiation, they do require a magnetic field in the order of 10s of Tesla to operate. This makes them impracticable for many of the applications discussed above.

The second approach is to down-convert higher-frequency and optical signals, normally generated through photonics or semiconductor-based lasers. Traditionally however, the lowest output frequency is limited by the semiconductor bandgap energy. Furthermore, the photon energy at these frequencies (4-40 meV) is similar to phonon resonances in many semiconducting materials, making it difficult to maintain a population inversion. This was overcome in 2002 with the invention of the first THz-quantum cascade laser (QCL) [33]. Since then, research dedicated to this device and advances in bandstructure engineering have lead to output powers >1 W [34], operating temperatures as high as 129 K [35] in continuous wave (CW) operation, and output frequencies ranging from 0.83 to 5 THz [36, 37]. However, despite this development these devices are still limited to cryogenic temperatures. These devices are discussed in detail in chapter 2. Another approach to down-converting optical signals is the generation of broadband THz radiation through photoconductive (PC) emission [38]. This involves the excitation of a semiconducting material, traditionally GaAs, with an ultra-short optical laser pulse. Research into different materials and electrode geometries has lead to IR-to-THz conversion efficiencies as high as $2.5x10^{-4}$ [39] and output powers ranging from 280 μW [40] upto 1.9 mW [41]. This is discussed in detail in chapter 3. Another means of generating THz radiation is through 'photomixing', where two CW optical signals at different frequencies are focused onto the surface of a semiconductor. The conductance of the material is modulated at the beating frequency of the two laser beams, generating coherent THz radiation at the difference frequency [42]. This method has been shown to produce output powers as high as 0.8 mW [43].

The recent development in amplified femtosecond lasers has brought about great interest in the generation of high-field THz radiation through optical rectification in non-linear crystals. These high-fields allow the coherent control of electronic, spin and ionic degrees of freedom in molecules and solid-state systems [44]. Optical rectification has been demonstrated to work with GaSe [45], LiNbO3 [46,47] and quasi-phase-matched GaAs [48]. However, one limitation to this technique is that phase-matching is required between the incident optical pulse and the THz radiation generated inside the crystal. One way of overcoming this issue is by tilting the crystal, such that the two pulses travel at the same speed through the crystal [46]. Alternatively, periodically-poled LiNbO3 crystals can be used, where the phase of the THz-radiation is flipped every half cycle to avoid 'walk-off' between the two pulses [49]. The generation of high energy pulses of THz radiation (5 μJ) has also been demonstrating using a gas-laser [50]. This method involves optically pumping a gas contained within a cavity, with the gas itself determining the output frequency. For instance, methanol is known to generate radiation at ~2.5 THz [51]. However, an issue with all of these techniques is that very expensive and bulky amplified femtosecond lasers are required, making them largely impractical for applications outside of academic research.

1.2 Terahertz detection methods

Generally speaking, all distinguished methods of THz detection can be divided into two categories: incoherent, where only the average power of the incident radiation is determined, and coherent, where both the magnitude and phase of the radiation field are resolved. Conventional methods of incoherent detection include the pyroelectric IR sensor [52], the Golay cell [53] and the more sensitive bolometer [54,55]. These can all be described as thermal detectors, as they are sensitive to a change in temperature caused by the incident THz radiation. The latter of these, the bolometer, is typically cooled through liquid helium to reduce thermal background noise, and employs a wheatstone bridge circuit with either silicon, germanium or InSb as a variable resistor [56]. As this detection scheme relies on heating and cooling of the sample, this limits the rate at which the detector can react and requires the THz radiation to be modulated prior to detection.

Methods of electrically detecting THz radiation include superconductor-insulator-superconductor (SIS) junctions [57, 58] and a single photon detector using a single-electron transistor, consisting of a quantum dot in a magnetic field [59]. For situations which require high frequency resolution such as space applications, heterodyne techniques using a planar Schottky-diode and a local oscillator have been demonstrated [18].

Two well-established optically-driven techniques for the coherent detection of THz radiation are PC [60] and electro-optic (EO)-sampling, the latter of which can be performed with a variety of non-linear crystals including LiTaO3, LiNbO3, ZnTe and GaP [61,62]. A comparison between these two methods concluded that PC detection provided greater sensitivity and a higher signal-to-noise ratio (SNR) between 0.1 and 3 THz [63]. However, this is dependent on many factors, including the materials used in both cases, the modulation frequency and the laser pulse parameters. This topic is discussed in detail in chapter 3.

1.3 Project motivation and thesis structure

While QCLs currently provide the best opportunity for a compact, high power and tunable source of THz radiation, the requirement for cryogenic temperatures and difficulties in mode-locking the device, discussed in chapters 2 and 4, mean that their is still much work to be done. This begins with a deeper understanding of the devices dynamic properties. In working towards this, new PC sources for time-domain spectroscopy (TDS) systems are required to generate higher fields and probe the carrier dynamics within the QCL.

This thesis begins in chapter 2 with a detailed introduction to THz-QCLs. Basic laser theory is introduced, along with an historic overview leading to the realisation of the first THz-QCL. Furthermore, an incite into the advantages and disadvantages of various active regions designs is provided.

The thesis continues in chapter 3 with a review of THz-TDS, discussing in detail the possible experimental arrangements and the various methods of THz emission and detection. Particular attention is given to the current limitations of the setup and improvements are proposed. Following that, a newly designed quartz-mounted PC device is introduced and

demonstrated as both an emitter and a detector. The improvements in output power, breakdown voltage and sensitivity, when used in detection, over the standard device and other techniques, is clear to see from the collected data. This is explained and understood.

In chapter 4 the gain recovery time (GRT) of a THz-QCL based on a bound-to-continuum (BTC) active region is measured using an adaptation of the THz-TDS setup, which is introduced in chapter 3. This parameter is of significant interest as it is thought to be heavily involved in the prevention of mode-locking in QCLs. To this end, a THz-pump-THz-probe technique is developed and used to study the dynamic properties of the device, with and without anti-reflective coating (ARC) applied to the facets of the device.

In the final experimental chapter (5), a THz-QCL incorporating a hybrid active region is investigated. By performing TDS on this ambipolar device, interesting incites into its gain dynamics below threshold are obtained. Furthermore, these findings have been reinforced through bandstructure simulations. Finally, the THz-pump-THz-probe technique is repeated on the hybrid device and reveals interesting findings regarding the carrier dynamics during the recovery process. Concluding remarks and possible future work are discussed in chapter 6.

Chapter 2

Terahertz Quantum Cascade Lasers

This chapter provides an overview of the historic groundwork leading up to the invention of the first THz-QCL. Section 2.1 discusses the general principles of the laser and the theory behind photon emission. Following that, various active regions and waveguide designs which have been developed to work at THz frequencies are introduced and explained in detail in section 2.3. The final section discusses the various means of carrier transport within the QCL.

2.1 Introduction to laser theory

For a simple two level system, the emission of a photon is caused by the transition of an electron from a higher energy state to lower energy state. The frequency of the emitted photon is equal to E_{12}/h, where E_{12} represents the energy difference between two discrete energy levels 1 and 2 and h is Planck's constant. A diagram of the two level system is shown in Figure 2.1, where (a) depicts the spontaneous emission of a photon which occurs in a random direction and phase, and at a random time. If an electron is populating the upper state (E_2) when a photon of equal energy (E_{12}) passes, the electron may be stimulated to fall to level 1 and emit a second photon of equal frequency, phase and in the same direction as the stimulating photon. This mechanism for photon amplification is known as stimulated emission and is depicted in Figure 2.1 (b). However, for there to be net gain a higher number of electrons must reside in the upper lasing level than in the lower energy level, known as a population inversion. The greater the population inversion, the higher the net gain available from this two level system. If this is not the case and more electrons reside in the lower energy level (E_1), (c) shows that

the incoming photon will be absorbed, promoting an electron from E_1 to the higher energy state, E_2.

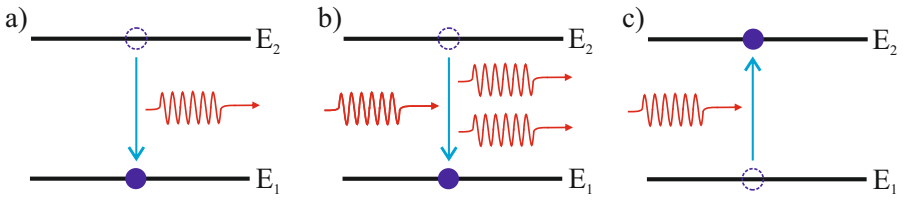

Figure 2.1: Schematic diagram of the three possible interactions between a photon and electron, within a two level system. (a) demonstrates spontaneous emission when an electron drops from E_2 to E_1 at any time and emits a photon of energy $E = E_2 - E_1$. (b) shows stimulated emission with an electron prompted to fall by an incoming photon of equal energy. (c) shows absorption of the photon providing the electron with enough energy to 'jump' up to E_2, having originally resided in E_1.

The simple but important concept of a population inversion resulted in the invention of the first laser by Theodore Maiman in 1960 [64]. This device generated radiation at wavelength of 649.3 nm from an optically pumped ruby crystal gain medium. A highly simplified illustration showing the operating principles of this device is given in Figure 2.2 a). Soon after, in 1962 the first semiconductor lasers were demonstrated simultaneously by two groups [65, 66]. These early devices only operated at cryogenic temperatures, through use of a GaAs p-n junction. The optical transition and electron-hole recombination occurred between edge states in the conduction and valence bands (Figure 2.2 b)). The concept and subsequent demonstration of a heterostructure laser, employing two different materials, was achieved by Kroemer and Alferov *et al.* between 1963 and 1969 [67]. Shortly after this JP Van der Ziel *et al.* presented the first example of an intersubband quantum well (QW) laser. This emits radiation through carrier recombination between individual energy states, which are confined within the QWs. This new design of laser, displayed in Figure 2.2 c), was shown to output radiation at 822 nm [68] using a GaAs-AlGaAs heterostructure.

The principle mechanism of a solid-state laser is very similar to a gas-based laser [69] and both can be simplified to diagram (2.2 a). They incorporate a gain medium possessing two or more discrete energy levels. The energy difference between these states relates to a desired output frequency and a population inversion is achieved through optical pumping with an external source. To drive electrons into the upper lasing level, it is important that

the energy of the optical pump be greater than the energy difference between the states. In a semiconductor laser (2.2 b), the minimum frequency of the emitted photon is determined by the material bandgap (E_{BG}), as electrons are stimulated from the edge of the conduction band (E_C) to the edge of the valence band (E_V), where they recombine with a hole. Either electrical or optical pumping can be used here. Finally, QW heterostructure lasers (2.2 c) are fabricated from alternating layers of two semiconducting materials with different bandgap energies. A narrow bandgap material is grown between two layers of a wider bandgap material, creating a QW with partially confined energy states known as subbands [70]. The energies of the subbands are dependent on the thickness of the QW and is governed very approximately by expression 2.1 [71], where n is an integer, m^* is the effective mass of the carrier (electron or hole) and L is the width of the QW. In this form of laser a photon is emitted when an electron falls from a confined state in the conduction band to a state the valence band. While the energy of the photon emitted from a heterostructure laser can be tuned by varying the layer thickness and thus the QW width, the lowest output frequency is still limited by the bandgap of the semiconductor used. It is noted here that all devices discussed so far can be described as 'bipolar', as the lasing mechanism includes electrons and holes.

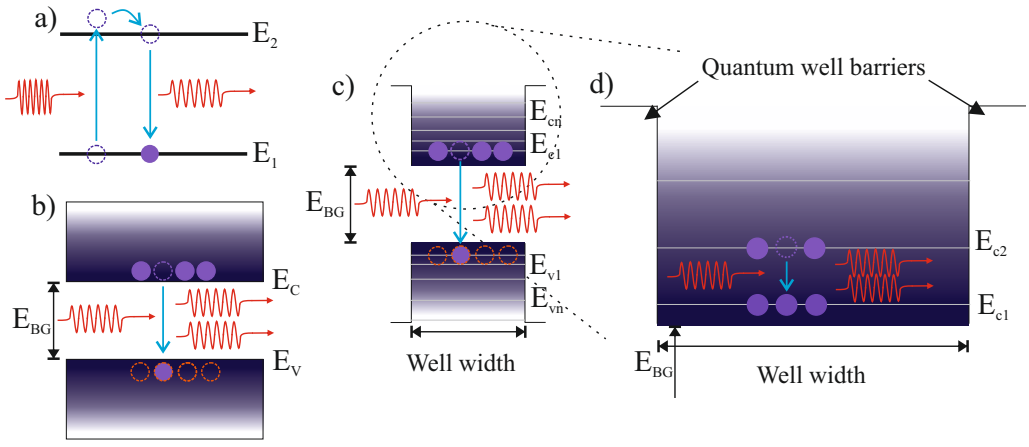

Figure 2.2: Schematic diagram of four different laser designs. (a) is a solid state/gas laser emission where electrons are optically pumped up to higher states, before falling and emitting a photon at energy $E = E_2 - E_1$. (b) is an interband laser where optical transitions occur between the conduction band E_C edge and the valence band E_V. In this case $E = E_{BG}$. (c) represent intersubband lasers where the optical transition occurs between subbands in the E_C and E_V, therefore $E > E_{BG}$. Finally (d) is an intersubband laser with electrons falling from E_{c2} to E_{c1} within the conduction band, therefore producing a photon of energy $E < E_{BG}$.

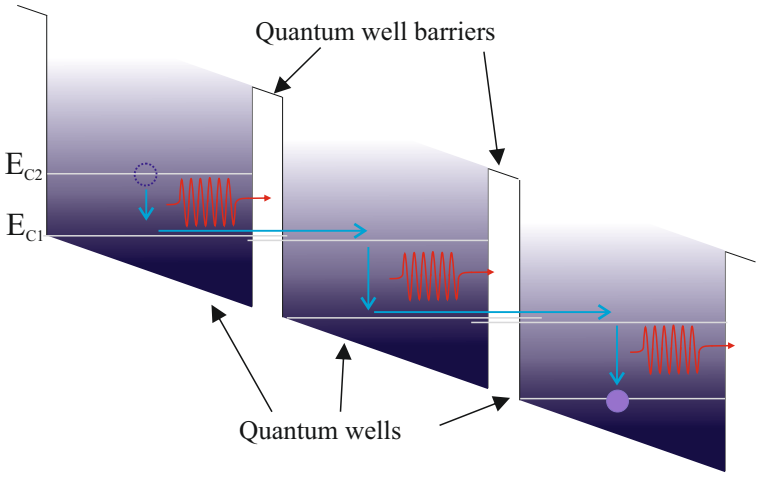

Figure 2.3: Simplified schematic diagram showing a lasing transitions in a QCL. The blue arrow shows the movement of the electrons over time as they drop from energy level E_{C2} to E_{C1} emitting a photon in each QW (curved red line). They proceed to tunnel through the QW barrier (labelled) and into the next QW.

$$E_n = \frac{h^2 n^2}{8m^* L^2} \tag{2.1}$$

2.2 Introduction to quantum cascade lasers

Shortly after the QW heterostructure laser was first demonstrated, in 1971 it was conceived by Kazarinov and Suris [72] that a population inversion could be generated between separate subbands of a QW periodic structure. This removes the use of holes from the lasing process and provided the possibility of light amplification through intersubband transitions within the conduction band of a heterostructure. It also means that energy and frequency of the emitted photon can be significantly reduced, compared with the earlier QW heterostructure laser (2.2 c), as it is no longer limited by the semiconductor bandgap. An illustration of this mechanism is shown in Figure 2.2 d). This concept formed the basis for the invention of the QCL, which was first demonstrated by Faist *et al.* [73] in 1994, after being suggested by Capasso *et al.* [74] and Liu [75] in 1986 and 1988 respectively. This unique device was formed from a AlInAs/GaInAs heterostructure, grown on an InP substrate. When cooled to cryogenic temperatures it had a maximum output power of 8 mW at a frequency of 71 THz (4.2 µm).

A simplified diagram of the QCL active region is displayed in Figure 2.3. While many vari-

ations of this design have been published, the basic principle of the QCL remains the same. By combining many QWs together into a chain or 'superlattice', the electronic wavefunctions penetrate through the barriers, formed from the wide bandgap semiconductor, and overlap multiple wells producing 'minibands' with other states. By applying a field across the device, the bandstructure bends and the electrons cascade 'downstream', emitting a photon in each QW by falling from energy level E_{C2} to E_{C1}. With this technique, a single electron can produce many photons, making it potentially more efficient than the other forms of laser displayed in figure 2.2. These photons are confined within a waveguide, between two partially reflective mirrors or facets. In practice each lasing module consists of several QWs, incorporating an 'injector' and 'extractor' region. This is to help couple electrons into and out of the QWs where the optical transition occurs. The barrier immediately 'upstream' from this QW is known as the injection barrier and is partly responsible for the rate at which electrons are transported into the upper lasing level (E_{C2}).

The first QCL [73] suffered from several issues which limited its operation to cryogenic temperatures. Two key issues are thermal backfilling and thermally activated phonon scattering. Thermal backfilling is when electrons are thermally activated into the lower-lasing level (E_{C1}), after having previously been transported 'downstream' into adjacent states. This decreases the population inversion between the two lasing states and therefore reduces the gain. Thermally activated phonon scattering is when electrons emit a longitudinal optic (LO) phonon, rather than a photon, as they fall from E_{C2} to E_{C1}. This again reduces the population inversion and decreases the overall gain. The gain of any laser, g, is related to its current density threshold, J_{th}, through expression 2.2 [73], in which Γ represents the overlap of the optical field with the active region, α_m is the combined mirror loss at each end of the cavity and β indicates the quality of the waveguide per unit length. α_w are the waveguide losses, which is dominated by free carrier absorption owing to the n+ doped semiconductor layers. For a QCL to lase, the gain must equal the total losses of the system (α_w+α_m). After threshold the gain is clamped to these losses. If its losses are too high or its gain is too low, the threshold current density (J_{th}) will not be reached and device will therefore not lase. It is noted here that in equation 2.2, it is assumed that the gain coefficient, g, is constant with a variation in current density. In reality this is not the case for QCLs.

$$J_{th} = \frac{\alpha_w + \alpha_m}{g\Gamma} = \frac{1}{g\beta} \tag{2.2}$$

Despite these issues and complexities, by 2002 the first mid-infrared (MIR)-QCL working in CW operation [76] and at room-temperature [77] had been demonstrated. Since 2002, MIR-QCLs have been reported which combine Watt-level output powers with CW operation at room-temperature [78].

2.3 Terahertz quantum cascade lasers

After the invention of the MIR-QCL, there were many attempts to re-engineer the device for the THz frequency range. It was important for the device to operate below the Reststrahlen band, a region of high reflectivity present in lll-V semiconductors ranging from 6 to 10 THz. However, there were several issues that needed to be overcome. Firstly, the intersubband lasing transition, E_{C2} - E_{C1}, required to generate frequencies in the region of 1 to 5 THz is between ~4 and 25 meV. This is significantly smaller than in MIR-QCLs and makes it difficult to selectively depopulate the lower-lasing level without inadvertently depopulating the upper-lasing level and increasing the parasitic current that does not contribute to the gain. Secondly, owing to the relatively small energy spacing between energy levels electron-electron, electron-impurity and interface-roughness scattering all become more significant and influence carrier transport within the device [79, 80]. Furthermore, the small energy spacing makes it more susceptible to the effects of heating, discussed in section 2.2. Lastly, the waveguide used for MIR-QCLs had to be re-engineered to work at THz frequencies, as the free-carrier losses of the waveguide is known to be proportional to the wavelength of the propagating radiation. Despite these issues, the first THz-QCL was demonstrated by Kohler *et al.* [33] in 2002. It consisted of a GaAs/AlGaAs heterostructure confined within a single plasmon waveguide (see section 2.3.2). It emitted a single frequency at 4.4 THz, had a output power of 2 mW and worked up to a maximum operational temperature of 50 K in pulsed mode.

Since then the development of various active region and waveguide designs, discussed

in sections 2.3.1 and 2.3.2 respectively, have led to a wealth of progress with devices being reported lasing at 3.5 THz [81], 2.1 THz [82], 1.9 THz [83] and as low as 0.83 THz [36] in the presence of a magnetic field. This is known to reduce the non-radiative scattering processes due to Landau-quantization [84], which results in a decrease in the threshold current of the device. This also helped to achieve the maximum operational temperature of 225 K [85]. With no external magnetic field applied, this record currently stands at ~200 K [86] and 129 K [35] for pulsed and CW operation respectively. The maximum output power achieved to date is ~1 W [34] for pulsed mode and 138 mW in CW [87].

2.3.1 Active-region designs

Figure 2.4 displays diagrammatic representations of the four main active region designs published to date. The first THz-QCL [33] used a chirped superlattice (CSL) (a) active region adapted from MIR-QCLs [88]. In a CSL design, the lasing transition occurs between two minibands, specifically between a lower energy state of the upper miniband and the highest energy state of a lower miniband. A population inversion is maintained owing to the ultra-fast elastic scattering of electrons out of the lower lasing level, through the lower miniband. However, this does result in greater thermal backfilling and non-radiative scatting between the upper and lower lasing levels, which limits its capabilities at higher temperatures. The second diagram shown in Figure 2.4 (b) is the BTC design. This design combines the extractor miniband from the CSL, with a diagonal lasing transition between a single upper-lasing level with a closely coupled injector state, and the miniband below in an adjacent QW. The spatial separation between the lasing levels is key to suppressing the undesirable transition between the injector state and lower lasing level. This technique ensures a high injection efficiency into the upper lasing level, while typically reducing the dipole matrix element between the upper and lower lasing levels. This concept was adapted from a three QW MIR-QCL design [89, 90], before being applied in a THz-QCL by Barbieri *et al.* [91] which lased at 2.9 THz. It was later varied to operate at lower frequencies [92]. Owing to reducing thermal backfilling a higher operational temperature and output power has been achieved with this active region, compared with CSL.

The third diagram, (c) in Figure 2.4, represents the resonant LO-phonon design. This was

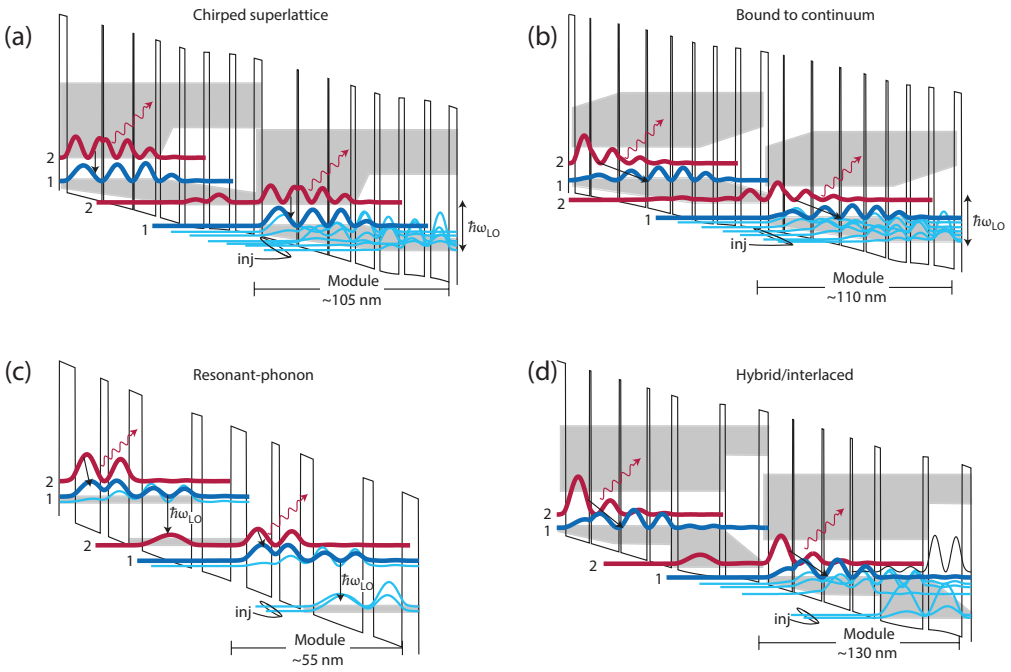

Figure 2.4: Simplified diagrams of four main types active region region. (a) is the CSL, (b) is the BTC, (c) is resonant phonon (RP) and (d) is the hybrid device, combining attributes from both b and c. The shaded area in each figure represents a miniband or tightly coupled region of states. This figure was originally taken from reference [37] and adapted for use in reference [1].

first developed by Williams *et al.* [93] in 2003. The key difference between this design and those previously discussed is the implementation of an LO-phonon (lattice vibration) assisted extraction technique, resulting in ultrafast depopulation of the lower lasing level. The extractor miniband has been removed and replaced with an additional energy state ~36 meV below the lower lasing level, in an adjacent QW to the now vertical lasing transition. The gap matches the energy of an LO-phonon in GaAs, therefore providing very fast resonant scattering. This assists in two respects: it creates a potential barrier against thermal backfilling and helps the lower lasing state to maintain a short lifetime, relative to the upper state. This is owing to the fact that as the temperature rises the LO-phonon population increases, stimulating more carriers to fall from the lower state. The disadvantage to engineering such an energy gap is that greater external voltage is typically required to initiate lasing. This results in increased leakage current, more heating and a poor CW performance. Since 2003, several adaptations of the original design have been demonstrated including a double phonon-depopulation scheme [94] and improved injection into the lasing module using an LO-phonon design [95]. In 2012, this design was used to achieve the highest operating temperature for a

THz-QCL [86].

The final diagram in Figure 2.4 (d) represents the interlaced design. This is more commonly known as a hybrid device, as it originates from the amalgamation of the LO-phonon and BTC designs with the intention of providing better high temperature performance. To achieve this the diagonal optical transition into a lower miniband was retained from the BTC design. An energy gap of ~36 meV is then engineered between the bottom of the miniband and the extraction state, providing LO-phonon de-population assistance out of the miniband. This approach was first demonstrated in 2005 by Scalari *et al.* [96], where a maximum operating temperature of 116 K was achieved in pulsed mode. Since then lower frequency hybrid designs have been reported [97], which are discussed in detail in chapter 5.

Other than the active region design, another important parameter to consider when growing a THz-QCL using molecular beam epitaxy (MBE) is what material to use, of which several options have been reported including InGaAs/InAlAs [73], InAs/AlSb [98] and AlGaAs/GaAs. This final combination was first demonstrated in a MIR-QCL in 1998 [99] but has since become the most commonly used material for THz-QCL, owing to its high carrier mobility, as well as AlAs and GaAs possessing almost identical lattice constants. This means that the concentration of aluminium can be used as an independent variable to change the height of the QW, without suffering from lattice dislocations. This is a very important factor to ensure good quality growth of the laser [100]. The level and profile of dopant atoms added in the growing process also has a significant effect on the performance of the device. Enough dopant atoms must be added to each lasing module to avoid carrier depletion and space-charge formation. However, at the same time the dopant concentration must be limited to reduce free-carrier absorption.

2.3.2 Waveguides

In order to achieve gain within the active region via optical feedback and direct radiation out of the laser, the propagating photons are confided within a waveguide between two partially reflective mirrors. The two principle types of waveguide used in THz-QCLs are the semi-

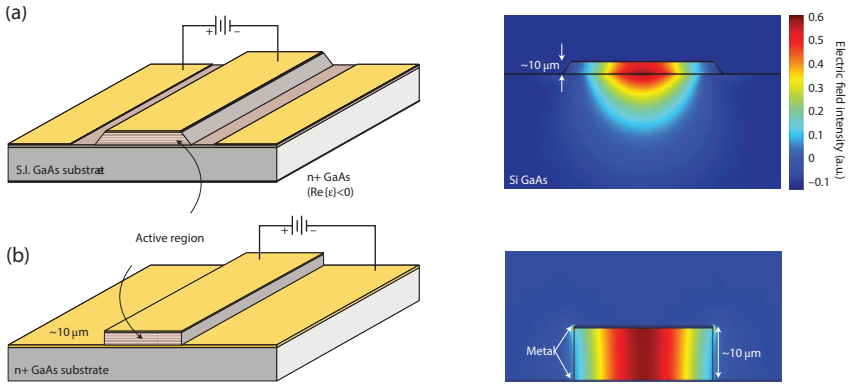

Figure 2.5: The two figures on the left show schematic diagrams of THz-QCLs confided within (a) a SI-SP waveguide and (b) a DM waveguide. The figures on the right depict side-on two-dimensional mode intensity patterns. This figure was originally taken from [37] and adapted for use in [1].

insulating surface plasmon (SI-SP) and the metal-metal or double metal (DM) waveguide. These are depicted in Figure 2.5 (a) and (b) respectively. In a SI-SP waveguide, the optical mode is confided between a metal contact, typically gold, fabricated on top of the device and highly doped (n^+) layer of GaAs below. At the upper metal/active region interface the surface plasmon is fully bound and confided to the active region. A surface plasmon is an electromagnetic oscillation which exists at the boundary between two media with dielectric constants of opposite signs. At the lower GaAs/active region interface, a quasi-plasmon exists meaning that only ~30 % of the optical mode is confined within the active region, as the majority leaks into the substrate below. This overlap reduces even further with increased wavelength. This waveguide was developed on the early THz-QCL designs [33], and was advantageous owing to its low loss of ~5 cm^{-1}, resulting in a relatively low threshold current density.

The alternative waveguide is the DM design which was first developed in 2005 by Hu *et al.* [101]. As the name suggests, the heavily doped GaAs layer is removed and replaced with a second layer of metal, fully confining the optical mode to the active region. Furthermore, the second metallic layer acts as a heat sink reducing the effects of heating within the device and allowing higher operating temperatures to be achieved [86]. However, this technique does result in losses as high as ~20 cm^{-1}. Furthermore, owing to the sub-wavelength confinement of the mode, the output radiation is extremely divergent relative to when using the SI-SP design. This significantly reduces the output power collected when using a DM waveg-

uide. Since the realisation of both types of waveguide, multiple variations of these have been demonstrated. These include waveguides formed from different materials [102] and those incorporating first-order and second-order distributed feedback gratings [103, 104] for single mode, tunable emission. However, these designs do typically add more complexity to the fabrication process.

2.4 Carrier transport and gain

When a THz-QCL is biased the carriers are forced in the direction of the applied electric field, perpendicular to the material layers. The key mechanisms for carrier transport both within and between the QWs have been investigated in detail in MIR-QCLs [79, 105, 106] and THz-QCLs [107, 108]. While intra-QW transport is dominated by carrier-carrier and LO-phonon scattering, the movement of carriers between QWs is believed to occur via resonant tunnelling [108]. Two distinct forms of this mechanism have been identified: a Fabry-Perot type coherent process and incoherent sequential tunnelling [74, 109]. The extent to which both of these contribute to carrier transport has been investigated in detail, with several reports suggesting that non-coherent sequential resonant tunnelling is the denominate process [110, 111] in MIR-QCLs. This is owing to dephasing mechanisms such as coulomb scattering [112], impurity scattering, as well as LO-phonon and acoustic phonon scattering [113]. It has been hypothesised that these effects are even more influential in THz-QCLs, owing to the smaller anti-crossing energy [108].

Figure 2.6 depicts a simplified bandstructure showing coherent tunnelling between two adjacent QWs, in which the lower laser level, $E_{1'}$, of QW_1 is separated from the upper lasing level, E_2, of QW_2 by $\Delta_{1'2}$. The blue arrows indicate the carrier direction of travel and suggest a coherent oscillation of the wave packet across the barrier. This is known to occur at a Rabi oscillation frequency (Ω) equal to $\Delta_{1'2}/\hbar$ [108]. This phenomenon has been explored in MIR-QCLs through use of pump-probe experiments [79, 105], a subject that will be discussed in detail in chapter 4. It has also been mathematically modelled in THz-QCLs [114, 115]. In the context of THz-QCLs, coherent carrier transport is important as it ensures very fast electron

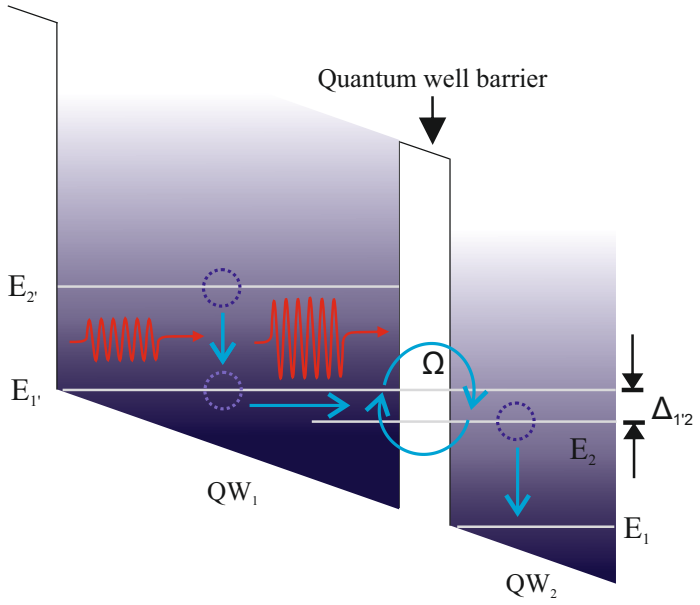

Figure 2.6: Depicts the coherent transport of carriers moving from left to right between two states ($E_{1'}$ and E_2) in adjacent QWs. This occurs at the Rabi frequency (Ω). This figure was adapted from a diagram in reference [108].

injection into the upper lasing level. Carrier scattering injection also assists in this process.

Although the means of carrier transport are very complex and differs with active region design, a basic understanding of the operating principles of a QCL can be obtained from a 2-level rate equation model. A diagram of this is provided in Figure 2.7, where the coloured arrows indicate carrier direction of travel. In this figure $(N_2 - N_1)W_{21}$ represents the stimulated emission rate, proportional the cavity photon density, and τ_{21} is the non-stimulated

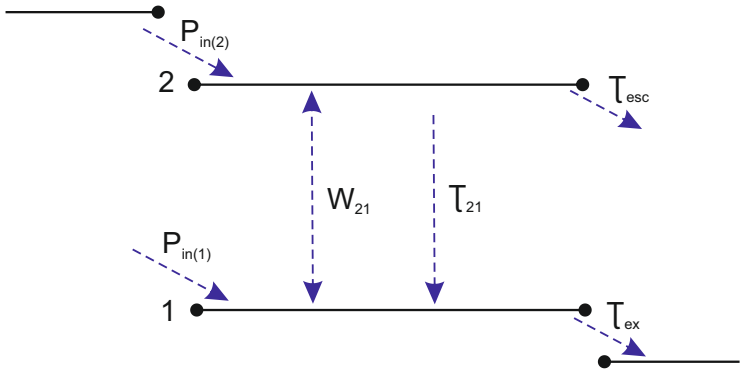

Figure 2.7: A simplified diagram of a two-level active region. This diagram is adapted from reference [116]. The unlabelled states at the top and bottom represent energy levels in the adjacent QWs. Lasing occurs been state 2 and 1.

emission lifetime (i.e. through spontaneous emission and scattering). $P_{in(2)}$ and $P_{in(1)}$ is the carrier transport rate directly into the upper and lower lasing level, while τ_2 and τ_{ex} are the lifetimes of the upper and lower lasing levels respectively. τ_{esc} is the lifetime for the non-radiative escape from the upper lasing level. The equivalent rate equations that govern the carrier population, N_2 and N_1, of the upper and lower lasing states, are given in 2.3 and 2.4 respectively [116]. When designing an active region it is important that $P_{in(1)}$ is kept as low as possible when the bandstructure is fully aligned, i.e. the majority of carrier are coupled directly into the upper lasing level. This helps to maintain high gain and reduces the threshold current density.

$$\frac{\mathrm{d}N_2}{\mathrm{d}t} = P_{in(2)} - \frac{N_2}{\tau_2} - (N_2 - N_1)W_{21} \tag{2.3}$$

$$\frac{\mathrm{d}N_1}{\mathrm{d}t} = P_{in(1)} - \frac{N_1}{\tau_{ex}} + \frac{N_2}{\tau_{21}} + (N_2 - N_1)W_{21} \tag{2.4}$$

By solving these two equations for the laser in equilibrium, i.e where $\frac{\mathrm{d}N}{\mathrm{d}t} = 0$, expressions 2.5 and 2.6 can be extracted in terms of the population inversion above (ΔN) and below (ΔN_0) threshold, where $W_{21} = 0$.

$$\Delta N = N_2 - N_1 = \frac{\left(1 - \frac{\tau_{ex}}{\tau_{21}}\right) P_{in(2)}\tau_2 - P_{in(1)}\tau_{ex}}{1 + W_{21}\left(\tau_2 + \tau_{ex} - \frac{\tau_{ex}\tau_2}{\tau_{21}}\right)} \tag{2.5}$$

$$\Delta N_0 = \left(1 - \frac{\tau_{ex}}{\tau_{21}}\right) P_{in(2)}\tau_2 - P_{in(1)}\tau_{ex} \tag{2.6}$$

where $P_{in(2)}$ and $P_{in(1)}$ can loosely be defined in term of, J, the current density, η, the injection efficiency and q, carrier charge. However, it is important to note that for QCLs, many parameters vary with current density therefore making this relationship non-linear.

$$P_{in(1)} = \frac{J\eta_1}{q} \tag{2.7}$$

$$P_{in(2)} = \frac{J\eta_2}{q} \tag{2.8}$$

In chapter 4 and 5 of this thesis, a pump-probe experiment is used to determine the gain recovery time of the THz-QCL. In relation to this simplified two-level system, a high-power pump pulse ($W_{21} \rightarrow \infty$) resonant with the energy gap ($E_2 - E_1$) is used to deplete the upper lasing (2) level, causing a sudden decrease in the population inversion ($N_2 - N_1$). To restore the gain to equilibrium the pump rate into the upper lasing level, $P_{in(2)}$, experiences a sudden increase. The amount of time taken for the gain to fully restore is measured through a low-power probe pulse. An expression for the peak material gain between the two lasing levels [117] is given in 2.9, where ε_0, L_p and λ are the vacuum permittivity, the width of single QCL period and the transition wavelength respectively. $2\gamma_{12}$ represents the full-width-half-maximum (FWHM) of the optical transition and z_{21} is the dipole matrix element between the upper and lower lasing states. This is defined in 2.10 and is a measure of the interaction strength between the two wavefunctions, ψ_1 and ψ_2. The gain coefficient, g, is equal to G_p/J.

$$G_p = \frac{4\pi q^2}{\varepsilon_0 n\lambda} \frac{z_{21}^2}{2\gamma_{12} L_p} \Delta N \tag{2.9}$$

$$z_{12} = \langle \psi_1 | z | \psi_2 \rangle = \int \psi_1^* (z)\, z \psi_2 (z)\, dz \tag{2.10}$$

2.4.1 Characteristic properties

A deeper understanding of the carrier transport mechanisms within the THz-QCL can been extracted from the light-current-voltage (LIV) characteristics of the device [114]. Other device-dependent properties which can be obtained from this data includes the maximum output power (P_{max}), the current density threshold (J_{th}), the maximum operating temperature (T_{max}) and the current at which lasing ceases. An example current-voltage (I-V) curve taken using a hybrid active region is plotted in black in Figure 2.8 a), with the corresponding light-current

(L-I) curve shown below (b) using the same X-axis scale[1]. A detailed description of the data acquisition process, together with the spectral output of a THz-QCL, is given in section 4.2 and the biasing conditions for this measurement are provided in the caption of Figure 2.8.

The important aspects of the LIV plots have been labelled with vertical dashed lines. The point at which the device begins to lase, I_{th}, corresponds to a slight kink in the I-V curve and a reduction in differential resistance. In terms of bandstructure alignment and with reference to Figure 2.6, this indicates that the extractor state in QW_1 ($E_{1'}$) and the injector/upper lasing (E_2) in QW_2 have began to align. Prior to this, much of the leakage current is flowing directly into the lower lasing level. Lasing commences when the increased gain, brought about by a rise in coupling efficiency, is equal to the losses in the system. A full description of J_{th} is given by equation 2.11. This combines the various properties of the active region and the waveguide design by combining equation 2.2 with 2.6, 2.9 and that for the gain coefficient.

$$J_{th} = \frac{1}{eta_2\tau_2\left(1-\frac{\tau_{ex}}{\tau_{21}}\right)-\eta_1\tau_{ex}}\left(\frac{\varepsilon_0\lambda n L_p\gamma_{21}}{4\pi q\beta z_{21}^2}\right) \tag{2.11}$$

After the maximum gain is reached and the power begins to rapidly reduce, a region of strong NDR is experienced. In the I-V curve (a), this equates to a reduction in current with rise in voltage. This is owing to the misalignment of states $E_{1'}$ and E_2 in adjacent QWs and is thought to be a direct consequence of the suppression of resonant tunnelling between states [106, 114]. It is also due to the loss of photo-induced current in the device as lasing ceases. A sharp drop in current can also be seen in the L-I curve (b). In many cases, the I-V characteristic of a device can reveal the existence of local field domains, or regions of uneven electric field distribution across the device [118]. This is typically caused by weakly coupled superlattice formation [119] and results in a jagged I-V plot, as different lasing periods align at different voltages. More information on this is given in section 5.2.

[1]This device was fabricated by Dr. Julie Zhu

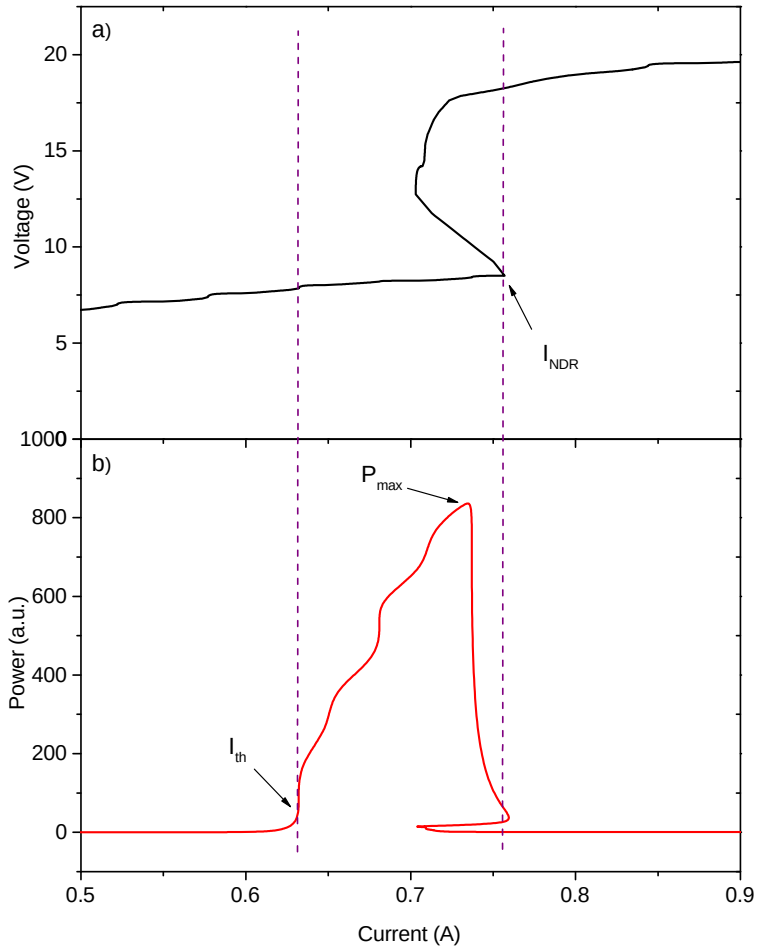

Figure 2.8: a) I-V and b) L-I curves taken with a 2.5-mm-long device lasing at 2.92 THz. It possessed a hybrid active region confided within an SI-SP waveguide. The data was taken using the experimental setup shown in Figure 4.2. The device was cooled to 10 K and electrically biased in pulsed mode, 10 kHz modulation frequency with a 2 % duty cycle. At this temperature P_{max} is equal to 35 mW and J_{th} is ~ 194 A cm^{-2}.

2.5 Conclusion

This chapter began with an introduction into laser theory, discussing concepts such as a population inversion, waveguide design and gain dynamics, the understanding of which are a prerequisite for the remainder of this thesis. A variety of different waveguides and active region designs were then introduced in section 2.2. Finally, the means of which THz-QCLs are typically characterised is discussed in section 2.4.1.

Chapter 3

Quartz-Mounted Free-Space Photoconductive Emitters and Detectors

This chapter focuses on the principles of THz-TDS, with emphasis on the various methods of emission and detection of THz radiation, as well as discussing its industrial and academic applications. In particular, PC emission using pulsed laser systems is examined. In the following sections, unique quartz-mounted PC devices for free-space THz emission and detection are introduced, explained and tested. The fabrication process required for these devices is explained before introducing experimental data and elaborating on the advantages of using such devices. Finally, the use of quartz-mounted devices is demonstrated in experimental applications.

3.1 Terahertz Time Domain Spectroscopy

THz-TDS [120–122] is a well established technique for the generation and time-resolved detection of free-space THz radiation. Using the unique properties of THz radiation, this can provide interesting information regarding a sample positioned within the beam. These properties, which have been briefly discussed in chapter 1, include the ability to transmit through cardboard, plastics and clothing and excite inter- and intra-molecular modes within many explosive substances and drugs-of-abuse [6]. This can provide a characteristic spectral signature

which is unique to the sample in question [5]. As well as security applications, these techniques have also proved successful in measuring the concentration of active ingredients in pharmaceutical products [123, 124] and for non-invasive identification of biochemicals [125, 126], such as DNA [127] and various crystalline and non-crystalline structured materials [128, 129]. Despite THz radiation being heavily absorbed in water, THz-TDS has also been used to investigate liquids including sugar, salt and protein solutions [130–132], and various alcohols [133]. One advantage THz-TDS has over other techniques, such as FIR spectroscopy [134], is that a relatively high SNR can be achieved without the need for a cryogenically cooled detection system [135]. Furthermore, it has been established that when imaging objects of a low refractive index, THz radiation provides a clearly image than X-rays [135]. Other advantages have been discussed in chapter 1.

Many of the studies referenced above use experimental arrangements similar to those discussed in this report. Diagrammatic representation of two types of setup are shown in Figure 3.1, illustrating both (a) a transmission and (b) a reflective arrangement. Throughout this project several variations on these have been used, employing different optical laser sources and detection methods. Each THz-TDS system was sourced by a mode-locked Ti:sapphire laser, generating pulses at a wavelength of 800 nm and a repetition rate of 80 MHz. However, the width of the optical pulse was system dependent but, generally speaking, was between 20 to 100 fs. Details regarding the different laser sources are provided with the corresponding data. The generated optical beam was split into two parts (9:1), the more powerful of which (the 'pump') was reflected off several optical mirrors before being focused down to a circular spot on the surface of a biased PC emitter. The diameter of the spot is limited by the wavelength of the radiation, but is also dependent on the width of the beam prior to being focused and the focal length of the convex lens.

A closer inspection of the two possible collection geometries is given in Figure 3.2. In reflection geometry the THz radiation generated by the emitter is collected from the laser excited surface, eliminating losses and dispersion from the substrate and resulting in higher bandwidths [136]. In this geometry, the incident optical beam must be focused through an off-axis parabolic mirror before reaching the emitter. This is then used to collect and collimate

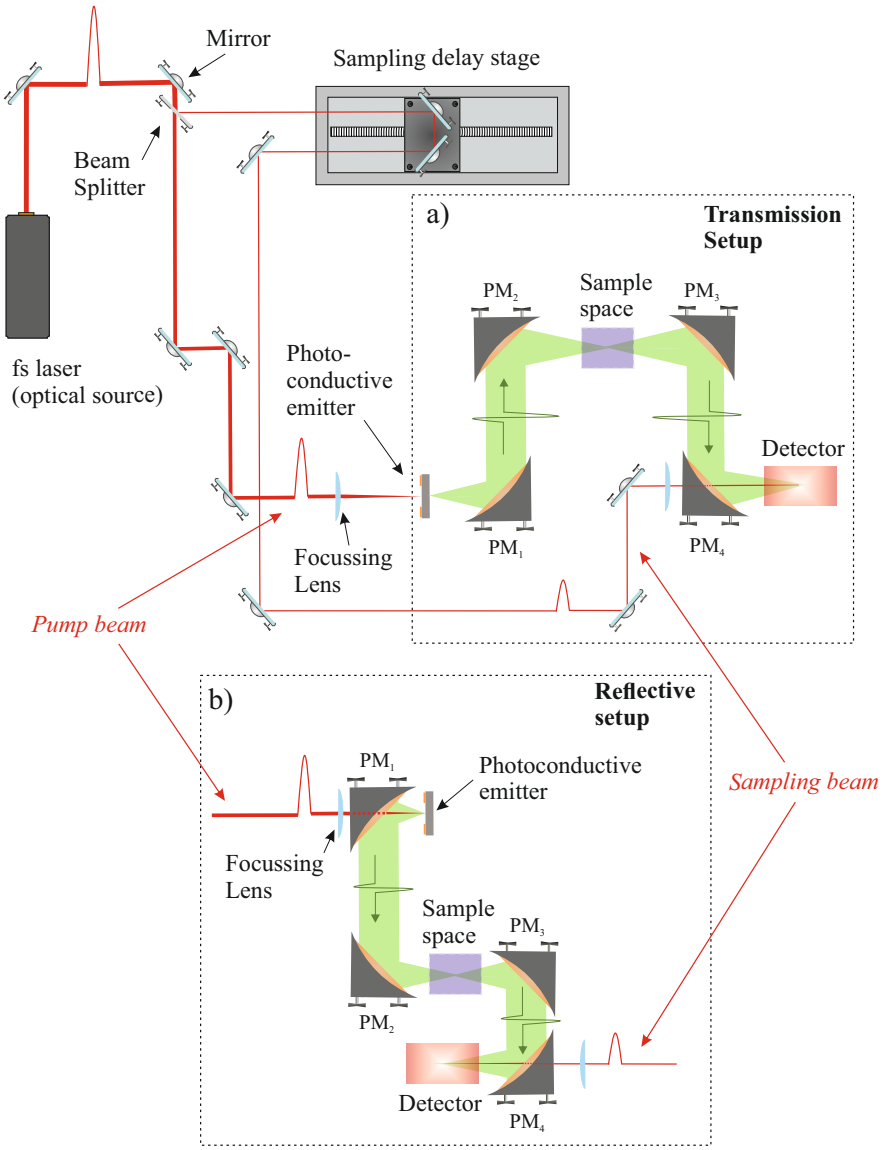

Figure 3.1: Schematic of TDS experimental setup in which both transmission (a) and reflective (b) collection arrangements are shown. The red and green beams represent the path of the optical and THz pulses respectively. The off-axis parabolic mirrors are labelled PM_1 to PM_4 on both setups. Both setups would typically be situated within a purge box (dashed line), to remove the effects of water vapour, present in the air.

the THz radiation. In Figure 3.1 b), this function is preformed by the first parabolic mirror (PM_1). In transmission geometry, however, radiation is collected from the substrate side of the PC device using a different set of off-axis parabolic mirrors. As shown in Figure 3.2, this means that the optical excitation and THz collection occur on opposite sides of the device. Due to the large refractive index difference between the active material, in this instance low-temperature grown (LT)-GaAs, and air, more of the power tends to radiate directly into the substrate. This is governed by the Fresnel equations for reflection and transmission coefficient [137], and results in a more powerful signal when collecting in the transmission geometry, than in reflection [138].

With the optical pulse incident on the surface of the emitter, a limited amount of THz radiation is typically generated through the photo-Dember effect [139]. In order to amplifier this signal the emitters need to be electrically biased. This can be done by using a direct current (DC) voltage and employing an optical chopper to modulate the signal or using a quasi-DC signal at a desired frequency. Electrical modulation typically results in a higher SNR, as it is more stable and higher modulation frequencies can be used, decreasing 1/f noise. Independent of the collection geometry, once the THz radiation is collected and collimated using the first off-axis parabolic mirror (PM_1), the second parabolic mirror (PM_2) focuses the radiation through the sample. In Figure 3.1 this is represented by a purple box. Briefly, by comparing the THz signal with and without the sample in place, one may obtain the complex index and dispersion of the sample [135]. Another set of off-axis parabolic mirrors (PM_3 and PM_4) can then been used to collect, collimate and refocus the radiation onto the detector.

The sampling beam, which was spilt from the more powerful pump beam using a 9:1 (transmission:reflection) beam splitter, is used in the detection of the THz signal. For this to occur the beam is first directed towards a motorised delay stage using optical mirrors. This allows the arrival time between the THz pulse and sampling pulse on the detector to be varied, the reason for which is discussed in detail in section 3.1.4. Fixed to the delay stage is either a set of optical mirrors or a retro-reflector, which are used to reflect the beam in the opposite direction such that it is parallel to the incoming beam. After the sampling pulse leaves the delay stage, it is focused through the final off-axis parabolic mirror (PM_4) and used in detec-

tion. Two separate coherent detection schemes were used in this project, the first being EO sampling [140] using an EO crystal paired with balanced photodiodes. The second method is PC detection, employing a similar device as used for emission. Both techniques are discussed in detail in sections 3.1.3 and 3.1.2, respectively. The signals are recorded using a lock-in amplifier, which is referenced to either the emitter bias-modulation frequency when the PC emitter is biased with a quasi-DC signal, or the optical chopper frequency when DC bias is used.

3.1.1 Photoconductive Emission

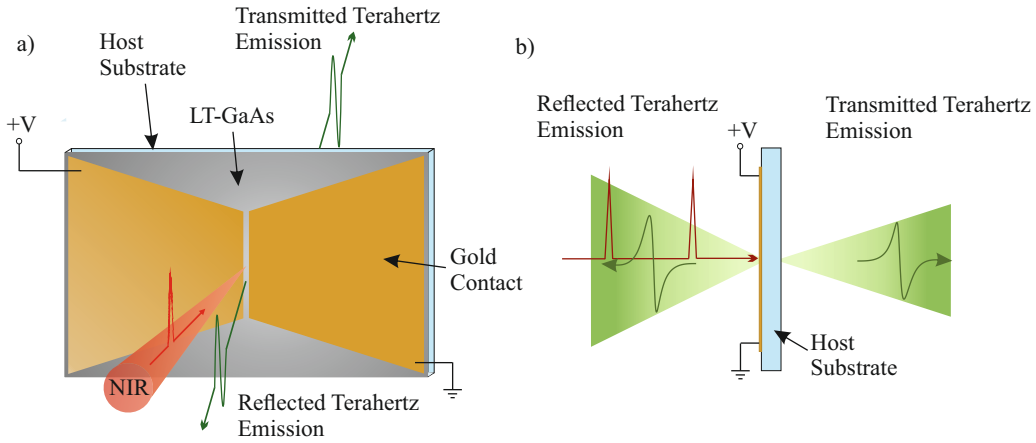

Figure 3.2: (a) Schematic diagram and (b) side-on diagram of a PC emitter indicating the angle of optical excitation (red) and the two possible collection geometries for the generated THz radiation (Green), transitive and reflective. Shown as an example, in this instance the active material is LT-GaAs, grown on a host substrate.

PC switches [141], triggered by femtosecond lasers are widely used for the generation of free-space THz radiation [60, 142]. PC emission is initiated when a femtosecond optical laser pulse, with energy greater than the semiconductor bandgap, is focused onto the PC material between a pair of biased electrodes. The bandstructure of an illuminated semiconductor is shown in Figure 3.3a). This generates electron-hole pairs and excites electrons into the conduction band. Due to an electric field being applied between the biased electrodes [38], depicted by the tilted bandstructure in Figure 3.3b), the negatively charged electrons and positively charged holes are accelerated in opposite directions. This transient current gives rise to a single cycle electromagnetic pulse, with a spectrum typically covering the 0.1–5 THz range [137]. The generated THz signal is proportional to the derivative of the transient photo-

current, which is expressed in equation 3.1. In this expression E_{THz} is the magnitude of the THz electric field far from the emitter, typically quoted in volts per centimetre, and I_{PC} is the generated photocurrent in the gap.

$$E_{THz} \propto \frac{dI_{PC}(t)}{dt} \tag{3.1}$$

$$E_{THz}(t) = \frac{\mu_0 \omega_0}{4\pi} \frac{sin\phi}{r} \frac{d}{dt_r} \left[I_{PC}(t_r) \right] \phi \tag{3.2}$$

$$E_{THz}(z,t) = -\frac{\mu_0 A}{4\pi z} \frac{dJ_s(t_r)}{dt_r} \tag{3.3}$$

However, this is a simplified expression and has been expanded in equation 3.2 [25] to take into account the magnetic permeability of free space μ_0. In many bulk semiconductors used for PC emission, electrons are believed to be the dominate carrier involved, as they are known to exhibit a higher mobility compared with holes [143, 144]. Other variables in this equation include the spot size of the optical beam ω_0, the far-field range from the device r and the angle perpendicular to the surface of the device ϕ. This expression uses a dipole approximation, as it assumes the active region is significantly smaller than the THz wavelength. For large areas emitters equation 3.3 [25] can be applied, where A represents the optically excited area, z is the distance from the emitter in meters and J_s is the idealized surface current density.

Examples of free-space THz pulses having been coupled from the surface of a PC emitter are illustrated in Figure 3.2 a) and b). When collecting in the far-field, the full cycle of the electric field exhibits both positive and negative peaks [145]. The magnitude of the first half-cycle is almost entirely dependent on the width of the incident optical pulse, whilst the size of the second peak is determined by the recapture time of the carriers within the material [146]. The THz power, SNR and bandwidth available from a PC material are dependent on a few fundamental parameters: the carrier lifetime, mobility, dark resistivity and breakdown voltage. A well-suited material will have a short carrier lifetime to ensure that the transient

photo-current is brief yielding a high bandwidth [60], a high mobility to ensure a large photo-current, a high dark resistivity to minimise excess heating from the applied bias, and a large breakdown voltage so that a high bias can be applied to maximise photo-current [147].

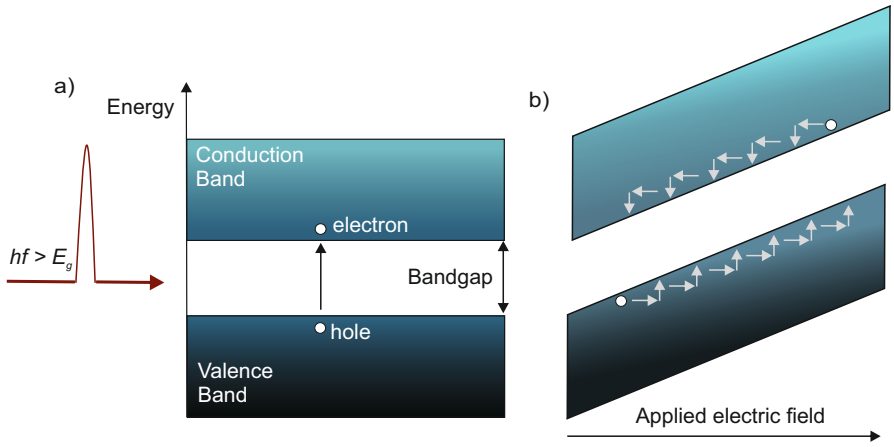

Figure 3.3: Bandstructure of a semiconductor as used in PC emission (a) Unbiased with incident optical photon (b) tilted bandstructure to indicate that an electric field is applied. E_g represents the bandgap energy of the semiconductor, situated between the conduction and valence bands. The red arrow represents the incident optical pulse.

When exciting at 800 nm, the best performing material for PC emission is LT-GaAs which incorporates excess arsenic trapping sites to ensure a very short carrier lifetime, (~300 fs) [148, 149]. It also exhibits very high breakdown fields (500 $\mathrm{kV\,cm^{-1}}$) [150] and high dark resistance, compared with semi-insulating (SI)-GaAs (10 - 100 $\mathrm{kV\,cm^{-1}}$) or silicon-on-sapphire (SOS) [142, 151]. In LT-GaAs, both of these properties are strongly dependent on the temperature of the post-grown annealing process [152]. Carrier mobility has been reported as high as 8000 $\mathrm{cm^2\,V^{-1}\,s^{-1}}$ [153] in SI-GaAs, significantly larger than in LT-GaAs (100 - 300 $\mathrm{cm^2\,V^{-1}\,s^{-1}}$) [149]. While carrier mobility is generally thought to be proportional to generation efficiency [135], when combined with low resistivity in SI-GaAs it can be seen as a drawback. This is because the higher photocurrent, owing to residual free-carriers, results in excess heating and thus causes an overall reduction in the generation efficiency [154]. This is especially the case when using powerful optical fluencies. LT-GaAs is typically fabricated by single crystal growth, either directly on a SI-GaAs wafer or separated by a thin insulating layer of AlAs or AlGaAs [152]. Electrodes are then fabricated directly on the LT-GaAs surface to form an LT-GaAs device on an SI-GaAs substrate.

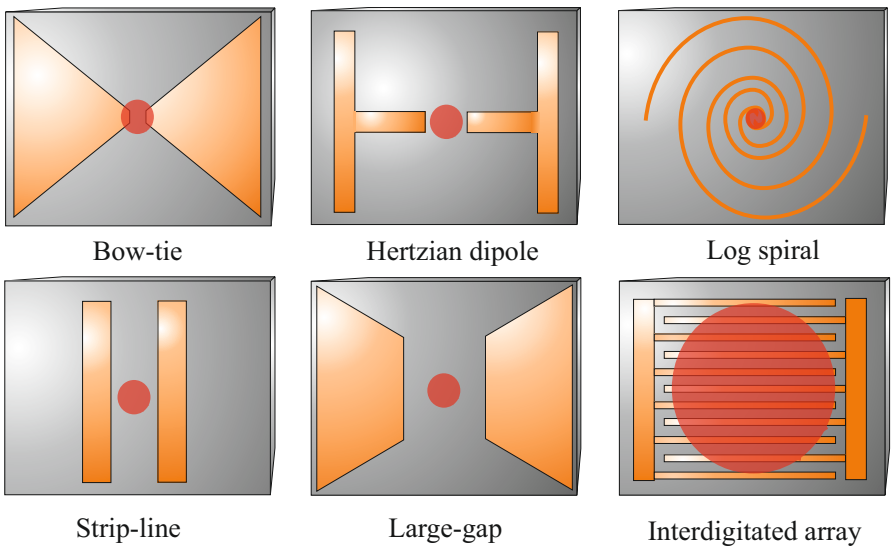

Figure 3.4: Six different designs of PC emitter. Each has been labelled and contains a red spot indicating the point of optical excitation.

Another important parameter dictating the behaviour of a PC emitter is the electrode design, as both the gap width and the general antenna shape influence the efficiency of the device [155]. To date many different designs have been reported, each with their own merit, including bow-tie, Hertzian dipole [156] and strip-line antennas [150, 157], as well as large-gap, sometimes referred to as parallel plate [158] and log spiral designs [41, 159]. Many of these are illustrated in Figure 3.4. It has been demonstrated that for a constant bias voltage and optical excitation power, the efficiency of the device is inversely proportional to the width of the electrode gap [135]. However, reducing the gap width tends to lower the breakdown voltage of the device, as well as increase the risk of saturation [154]. For large-gaps (>1 mm), the design of the electrodes makes very little difference to the efficiency of the device. However, the position of the optical excitation beam within the gap and its focal spot size have been shown to effect the output field and bandwidth of the device, owing to a near-anode enhancement [143, 160]. The key advantage to using large-gap devices is that significantly higher bias voltages and optical powers can be applied, compared with smaller gaps, allowing the generation of higher THz fields without damaging the device [146, 154]. Furthermore, the alignment procedure for large gap devices within a THz-TDS setup is relatively simple, as the generated photocurrent is less sensitive to movement of the PC emitter. It is for these reasons that a semi-large area electrode design, encorporating either a 100 or 200-μm-wide gap, was

used to collect the majority of the data shown in this report.

For small aperture devices (<100 μm) the design and shape of the electrodes can have a significant effect on the output spectrum of the device. A study conducted by Stone *et al.* [154] suggested that smaller PC gaps favoured higher frequency emission and that a broader frequency spectrum could be obtained by using pointed electrodes. Other research groups have found that the use of electrodes with sharp edges, such as the bow-tie design in Figure 3.4, can increase the efficiency of the device [150, 161]. An explanation for this is that by changing the shape of the electrodes and reducing the gap width, this alters the bias field experienced by the carriers and therefore their acceleration, recapture times and transient currents. If the electrode gap-width is significantly smaller than the THz wavelength the outputted radiation can be highly divergent, meaning a high proportion of it is not collected by the first parabolic mirror (PM_1). A silicon lens attached to the back of the substrate can solve this problem, as it is well index matched to the substrate and can collimate the radiation. The most commonly used type of silicon lens is the hyper-hemispherical [25]. This is only applicable when collecting the radiation in transmission, as opposed to reflective geometry. For a larger gap device, the radiation is not as divergent as it leaves the PC gap, so the advantages of using a silicon lens is not necessary as apparent.

Another factor which limits the efficiency of PC emitters is that they tend to saturate at high optical fluencies. In small gap emitters this is owing to the screening of the external electric field by an induced local field, created by the separation of carriers [162]. However, in large-aperture PC devices saturation is believed to be caused by the boundary conditions on the electric and magnetic fields on the surface of the device [138]. Both forms of saturation have become more common with owing to developments in amplified femtosecond lasers [163, 164].

To overcome this problem, large-area microstructure array emitters have been developed [165, 166]. These consist of interdigitated finger electrodes, with the excitation beam defocused and spread over the entire surface of the emitter. This decreases the optical intensity at each electrode and reduces the chance of saturation [151, 167]. A schematic of this geometry is shown in Figure 3.4, where each electrode spacing represents an individual strip-line design

with a small gap width (~5 μm). To avoid deconstructive interference of the generated THz radiation, either every other electrode gap is required to be optical opaque [165], or more efficiently, a microlens array can be employed to selectively illuminate the desired gaps [166]. Both these techniques have been shown to produce significantly higher THz fields than conventional emitters, in the region of 80 kV cm^{-1} [167]. There has also been much interest in the use of plasmonic contact gratings, where the spacing between the individual electrodes is in the order of several nanometers [168]. By illuminating just the anode this excites a surface plasmon allowing a large portion of the pump pulse through the grating. This effect, combined with very short carrier path length, has provided output powers as high as 1.9 mW [41].

3.1.2 Photoconductive Detection

Figure 3.5 depicts the experimental arrangement required for the PC detection of THz radiation. The fundamental mechanisms are similar to PC emission, described in section 3.1.1, and the types of device used are almost identical to those pictured in Figure 3.4. The setup on the left of the figure shows the probe branch of the same optical beam used to generate THz radiation, being focused onto a semiconducting material between two metal contacts. In PC detection no external bias is required. Instead the electron-hole pairs are generated by the incoming sampling pulse and are accelerated by the THz field, focused onto the surface, before the carriers are then recaptured. To detect the induced photocurrent, the PC detector is normally connected directly to a transimpedance amplifier with a tunable gain, which converts this into an equivalent voltage. This is typically then detected using a lock-in amplifier, which is referenced to either the optical chopping frequency or the electrical bias modulation frequency of the PC emitter. To map out the shape of the THz pulse, the path length of the sampling delay beam is varied, which alters the arrival time between the THz signal and the sampling pulse on the PC detector. As the optical pulse is significantly shorter than the THz pulse, which is proportional the induced photocurrent, the full THz pulse can be traced using this technique. As such, the magnitude and phase of the THz signal can be determined. This technique is discussed in more detail in section 3.1.4.

When using material with sub-picosecond carrier lifetimes such as LT-GaAs, the induced measurable photocurrent $J(t)$, is proportional to the THz field incident upon it E_{THz}, while

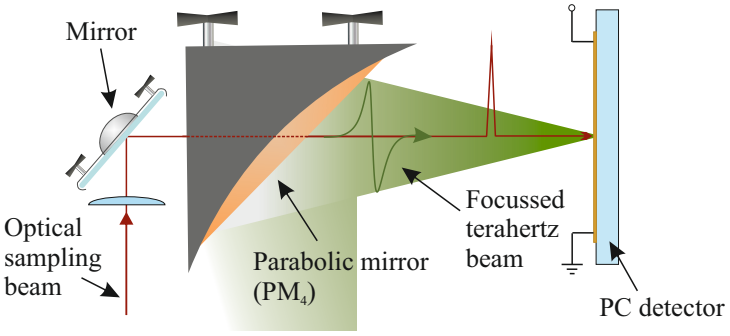

Figure 3.5: Experimental arrangement for PC detection. The optical and THz pulses are shown in red and green respectively. The parabolic mirror labelled PM_4 indicates its position in the THz-TDS setup in Figure 3.1, a) and b).

also being related to the transient surface conductivity σ_s, through equation 3.4 [25]. This suggests that the induced photocurrent is the convolution of the two parameters and that the photocurrent is also related to the carrier lifetime through the time-dependent conductivity. As such, for detection a good material will possess a very short carrier lifetime and high mobility to not limit the bandwidth of the system, as well as high dark resistivity as dark current is a source of noise [146].

$$J(t) = \int_{-\infty}^{t} \sigma_s (t - t') E_{THz}(t') dt' \tag{3.4}$$

To date, PC detection of THz radiation has been shown to work using several different materials including radiation-damaged SOS [120], LT-GaAs [142], SI-GaAs [169] and InP [170]. It has been established that LT-GaAs presents the best option for PC detection, as it possesses the shortest carrier lifetime and high dark resistance. While it has a significantly lower carrier mobility than SI-GaAs, this has been shown to cause SI-GaAs to saturate at low sampling optical powers [170]. In regards to the antenna design of the detector, a study performed by Jepsen *et al.* [171] reveals that the electrode gap width is inversely proportional to the detection sensitive. This is attributed to the fact that as the gap width reduces, this increases the laser intensity and thus the number of photogenerated carriers. Interestingly, the spectral shape of detected signal is dependent on the length of the electrodes. Designs with longer contacts, such as the strip-line design shown in Figure 3.4, tend to be more sensitive to lower frequencies.

3.1.3 Electro-optic Sampling

EO sampling [140] is a method of THz detection that utilises the Pockels effect [172]. Birefringence is induced in a non-linear crystal by a time-varying or constant electric field, which in this instance is the THz electric field. The induced birefringence is proportional to the THz field strength. The experimental arrangement shown in Figure 3.6 is used to probe this instantaneous change in birefringence and thus extract a relative value for the THz field incident on the crystal. Similar to PC detection described in section 3.1.2, the sampling beam is split from the pulse used to generate the THz signal. It is then focused onto the same point on the EO crystal as the THz radiation. The position of the delay stage can be varied to ensure that the optical and THz pulses arrive at the crystal simultaneously. The change in birefringence of the crystal, induced by the THz pulse, causes the linearly polarised optical beam to become slightly elliptical. The beam is then directed through a $\lambda/4$ plate, which, if it was still linearly polarised would cause it to become circularly polarised in the same orientation. However, as it is now elliptical in shape, the beam is split into its uneven orthogonal X and Y components, which are then divided using a Wollaston prism. The difference in intensity between the two orthogonal components is detected using balanced photodiodes, the linear output of which is connected to a lock-in amplifier. The incident THz field can be calculated from this signal using equation 3.5, where I_y and I_x are the optical intensities on each diode and I_s is the difference between them. I_0 represents the beam intensity with no THz signal, ω is the angular frequency and n_0 is the refractive index of the crystal at 800 nm. L is the length of the EO crystal, r_{41} is the EO coefficient and c is the speed of light in a vacuum. The full evolution of the polarisation of the optical sampling beam is shown in Figure 3.6, with and without the presence of THz radiation. To map out of the profile of the THz field the same technique described in section 3.1.2 in used.

$$I_s = I_y - I_x = \frac{I_0 \omega L}{c} {n_O}^3 r_{41} E_{THz} \tag{3.5}$$

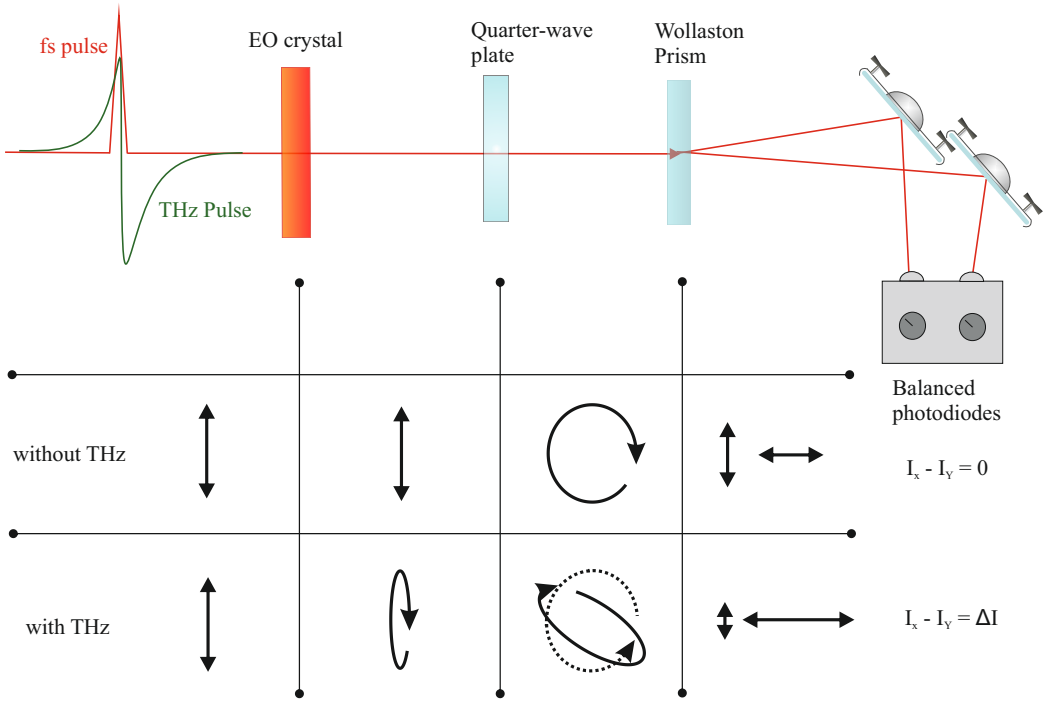

Figure 3.6: First row illustrates a close-up of the experimental setup for EO detection (original shown in Figure 3.1. Bottom and middle rows display the polarisation of the incident optical pulse, with and without THz radiation present respectively.

A disadvantage of using this detection method is that as the two pulses propagate through the EO crystal at different velocities, eventually the pulses destructively interfere with each other. As such, this creates a frequency dependent coherence length defined by equation 3.6 [161], where L_C is the coherence length, n_{eff} is the effective refractive index of the crystal at THz, ω_{THz}, and optical, ω_{opt}, frequencies. From the equation it can be shown that the coherence length is shorter for higher frequencies and therefore a thin crystal will allow the detection of higher frequencies as the interaction time between the pulses is reduced [173]. However, a thin EO crystal will decrease detection sensitivity and so there is a compromise to be made between bandwidth and sensitivity. Another disadvantage of using thin EO crystals for this purpose is the close proximity of reflections in the time-domain, which will be discussed in detail in section 3.1.5. This technique has been shown to work with various EO crystals including ZnTe [174, 175], GaP [176], GaSe [177] and $LiNbO_3$ [61]. ZnTe is a popular option as it is well velocity-matched at 800 nm and has a large EO coefficient, (3.9 pm V^{-1}) compared with GaP (1 pm V^{-1}) [25]. However, the transverse optical (TO) phonon absorption in ZnTe at 5.3 THz limits its usefulness for high frequency spectroscopy of materials.

$$L_C\left(\omega_{THz}\right) = \frac{c}{\omega_{THz}\left|n_{eff}\left(\omega_{opt}\right) - n_{eff}\left(\omega_{THz}\right)\right|} \tag{3.6}$$

3.1.4 Time-domain Sampling and spectra acquisition

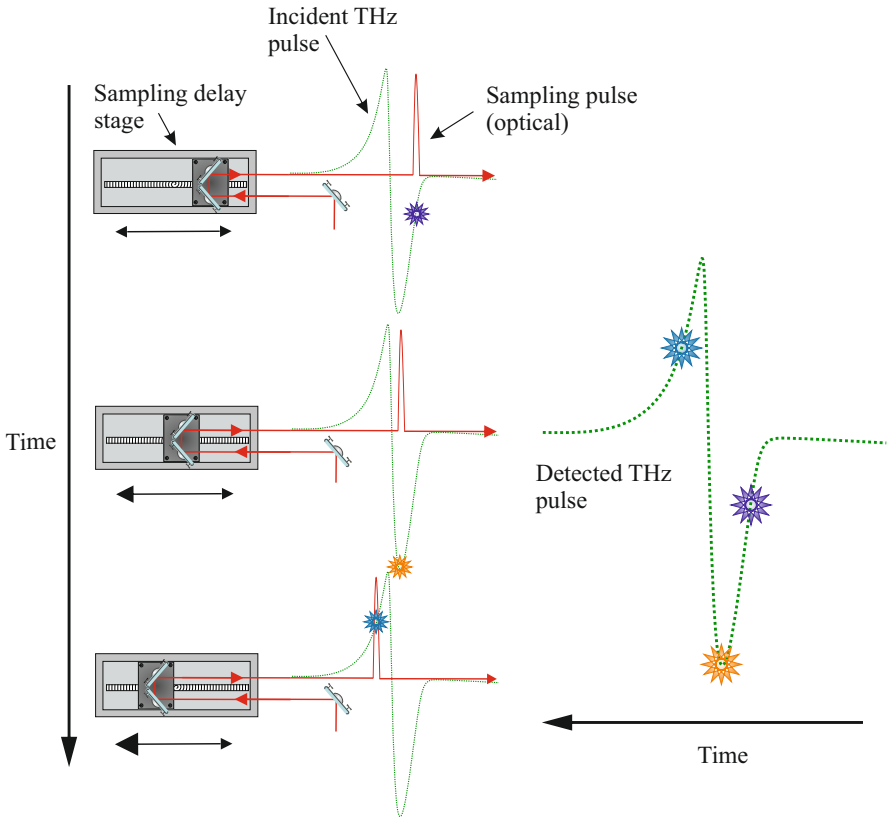

Figure 3.7: THz pulse sampling using the translation of the optical pulse with movement of the mechanical delay stage. The red curve represents the sampling optical pulse and the green dotting curve is the THz pulse. Random sampled points on the THz pulse are represented by purple, yellow and blue spots.

A significant advantage to using PC detection or EO sampling is that they enable the coherent measurement of the THz pulse, meaning both the phase and the magnitude of the detectable signal is recoverable. This is in contrast to incoherent methods of THz detection, such as a liquid helium cooled bolometer or pyro-electric detectors, which only sense a time averaged THz power. To achieve this the mechanical delay line, which in this example is placed in the sampling beam path and enabled using a motion controller, is systematically moved altering the optical path length of the sampling beam. This, therefore, varies the arrival

time between optical and THz pulses on the detector. It is noted here that the same effect can be achieved by placing the mechanical delay line in the pump beam path and fixing the length of the sampling beam. Figure 3.7 shows how the full profile of the time-domain THz pulse can be formed by systematically stepping the delay line, allowing a relative value for THz signal to be extracted for each point in time as the two pulses overlap. This is made possible by the fact that the ultrashort optical pulse, typically between 20 to 100-fs-long, is used to sample the THz pulse which is in the order of several picoseconds. The resolution in the time-domain is controlled by the predetermined step size of the scan and each data point is averaged within the lockin-amplifier to improve the SNR. All data is accumulated and plotted using LabView software, either point-by-point as the scan is performed or at the end of the scan. This requires storing the data in either the motion controller or the lockin-amplifier. A fast Fourier transform (FFT) is performed on the time-domain data to establish the frequency components present. The resolution in the frequency-domain is dependent on the length of scan in the time-domain.

3.1.5 System constraints

For THz-TDS, driven by PC switches, to be a viable option in many of the applications discussed in section 3.1, two potential problems have to be overcome. Firstly, as a pulse of THz radiation is transmitted through a sample it tends to disperse and attenuate, contributing to a loss in signal. The dispersion of the THz pulse is owing to different frequencies propagating through the medium at different speeds [25]. This is made worse by the fact that thicker samples tend to yield better results, as they are more sensitive to interactions with the passing radiation. Consequently, high SNRs, using powerful PC emitters and sensitive detection schemes are both vitally important to penetrate and measure a range of samples. However, when generating free-space broadband THz radiation using LT-GaAs-on-SI-GaAs (LoG) PC emitters, the risk of over-biasing or exciting it with too high an optical pump power is likely, and can result in permanent damage to the emitter. This limits the output power available from the device. A picture of an LoG emitter having sustained damage due to over-biasing is shown in Figure 3.8. This typically results in an instantaneous drop in resistive across the gap and a loss in output power from the device. The reasons why this occurs are discussed in the following sections.

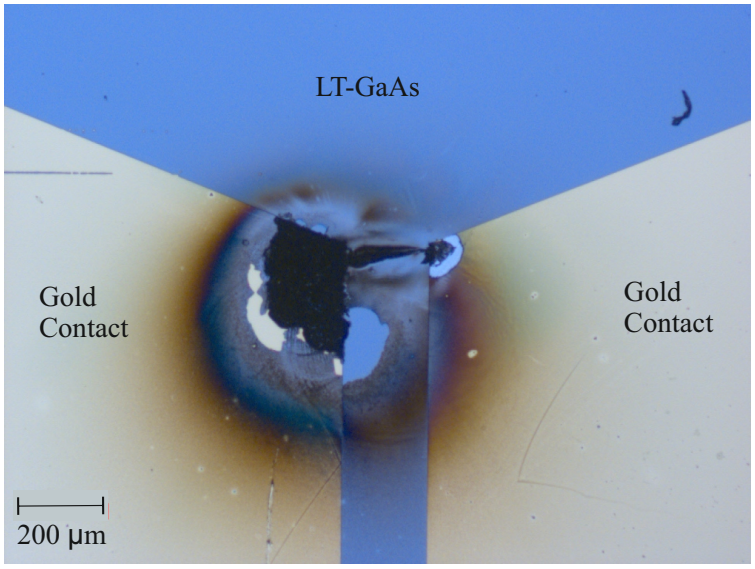

Figure 3.8: PC emitter with a parallel plate electrode design incorporating a 200-µm-wide gap. This device is fabricated using LT-GaAs-on-SI-GaAs and has been over-biased, resulting in a shorting over the gap.

Secondly, when an electromagnetic wave propagates through a material, each interface it encounters causes a certain percentage of it to be reflected. The reflectivity of the boundary is governed by the Fresnel equations [25], but for a situation when a propagating pulse is perpendicular to the interface, the reflectivity is proportional to the ratio of the refractive indexes of the two materials. The diagram shown in Figure 3.9 illustrates a THz pulse passing through a sample. Due to the partial containment of the pulse inside the sample, the initial attenuated output pulse is followed by echoes of the original incident pulse. The time, t, between the reflections is related to the refractive index and thickness of the sample, n and L, through equation 3.7.

$$t = \frac{2nL}{c} \tag{3.7}$$

In a THz-TDS arrangement, such as those illustrated in Figure 3.1, these reflections occur from any sample being placed in the THz beam, including the substrate of the PC emitter and detector, and the EO crystal. As the frequency resolution of the spectrum, obtained from

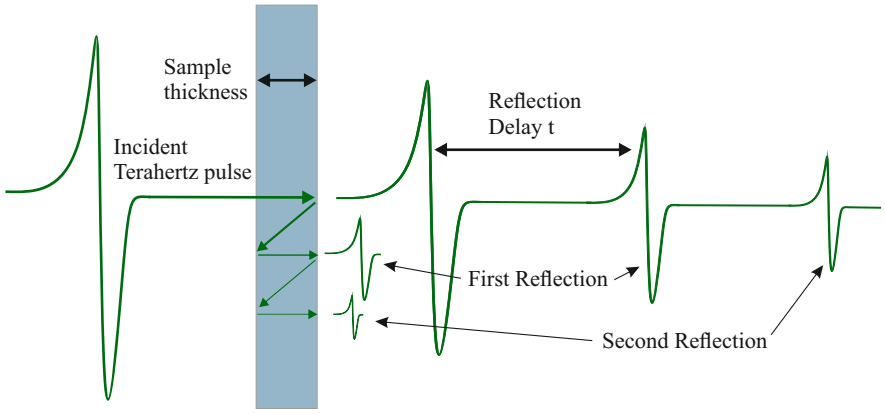

Figure 3.9: The production of system reflections as the THz pulse passes through a medium.

performing an FFT, is proportional to the length of scan in the time-domain this creates a problem, as to include these time-domain reflections in time windowed FFT would cause oscillations to appear in the frequency domain [178]. This is owing to the collection of spectral information from different sized THz pulses. This could potentially hide narrow spectral artefacts and make the data misleading. While truncating the data before the first reflection would prevent these oscillations, using a thin EO crystal to ensure a high bandwidth will result in low frequency resolution, which could make distinguishing narrow linewidth absorptions difficult. There have been several attempts to remove these reflections by adding a thin layer of ARC to the EO crystal, such as chromium to GaP [178–180]. However, this typically results in a significant reduction in the overall detected signal, due to absorption of the incident THz pulse [155]. Despite the emergence of post-measurement mathematical techniques to help remove reflections [181–183], they ultimately still remain an issue and limit the frequency resolution of the system.

3.2 Introduction to quartz-mounted photoconductive emitters and detectors

The use of LT-GaAs epitaxially transferred onto quartz substrates for high power broadband free-space emission and sensitive detection of THz radiation was inspired by its successful application in on-chip THz waveguide guides [184, 185] and originated as a concept for use in the experiments shown in chapters 4 and 5. In these chapters, high powered PC emitters are required to couple as high a THz field as possible into the facet of THz-QCL [37, 186]. However,

the previously used devices, fabricated directly onto their SI-GaAs growth substrate, were not able to generate the output field required for this measurement and were very susceptible to lasting damage by being over-biased. The devices presented here have helped to overcome these issues. Furthermore, owing to the success of these devices, they have since been used in numerous applications discussed in section 3.10. To date, four examples of free-space THz radiation emission have been demonstrated using LT-GaAs bonded with sapphire [151,187–189]. However, these did not provide a comprehensive comparison between lift-off-transfer (LOT) devices and devices fabricated 'as-grown' on the SI-GaAs substrate, the latter of which are very widely used. In this work, z-cut quartz has been chosen as a substrate as it possesses a significantly higher electrical resistivity [190], when compared with SI-GaAs [147]. It also exhibits low-losses in the THz region [191], and is transparent to 800 nm light. This provides the option to perform through-substrate illumination of the PC switch. Its low refractive index in the THz region of approximately 1.9 [192], compared to 3.8 in SI-GaAs [122], can also be a useful attribute in THz-TDS systems. Reasons for this are discussed in section 3.4.

3.3 Fabrication

This section begins by discussing the initial fabrication procedure at the start of the project, which was used to construct PC devices using LT-GaAs on its SI-GaAs growth substrate. This process was later adapted to incorporate an epitaxial lift-off step, removing the LT-GaAs active layer from its original substrate and replacing it with quartz. As such, this is employing a technique commonly used in on-chip THz waveguide design. A detailed description of this process is also provided, along with any improvements made, either to save time, material or increase yield. Furthermore, any revisions made to the process required for devices made on thick substrates are also discussed.

3.3.1 Fabrication process on an SI-GaAs substrate

In the initial stages of the project, the PC devices used consisted of a 2-µm-thick layer of LT-GaAs grown at 210 °C, using molecular beam epitaxy, on a 100-nm-thick sacrificial AlAs layer, itself grown on a 500-µm-thick SI-GaAs wafer. As metal contacts were attached directly

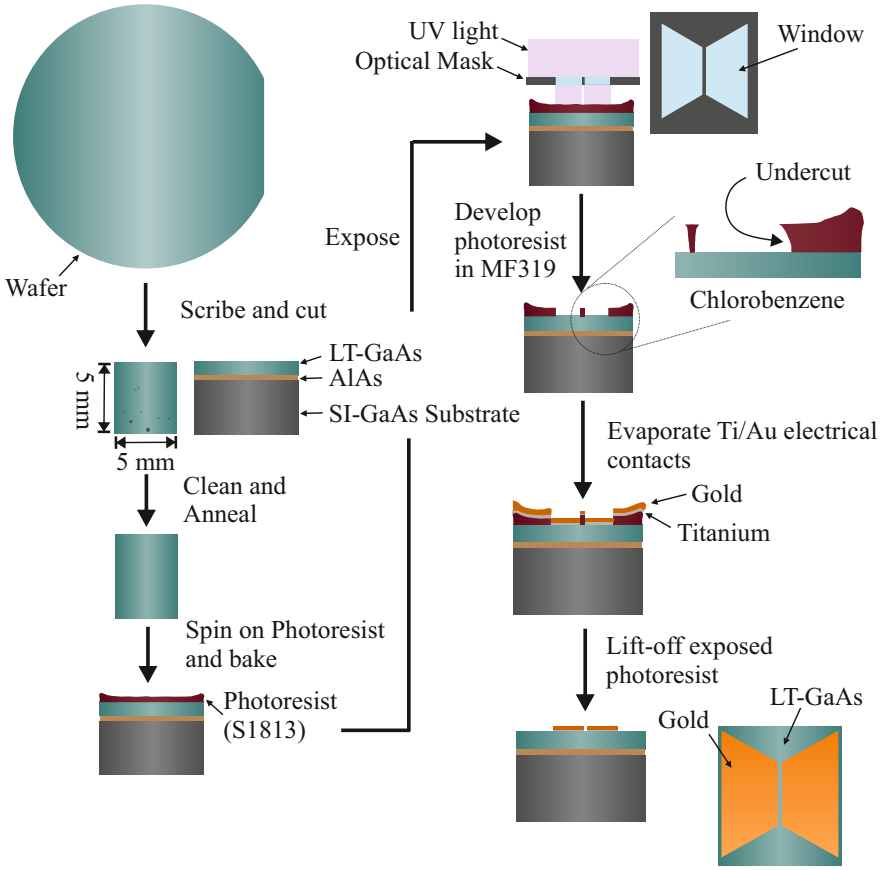

Figure 3.10: Shows the detailed steps used to fabricate a LT-GaAs PC device on the SI-GaAs substrate (LoG devices), which the LT-GaAs is originally grown on.

to the surface of the LT-GaAs, this type of device is referred to as LoG (LT-GaAs-on-SI-GaAs). To achieve this the fabrication procedure shown in Figure 3.10 was followed, beginning with the scribing and cutting of a 50-mm-diameter wafer. The wafer was cut into 5 mm^2 pieces, placed in a beaker containing acetone and positioned in an ultrasonic bath for 5 minutes on 10 % power to avoid damaging them. This process was then repeated using isopropyl alcohol (IPA) to remove any inorganic contaminants left on the surface. The final step of the cleaning process involved placing the sample onto a hot plate at 200 °C for 5 minutes, to remove any excess moisture. The sample was then placed in a rapid thermal annealer for 15 minutes at 575 °C, to increase resistivity [193]. This length of time and temperature was chosen as it provided a good compromised between the carrier lifetime and resistivity in LT-GaAs [194].

Once removed from the annealer, positive photoresist (S1813) was added to the top of the wafer using a pipette, before being placed on a spinner at 4000 rpm for 30 seconds. The sample

was then baked on a hotplate at 115 °C for 4 minutes. It was then placed in a mask-aligner (Karl Suss MJB3) where it underwent contact photolithography and was exposed to ultraviolet (UV)-light (wavelength of 310 nm) through a darkfield optical mask. The exposure time depends on the intensity of light but is typically between 2 to 4 seconds. Each sample was then developed in photo-developer (MF319) for approximately 1 minute, which removes any photoresist that has been exposed to UV-light. A 30 second-long dip in chlorobenzene is often used prior to development to harden the surface of the photoresist. This slows the development process of the surface layer, relative to the photoresist underneath, ensuring a substantial undercut which is vitally important for lift-off at the end of the fabrication process. The sample was then rinsed in DI-water, dried using a nitrogen gun and inspected under a microscope. Assuming all the desired photoresist has been removed, the sample could be positioned up-side-down in a thermal evaporator, where, in a low vacuum environment ($< 1.9x10^{-6}$mbar), ~10 nm of adhesive titanium and 150 nm of gold were evaporated onto the surface of the LT-GaAs. Once completed and cooled, the unexposed photoresist and the unwanted gold were removed by placing the sample back in a beaker of acetone for 5 minutes, in an ultrasonic bath. An example of a fully fabricated LoG device is shown in Figure 3.11. The remaining metal acts as electrical contacts, allowing bias to be applied across the PC gap. Bulk SI-GaAs has also traditionally been used as a material for PC emission and detection. To obtain typically resistance values for this material and to determine its sensitivity to 800 nm light, a bulk SI-GaAs device was also required. The fabrication procedure was very similar to that described above, the one notable difference being the absence of the annealing step as no LT-GaAs or AlAs layers are present.

3.3.2 Fabrication Process on an quartz Substrate

As the project progressed the need for a more reliable, durable and high-powered PC emitter and sensitive detection scheme brought about the realisation of an LoQ device. The fabrication procedure for a typical LoQ device is shown in Figure 3.12. The starting wafer (LT-GaAs grown on an SI-GaAs substrate) is precisely the same as that used in the fabrication of LoG devices. However, due to reasons described later in the section, the wafer can be scribed and diced into significantly smaller pieces, ~2.5 mm^2. After the cleaning and annealing process described in section 3.3.1, the fabrication procedure is similar to that described in reference [185].

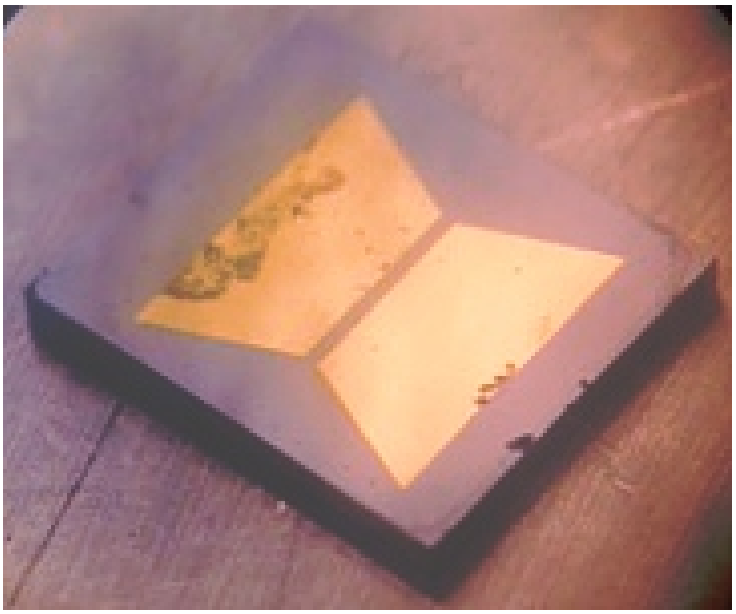

Figure 3.11: LoG PC device with 400-µm-wide semi-large-area slot electrode design. This picture was taken using an optical microscope.

The 2-µm-thick LT-GaAs layer on the top of the wafer undergoes epitaxial lift-off where it is removed from its growth SI-GaAs substrate. In order to achieve this, protective wax (Wax W, Apiezon) was melted (~100 °C) onto the surface of the LT-GaAs, before a swab dipped in trichloroethylene was used to carefully remove any wax near the edge of the sample, as this could cause complications in the proceeding lift-off. The sample was then placed in a sulphuric etch solution (H_2SO_4:H_2O_2:H_2O, 1:40:80 by volume) for 5 minutes, to expose the AlAs layer. Each sample was then placed in a dilute HF solution (HF:H_2O, 1:9 by volume) for 24 hours at 4 °C, to remove the AlAs layer. Once released, the 2-µm-thick LT-GaAs layer, supported by the wax, was transferred onto a clean double-side polished z-cut-quartz substrate and left for ~1 week for the excess moisture between the layers to evaporate and van der Waals [195] bonds to form. The wax was then removed using trichloroethylene and the samples were placed in a vacuum oven (20 mbar) for 15 hours at 250 °C, to remove any excess moisture and aid further adhesion.

To perform photo-lithography on the sample, a bi-layer resist process is utilised. This is done for two reasons: firstly to ensure an effective undercut vital for the lift-off process and secondly, as S1813 has proven to have bad adhesion with the quartz substrate. Initially a primer layer (HMDS) is spun onto the surface of sample at 2000 rpm for 30 seconds, covering both

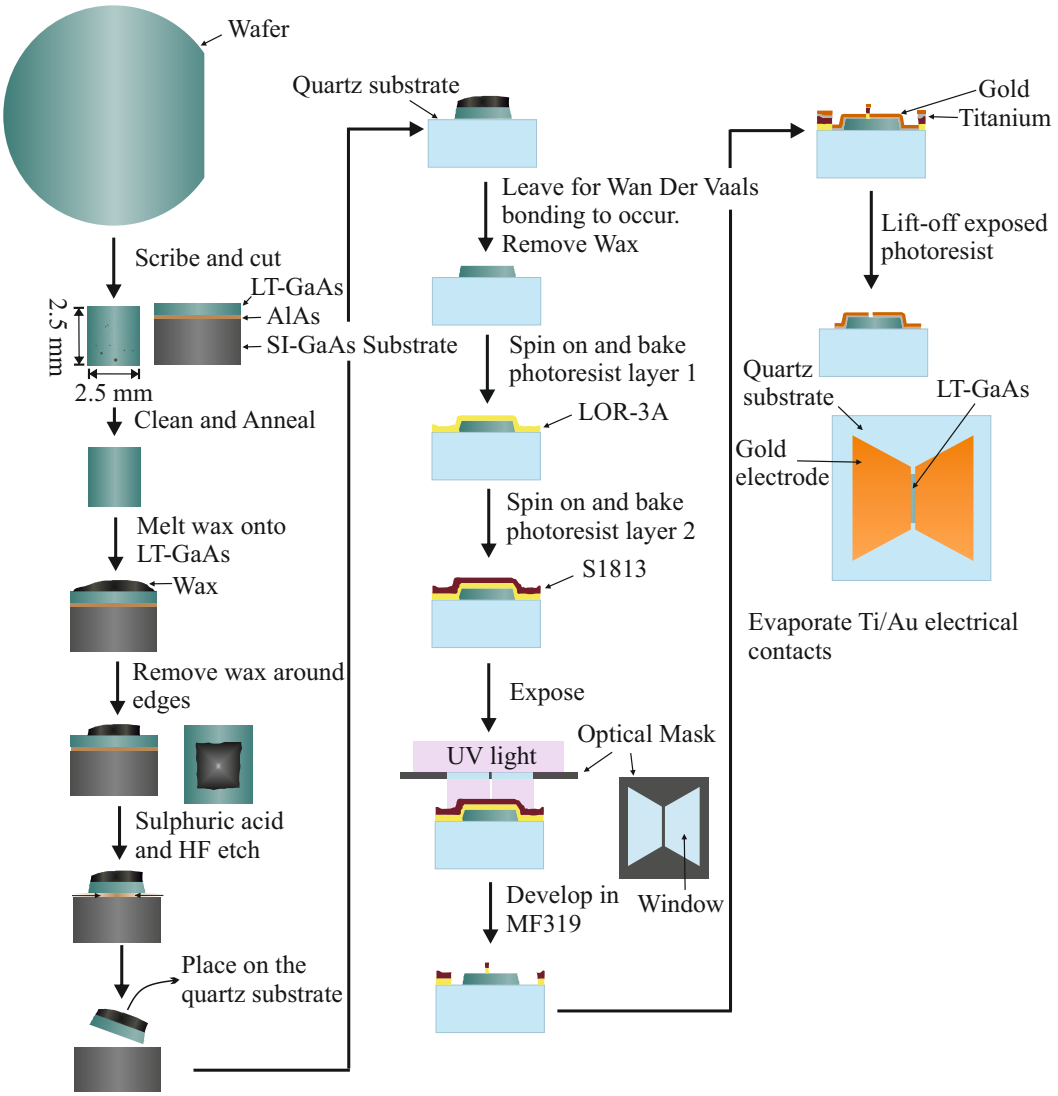

Figure 3.12: Shows the steps required to fabricate an PC device, incorporating an LT-GaAs active region and mounted onto a z-cut quartz substrate. The process is based on the work shown in reference [191] and [185]. The LT-GaAs-on-quartz (LoQ) device is used throughout this project.

the LT-GaAs and the surrounding quartz substrate. It is then baked at 200 °C for 1 minute. The primer layer acts to improve the adhesion between the photoresist and the substrate. To remove excess primer and clean the sample, a rinse in IPA and a further bake at 200 °C for 1 minute is advised. Next, the first layer of resist (LOR-3A) is spun on at 2000 rpm for 30 seconds (thickness of ~0.4 µm), which is once again baked at 200 °C, this time for 3 minutes. Once cooled, a second layer of photoresist (S1813) is spun onto the surface. For samples fabricated using thin quartz substrates (500 µm), this spin occurs at 4000 rpm for 30 seconds (thickness of ~1.4 µm), followed by 4 minute bake at 115 °C. However, for samples fabricated

using a larger thickness of quartz (2-5 mm), 3000 rpm is used (thickness of ~1.5 µm). Owing to the weight of the thicker substrates, rotating the sample any faster than this would cause the samples to fall off the chuck. As well as this, it is important to decrease the ramp setting when spinning photoresist onto thick samples, as a sudden change in speed will cause the sample to become unstable. Another important consideration when using thick samples is to incorporate a 3 minute rest period after every bake to allow for heat dissipation within the substrate.

To expose a thin quartz substrate sample to UV light, the same mask-aligner described in section 3.3.1 is used. The exposure time is typically shorter than when fabricating a LoG device, as unlike in SI-GaAs, the excess radiation is not absorbed in the substrate but is instead reflected back to the photoresist. Once again, the exposure time is determined by the intensity of the light, which is dependent on lifetime of the bulb. Unfortunately, it was infeasible to use the original mask aligner (Karl Suss MJB3) to expose a 5-mm-thick quartz sample, as there was not the clearance required between the sample holder and the optical mask. As a result an alternative mask aligner (EVG 610) was used, with an exposure time of approximately 8 seconds. Each sample, independent of its thickness, was then developed in MF319 for 1 minute, before being rinsed in water and dried using a nitrogen gun. To ensure an undercut in the photoresist, the sample undergoes a bake at 180 °C to crosslink the top layer (S1813), followed by a further 30 seconds in MF319. The definition of metal electrodes on the surface of the device is the same process as described in section 3.3.1. However, the lift-off process to remove excess metal around the contacts is achieved using cyclopentanone, as LOR-3A resist does not dissolve in acetone. This process can be sped up by heating the cyclopentane to 50 °C. Any remaining LOR-3A residue can be removed using MF319 developer, but it is not suited for lift-off as it reacts with GaAs.

It is noted here that for the LoQ device, the gold contacts overlay the LT-GaAs and the quartz, therefore the initial sample size used for fabrication is limited only by the desired gap width of the antenna. However, this is not the case for the LoG device, described in section 3.3.1, as the LT-GaAs layer is supported by the SI-GaAs substrate. Consequently, the sample size of the LoG device is limited by the size of the electrical contacts and the device mounting technique used in the experimental setup. The fabrication process for an LoQ device

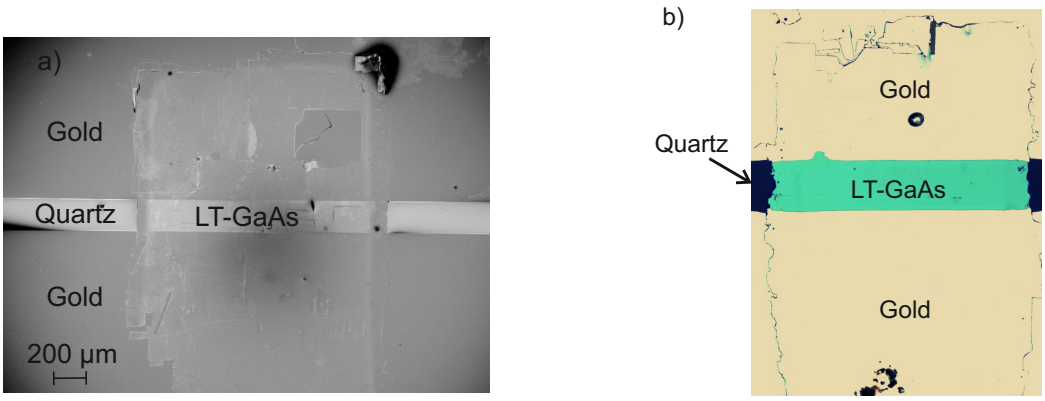

Figure 3.13: Shows a fully fabricated LoQ device taken using a) a scanning electron microscope and b) an optical microscope using a 20x objective lens. The different materials are clearly labelled and the PC gap is present in the middle of both devices.

proves to be significantly more efficient in its use of LT-GaAs and therefore more cost effective. Figure 3.13 shows pictures of fully fabricated LoQ devices, taken using (a) a scanning electron microscope and (b) an optical microscope respectively. For the latter a 20x objective lens was used. The presence of LT-GaAs underneath of the gold contacts is visible in both pictures.

Improvements to the fabrication process

Throughout the duration of this project efforts were made to improve this process, in order to decrease fabrication time and increase yield. Firstly, by not placing an excess amount of wax on the surface of the sample prior to epitaxial lift-off, this can prevent the wax from flowing over the sides and avoid having to use trichloroethylene to remove it from the edges. This process can take several hours, depending on how many samples are required. In the original process described in section 3.3.2, the samples were left for ~1 week for van der Waals [195] bonding to occur. While the yield of the devices fabricated using this method was very high, it doubled the fabrication time. Furthermore, the stress it created on the lifted off LT-GaAs layer could result in substantial micro-cracking, an example of which is shown in Figure 3.14 a). An alternative technique is to first bake the samples on a hot place at 80 °C for ~ 30 minutes, immediately after the LT-GaAs (with wax still on top) has been transferred to the quartz substrate and excess moisture removed. This is hot enough to initiate the bonding process but not too hot such that the wax melts away from the LT-GaAs. Immediately afterwards the samples are placed in a vacuum-oven at a pressure of 30 mbar and 80 °C for 15 hours. Heating

the devices is believed to have two effects: firstly it removes excess water much quicker than at room temperature and improves the bond between the LT-GaAs and the substrate. Secondly, heating the wax on top of the device makes it more malleable, allowing the transferred LT-GaAs to bend without breaking. An example of a sample bonded using this method is shown in Figure 3.14 b)[1].

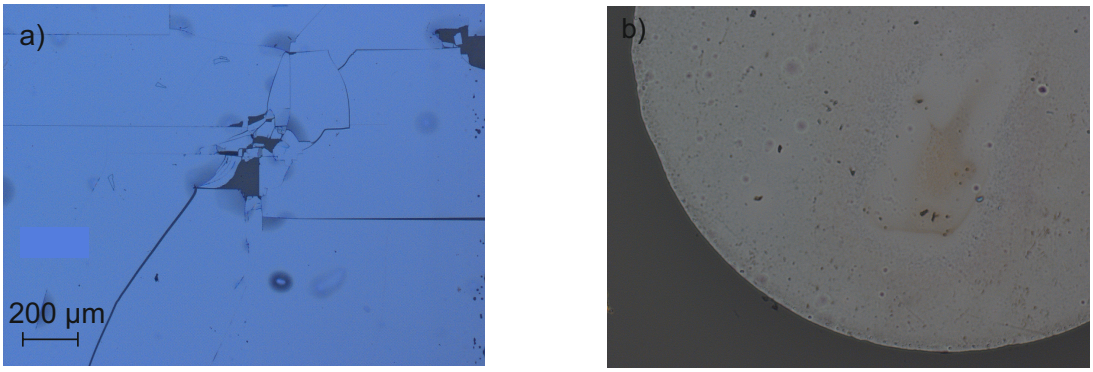

Figure 3.14: a) Shows LT-GaAs wafer epitaxially transferred onto a quartz substrate. Transfer process was performed using the longer method, leaving it for 1 week at room temperature. Micro-cracking in the wafer is shown in the middle of the figure. b) shows a piece of LT-GaAs attached to quartz using the faster heating method, with no visible micro-cracking.

3.4 Large-area emitters on z-cut quartz substrates

To help demonstrate the advantages of using z-cut quartz as a substrate, the experimental data presented here has been obtained using both transmission and reflective collection techniques (see Figure 3.1). The initial data was collected in THz transmission geometry, in which optical excitation and THz collection occur on opposite sides of the device; in this geometry the advantage of a low refractive index substrate is that a smaller percentage of the THz pulse is reflected back into the substrate at the substrate-air interface, than when using SI-GaAs. As previously discussed, the use of z-cut quartz in transmission also allows for through-substrate illumination, potentially removing any attenuation or dispersion inflicted on the THz pulse. In reflection geometry excitation and collection occur on the same side of the device. In this orientation, a higher percentage of the generated signal will be emitted from the excited side, when compared with a device mounted on SI-GaAs. Another benefit of fabricating PC devices on z-cut quartz is that the substrate thickness can be chosen for a specific TDS system. A thick

[1]Many of these improvements were developed with the help of Nicolas Peters [University of Leeds]

substrate can be chosen with the intention of delaying the substrate reflections in time and improving frequency resolution. This is in contrast to using as-grown LoG devices, where the growth procedure of the LT-GaAs wafer has been engineered and refined over time to provide the most desirable properties, beginning with a commercially determined thickness of the SI-GaAs substrate.

3.4.1 I-V characteristics

To determine the I-V characteristic response of both types of device, the LoQ and LoG devices were mounted onto a pre-designed printed circuit board (PCB) using conductive silver paint. The LoQ device chosen for this study consisted of a 2-µm-thick piece of LT-GaAs transferred onto a 500-µm-thick piece of z-cut quartz. The antenna used was a semi-large-area slot electrode design with a 200-µm-wide and 4-mm-long gap. An image of the design is shown in Figure 3.13. An equivalent LoG device was also fabricated to act as a reference, using the method described in section 3.3.1. These devices were placed one at a time into the THz-TDS transmission setup shown in Figure 3.1 a), which was sourced by a mode-locked Ti:sapphire laser, providing 100-fs-wide pulses at 80 MHz repetition rate. The experiment was conducted in two conditions, in the dark with no optical illumination and in the light with a predetermined optical power, in this case 200 mW, focused onto the active region. A knife edge measurement performed at the focal point of the convex lens (35 mm) found a spot size of $\sim$10 µm^2 incident on the active region. Each device in turn was connected to a DC power supply (Keithley 2400). A sweep was then performed, where a range of voltages were applied to the device and the measured current values were recorded and plotted.

Figure 3.15 a) and b) show the I-V curves for both devices, in dark and light conditions respectively. In this and all subsequent figures, the black and red curves represent the response from the LoQ and LoG devices, respectively. For clarity, both plots use different Y-axis scales for each device. It is apparent from Figure 3.15 a) that the LoQ device draws a significantly lower current than the LoG device with the same electrode geometry. The low dark current and hence high dark resistance seen from the LoQ device, relative to the LoG device, is attributed to the absence of an additional current path through the SI-GaAs substrate and the reduced area of LT-GaAs used in fabrication. Values for dark resistance have been calculated

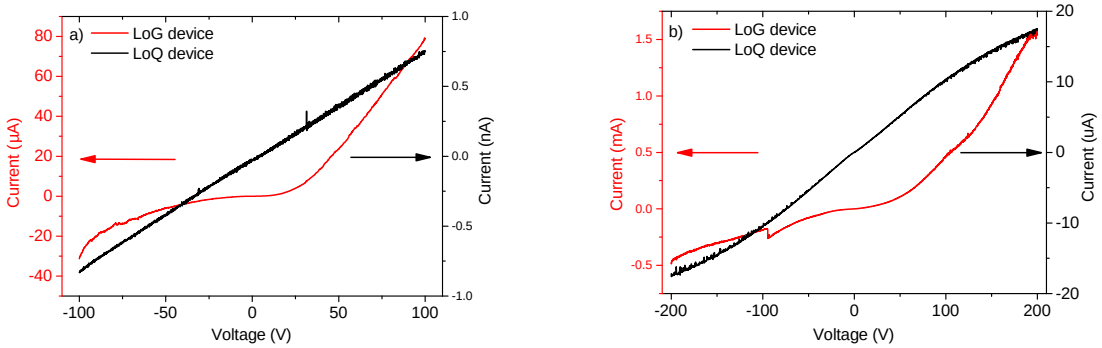

Figure 3.15: I-V curves taken a) in dark conditions with no optical power focused on the devices and b) in light conditions with 200 mW of optical power focused onto each device. In both cases, the response of the LoQ device (quartz substrate) is in black and corresponds to the right-hand Y-axis and that of the LoG device (SI-GaAs substrate) is in red and corresponds Y-axis to the left-hand side. Arrows have been drawn to help indicate this.

Condition	Device Type		
	LT-GaAs-on-SI-GaAs (LoG)	LT-GaAs-on-quartz (LoQ)	Bulk SI-GaAs
Dark	2 MΩ	126 GΩ	31.0 MΩ

Table 3.1: Typical values of resistance for the three types of devices (LoQ, LoG and bulk SI-GaAs). The values have been extracted from linear fittings of the I-V curves for each device.

from a linear fit of the I-V curves and summarised in Table 3.1 below. As well as the LoG and LoQ devices, the dark resistance of a device made on bulk-SI-GaAs, incorporating the same electrode design, has also been shown as a reference. The large resistance seen for the LoQ device, compared with that from the LoG and the bulk-SI-GaAs devices, confirms that the SI-GaAs substrates acts as a parasitic current channel. For THz emission, the principal benefit of a high resistance is that current induced heating in the device is reduced; heating is known to have a detrimental effect on both the carrier mobility and the efficiency of SI-GaAs PC emitters [196]. A high dark resistance allows higher bias to be applied and therefore greater output fields can be generated [188].

An inspection of the light I-V curves plotted in Figure 3.15 b), suggests there is still a significant difference in the generated photocurrent when under illumination, with the LoG device drawing considerably more. This can be accounted for by considering transmission of the excitation beam through the LT-GaAs layer. For 2-μm-thick LT-GaAs used here, it has been calculated using Lambert-Beer's law (equation 3.8) that ~5 % of the incident optical beam was transmitted into the SI-GaAs substrate. For this calculation, I_0 represents the incident optical intensity and L is the thickness of the LT-GaAs. An absorption coefficient, α, at 800 nm

of 1.3 μm^{-1} [197] was assumed, and the interface reflections were taken into account using the Fresnel equations. The thin layer of AlAs was deemed to have a negligible effect on the transmission of the optical beam, since it possesses a large bandgap of 2.13 eV relative to the LT-GaAs [198]. Despite only 5 % of the incident optical beam generating electron-hole pairs in the SI-GaAs substrate, this clearly has a significant influence on the overall resistive properties of the LoG device. This is understandable when considering that when only 20 mW of optical power was focused onto the bulk SI-GaAs device, a value for resistance of 8.5 kΩ was obtained. When the optical power was increased higher than this, the current became unstable and the device began to show signs of overheating.

$$I = I_0 e^{-\alpha L} \tag{3.8}$$

To gain a full understanding of the resistive properties of each device, an I-V sweep was completed for a range of optical pump powers. A linear fit was then performed on each curve and the resulting resistances have been plotted in Figure 3.16, as a function of optical power. The values for resistances have been plotted on a logarithmic scale. The difference between the two curves is immediately apparent, with the LoQ device again exhibiting higher values for resistance for all optical powers.

3.4.2 Lifetime measurements

To demonstrate another effect the SI-GaAs substrate has on the properties of a LoG device, carrier lifetime measurements have been performed. In LT-GaAs, this lifetime is approximately 300 fs and is dependent on its annealing temperature and its growth conditions [152,199]. In SI-GaAs, however, the carriers exist for several hundreds of picoseconds after excitation [154,194]. In quartz, no free carriers will be generated. In order to draw a comparison, approximate values for the overall lifetime of the devices were required. To obtain this a pump-probe experimental setup was used, similar to that shown in Figure 4.6. However, contrary to in chapters 4 and 5, where a THz-pump-THz-probe experiment is performed on the THz-QCL, in this instance

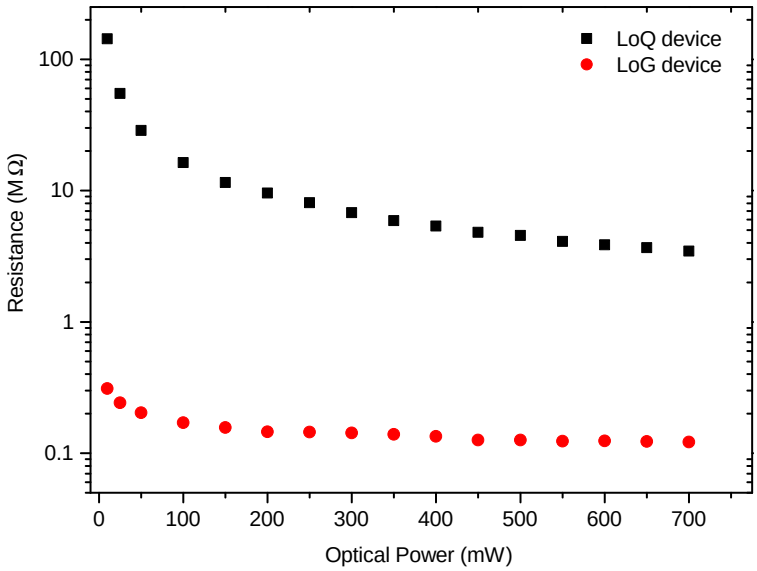

Figure 3.16: Resistance values for both types of device, plotted as a function of incident optical power. The resistances have been extracted from the I-V curves by using the gradient of a linear fit. The response of the LoQ device (quartz substrate) is in black and that of the LoG device (SI-GaAs substrate) is in red.

each PC device undergoes an optical-pump-optical-probe experiment. A powerful pump pulse is first used to generate electron-hole pairs, while the capture and recombination times of the carriers is measured with the arrival of a second probe pulse. If the optical probe pulse arrives within a carrier lifetime of the earlier pump pulse, fewer carriers are available for the generation of the THz probe pulse and the amplitude of the resulting THz signal will be reduced. To determine this inherent lifetime, the peak-to-peak amplitude of the THz probe pulse is measured as function pump-probe delay (PPD), i.e. the arrival time between the optical pump and probe pulses on the device.

Unfortunately, owing to the dynamic nature of the project, this experiment was not performed on the two devices consecutively. While the main elements of the experimental setup remained consistent throughout, the optical pump and probe powers were varied, with 282 and 50 mW respectively used to collect the LoG device data, and 225 and 100 mW used on LoQ device. As well as this, for the LoG device the electrode gap was kept the same as that previously presented, while a LoQ device with a 100-µm-wide gap was used. Neither of these alterations are deemed to have a significant effect on the measured carrier lifetime. The results have been normalised and plotted in Figure 3.17. Exponential fittings have been performed

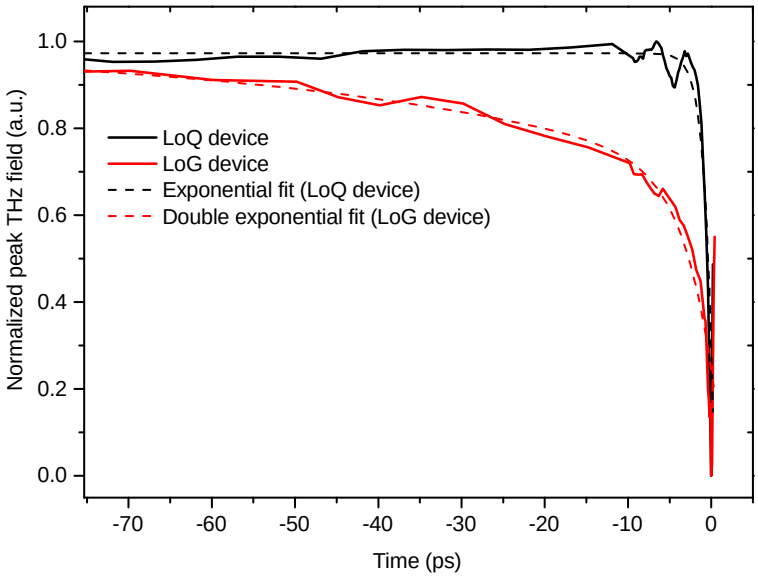

Figure 3.17: Carrier lifetime measurements performed using a optical-pump-optical-probe arrangement. The response of the LoQ device is in black and that of the LoG device is in red. A exponential fitting has been performed on both sets of data (dashed line)

on both sets of data, the time constants for which are taken to be the lifetime of the carriers. For a time >0 ps the optical probe pulse arrives at the emitter prior to the pump pulse. This results in a sudden increase in the amplitude of the recorded THz probe pulse, which can be seen in Figure 3.17.

For the LoQ device a lifetime of 1 ps was measured, which agrees reasonably well with that stated above. For the data from the LoG device, a more accurate fitting was performed using a double exponential curve, with time constants of ~2 and 100 ps. This indicates that the first few pico-seconds after the arrival of the optical pulse are dominated by the carriers in the LT-GaAs. After this period, the recovery of the device is dominated by the longer-lifetime carriers excited within the SI-GaAs substrate. One consequence of this is that the average current in the device is significantly higher as there is a shorter cooling period between the arrival of the optical pulses. This is detrimental to the efficiency of the LoG device. Furthermore, the THz pulse emitted from the LoG device could be the superposition of pulses generated from both materials. As such, the device's overall characteristics are dictated by the properties of both semiconductor layers. As LT-GaAs has proved to be superior in this respect, this could have a negative influence of the overall output pulse, especially the size of second peak which is related to the carrier recombined time.

3.5 THz Emission in Transmission geometry

After the initial resistance measurements, the devices were fully characterised for their emission properties, in the transmission setup. As discussed previously, this involves focussing the optical beam directly onto the LT-GaAs and collecting the THz radiation from the opposite (substrate) side of the antenna. Unless otherwise stated, all data shown here was collected using the same devices as for the I-V measurements and discussed at the beginning of section 3.4, employing a 200-µm-wide electrode gap and fabricated on a 500-µm-thick substrate. This thickness of substrate was chosen to limit the dispersive effects of the THz pulses. In this instance, no silicon lens is used to collimate the emitted THz radiation from the back of the device, as at this stage it could complicate a comparison between the two devices. For detection a 2-mm-thick ZnTe crystal was used for EO-sampling. Time-domain pulses from both devices are shown in Figure 3.18 a), with the corresponding FFT data plotted in b). In this case, the time-domain data was zero padded to smooth the FFT response. These were collected using an average optical power of 300 mW and an applied bias field of 10 kV cm^{-1}, which was electrically chopped at 7 kHz. The difference in response from the two devices is apparent, with the THz pulse from the LoQ emitter possessing a peak-to-peak signal in time-domain 1.6 times higher than that of the LoG emitter. This is reflected in the frequency-domain. The response from the LoG device also appears to be slightly broader, and have a larger trailing oscillation, compared with that of the LoQ emitter. This indicates higher dispersion with the SI-GaAs substrate and could be one of the reasons for the difference in responses. This data was collected in a nitrogen purged environment to remove the effect of water-vapour absorption. Unless otherwise stated, this can be assumed for each of the following measurements discussed. In this instance, the bandwidth in the frequency domain is limited by the 2-mm-thick ZnTe crystal to ~2.5 THz. This creates a low-pass filtering effect that results in oscillations in the time-domain trailing the main THz pulse.

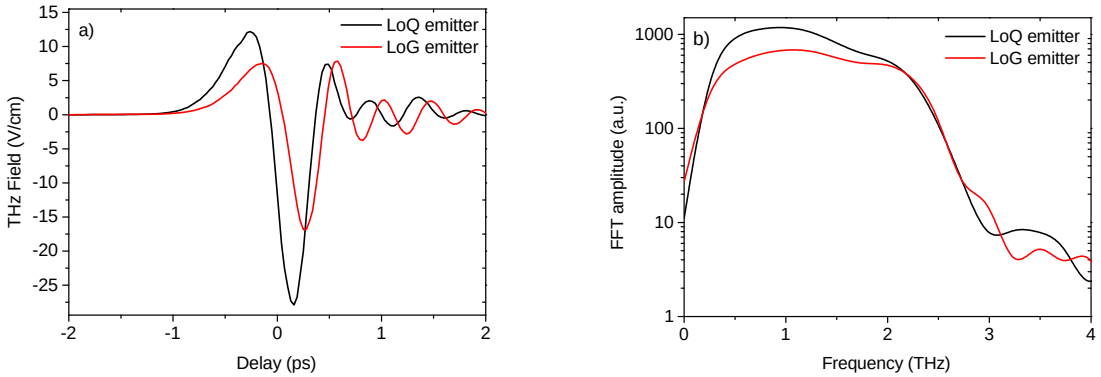

Figure 3.18: Examples of THz pulses in the time-domain (a) and frequency-domain (b). In both instances the the response of the LoQ device (quartz substrate) is in black and that of the LoG device (SI-GaAs substrate) is in red. To obtain these measurements an average optical power of 300 mW and at an applied field of 10 kV cm^{-1} has been used. The time-domain data a) is zero-padded to smooth the FFT response b).

3.5.1 THz emission as a function of applied bias and optical excitation power

Figure 3.19 shows the peak-to-peak THz field, extracted from time-domain pulses, plotted as a function of applied bias. This measurement was also performed using an average optical power of 300 mW. The difference in the response of the two emitters at high applied fields ($\gtrsim$ 6 kV cm^{-1}) is attributed to the detrimental effects of heating in the LoG device, originating from parasitic current in the SI-GaAs substrate, causing a reduction in the emitted power at a given bias and optical fluence. In bulk SI-GaAs, a reduction in carrier mobility and thermal conductivity with increased temperature is well documented [196, 200], and is attributed to the increased probability of carriers occupying low mobility valleys higher in the conduction band [201]. Additionally, a higher phonon density results in increased scattering. It is noted here, however, that despite LT-GaAs being a commonly used material for THz emission, a detailed analysis of its high temperature (>300 K) photoconductive emission performance is lacking. However, there is no reason to suggest that these heating effects are not a common characteristic and reduce the THz generation efficiency in LT-GaAs.

The response at lower applied fields may be due to higher THz dispersion in the SI-GaAs substrate reducing the peak-to-peak field. Any emission directly from the SI-GaAs substrate may also have a detrimental effect on the overall THz pulse shape and magnitude, and could be a contributing factor. The LoG device exhibits a distinctive point of saturation at an applied bias field of ~6 kV cm^{-1}, which agrees well with the breakdown field of SI-GaAs [193].

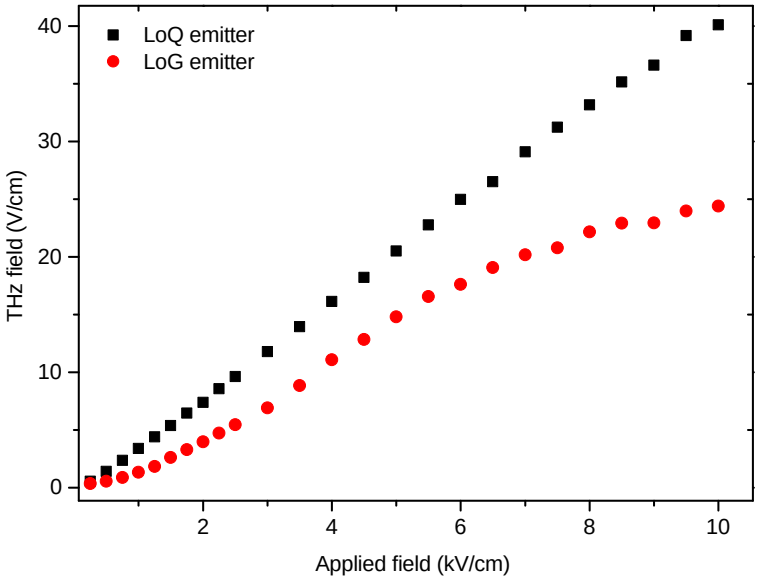

Figure 3.19: Shows peak-to-peak of the measured time-domain pulses as a function of bias field across the device, for both the LoQ (black) and the LoG (red) emitter. An optical power of 300 mW was used.

This response could also be related to the carrier saturation velocity in SI-GaAs [202]. It has calculated that overall the lower refractive index of quartz has an insignificant effect on the strength of the emitted THz pulse in the transmission geometry. While slightly less of the original pulse propagates into the substrate, owing to the larger difference in refractive index between LT-GaAs and quartz, compared with LT-GaAs and SI-GaAs, less of that pulse will be reflected at the interface between quartz and air. Therefore, there is expected to be no net gain from this effect. A similar comparison can be made between the devices as function of optical power, which is plotted in Figure 3.20. However, unlike in Figure 3.19 where the response of the LoG device parallels that of the LoQ emitter at low applied fields, here, the response of the two devices appear divergent even at relatively low excitation powers. This difference in response from the two devices is owing to the reasons discussed above and in section 3.4.2, and originates from the increased number of carriers generated in the SI-GaAs substrate. At the highest optical power, this results in almost three times the peak-to-peak signal emitted from the LoQ emitter, compared with the LoG device. This data was obtained with both emitters bias at 6 kV cm^{-1}.

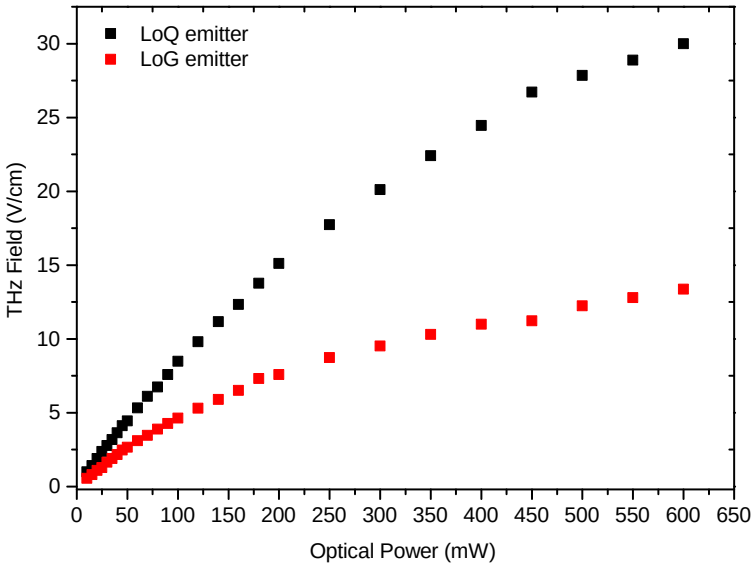

Figure 3.20: Shows peak-to-peak of the measured time-domain pulses as a function of optical power incident on the device, for both the LoQ (black) and the LoG (red) emitter. A constant bias field of 6 kV cm^{-1} was used.

3.5.2 Backside illumination of quartz-mounted devices

One advantage to the use of z-cut quartz as a substrate in photoconductive emission, is that it is optically transparent, providing the ability to perform backside-illumination (BSI) of the active region. In this orientation the optical pulse is transmitted through the substrate and excites the biased LT-GaAs on the opposite side. The generated THz pulse, when collecting in transmission geometry, does not suffer any of the attenuating or dispersive effects that arise from it passing through the substrate. Another advantage of this technique is that it allows the illumination of LT-GaAs fabricated underneath the metal contacts. This is obviously not possible in a LoG device, as the optical beam will be completely absorbed in the SI-GaAs substrate. Once again, this is a technique developed for use in on-chip THz waveguide. Front-side-illumination (FSI) and BSI are illustrated in Figure 3.21 and are labelled accordingly.

Figure 3.22 shows two THz time-domain pulses taken using the same LoQ PC emitter. Both traces have been shifted in time to align at 0 ps. The device in question consisted of a large-area slot electrode design as previously demonstrated, fabricated with a 100-µm-wide PC gap. However, in this instance, the LT-GaAs was removed from its growth substrate and transferred onto a 350-µm-thick piece of z-cut quartz. In Figure 3.22 the black trace is taken using conventional FSI geometry, where the pump beam is incident on the surface on the

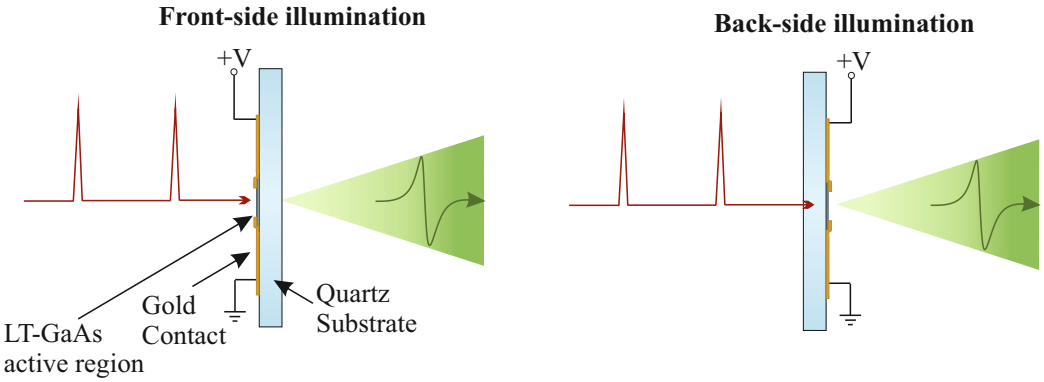

Figure 3.21: Shows two separate PC emission techniques with illustrating the conventional FSI method and showing BSI, where the optical pulse first propagates through the transparent quartz substrate of the LoQ device before illuminating the LT-GaAs. The resulting THz radiation is collected without it passing back through the quartz substrate.

LT-GaAs and the THz pulse is detected after passing through the substrate. The response of the emitter in BSI is shown in the red trace. Both devices were tested with an average optical power of 225 mW and a bias of 5 kV cm^{-1}. BSI is shown to provide the more powerful of the two signals. One reason for this is evident when the two pulses are normalised in Figure 3.23 a), as the THz pulse generated using FSI experiences broadening, relative to the BSI pulse. This results in a slightly broader frequency response when using BSI, which is evident from the FFTs of the pulses displayed in Figure 3.23 b). In this spectra, the sudden increase in amplitude at low frequency is owing to a DC-offset in the time-domain. These dispersive effects, combined with the avoidance of the THz pulse with the attenuating quartz substrate, explains the difference in response of the two geometries.

From a comparison of the two traces plotted in Figure 3.22, it is evident that the reflected pulse from the substrate-air interface, which arrives ~5 ps after the main pulse, undergoes a 180° phase change. This reflection has been highlighted in the dashed box. The reason for this is that when using the conventional FSI geometry, this second pulse travels three lengths of the quartz substrate prior to detection, compared with just two lengths when using BSI. This is illustrated in Figure 3.24, where the propagating pulses are labelled as either 1, 2 or 3. It is thought that the single extra reflection experienced by the pulse in FSI contributes to this phase change. As well as this, the extra distance travelled inside the quartz substrate causes the reflected pulse to become misshapen due to dispersion. One traditional advantage

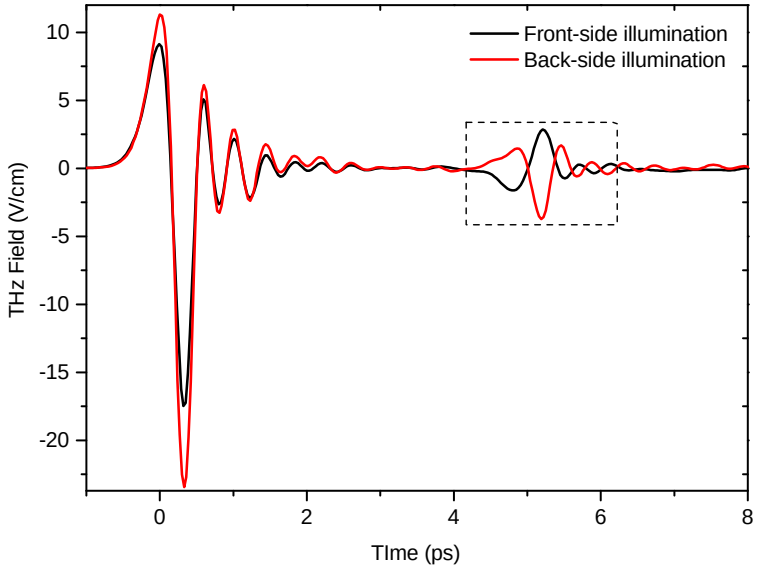

Figure 3.22: Time-domain pulses taken using the same LoQ PC emitter, fabricated on a 350-µm-thick quartz substrate. The black trace shows the pulse emitted in FSI, while the red pulse is taken using BSI. An average optical power of 225 mW and a bias field of 5 kV cm^{-1} was used in both cases. The first reflection from the substrate-air interface is highlighted inside the dashed box.

of collecting the emitted THz radiation in the transmission geometry is that a silicon lens can be attached to collimate the output beam and increase signal. Unfortunately without further fabrication techniques, this is not possible when using BSI as the lens would damage the LT-GaAs active region. For now this provides a limitation to the technique for practical purposes but has interesting potential for the future.

3.5.3 Substrate thickness tests on quartz-based devices

It has already been demonstrated that LoQ devices can be fabricated on different thicknesses of z-cut quartz. In transmission geometry, a thin substrate is traditionally desirable as it limits any attentuation and dispersion of the THz pulse passing through it. However, there are some drawbacks. Firstly, as discussed in section 3.1.5, the reflections produced at the substrate-air interface will arrive closer in time to the original pulse, limiting the potential frequency resolution of the system. Secondly, the substrate acts to dissipate the heat generated from the optical pulse being absorbed in the LT-GaAs and therefore a thinner substrate will do this less effectively. When working in transmission, it is important to consider both of these aspects and to tailor the system accordingly.

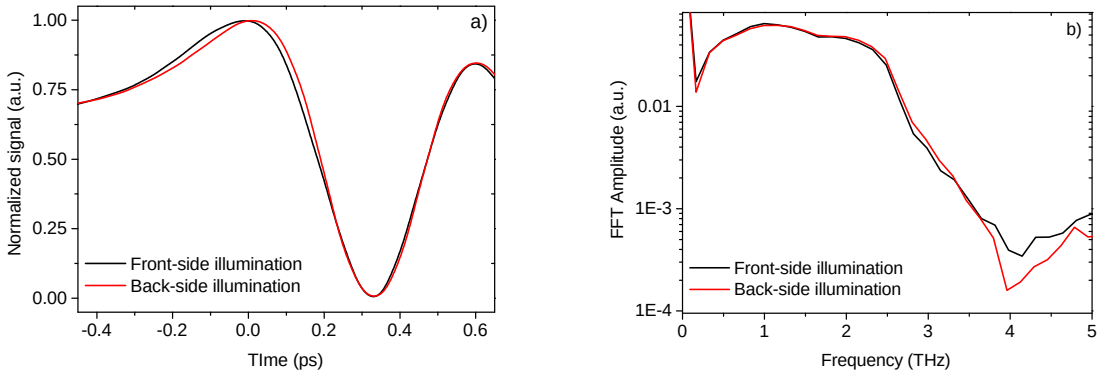

Figure 3.23: a) is an enlarged picture of the main time-domain pulses shown in figure 3.22, close to 0 ps. The black trace shows the pulse emitted in FSI, while the red pulse is taken using BSI. b) is the FFT of both pulses shown in a), which has been truncated before the first reflection.

To overcome these issues, two potential solutions have been investigated. The first option is to fabricate the emitter on a thick substrate. This is beneficial as it increases the optical path of the first substrate reflection and thus the time-delay between it and the original THz pulse. Furthermore, it provides good thermal conduction for heat away from the active region. However in a conventional system, with the optical pulse incident on the active region, the THz pulse collected from the opposite/substrate side of device would significantly broaden, decreasing the bandwidth and usable THz output field. Therefore, this method can only be applied when used in BSI, introduced in section 3.5.2. Another option is to use a thin substrate, as reflections can be prevented if the substrate is thinner than the wavelength of the emitted radiation. While this fails to provide as good thermal protection for the device, it is a useful means of dealing with reflections. Another drawback to this approach is that it is practically difficult to handle thinner devices, as they are more easily damaged. It should be noted here that neither of these options allow for the use of a silicon lens, as BSI is required for a thicker substrate device and any contact with a device fabricated on a thinner substrate could danger it. As mentioned earlier, these developments are not feasible when using a LoG device, as this would require one to significantly alter the wafer growth conditions. Therefore, this are only feasible when using a LoQ device.

The main graph in Figure 3.25 shows normalised time-domain scans taken using three different devices, with the equivalent FFT data shown in the inset. For each LoQ device a

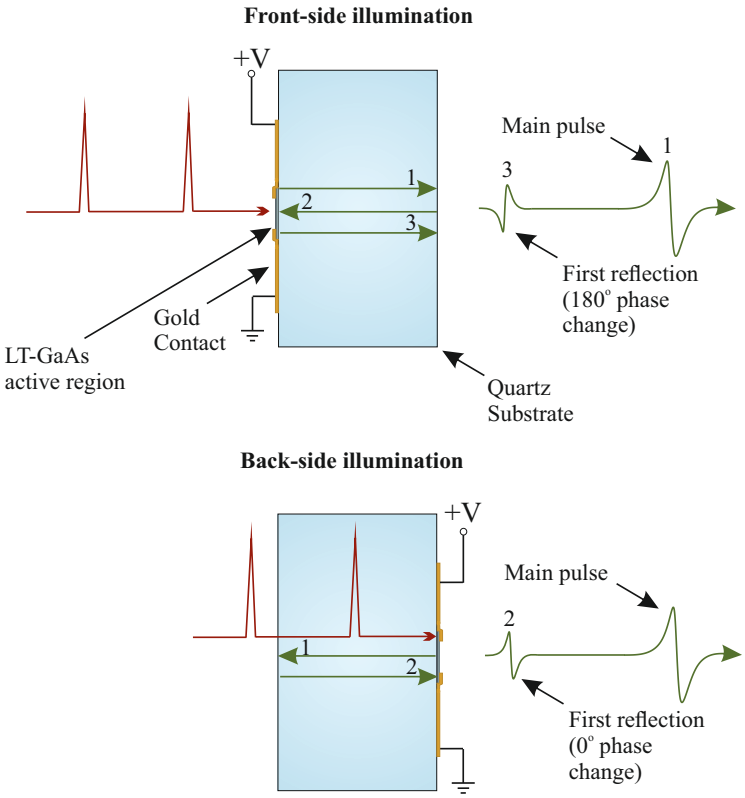

Figure 3.24: Shows the output pulse train when using FSI and BSI illumination geometries. Each pass of the first reflection from the quartz substrate-air interface is labelled as 1, 2 or 3. The incident optical pulse is in red and the output THz pulses are shown in green.

200-µm-wide slot electrode design was used but was fabricated on a different thickness of quartz substrate. For this experiment the bias conditions were kept consistent throughout, applying an average optical power of 200 mW and a bias field of 5 kV cm^{-1} to each device. For comparisons sake, each time-domain trace has been normalised to its second peak. All traces were truncated at the same point in time to provide a comparable resolution in the frequency domain. The first trace, shown in red is taken using a device fabricated on a 500-µm-thick quartz substrate, very similar to the devices presented earlier. The time-domain scan shows the reflection from the substrate-air interface appearing ~7.5 ps after the original pulse. The corresponding FFT data shows oscillations as a result of this reflection.

Following that, the next device to be tested possessed a ~40-µm-thick quartz substrate. Fabricating the device directly onto this thin a substrate would be difficult as it is very fragile. Therefore, the simpler option was to fabricate a device on a thicker substrate, in this instance 500 µm, and systematically thin it to desired thickness. The backside of the substrate could then

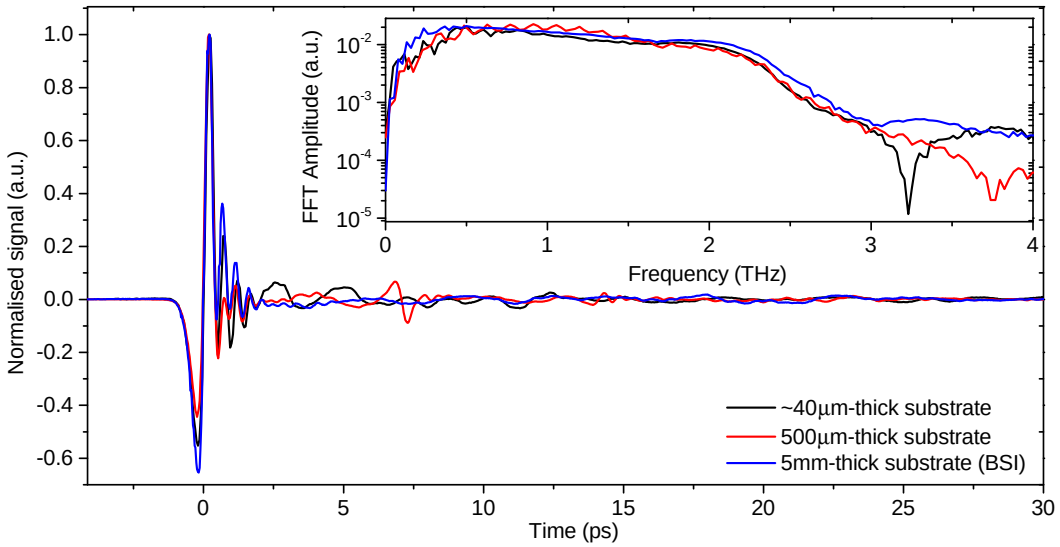

Figure 3.25: Main: Time-domain pulses normalised to their second peak. Inset: the equivalent FFT data from three different sources. In both the main and inset, the red curve shows a reference pulse from a LoQ device fabricated on a 500-µm-thick quartz substrate. The black and blue curves have been taken using devices fabricated on 40-µm-thick and 5-mm-thick quartz substrates respectively. The blue curve was taken using BSI. Each trace was taken using 200 mW of optical power and a applied bias field of 5 kV cm^{-1}.

be polished to improve the coupling efficiency of the THz pulse into free-space. To achieve this a layer of photoresist (S1813) was spun onto the LT-GaAs/contact side of the device. This was performed at 1000 rpm for 30 seconds and created a protective layer for the active region, ~2.2 µm-thick. It then underwent a 4 minute bake at 115 °C. In order to mechanically lap the device, it was stuck active region face-down to a glass block, using a layer of adhesive wax. It was then mounted into the logitech PM5 precision lapping and polishing system. Once lapped to as thin as possible without damaging the device, the thickness of the substrate was measured *in situ*, using a non-contact gauge [2]. The adhesive wax adds uncertainty to this measurement, as it needs to be taken into account. This was achieved by measuring the thickness of the wax before adding the device and subtracting this value afterwards.

The black line in Figure 3.25 represents data taken using this PC emitter. It is clear that the reflection present in the red trace has been removed and thus the corresponding FFT data appears smoother. However, in the black curve there does appear to be a low frequency oscillation extending for ~7 ps after the main THz pulse, which is also apparent in the FFT. It is unclear where this originates from as it is not present in the other traces. However, it

[2] This work was completed by Matthew Swithenbank [University of Leeds]

could be a result of the substrate reflections now overlapping the original THz pulse. Furthermore, in the frequency domain there appears to be an absorption-like dip at ~3.3 THz, not present in the other traces. While this could potentially just be noise as it is higher then the usable bandwidth of the system, it might also be $\lambda/2$ resonance of the pulse inside the substrate, as the wavelength, λ ,(90 μm) agrees reasonably well with the thickness of the quartz.

The final pulse shown in blue in Figure 3.25 is the response of a device made with a 5-mm-thick quartz substrate. The extracted time-domain trace is shown to have no echoes present, which equates to a smooth frequency response. In this instance, the substrate is so thick that the reflected pulse is fully absorbed and does not appear anywhere in the time-domain. To fabricate a device on this size substrate, extra steps are required that are discussed in section 3.3.2. As previously mentioned this scan can only be taken using BSI. For the 100-fs-wide optically pulse used here, the dispersive effects of passing through 5 mm of quartz before exciting the LT-GaAs, were deemed insignificant [203, 204]. However, when using a shorter optical pulse this would cause it to broaden and would limit the outputted THz signal. The attenuation of the optical pulse inside the quartz was also deemed negligible, after an experiment with and without a different 5-mm-thick quartz sample in the optical beam path, resulted in a loss of power of <1 %.

3.5.4 Power measurements

To measure the output power from a LoQ device, the experimental setup shown in Figure 3.26 was used. Similar to the previous THz-TDS arrangment, this is sourced by mode-locked Ti:sapphire laser providing 100 fs-wide pulses at a wavelength of 800 nm and a repetition rate of 80 MHz. However, in this instance no sampling beam is required as the detection is performed using either a liquid helium cooled bolometer or a room temperature VDI Erickson PM5 power-meter, with a WR10 input horn. As such, despite generating pulsed radiation, the detection schemes are incoherent and thus only measure an average power as they can not detect the phase of the pulse. Prior to being focussed on the active region of the device, the beam is steered through an optical chopper rotating at 167 Hz. This modulates the beam at a frequency slow enough such that the emitted THz radiation can be detected using the bolome-

ter. The reason for this are discussed in chapter 1. This frequency also acts as a reference for the lock-in amplifier.

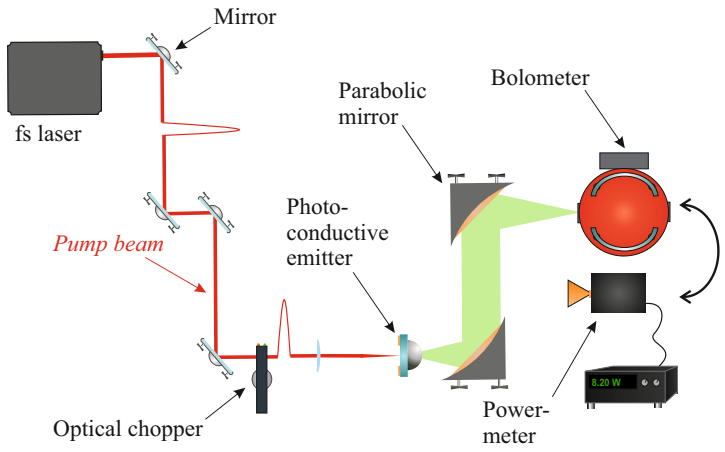

Figure 3.26: Shows a schematic of the experimental setup used to measure the output power of average output power of a PC emitter. Two methods of detection can be observed, a helium cooled bolometer and a power-meter VDI Erickson PM5, employing a WR10 input horn. The optical beam is shown in red and the THz radiation is in green.

The LoQ emitter used in this study consisted of a 100-µm-wide slot electrode design and was again fabricated on a 500-µm-thick quartz substrate. To increase the coupling efficiency of the emitted THz radiation, a 5-mm-diameter silicon lens was attached to the back of the quartz substrate. An X-Y mount was used to align the position of the silicon lens relative to the emitter. A set of off-axis parabolic mirrors were used to collect, collimate and focus the radiation onto the detector. The full setup is shown in Figure 3.26, with the liquid-cooled bolometer aligned for detection. The power-meter, illustrated below this, has an integration time of approximately 30 seconds and built-in lock-in amplifier. This slow response time, relative to the bolometer, means that this device is well suited to obtain a single accurate value for THz power, rather than a quickly varying signal. However, the response time of the bolometer is significantly quicker as it is limited by the time-constant of the lock-in amplifier, which in this instance was set to 50 ms.

Figure 3.27 shows the average THz output power as a function of electrical field across the device, measured using an optical power of 200 mW. For applied fields between 0 and 10 kV cm^{-1} the emitter appears to have a quadratic response. This is expected as output power

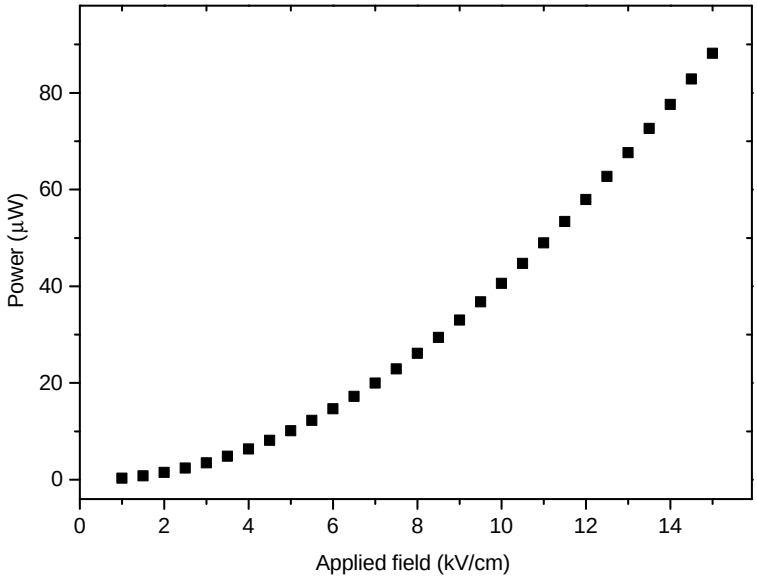

Figure 3.27: Output power as a function electrical field across the device for a LoQ device with a 100-μm-wide gap. This measurement was performed with an average optical pump power of 200 mW and electrically chopped at a 50 % duty cycle.

is the square of the applied field. Increasing the bias further results in a linear relationship, which could indicate the beginning of saturation. The highest output power measured using this device was ~90 μW. This data was first taken with the bolometer, which outputs a voltage that is proportional to the incident THz power. The bolometer was then replaced with the power-meter, indicated by the arrow in Figure 3.26, and the voltage applied to the device was manually varied to obtain accurate values for output power. The rest of the curve could then be scaled accordingly. The power was also multiplied by 2 to account for the 50 % duty-cycle of the bias applied to the emitter.

3.6 Small-gap bow-tie emitter designs on a quartz substrate

In section 3.4 the LoQ device has been presented and demonstrated with several different thicknesses of quartz substrate. These newly fabricated LoQ devices were compared with the traditionally used LoG devices and proved to have superior performance based on their emission properties. The only antenna design discussed so far consists of a large-area parallel plate geometry, separated by either a 100 or 200-μm-wide gap. In this section, a new design of LoQ emitter is introduced, incorporating a small-gap bow-tie antenna geometry. This is a

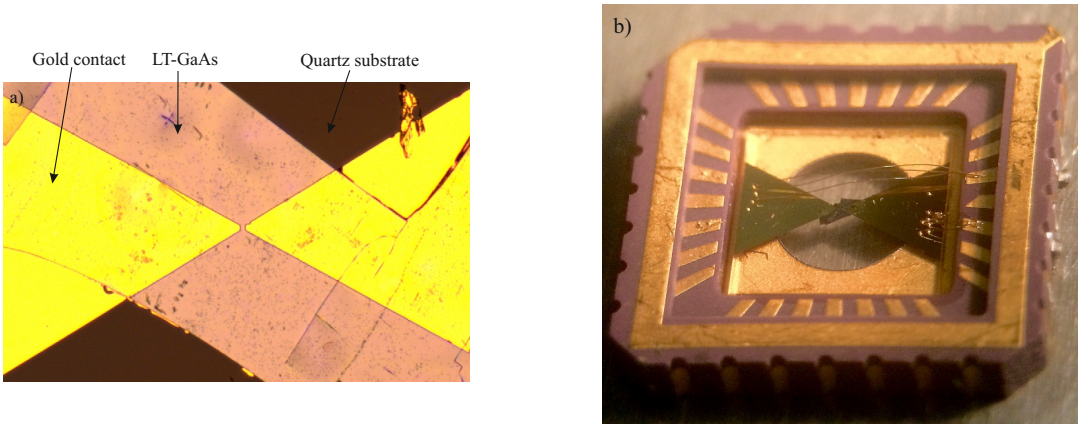

Figure 3.28: (a) shows a fully fabricated and labelled LoQ bowtie device, possessing a 10x10 µm active region. This was taken using a Carl Zeiss Axio-Imager A1m microscope with a x 5 objective lens. (b) Shows the device enclosed within the recess of a chip package. The device is stuck to the package using clear nail varnish and the bonded to the contact pads using a wedge bonder. The chip package was approximately 10 x 10 mm and was used for measurements performed at TeraView Ltd.

very commonly used electrode design for PC devices, as it allows high bias fields to be applied and is believed to be more efficient than using larger gaps [135]. With this being a popular choice of electrode design, this work was conducted in collaboration with Delft University of Technology and TeraView Ltd. The fabrication process for small-gap emitters was very similar to that discussed in section 3.3. The electrode design, shown in Figure 3.28 a), was a bow-tie arrangement with a 10 μm^2 active region. Owing to the smaller gap width, compared with the design discussed previously, the LoQ device required the transfer of less LT-GaAs. This was then overlaid with a metal bow-tie design acting as electrical contacts. The LoQ devices were fabricated on a 350-µm-thick double-side polished z-cut quartz substrate, while the reference LoG device remained on its 500-µm-thick SI-GaAs growth substrate. A fully fabricated LoQ device is shown in Figure 3.28 b), enclosed within a chip package. The quartz substrate was cut to the precise dimensions of the package recess (6 x 6 mm) using a wafer saw (Microace 66) and the gold contacts are electrically connected to the package using 25-µm-diameter gold bond wires, performed with a wedge-bonder. Electrical bias was applied to the device via soldered connections on the underside of the chip package.

To determine the emission characteristics of the small-gap bow-tie designed antennas, two experimental setups were used, the first within the IMP at the University of Leeds and the second at TeraView Ltd in Cambridge. The first setup was similar to the transmission

arrangement presented in Figure 3.1 a), combining the same specification of Ti:sapphire laser discussed in section 3.5.4 with four off-axis parabolic mirror arrangement. As discussed in section 3.4, the devices were mounted in the system on a specially designed PCB. The spot size of the focused beam, which measured to be ~10 μm^2 in section 3.4.1, is now comparable to the electrode gap width. For detection a 1-mm-thick ZnTe crystal was used for EO-sampling. Data from this setup is shown in Figures 3.29, 3.32 and 3.33.

In collaboration with TeraView Ltd, the devices were also tested on a second experimental setup in Cambridge. This is shown in Figure 3.30 and there was several key differences to be noted. The laser used in this instant was a C-Fiber 780 Femtosecond Erbium Laser, providing 85 fs-wide pulses at a wavelength of 780 nm and a repetition rate of 80 MHz. The convex lens used to focus the beam onto the PC emitter had a focal length of 10 mm, providing a tighter spot than before, ~3 to 5μm-wide. To record the THz pulse PC detection was used, utilising another bow-tie antenna with 10-μm-wide gap, fabricated on bulk SI-GaAs at TeraView [3]. The divergence of the THz signal is much greater when using a small gap emitter, owing to greater confinement of the pulse [25]. To compensate for this and increase the detectable signal, two 10-mm-wide silicon lenses were aligned onto the emitter and the detector. A schematic diagram of the active region is shown in Figure 3.30. The emitter mounting technique used here is shown in Figure 3.28 b). The four parabolic mirrors were replaced by 2 ellipsoidal mirrors to ease the alignment process. Data taken using this setup is shown in Figure 3.31.

3.6.1 I-V characteristics

The I-V traces for these devices were taken using the same techniques as discussed in section 3.4.1. For the light condition an average optical power of 5 mW was used, similar to that used in other studies of small-gap designs [150]. The results of the dark and light measurements are shown in Figure 3.29 a) and b) respectively. As before the device fabricated on the quartz substrate exhibits the lower dark current for a given bias, and therefore a higher resistance. However, the contrast in current between the LoG and LoQ devices presented here is significantly smaller than for the large-area devices. This is understandable as the

[3] This was fabricated by Mike Evans [TeraView]

gap-width is now only 5 times the thickness of the transferred LT-GaAs layer. As such, the electric field between the contacts does not penetrate as far into the SI-GaAs substrate and thus the parasitic current channel has a diminished effect on the device characteristics.

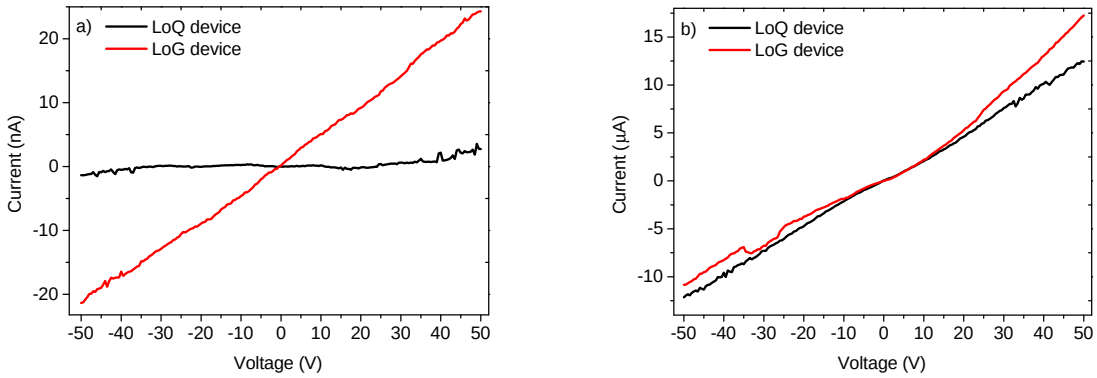

Figure 3.29: I-V measurements performed on the bow-tie design antennas in the dark (a) and the light (b)(5 mW). The response of the LoQ device is shown in black and the LoG device in red. These measurements were performed on the first experimental arrangement discussed above, at the University of Leeds.

Further analysis of the I-V traces reveals that the bow-tie device exhibits a reduced dark current, when compared to the previous slot design, despite the width between the electrodes becoming 10 to 20 times smaller. This is especially the case for the LoG device, that now boasts 3 orders-of-magnitude higher dark resistance. This is believed to show one of the key advantages of using a bow-tie design, as even though the sharp points of the contacts are close to one and other, the active area is significantly smaller then before. The result of this is that significantly higher fields can be applied to the device without damaging it. Furthermore, this is assisted by Paschen's law, which shows that the breakdown field of air is inversely proportional to the width of the PC gap [205]. The light I-V measurements, plotted in Figure 3.29 b), show very similar results for both devices at a low voltage. However, the response of the two devices diverge as the bias is increased, with the LoG drawing more current. This implies that the carriers excited within the SI-GaAs substrate of the LoG device are still having an effect on the overall current.

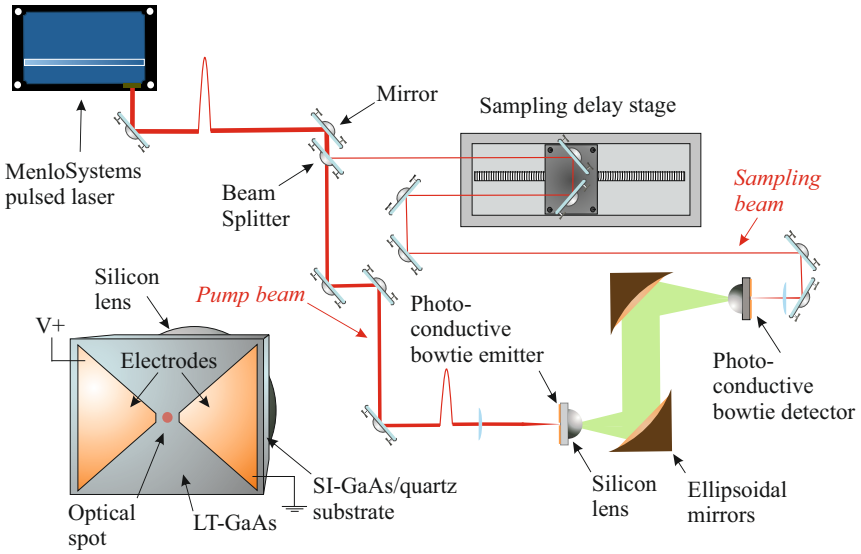

Figure 3.30: THz-TDS experimental setup to test small-gap bow-tie PC emitters at TeraView Ltd. PC detection is shown, employing another small-gap device fabricated on bulk SI-GaAs. Bottom left corner shows a schematic diagram on the bow-tie design under investigation. The optical beam is shown in red and the THz radiation in green.

3.6.2 Teraview Experiments

Figure 3.31 shows time-domain pulses for both devices, obtained on the experimental setup shown in Figure 3.30, at TeraView. For these measurements an applied bias field of 75 kV cm^{-1} was used, with an optical pump power of 10 mW. For detection the power of the sampling beam was kept constant at 4 mW. For these conditions, the LoQ device produces a peak-to-peak signal of approximately 3 times that of the LoG emitter. It is clear by looking at the corresponding frequency domain data that the majority of the additional power is due to an enhancement at low frequencies ($\leq$1 THz). As this is unexpected and is the only time it is observed, it could be due to the misalignment of the silicon lens on the LoQ device. This would also explain the slightly misshapen THz pulse in the time-domain. Despite this though, the benefit of using a LoQ device is clear to see. This measurement was not performed in a dry air or nitrogen purged environment, as can be seen from multiple water vapour lines in the FFT data. As this typically has more of an effect at higher frequencies, it might also help to explain the difference in results between the systems.

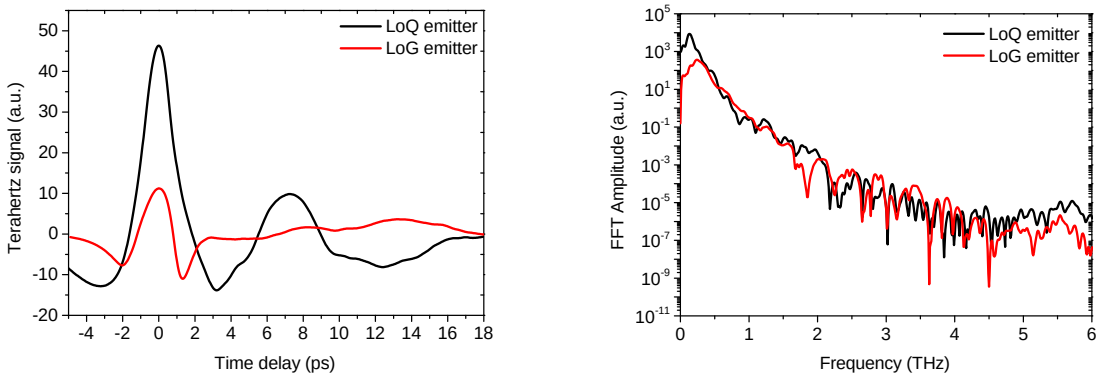

Figure 3.31: THz time-domain pulses (left) and their equivalent FFT (right) measured at TeraView in Cambridge. The Response of LoQ is shown in black and the LoG emitter response is in red. Both devices were measured at an applied field of 75 kV cm^{-1} and an optical pump and sampling power of 10 mW and 4 mW respectively. Both scans were performed in a non-purged environment.

3.6.3 Response as a function of applied field and optical excitation

A comparison of the emission properties of the two devices are shown in Figure 3.32 and 3.33. These measurements were performed on the initial setup which is illustrated in Figure 3.1 a) and discussed in section 3.6. Firstly, the outputted THz field has been plotted as a function of applied field. The values for THz field were extracted from the peak-to-peak signal of time-domain traces. This measurement was performed with an average optical power of 5 mW. Once again, the response of the LoQ emitter is shown to be superior, with a maximum output more than twice that of the LoG device. This agrees well with the data plotted in Figure 3.31. The difference in the response of the two devices is understandable when considering the higher breakdown field in LT-GaAs (500 kV cm^{-1}), compared with SI-GaAs (10 - 100 kV cm^{-1}) [151]. However, contrary to data taken with the large-gap emitters plotted in Figure 3.19, in this instance the output field from the LoQ emitter appears to saturate at high bias conditions. This could be owing to the carrier saturation velocity of the LT-GaAs, which has been shown to occur at ~100 kV cm^{-1} [206].

Figure 3.33 shows the peak-to-peak THz field plotted as a function of optical power. Compared with the equivalent results taken using large-area devices (Figure 3.20), fewer carriers appear to be generated in the SI-GaAs substrate and therefore the effects of heating might not be as severe. This explains why for large-area devices, the peak THz field from the LoQ emitter is ~3 times that from the LoG device, when using the highest measured optical power

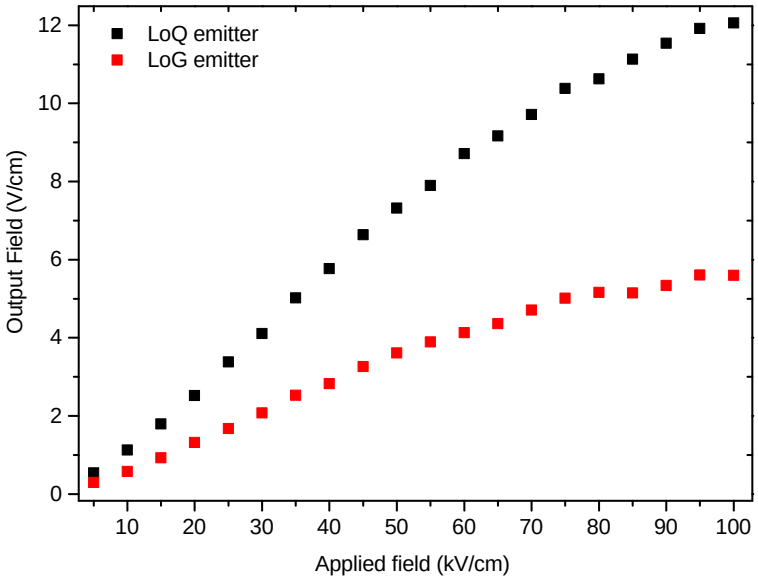

Figure 3.32: THz output field (peak-to-peak of time-domain pulses) plotted as a function of applied field. The response of the LoQ is shown in black and the LoG emitter response is in red. Measurements taken at the IMP, University of Leeds.

(600 mW). This reduces to only ~1/3 higher, when using the small-gap designs. At high optical powers, the response from both the LoQ and LoG small-gap devices appear to exhibit clear signs of saturation, which was not as evident when examining the large-area devices. This could be owing to localised field saturation, which is discussed in detail in section 3.1.1 and is known to have a significant effect on small-gap devices.

3.7 THz emission in reflection geometry

Up until this point, each PC device has been characterised based on its emission properties in transmission orientation. However, the benefits of using quartz-mounted emitters for free-space THz generation should prove just as effective if placed in a reflection system. In this arrangement, the emitted radiation is collected from the same side of the device as is focused onto by the optical pump beam. Illustrations of this are shown in Figures 3.1 b) and 3.2. In this geometry, the difference in refractive index between LT-GaAs and z-cut quartz should result in more of the power being emitted away from the quartz, compared with the use of LoG. This arrangement is typically used in a system which requires a broadband frequency response, as any dispersive effects of the THz pulse passing through the substrate are avoided.

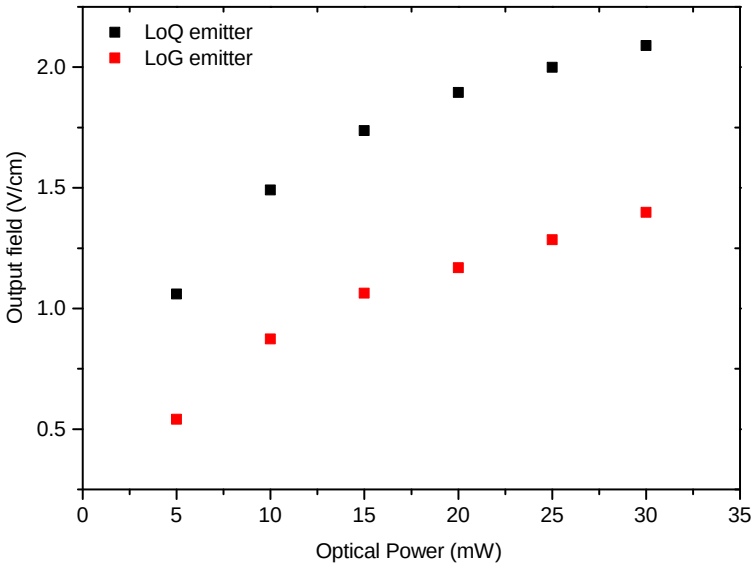

Figure 3.33: THz output field (peak-to-peak of time-domain pulses) plotted as a function of optical power on the emitter. The response of the LoQ is shown in black and the LoG emitter response is in red. Measurements taken at the IMP, University of Leeds.

However, there are several components in the system that also influence its bandwidth. Firstly, a shorter optical pulse width causes a decrease in the generation time of carriers, exciting higher frequencies. The second factor limiting the bandwidth is the detection technique. As previously described in section 3.1.3, each EO-crystal has a frequency-dependent coherence length associated with it, limiting the detectable bandwidth of the signal. The thinner the EO crystal used, the higher the frequency components that can be detected, at the cost of sensitivity. Taking these aspects into account, the following measurements were performed on a system driven by a 800 nm wavelength mode-locked Ti:sapphire laser (Vitara, Coherent) providing pulses with a width of 20 fs at an 80 MHz repetition rate. For detection, a 150-µm-thick GaP crystal was used in EO sampling. GaP was preferred to ZnTe in this instance owing to the absorption at 5.3 THz in ZnTe [136].

To demonstrate the benefits of using a LoQ emitter in this setup, the LT-GaAs was transferred onto a 2-mm-thick quartz substrate. Unlike in transmission measurements, other than a difficulty in mounting techniques, there are no apparent disadvantages to using a thick substrate, as it provides good heat dissipation. It also increases the optical path length of the substrate-air reflection. The device design was the same 200-µm-wide slot pattern used in section 3.5. The LoG device acting as a reference, is the same electrode design fabricated on

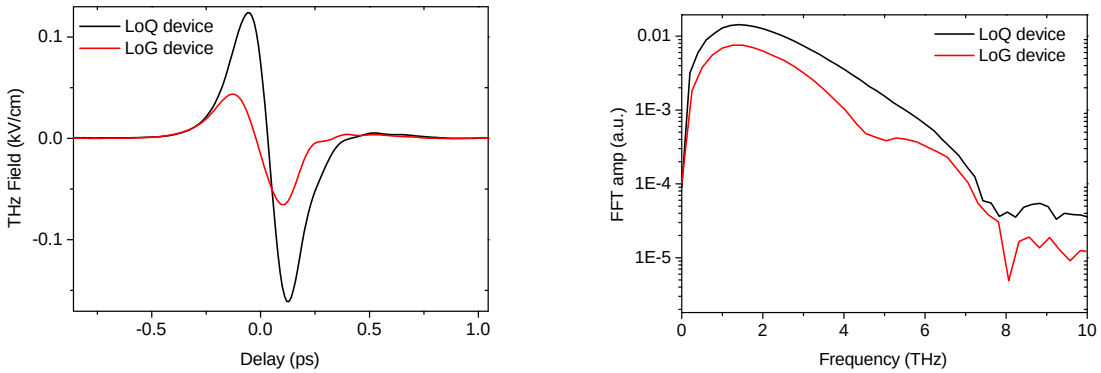

Figure 3.34: Time-domain pulses (left) from the LoQ (Black) and the LoG (Red) emitter. Corresponding FFT data shown on the right. Measurements taken at an applied field of 12.5 kV cm^{-1} and an optical power of 500 mW and the pulses are collected in reflection geometry.

a 500-µm-thick substrate. The time-domain pulses and the equivalent FFT data from the two types of emitter are shown in Figure 3.34, on the left and right respectively. For this scan the bias field was set to 12.5 kV cm^{-1} and an average optical power of 500 mW was used. Under these conditions, the peak THz field measured from the quartz device was approximately 2.6 times that of the as-grown LT-GaAs device.

3.7.1 Response as a function of applied field and optical excitation

The dependence of the peak-to-peak THz field on applied bias for both emitters is plotted in Figure 3.35. At bias fields below 5 kV cm^{-1}, the response of the emitters is almost identical. This implies that in this geometry, no significant advantage is gained from the lower refractive index of the z-cut quartz. As the bias field across the emitter is increased, the output signal from the LoQ device rises linearly to a maximum THz field of ~1 kV cm^{-1}, achieved at an operating bias field of 40 kV cm^{-1}. This working range is limited by the breakdown field of the nitrogen purged atmosphere (35 kV cm^{-1}) [207]. As previously mentioned, this value is dependent on the separation between the electrodes, as well as the pressure inside purging box [208]. The response of the LoG emitter however, was sub-linear until the device suffered catastrophic failure at 13 kV cm^{-1}. This maximum bias point agrees well with the breakdown field in SI-GaAs [193], suggesting that the field that can be applied across a given electrode gap is limited by its substrate properties. At the maximum operating voltage for each device, the LoQ device emitted approximately eight times higher peak THz field than the equivalent

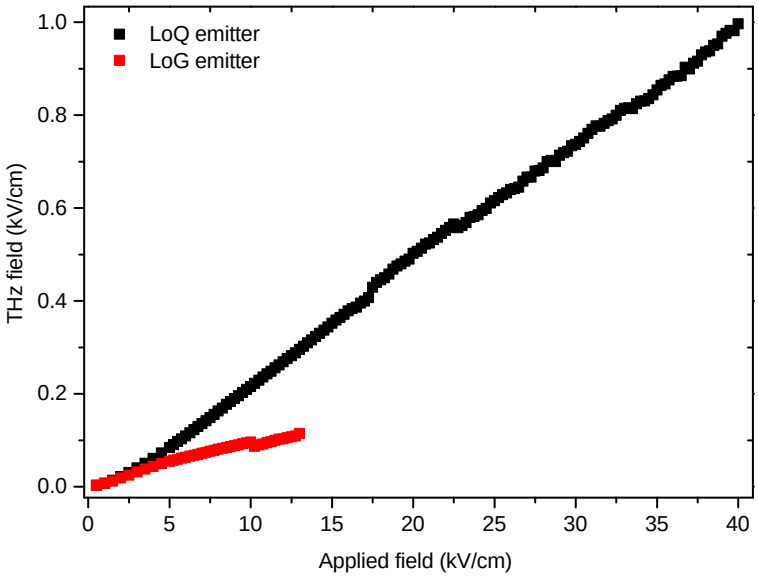

Figure 3.35: THz output field as function of applied bias field, collected in reflection geometry. Measurement performed with an optical power of 500 mW. Response of the LoQ device plotted in black and LoG device in red.

LoG emitter. The higher output fields, compared with transmission data shown in Figure 3.19, is owing to the higher peak optical power available from the Ti:sapphire (Vitara, Coherent) laser used here. This measurement was performed with an average optical power of 500 mW.

Figure 3.36 shows the outputted THz field as a function of optical power, for an applied bias field of 5 kV cm^{-1}. Due to the damage incurred to the LoG device in the previous measurement, an identical device fabricated in the same batch was used. Again, saturation behaviour is observed in the LoG device, while the LoQ device remains almost linear. This measurement was performed using PC detection, employing a LoQ device with the same active region design used for emission. This is discussed in detail in section 3.8. The output signal was amplified using a transimpedance amplifier with a gain of 1×10^8 Ω. The reasons for the difference in responses of the two devices have been discussed in detail in section 3.5, and can mainly be attributed to the parasitic current channels in the SI-GaAs substrate. This is known to cause heating in the device and reduce efficiency. It has also been shown that an elevated temperature reduces the breakdown field in LT-GaAs [193], which might have contributed to the failure of the LoG device. The use of the 2-mm-thick substrate for the LoQ emitter provided good heat dissipation and prevented damage to the device.

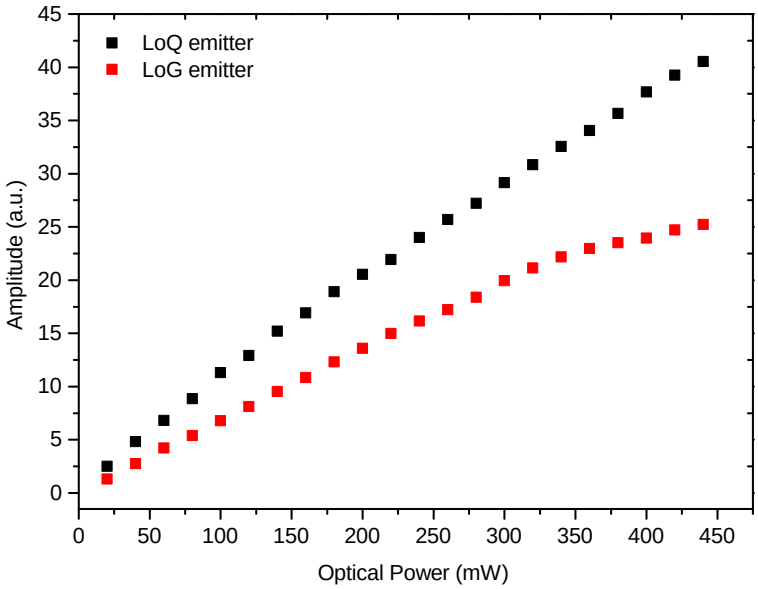

Figure 3.36: THz output field as function of optical excitation power, collected in reflection geometry. Measurement performed at an applied bias field of 5 kV cm^{-1}. The response of the LoQ device is plotted in black and the LoG device is in red.

3.8 Terahertz detection

In addition to PC emission, these devices were also characterised as PC detectors. To achieve this, the pulsed excitation laser and general experimental arrangement used for the reflective THz emission measurements (section 3.7) was again used. To generate the THz pulse a single LoQ emitter with a 200-µm-wide slot pattern, fabricated on a 2-mm-thick quartz substrate was used. Unless otherwise stated, it was biased at 5 kV cm^{-1} and illuminated with an average optical power of 500 mW. The LoG detector used in this comparison was identical to the emitter described above; the 200 µm gap is larger than would typically be used for PC detection [209] and the device geometries have not been optimised for this purpose. For reasons discussed in section‘3.1.2, PC detectors typically use smaller gaps than this. The comparative LoG detector was the same as that used in section 3.7. Both devices were fully characterised with the arrangement shown in Figure 3.5, such that the THz pulse and the optical beam were incident on the surface of the LT-GaAs. The generated photocurrent, proportional to the field of the THz pulse, was amplified using a transimpedance amplifier with a gain of $1 \times 10^8\,\Omega$. This was then connected to a lock-in amplifier, referenced at the emitter modulation frequency.

Figure 3.37 shows a) the peak-to-peak signal as a function of incident optical power fo-

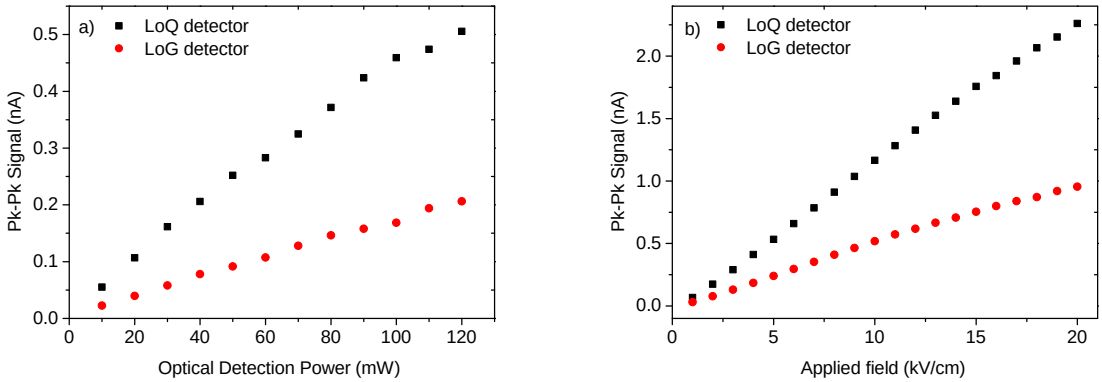

Figure 3.37: a) shows the peak-to-peak signal as a function of incident optical power focused onto the detector. (b) peak-to-peak signal as a function of bias applied to the emitter, with a fixed applied field of 5 kV cm^{-1}. In both cases the response of the LoQ detector is plotted in black and the LoG detector is in red.

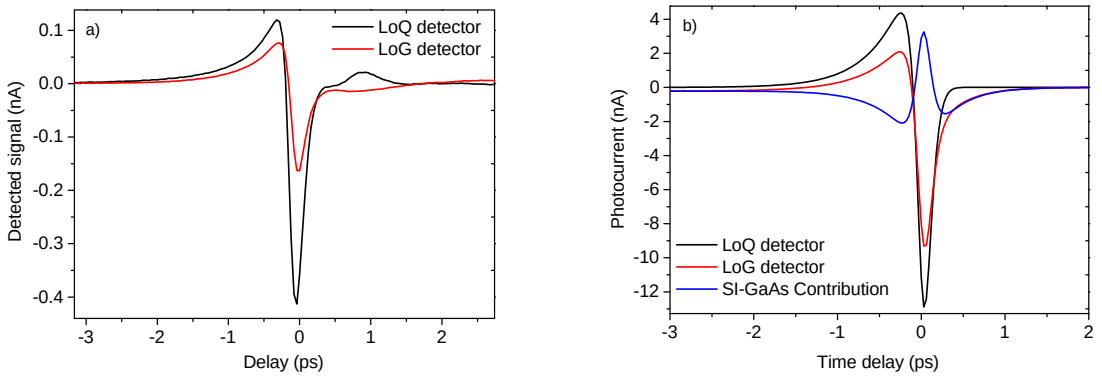

Figure 3.38: a) Two time-domain THz pulses measured using PC detection. In both cases the optical power of the sampling beam is set at 120 mW and a transimpedance gain of 1×10^8 Ω has been used. The bias conditions for the LoQ emitter are maintained constant. b) Simulation results of time-domain traces for both detectors. The blue curve shows the contribution from the SI-GaAs substrate. In both plots the response of the LoQ and LoG detectors are plotted as black and red lines respectively.

cused onto the detector, and b) peak-to-peak signal as a function of bias applied to the emitter, proportional to the incident THz field. In both instances, the peak measured field from the LoQ device was more than twice that measured from the LoG detector. Figure 3.38 a) shows the THz time-domain pulses, detected from both devices. The quartz detector shows a significantly larger second (negative) peak, when compared with the trace from LoG detector. This feature suggests that the SI-GaAs in the LoG device has a detrimental effect on its detection sensitivity. For these measurements the optical power of the sampling beam was maintained at 120 mW. Figure 3.38 b) shows the numerical simulations of the corresponding signals, calculated by solving the set of coupled differential equations given in Reference [171] for the free-carrier density, carrier velocity, and space-charge separation. These equations have been extended to account for two layers (LT-GaAs and SI-GaAs in this case): where the subscripts

Parameter	Value	Description
ϵ_r	13.1	Relative permittivity of GaAs
m^*	$0.067m_e$	Effective electron mass
η	3	Geometric factor
τ_{r1}	1 ns	Recombination time, LT-GaAs
τ_{c1}	0.4 ps	Carrier lifetime, LT-GaAs
τ_{s1}	30 fs	Momentum scattering time, LT-GaAs
τ_{r2}	1 ns	Recombination time, SI-GaAs
τ_{c2}	400 ps	Carrier lifetime, SI-GaAs
τ_{s2}	325 fs	Momentum scattering time, SI-GaAs
α	0.97	Optical pulse fraction absorbed

Table 3.2: Parameter values used to simulate the measured signal.

'1' and '2' denote the LT-GaAs top layer and SI-GaAs/quartz substrate respectively. Here, P_{sc} is the space-charge, v is the carrier velocity, n_f is the free-carrier density, $G(t)$ is the carrier generation function from the optical pulse, α is the fraction of the optical pulse absorbed in the top layer, and $E_{bias}(t)$ is the bias applied by the THz pulse. In this implementation, the space-charge effects in each layer are summed to find the reduction in effective bias across both layers; this assumption is valid since the layer thicknesses are significantly less than the antenna gap width. The parameters used in the calculation are given in Table 3.2. [4]

$$\frac{dP_{sc1}}{dt} = -\frac{P_{sc1}}{\tau_{r1}} + n_{f1} e v_1 \tag{3.9}$$

$$\frac{dv_1}{dt} = -\frac{v_1}{\tau_{s1}} + \frac{e}{m^*}\left(E_{bias}(t) - \frac{P_{sc1} + P_{sc2}}{\eta \epsilon_0 \epsilon_r}\right) \tag{3.10}$$

$$\frac{dn_{f1}}{dt} = -\frac{n_{f1}}{\tau_{c1}} + \alpha G(t) \tag{3.11}$$

$$\frac{dP_{sc2}}{dt} = -\frac{P_{sc2}}{\tau_{r2}} + n_{f2} e v_2 \tag{3.12}$$

$$\frac{dv_2}{dt} = -\frac{v_2}{\tau_{s2}} + \frac{e}{m^*}\left(E_{bias}(t) - \frac{P_{sc1} + P_{sc2}}{\eta \epsilon_0 \epsilon_r}\right) \tag{3.13}$$

$$\frac{dn_{f2}}{dt} = -\frac{n_{f2}}{\tau_{c2}} + (1-\alpha) G(t) \tag{3.14}$$

.

The generation function, $G(t)$, is given by a Gaussian pulse shape, assuming a FWHM of 20 fs, and corresponding to a power of 120 mW, $G_2(t)$ is set to zero for a quartz substrate. The

[4] These simulations were performed by Dr Joshua Freeman

applied bias is parametrised using the function:

$$E_{\text{bias}} = E_{\text{THz}} \sin(\omega_{\text{P}}(t - t_0)) \text{sech}\left(\frac{1.76(t - t_0)}{t_{\text{p}}}\right) \tag{3.15}$$

Where the parameter values $E_{\text{THz}} = 0.2\,\text{kV cm}^{-1}$, $\frac{\omega_{\text{P}}}{2\pi} = 1\,\text{THz}$ and $t_{\text{p}} = 0.1\,\text{ps}$ were determined by comparison to the pulse measured in Figure 3.34.

The simulation then proceeds by integrating the net transient current flowing in the PC detector at each delay, t_0, to find the expected measured current, shown in Figure 3.38 b). From the simulation we determine that the reduction in detected current measured for the LoG device relative to the LoQ device is due to space-charge effects in the SI-GaAs substrate. Because of the longer momentum scattering time (higher mobility) in the SI-GaAs, the space-charge builds up more quickly in this layer, despite the smaller optical intensity. This amounts to screening of the THz pulse, particularly the second peak, in the SI-GaAs substrate that leads to a current acting in the opposite direction to the photo-current in the LT-GaAs layer, reducing the overall measured current. Using the same parameters, these simulations also allow the light resistance values to be accurately recovered for the two LT-GaAs-based-devices, given in Table 3.1. The spot size used in the simulation was adjusted to maximise signal, or photo-current, as in the experiments. Furthermore, simulations were also performed to determine the effect that carrier screening has on THz emission. However, due to the unidirectional acceleration of carriers, the contribution is minimal.

3.9 Substrate thickness tests on quartz-based devices in reflection geometry

To further compare the emitters and detectors under investigation in this chapter with a more conventional system, normalised time-domain traces have been plotted in Figure 3.39. The red curve shows the response of the conventional TDS arrangement, with a LoG emitter (THz collection from the laser excited surface) and EO sampling for detection. This response shows four separate system reflections; as labelled, those occurring at 5, 10 and 17.5 ps originate from the 150-μm-thick EO crystal, while the largest system reflection, arriving at 12.5 ps is

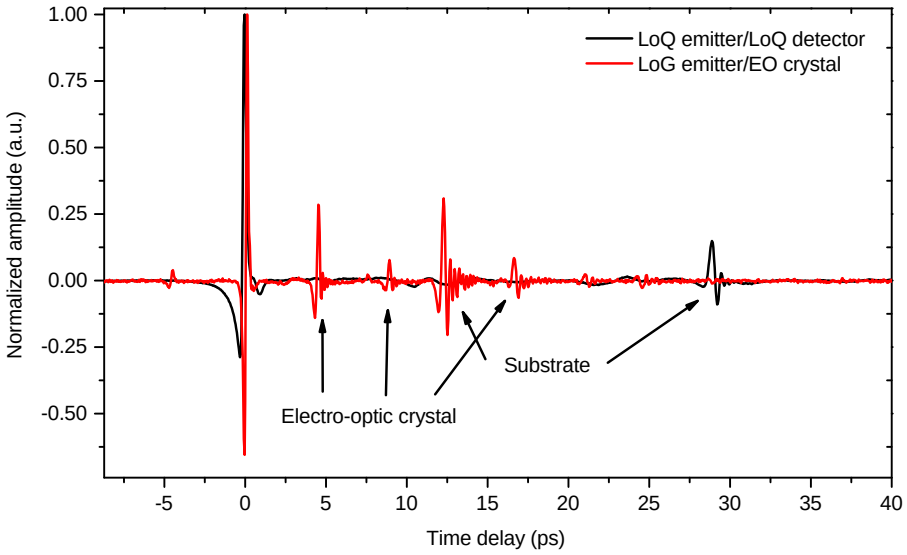

Figure 3.39: Normalised time-domain trace using LoG emitter with 150-µm-thick GaP electro-optic detection crystal (red line) and LT-GaAs on a 2-mm-thick quartz substrate as emitter and detector (black line). In both instances a 5 kV cm^{-1} bias and 500 mW average optical power were applied to the emitter.

from the 500-µm-thick SI-GaAs emitter substrate. The black trace shows the response when both emitter and detector are replaced with LoQ devices (2-mm-thick quartz substrates). In this case the first system reflection arrives 30 ps after the original pulse, originating from the interface between the air and the 2-mm-thick z-cut quartz substrate. Owing to smaller contrast in refractive index between quartz and air, than SI-GaAs and air, this reflection appears significantly smaller in the LoQ system. This reduction in system reflections increases the available frequency resolution of the system without the need for post-processing techniques [181–183].

Plotted in Figure 3.40 displays the corresponding FFTs, normalised to the noise in each case. The FFTs have been calculated with a time window of 35 ps. In addition to the significantly greater SNR from the LoQ devices, the smoother frequency domain response caused by the reduction in system reflections, is also evident. In this instance, we are able to perform a scan six-times longer before the first reflection is recorded, resulting in a six-fold improvement in frequency resolution. However, in principle, there is no limit to the thickness of quartz substrate that can be fabricated on, and used in reflective orientated emission and THz detection. The use of an emitter boasting a 5-mm-thick quartz substrate has been demonstrated in section 3.5.2. While these measurements were performed in transmission using BSI, this device could just as easily be used in a reflective system. It should also be noted that here both

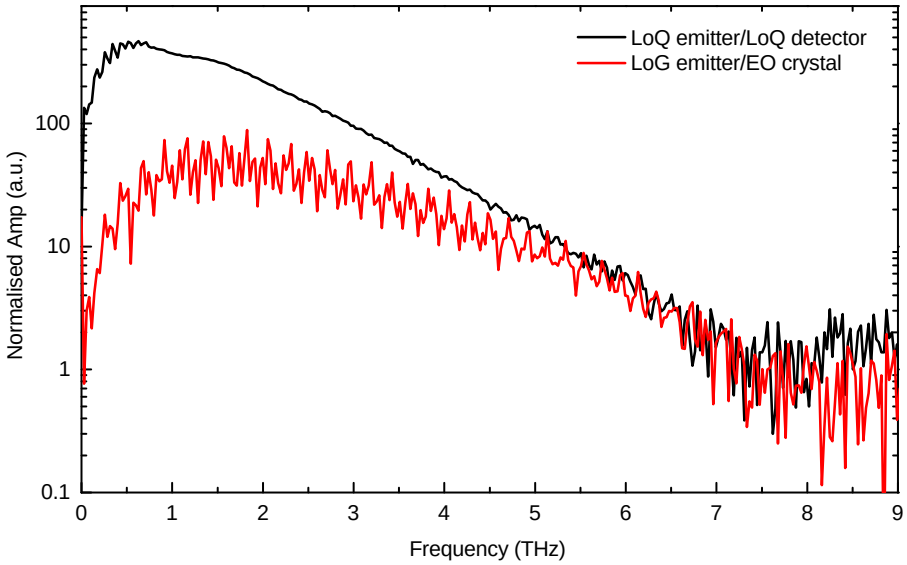

Figure 3.40: FFT of the same data, normalised to the noise level and calculated with a time window of 35 ps, i.e. truncated before the quartz substrate reflection

emitters have been biased with the same field/bias of 5 kV cm^{-1}/100 V. The bias of the LoQ emitter can be increased further by approximately 8 times.

3.10 Applications of Quartz-based devices in time-domain spectroscopy systems

Since the initial realisation of quartz-based PC devices and the demonstration of the advantages they can provide over LoG devices, there has been a considerable interest for their use in spectroscopy applications. The first example uses the enhanced emission properties to transmit a THz pulse through temperature controlled liquid flowcell (Specac), which has been placed in the sample-space of a time-domain spectroscopy transmission setup. By systemically filling the flowcell with a series of alcohols and comparing the transmitted data with a reference scan, the frequency dependent refractive index and absorption coefficient for each substrate can be obtained. Example data of the THz pulse having passed through different samples is shown in Figure 3.41. The greater power available from the LoQ device means that thicker liquid channels can be used, making the system more sensitive to the variation to the properties of the liquids, owing to an increase in the interaction length [5].

[5]This work was completed in collaboration with Matthew Swithenbank

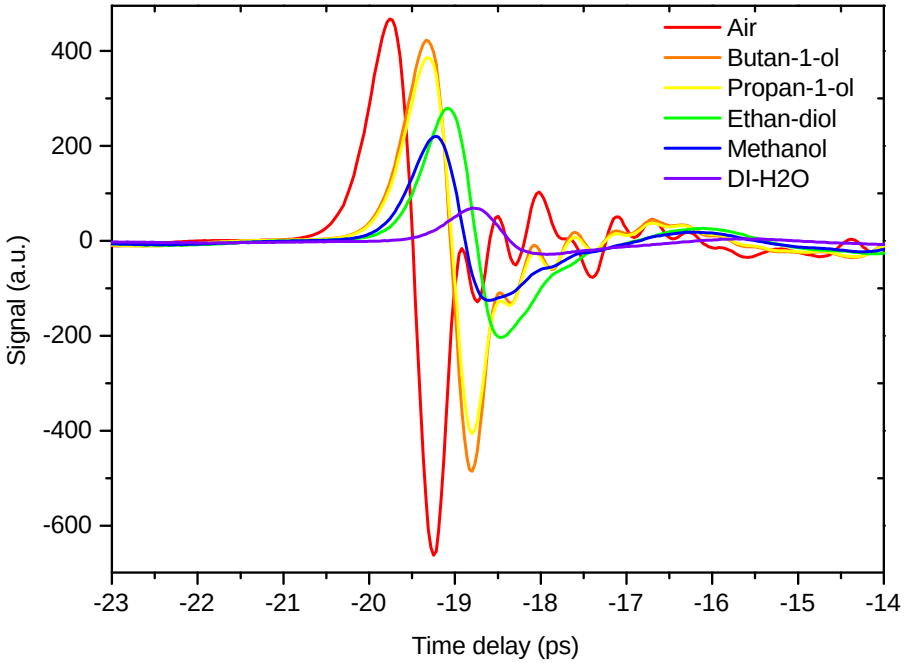

Figure 3.41: Time-domain THz pulses having passed through a flowcell, containing a series of temperature controlled alcohols. A reference sample 'air' has also be taken through an empty flowcell.

Another application of LoQ devices is for the development of tunable single frequency THz sources. In this work an amplified Ti:Sapphire laser, producing 1 mJ pulses at a repetition rate of 5 kHz, sources a TDS transmission setup. In this system LoQ devices are used as both an emitter and a detector. Before exciting the emitter the optical pump pulse is passed through a Fabry-Perot cavity with semi-reflecting mirrors on the front and back. This generates a pulse train in which the frequency of the pulses is governed by the cavity length. Figure 3.42 show three time-domain pulses generated with varied FP cavity lengths, each with oscillations

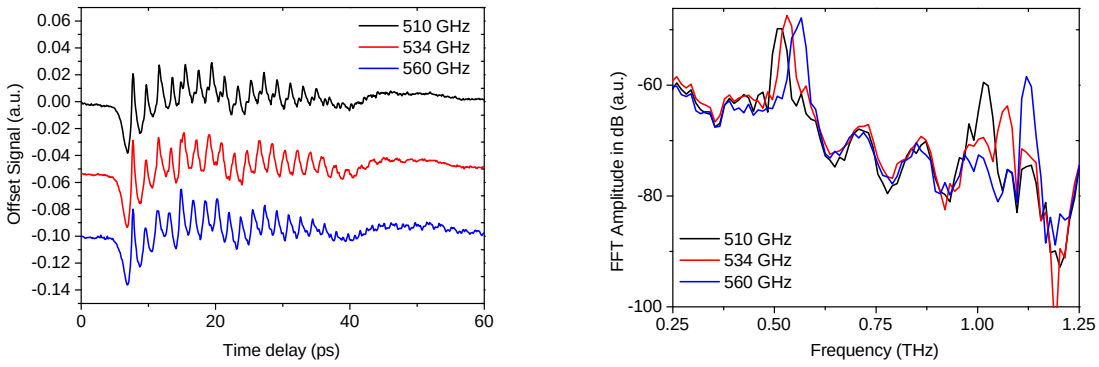

Figure 3.42: (left) Time-domain data taken with a Fabry-Perot cavity in the optical pump path, set to three different round-trip times. (right) FFTs of the data plotted to the left, revealing the fundamental mode set by the round-trip frequency and the first harmonic.

trailing the initial THz pulse. When converted to the frequency-domain, which is shown on the right, peaks relating to the round-trip frequency of the Fabry-Perot cavity are present, together with the first harmonic of the fundamental mode. While this method has been used before [210, 211], it normally involves non-linear optical crystals, such as lithium niobate, as amplified lasers tend to saturate and damage PC devices. The LoQ devices are beneficial to this experiment as they allow the generation and detection of THz pulses with an amplified laser without being damaged through overheating. This is owing to the low current being drawn by the device, compared with that on SI-GaAs. This work was conducted by Dr Nick Hunter in collaboration with the University of Nottingham.

3.11 Conclusion

In conclusion, epitaxial lift-off and van der Waals bonding techniques have been used to transfer LT-GaAs active layers onto quartz substrates, realising an alternative layered material combination for large-area THz PC emitters and detectors. It has been shown that these devices have three significant advantages over more widely used PC emitters and detectors. The reduction in dark current and parasitic photo-current in quartz-based devices leads to reduced heating and increased breakdown voltages. In the most significant comparison this has resulted in THz field amplitudes approximately eight-times larger than equivalent LoG devices. This technique has been shown to work with several different active region designs and electrode geometries. When used for PC detection the absence of an SI-GaAs substrate eliminates the long-lifetime carriers and increases the measured signal.

The ability to choose a thicker substrate allows system reflections to be delayed in time and their amplitude to be reduced without a loss of bandwidth, thereby increasing the available frequency resolution. To demonstrate this, data from devices with quartz substrates ranging from 40 μm to 5-mm-thick has been presented. Lastly, two examples of applications in which LoQ devices have already been used are presented, with the advantages they possess over the previously used LoG devices made clear.

Chapter 4

Measuring the Gain Recovery Time of a Bound-to-Continuum Terahertz Quantum Cascade Laser

This chapter is divided into two parts. Section 4.2 begins with the full characterisation of a THz-QCL with a BTC active region design. This device is then applied in section 4.4.2, where the GRT of the QCL is experimentally determined. This is accomplished using a THz-pump-THz-probe technique, employing an experimental setup derived from the THz-TDS arrangement described in chapter 3. The motivation behind this work is discussed in detail, before the experimental setup and the alignment procedure are introduced. The data collected from these measurements is then discussed and conclusions are drawn. It has been found that the measured GRT reduces to a value of ~17 ps as the QCL is brought closer to threshold. However, owing to instabilities in the signal as the QCL is driven above threshold, brought about by a sudden increase in the photon density, the SNR of the measurement was found to decrease dramatically.

To avoid these issues, the same device was subsequently prevented from lasing by applying ARC to the facets, causing an increase in both the overall mirror loss and the threshold current density. The experiment was then repeated on the coated device with the intention of measuring the GRT response at high QCL bias conditions. In fact, with the addition of a high

powered LoQ PC emitter in the setup, and the resulting increase of the coupling efficiency into the cavity, the greater injected pump pulse was found to provide an interesting incite into the time-resolved carrier dynamics and gain properties of the laser. Furthermore, measurements conducted before and after the ARC was applied to the device, revealed that the GRT of this laser increased at high bias conditions above the previous threshold current. This experiment and findings are discussed in section 4.5.

4.1 Introduction

There has been significant interest in understanding the dynamics of emission from QCLs, and the generation of pulses on ultrafast timescales. The integration of THz-QCLs with TDS [186, 212, 213] techniques has allowed the measurement of the electric field of the laser emission with an extremely high time resolution. This has revealed a complex time-domain pulse structure, even when the QCL is operated at a fixed current [214]. At the same time active modelocking has also been developed. Coherent measurements have been reported using both an frequency stabilization technique [215] and a time-domain technique based on THz pulse injection seeding of a QCL [216]. This research has highlighted the instabilities present in QCL emission [217] and the difficulty of forming stable modelocked pulses from this type of device owing to the interplay of the inherent characteristic lifetimes. In fact, there are several lifetimes that are important in determining the characteristics of the laser emission, including the dephasing time of the laser transition, the photon lifetime, the cavity round trip time, and the GRT. In many lasing systems these lifetimes will be significantly different, leading to predictable dynamics. In QCLs however, they are expected to have similar values, in the range of 1-50 ps, with the value of the GRT being least well established. Crucially, it is the ratio between the GRT and the round-trip time of the laser cavity that is important for achieving modelocking; if the GRT is short compared with the round trip time, then the gain will recover before a pulse circulating in the cavity returns to the same point, enabling several pulses to propagate simultaneously and thus preventing the onset of modelocking.

There has been one experimental measurement of the GRT in THz-QCLs to date [218].

This work did not, however, measure gain directly, but rather the recovery of photo-current as a function of time delay between two high-power THz pulses injected into the QCL, generated by a free-electron laser. A value of 50 ps for the GRT was found, which is significantly longer than the 2-3 ps measured for mid-IR frequency QCLs [219,220] using an IR pump-probe technique. The GRT has also been inferred indirectly from simulations of pulse-seeding in THz-QCLs; this enabled an estimate of ~15 ps to be made for the GRT [221], which agrees well with the value for the upper state lifetime of 12 ps found by Scalari *et al.* [107]. In the first half of this chapter, the measurement of the GRT of a BTC THz-QCL, similar to the device used in reference [218], is described. For this experiment the THz-QCL was seeded by broadband THz pulses generated from a PC emitter [150]. This experiment provided a value for GRT of ~17 ps [222], measured just below the threshold current of the device. However, this experiment did not allow measurements of the GRT above threshold, without the addition of excess noise. In the second part of the chapter, ARC [223] is applied on the same device to prevent it from lasing, allowing the measurement to be repeated at higher QCL bias conditions without incurring excess noise. This also allows one to investigate the gain dynamics of the laser in more depth. The BTC active region was chosen as much of the theoretical background work has been achieved using a similar design and thus a comparison could be made. Furthermore, THz-QCLs based on LO-phonon extraction (rather than the miniband extraction design measured here) are expected to exhibit faster dynamics [93, 212]. As such, it was believed that BTC active region would provide a better opportunity of measuring GRT.

4.1.1 Terahertz Quantum Cascade Laser

The THz-QCL used in this study was based on BTC active region design [90], contained within a SI-SP waveguide [33]. The active region itself is based on a published BTC design lasing at 2 THz [92], that was later revised to demonstrate an improved wall-plug efficiency [224]. The initial heterostructure compromising of alternating GaAs/AlGaAs layers was grown directly onto an SI-GaAs substrate using MBE. This was performed by Dr. Lianhe Li in the MBE machine at The University of Leeds. It was then processed in the Wolfson nanotechnology cleanroom by Dr. Reshma A. Mohandas. A detailed description of the fabrication procedure used can be found in reference [225]. The ridge was scribed and divided to form a device

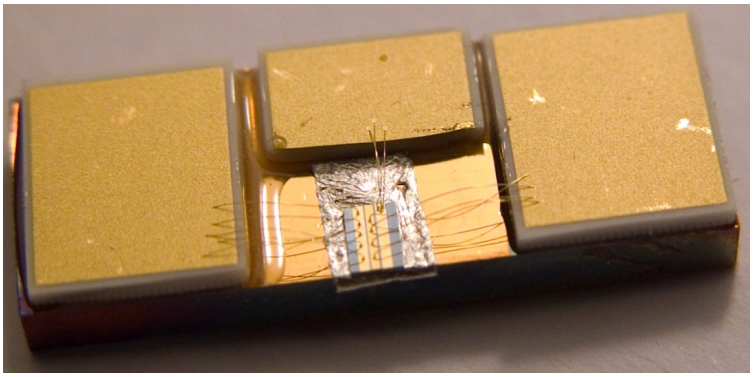

Figure 4.1: Picture of THz-QCL mounted onto a copper block using a thin layer of indium. The two gold contacts on the device are gold wire bonded to the ceramic contact pads.

4.4-mm-long and 200-µm-wide. A long cavity device was necessary for this work, compared with those used in previous studies [92, 224], as it means that the THz pump pulse remains in the cavity for a longer time period. It therefore experiences higher amplification resulting in a greater reduction in the population inversion, and a better opportunity to measure the GRT of the device.

To position the device in a cryostat and apply a bias to it, the QCL was mounted onto a copper block with dimensions 20 mmx7 mmx2 mm. Prior to this, the copper block had been polished to remove any non-uniformities from its surface and thereby improve the thermal contact between the device, the block and cold finger of the cyrostat. Two gold coated ceramic pads were glued at the two ends of the copper block using GE varnish. These act as electrical contacts when mounted in the cyrostat and were gold wire bonded to the device. To mount the QCL in between the two contact pads, the copper block was positioned onto the hotplate of a ball bonder and heated to 145 °C. An indium sheet was placed between the two contact pads and as it melted it was spread uniformly into a thin layer using a flat-end blade. The melting point of indium is 142 °C. The temperature of the hotplate was then reduced to 100 °C, as the device was placed on top of the solid layer of indium. The hotplate was once again increased to 145 °C as the device was forced downwards onto the copper block using two metal needles. The melted indium solders the device to the copper block. The hotplate temperature was again reduced to 100 °C before the top and bottom contacts of the device were bonded to the ceramic pads using gold wire bonds. An example of a fully mounted QCL is shown in Figure 4.1 [225].

4.2 LIV Characterization of THz-QCLs

It was necessary to optically and electrically characterise the device. For this the QCL was mounted onto the cold-finger of a continuous flow liquid helium Janis cryostat (ST-100). A thin-layer of thermal grease was applied between the device and the cold finger to ensure a good thermal contact. Two copper pins were used to fix the device in place and apply voltage. A heat shield and outer casing was attached around the outside of the cold finger. The outer casing has 4 windows, 2 made from quartz and 2 from polytetrafluoroethylene (PTFE). The output radiation was coupled through the PTFE windows, as this material has low absorption in the THz region, while the optically transparent quartz windows are used to accurately position the laser, relative to the rest of the experimental setup. The alignment was performed by clamping the cryostat to a specifically designed mount, positioned on XYZ translation stages. The cyrostat chamber was pumped down to a pressure as low as 4×10^{-6} mbar. It is then cooled to ~15 K using liquid helium (L:He). The following experiments presented in this chapter only require the laser to be driven in pulsed mode and therefore the device is tested as such. The experimental setup used to obtained LIV curves is presented in Figure 4.2.

A 10 kHz pulse train with a 2 % duty cycle was used to bias the QCL. This was sourced from a pulse generator (Agilent 8114A), which was electrically gated at 167 Hz to allow the signal to be detected using a L:He cooled bolometer. The output signal from the bolometer, which is proportional to the detected THz power, was connected to a lock-in amplifier also referenced at 167 Hz. To measure the voltage across the device a separate set of copper pins in the cyrostat was connected to channel 1 of an oscilloscope (Keysight 2002A), which itself was connected to an operational computer. An inductive loop probe was used to measure the current through the laser and was connected to the channel 2 of the oscilloscope. A LabView program was used to control the instruments, setting the bias voltage of the device and measuring values for the current and detected THz power, from the oscilloscope and the lock-in amplifier, respectively. LIV curves taken using the device discussed in section 4.1.1, have been plotted in Figure 4.3. The threshold current density for this device was found to be ~124 A cm^{-2} at 15 K.

To obtain the spectra of the radiation output from the device, a FTIR was positioned be-

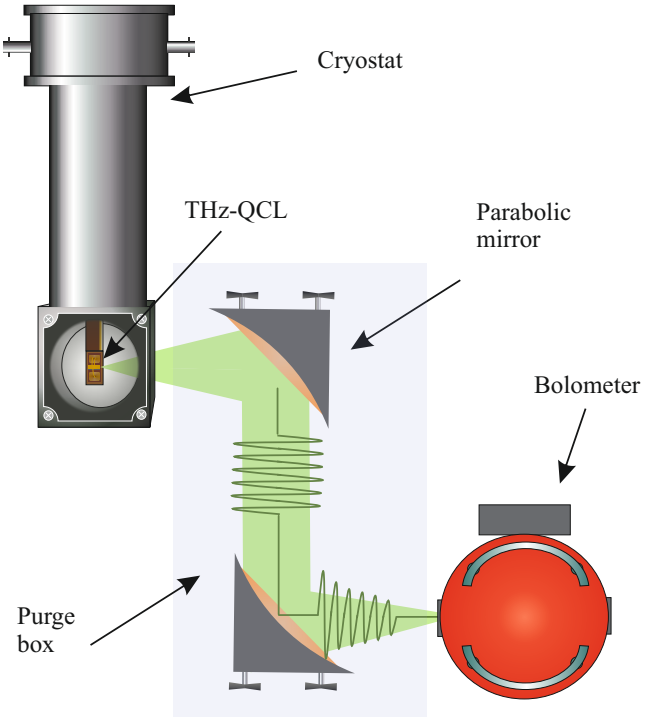

Figure 4.2: Experimental setup used to acquire LIV data. The QCL is mounted in a pressurised cryostat and cooled to ~15 K. The detection of emitted THz radiation is performed using a helium cooled bolometer.

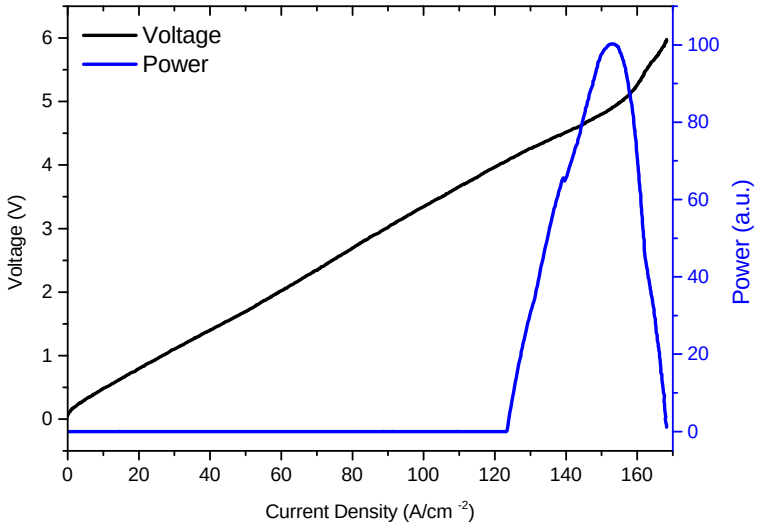

Figure 4.3: LIV data for a 4.4-mm-long QCL, with a BTC active region. It is was fabricated with a SI-SP waveguide. This QCL was biased with 10 kHz modulation frequency and a duty cycle of 2 %.

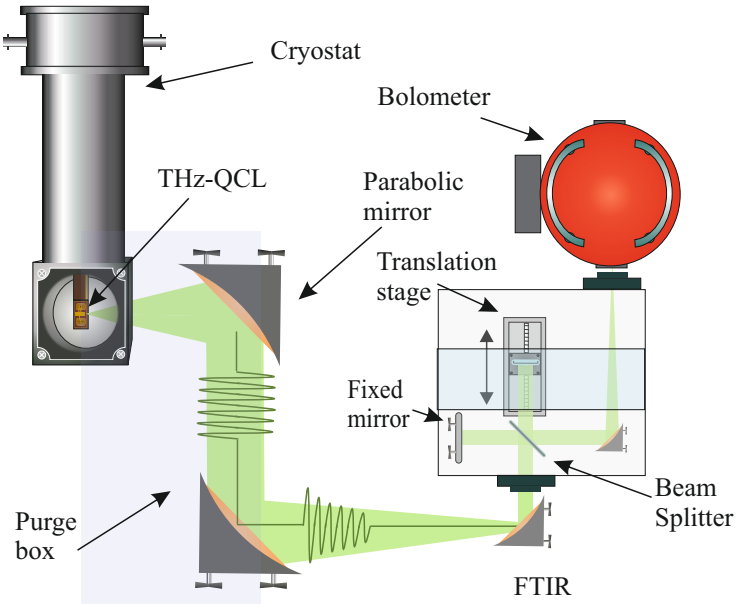

Figure 4.4: Experimental setup incorporating a Fourier transform infrared spectroscopy (FTIR) to obtain the spectral output of the QCL. Within the FTIR, a Michelson interferometer is illustrated. The heatsink temperature was kept at 15 K using a constant flow of L:He and as much of the setup is purged to remove the effect of water absorption from the air.

tween the device and the bolometer. The means of electrically biasing the device remains the same, with the QCL still cooled to ~15 K. The experimental setup is illustrated in Figure 4.4, where a Michelson interferometer is shown within the FTIR. This is a well-established technique for measuring the frequency components present in the output signal. The output radiation from the QCL is collimated using three off-axis parabolic mirrors, before passing into the FTIR, where it is split along two optical paths. Both paths contain mirrors that reflect the radiation back towards the beam splitter and onto a detector. By varying one of the path lengths using a translation stage, relative to the other, an interference pattern ('interferogram') between the two signals is detected using the bolometer. The spectrum of the QCL output signal can then be obtained by performing an FFT on the interferogram.

This measurement was performed for a range of QCL bias conditions and the resulting spectra are plotted with an offset in Figure 4.5. As the bias is increased the spectral output of the QCL tends to decrease in frequency, reducing from 1.99 to 1.97 THz across the lasing dynamic range. This apparent red shift with a rise in bias has also been observed in similar active region designs [92, 224]. One explanation for this is due to mode-hopping, which is discussed

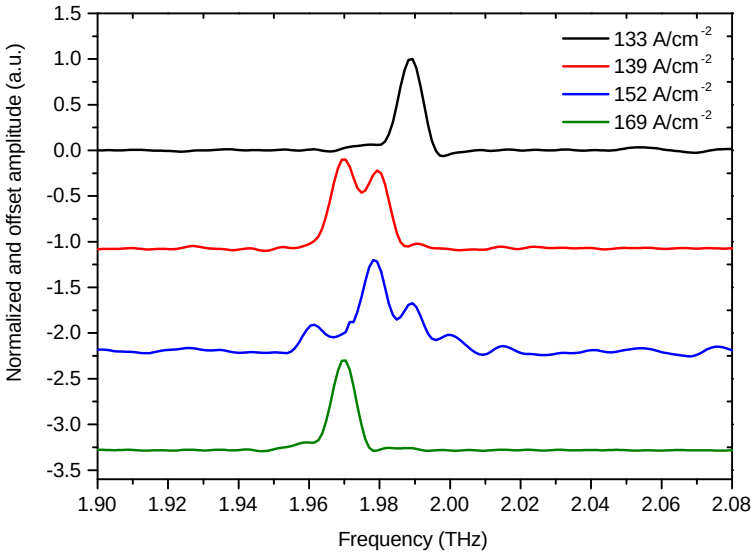

Figure 4.5: Spectra obtained using the FTIR setup shown in Figure 4.4, at four different bias conditions that are offset on the Y-axis. The frequency of the maximum peak is shown in decrease as function of bias after the device (red shift).

in section 4.5.2. THz-QCLs in general produce a blue shift, owing to the separation of electron states in the active region with a rise in bias, which is known as the Stark effect [226, 227]. The relatively low frequency emission of this laser was important as it is within the spectral region of the THz pulses generated through PC emission on a TDS transmission setup (see section 3.5). Previous measurements performed by Dr Reshma A. Mohandas revealed that this device had a maximum operating temperature of ~55 K.

4.3 Experimental Setup

After LIV characterisation of the device was complete, the next stage was to configure a means of effectively coupling a broadband THz pulse into the QCL cavity. To achieve this, the cyrostat still containing the device, was positioned in the experimental setup shown in Figure 4.6, which was adapted from the TDS setup discussed in chapter 3. The system is based on a femtosecond laser, centred at 800 nm, providing 100 fs pulses at an 80 MHz repetition rate and 2 W average power. The beam was first split, and the more powerful (90 %) component was further divided into the 'pump' and the 'probe' beams. The pump beam, with an average power of ~1 W, passed through a delay stage, allowing independent variation in arrival times of the pump and probe signals at the QCL. The probe beam, with an average power of

100 mW, passed through a half-wave plate and an optical chopper, to discriminate between the pump and probe signals. The half-wave plate was set to ensure the pump and probe beams had orthogonal polarization; this reduced any interference effects between the near-IR pulses incident on the emitter. The probe beam was then recombined with the pump beam after a delay stage, and focused onto a single PC emitter. For large-area PC emitters used here the dependence of the THz power on the polarization of the incident near-IR pulses is weak, and the resulting linear THz polarisation depends only on the electrode geometry.

The type of PC emitter used here varied throughout the project. For the initial measurements an LoG device was used, consisting of a 2-μm-thick layer of LT-GaAs grown onto a 500-μm-thick SI-GaAs substrate, with a 100-nm-thick sacrificial AlAs layer grown in between. A large-area slot electrode antenna with a 100-μm-wide gap was fabricated directly onto the LT-GaAs surface. For the second set of measurements the LoG device was replaced by a LoQ [228] emitter, which was deliberately fabricated with the same electrode geometry. To gain the highest possible output signal from the device the radiation was collected in transmission geometry (Figure 3.2), where the emitter is optically excited from the opposite side of the wafer as the collected THz radiation. As such a hyper-hemispherical silicon lens could be attached to the back of the emitter to increase the detected far-field signal, as well as to limit surface reflections. A four off-axis parabolic mirror setup was used, where the first 2 mirrors collected, collimated and focused radiation through the sample-space. The radiation was then collected using the third parabolic mirror and focussed onto a detector with the fourth. A weaker 20 mW 'sampling' beam formed at the first beam splitter was steered through a second variable delay-stage before being used for electro-optic signal detection using a 2 mm thick ZnTe crystal. An optical scan-delay or 'shaker' (scanDelay USB - A.P.E) was also positioned within the sampling beam to enable real-time observation of the THz pulse. This was mainly used to assist in the alignment of the parabolic mirrors and silicon lens, as these are known to effect the optical path length of the generated THz pulse, relative to the optical sampling beam. The 4-parabolic mirror setup was constructed inside a plastic purge box, and purged with dry air to reduce the absorption of THz radiation by atmospheric water vapour.

With the QCL still mounted inside the cyrostat, it was positioned within the sample-space

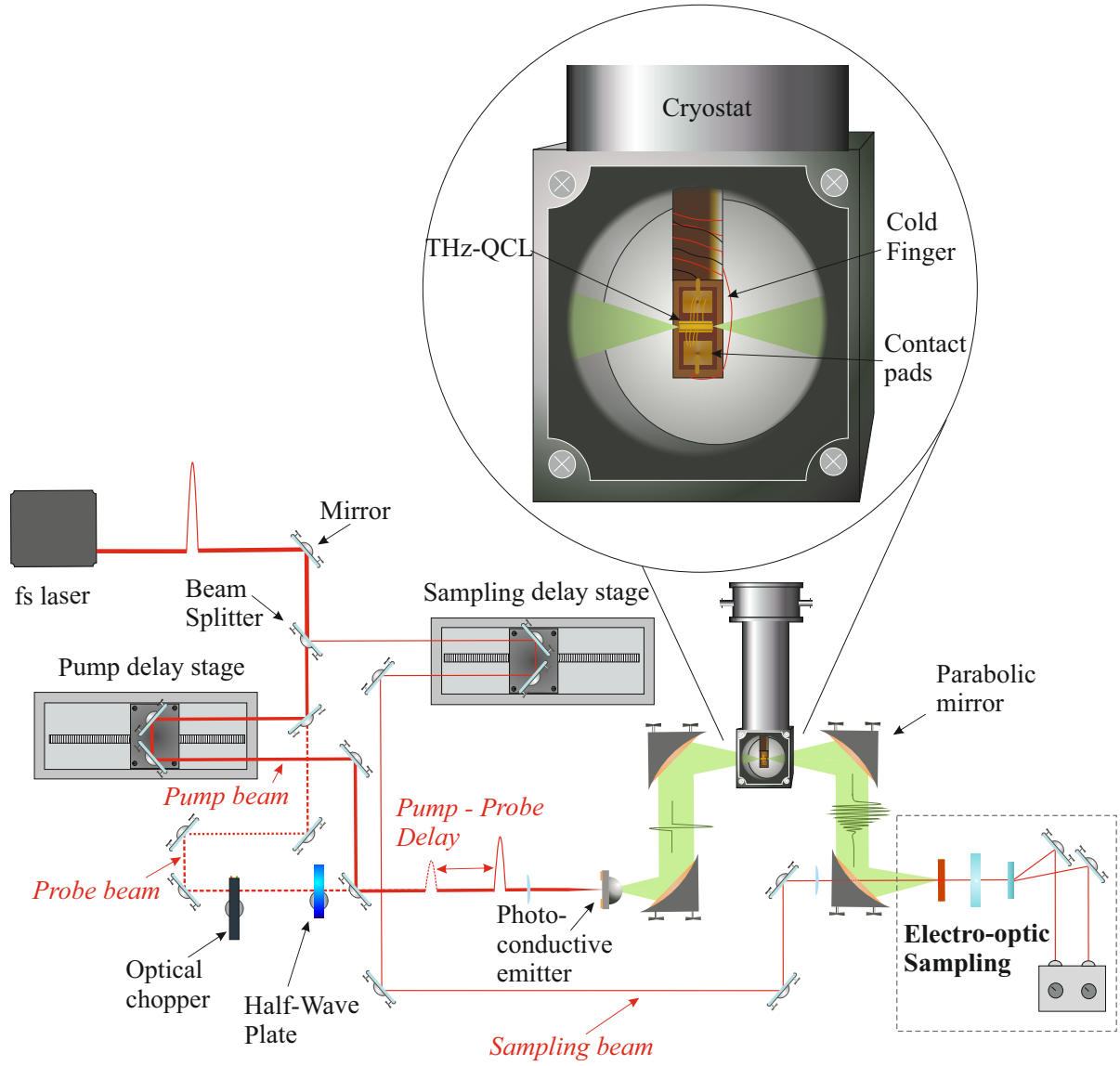

Figure 4.6: Experimental layout designed for THz-pump-THz-probe on the THz-QCL, derived from a THz-TDS transmission arrangement. Optical beam (pump, probe (dashed), samplng) shown in red. The relative average power in the optical beam is related to the width of that beam, with the pump-beam being the most powerful and therefore thickest. The THz-pulse is shown in green and is focused through the waveguide of THz-QCL before being detected using EO sampling. The bottom of the cryostat, housing the THz-QCL is enlarged above the main diagram.

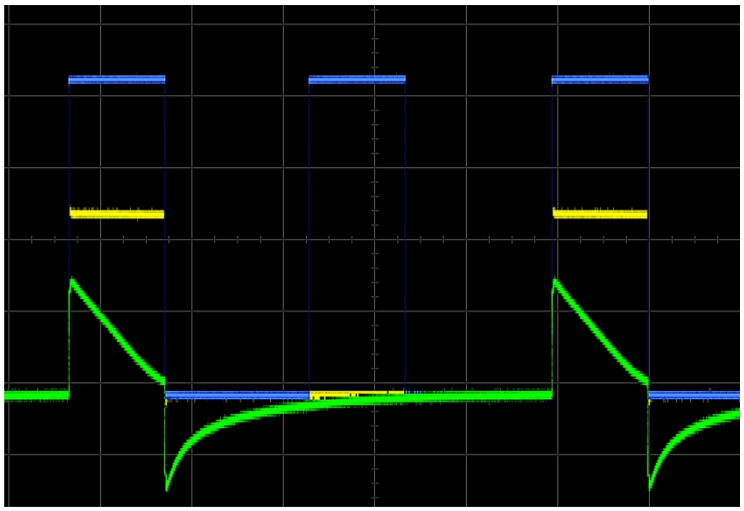

Figure 4.7: Pulsed electrical signals biasing the THz-QCL and the PC emitter. The emitter voltage is in blue (7.6 kHz), the QCL voltage is in yellow (3.8 kHz) and the QCL current is in green. The emitter is being driven at twice the frequency and duty cycle as the QCL.

in Figure 4.6. The broadband THz pulses generated from the PC emitter were coupled into the QCL facet using the first set of off-axis parabolic mirrors. During the mounting process it was ensured that the polarization of the THz radiation was parallel to the growth direction of laser. To perform the THz-pump-THz-probe experiment on the laser, it was engineered that the THz 'pump beam' would arrive first at the QCL's input facet, causing stimulated emission of the population inversion within the active region and thereby depleting the available gain. At a later time the THz probe pulse was coupled into the cavity and experiences amplification proportional to the population inversion in the active region. The probe pulse is then collected and measured through EO sampling. To electrically bias the QCL and the PC emitter the pulse train shown in Figure 4.7 was used. In this diagram the voltage and current applied to the QCL are represented by the yellow and green traces respectively. The QCL was driven by a square wave with frequency 3.8 kHz and 20 % duty cycle (52.6 µs pulse width). The emitter bias, which is shown in blue, was synchronized to the second harmonic of this signal at 7.6 kHz, also with a 52.6 µs pulse width (40 % duty cycle). A lock-in amplifier referenced to the QCL bias was used to monitor the signal from the balanced photodiodes such that it measured the difference signal between the QCL on and off states, thereby removing spurious signals, such as those arising from pulses not travelling through the QCL. By locking into the 1st or 2nd harmonic of the reference frequency, signals produced by the QCL and the PC emitter respectively can be retrieved.

4.3.1 Alignment Procedure

To perform this experiment effectively and observe any effect caused by the pump pulse, enough of the THz pump and probe pulses was required to be successfully coupled into the facet. The more photons that are injected into the cavity and are resonant with the QCLs lasing frequency, the greater number of carriers relax to the lower lasing level. As such, the effect of the THz pulse on the population inversion is related to its coupling efficiency. It is vital for this measurement, therefore, that the coupling efficiency of the THz pump pulse be high enough to have a measurable influence on the active region. To overcome this problem, two potential solutions were proposed. The first involved increasing the coupling efficiency by attaching a hyper-hemispherical silicon lens to the input facet of the QCL. This technique has proved successful in decreasing the divergence of a THz beam coupled out from a double-metal waveguide [229, 230]. However, this situation is less sensitive to alignment compared with coupling into the waveguide, due to the fact that as long as the radiation is coupled into the silicon lens from the output facet, it should be effectively collected by an off-axis parabolic mirror. For coupling into the device, however, the lens is required to be aligned such that the radiation is focussed onto the facet.

To achieve this the QCL was attached to the cold finger and posited in the sample-space of the setup shown in Figure 4.6, with neither the cyrostat outer-casing or heat shield attached. The THz pulse generated from the biased PC emitter was coupled through the device and detected using EO sampling. A 5-mm-diameter hyper-hemispherical silicon lens was mounted in a circular plastic holder and positioned adjacent to the input facet of the QCL. In this geometry the THz pulse propagated through the silicon lens before reaching the device. An IR-camera with a 10x magnifying lens was positioned in the setup to help with the alignment of the silicon lens on the front of the laser. Labelled pictures taken using this camera are shown in Figure 4.8 (a - c). Using the shaker together with specially designed LabView software[1], the real-time THz pulse was displayed on a computer screen and refreshed at the scanning delay frequency (5 Hz). Using XYZ translation stages, the position of the silicon lens was aligned

[1] This software was written by Dr Joshua Freeman

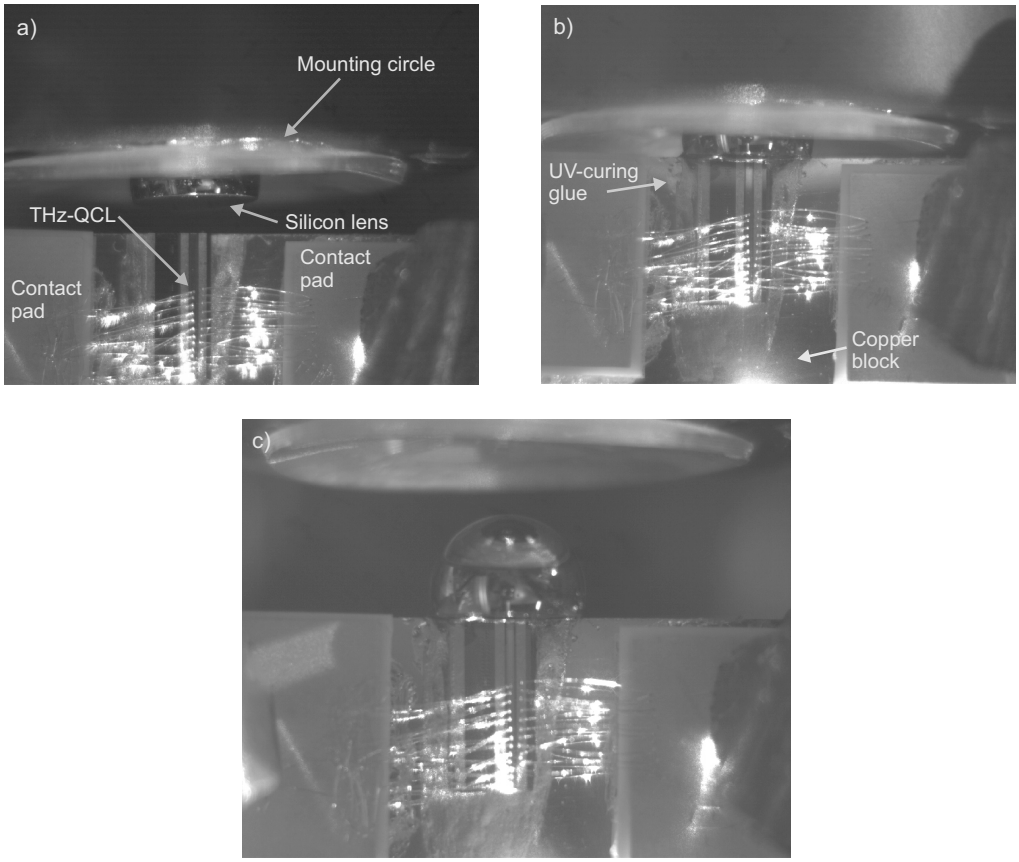

Figure 4.8: Shows a hyper-hemispherical silicon lens being incrementally stuck to the input facet of THz-QCL, mounted at the edge of a copper block. The adhesive used, which is added in b), was UV-curing glue and a plastic mounting ring was used to hold the silicon lens steady. This was performed with the shaker on, allowing the silicon lens to be alignment to maximize the time-domain signal in real-time.

relative to the facet of QCL, in order to maximise the signal in time delay (a). As the lens was moved in close proximity to the facet and positioned to maximise the peak-to-peak signal, UV-curing glue was applied to the silicon lens and the device and set with a 30 s exposure (b). The plastic mounting ring was then retracted leaving the silicon lens attached to the facet (c).

Unfortunately, despite the careful alignment it was found that having a silicon lens attached to the device did not have a significant effect on the coupling efficiency. Furthermore, the process used to attach the lens presents a substantial risk to the QCL, as any damage sustained by the facet will stop the QCL from lasing. Another means of increasing the coupling efficiency of the THz pulse involves a thorough and repeatable alignment process, undertaken before each experiment. This began by confirming that the optical pump and probe beams were collinear prior to the PC emitter, ensuring that both generated THz pulses were focused

at the same position in the sample-space. For this purpose, two irises were positioned in the optical beam path between the final optical mirror of the setup and the PC emitter. Each beam was independently aligned to the irises using 2 different sets of optical mirrors. This was achieved by mounting an optical power meter directly behind the second iris (closest to the PC emitter) and aligning to maximise the signal.

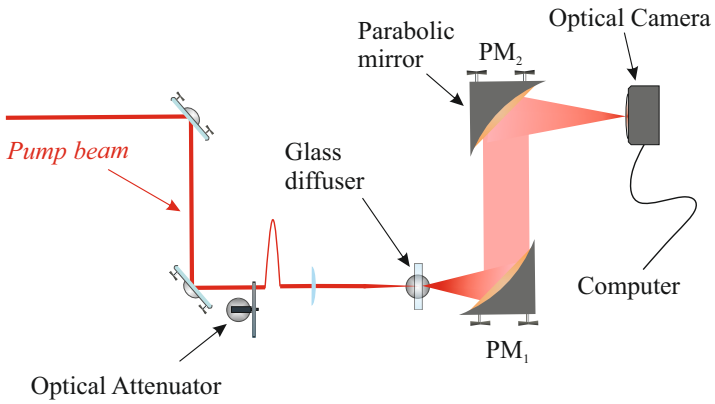

Figure 4.9: Alignment process for the first set of off-axis parabolic mirrors (PM_1 and PM_2), using a neutral density (ND) filter to limit the optical power of the pump-pulse to less than 5 µW, such that it does not saturate the IR camera in the sample-space.

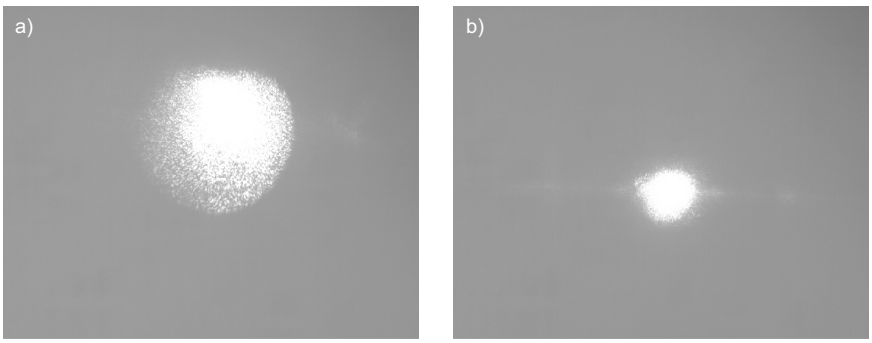

Figure 4.10: shows the IR spot incident on the camera which is positioned in the sample-space a) before the alignment process and b) after the alignment process.

The next step was to align the off-axis parabolic mirrors to ensure the tightest focus of the THz beam in the sample-space. For this the probe beam was blocked and the PC emitter was replaced by a ground glass diffuser. A variable metallic ND filter wheel was used to set the optical pump power to be as low as 5 µW. This was to prevent damage or saturation of an IR camera as it was positioned in the sample-space (Figure 4.9). The pump beam was focused

onto the diffuser where it scatters, and is collected and collimated by the first off-axis parabolic mirror (PM_1). It is then focused onto the IR camera using the second off-axis parabolic mirror (PM_2). This was connected to a computer via USB, allowing the IR spot incident on the surface of the camera to be displayed on the computer screen. By careful alignment of the lens, the diffuser, the camera and the set of parabolic mirrors, the IR spot was configured to be as small as possible on the camera. Pictures of the IR spot incident on the camera are given in Figure 4.10, where a) is taken prior to alignment and b) after alignment. This process was then repeated after repositioning the IR camera into the EO-crystal position, adjacent to the fourth off-axis parabolic mirror (PM_4). This new arrangement is illustrated in Figure 4.11. The optical power of the sampling beam is again limited to less than 5 µW using an ND wheel filter. The third and fourth parabolic mirrors (PM_3 and PM_4) could then by configured to obtain the smallest feasible focused spot with the incoming pump beam. It was also important to ensure that the optical spots from the pump and sampling beams overlap on the camera. As the directionality of the generated THz beam is dictated by its incident excitation beam, this process insures that the THz and sampling pulses overlap on the EO-crystal, and thus a THz signal will be detected. The diffuser and IR camera are then removed and replaced by the PC emitter and detection crystal.

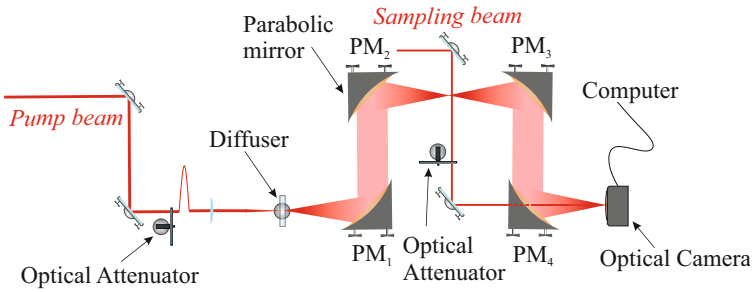

Figure 4.11: Alignment process for the second set of off-axis parabolic mirrors (PM_3 and PM_4). However, all 4 parabolic mirrors (PM_1 to PM_4) are shown in the image. An ND filter is placed in both beam paths to limit the overall IR power incident on the camera.

With a THz pulse detected, the next step was to mount a 1-mm-wide pinhole iris onto an X-Y-Z translation stage, and position it in the sample-space between the second and third off-axis parabolic mirrors (PM_2 and PM_3). The signal passing through the iris was then maximised by aligning the position of the PC emitter, the EO-crystal and the iris itself, together

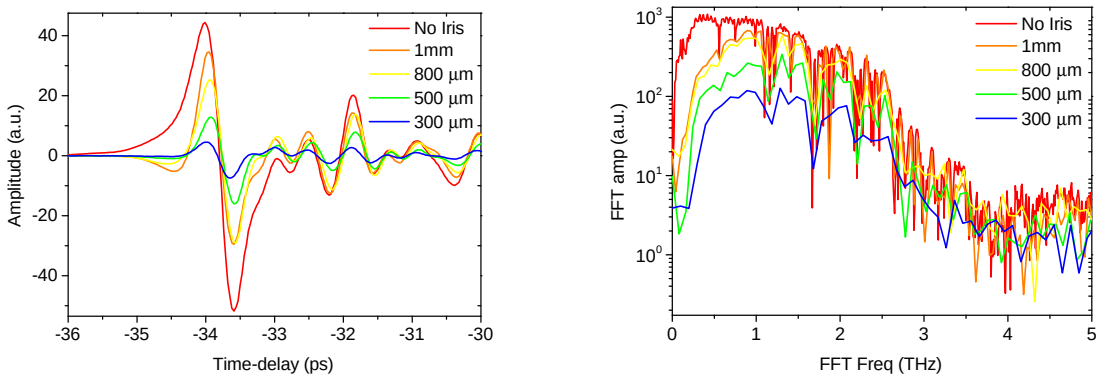

Figure 4.12: (left) THz time-domain pulses being focused through a series of irises with decreasing diameter, ranging from 1 mm to 300 µm. Also plotted is the time-domain trace taken with no iris in the sample-space. The corresponding FFT data is shown on the right, with the colour coding kept consistent between the two figures. The emitter was biased at 5 kV cm^{-1} and with an optical power of 225 mW. This measurement was taken at room temperature, with the QCL unbiased.

with the position of the silicon lens relative to the emitter. Once the signal saturates, the diameter of the iris was reduced and the process was repeated. The diameter of pinhole was reduced from 1 mm to 800 µm, then again to 500 and 300 µm, each time aligning for the highest signal and thereby reducing the overall spot-size of the focused THz beam. Examples of the recorded THz pulses after having passed through the different diameter pinholes are plotted in Figure 4.12. It is clear from the equivalent FFT data, displayed on the right of the figure, that as the diameter of the hole is reduced the iris acts as a high-pass spatial filter, preventing the transmission of the lower frequency components of the signal. When the iris is removed (trace shown in red) the extent of this filtering effect is apparent.

Once complete the iris mounting was removed from the setup, the QCL was mounted in the cyrostat and positioned at the focal point of the THz pump beam. As mentioned in section 4.2 the cryostat contains 2 windows made from PTFE, allowing the incoming and outputted THz pulses to pass through them with relatively low absorption. Figure 4.13 displays a THz time-domain trace containing 2 pulses. The more powerful pulse at −40 ps has passed through the cryostat without being coupled into the QCL, whereas the smaller pulse at ∼−7 ps has propagated through the QCL. The time delay between the two pulses is dependent on the reflective index and the cavity length of the laser. By comparing the second pulse shown here with the a scan taken with no QCL present, the coupling efficiency of this alignment method was calculated to be ∼5 %. For this scan the QCL was not biased and remained at room temperature.

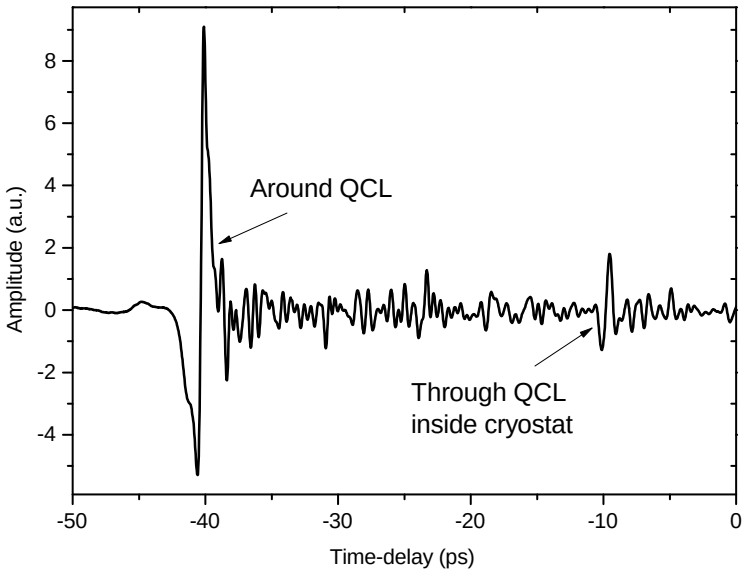

Figure 4.13: THz time-domain scan taken with the QCL (contained within a cryostat) in the sample-space, as shown in figure 4.6. The origin of the two pulses are labelled. The PC emitter is biased at 5 kV cm^{-1} and with an optical power of 225 mW.

4.4 THz-QCL Spectroscopy measurements

Before the GRT of the QCL could be determined, it was important to establish whether the injected THz pump-pulse could have a measurable effect on the population inversion in the active region, and to what extend the gain could be saturated. This was achieved by measuring the energy of pulses output from the QCL as a function of the injected input pulse energy. For these measurements only the pump beam of the setup was required, so the probe beam was blocked.

4.4.1 QCL Saturation through pulsed transmission

Figure 4.14 shows two time-domain signals obtained by focusing the THz pump beam through the QCL. For these measurements the QCL was cooled to 15 K inside the cryostat. The bias condition of the PC emitter was kept consistent, with a bias field of 8 kV cm^{-1} and an average optical pump power of 900 mW. For comparisons sake, both traces have been normalised to their highest peaks. The trace shown in red was taken with the QCL unbiased and the lock-in amplifier referenced to the modulation frequency of the PC emitter (7.6 kHz). The

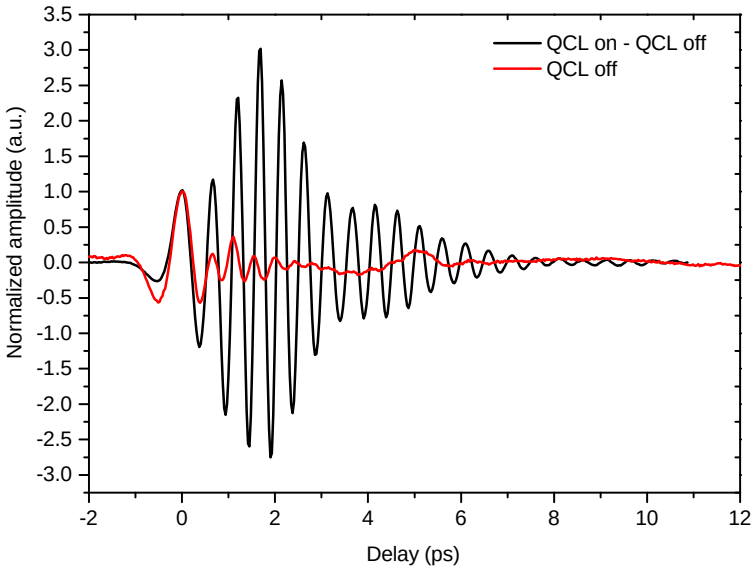

Figure 4.14: Normalised time-domain traces showing a broadband THz pulse having propagated through a THz-QCL. In one trace the QCL was biased below threshold at 114 A cm^{-2}, while in the other trace the laser is turned off. The PC emitter was biased at 8 kV cm^{-1} and an optical pump power of 900 mW was used.

small oscillation trailing the main pulse is due to the low-pass filtering effect caused by the confinement of the pulse in the cavity. The second trace shown in black was obtained with the QCL biased below threshold at a current density of 114 A cm^{-2}. In this instance the lock-in amplifier was referenced to the QCL modulation frequency (3.8 kHz) and the oscillations in the pump pulse correspond to relative amplification in the QCL cavity. This is confirmed by the FFT of the data, which is plotted in Figure 4.15. With the QCL biased the FFT shows a peak in amplitude at its lasing frequency. This is not present when it is not biased as there is no population inverse and therefore no amplification at the QCL's lasing frequency. However, due to the off state scan being referenced at the PC emitter modulation frequency, the overall detected signal is significantly higher in this case.

Using the two spectra plotted in Figure 4.15, it is possible to determine the frequency dependent gain of the device using equation 4.1 [231]. In this expression γ is the gain, L represented the cavity length and $S(\omega)$ and $R(\omega)$ represent the frequency dependent amplified signal (QCL on - QCL off) and the reference signal (QCL off) respectively. As $S(\omega)$ is measured directly from the lock-in amplifier which is performing a difference frequency measurement, the output signal $S(\omega)$ is either equal to $R(\omega) - QCL(\omega)$ or $QCL(\omega) - R(\omega)$. As this was not

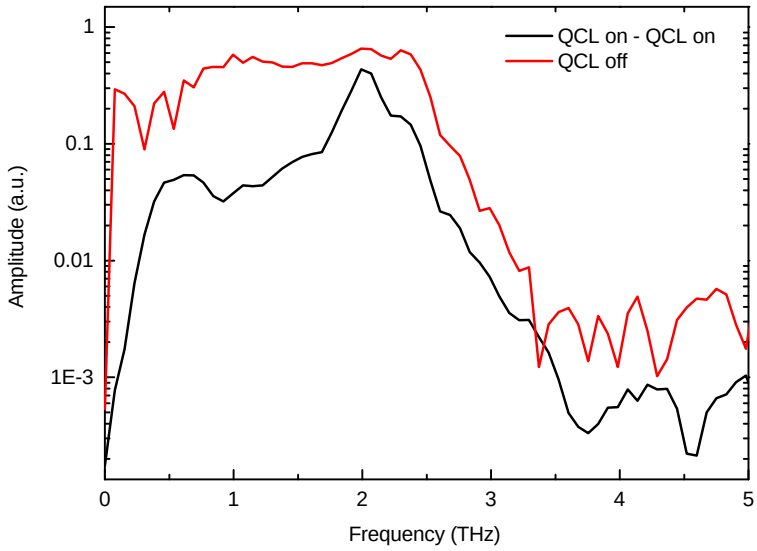

Figure 4.15: Non-normalised FFT plots of data taken from Figure 4.14. The data taken with the QCL off (Red) was referenced to the PC emitter modulation frequency. The data taken with the QCL on (Black) was taken was referenced at the QCL modulation frequency.

known prior to this calculation, it was performed for each scenario (±) and the least plausible response was discarded. The main plot in Figure 4.16 shows the spectral gain distribution calculated in this way for various biases applied to PC emitter, thus varying the pump pulse energy. The inset shows the peak gain plotted as function of field applied, along with an linear fit. Interestingly, the figure reveals that for the high energy THz seed pulse used here, the peak gain of the THz-QCL is inversely proportional to the bias applied to the PC emitter (and hence the THz pump pulse energy). This is an indication that the population inversion in the active region is becoming saturated, as the amplification factor starts to reduce relative to the magnitude of the injected pump pulse.

$$\gamma = \frac{2}{L} ln \left(\frac{|R(\omega) \pm S(\omega)|}{|R(\omega)|} \right) \tag{4.1}$$

The data presented in Figure 4.16 indicates that the pump-pulse has a significant effect on the active region. However, using the information plotted in Figure 4.15 it was also possible to quantify the level of saturation, as well as calculate the saturation energy of the laser. To achieve this, the bias applied to the PC emitter was again systematically increased to determine how the amplification factor varies with input THz power. From Figure 4.16, the measurement taken with the QCL 'on' (black) represented the output signal from the QCL,

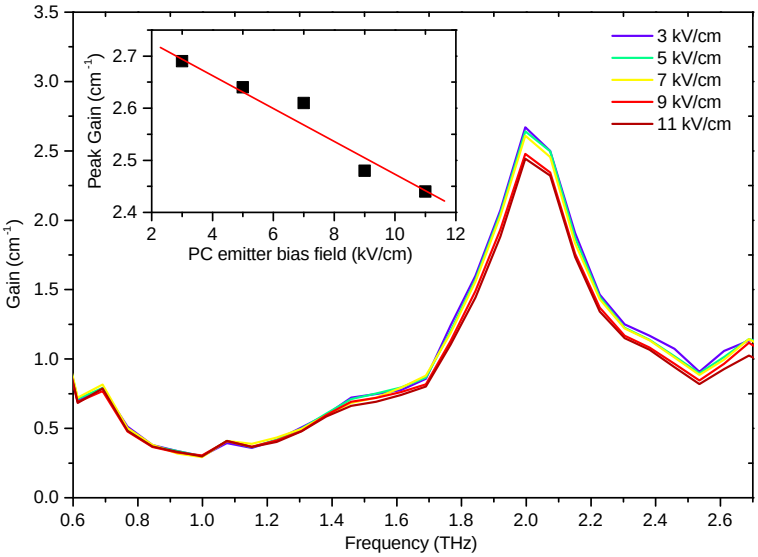

Figure 4.16: Main: Gain spectra for different PC bias conditions, varying the applied bias but maintaining the optical pump power at 900 mW. The current density of the QCL was kept constant at 114 A cm^{-2}. Inset: The extracted peak gain as function of the field applied to the PC emitter (black scatter) with a line of best fit plotted (red).

while that taken with the QCL unbiased (red) was used as the input signal. In both cases the pulse energy was estimated from the signal FFT at 2 THz. Figure 4.17 shows the QCL gain (E_{out}/E_{in}) plotted as a function input energy (E_{in}), normalised to the QCL's saturation energy (E_{sat}). The experimental data has been plotted on a black scatter graph and has been fitted to the Frantz-Nodvik equation 4.2 [232], which describes the growth of the pulse as it propagates through a amplifying medium, in this case a QCL. In this expression E_T is the total energy available from the amplifier (QCL). The quality of the fit was improved by fixing the small-signal net gain equal to the loss from one mirror (2.7 cm^{-1}), which was a fair assumption as the laser was below threshold. E_{sat} was the single free fitting parameter.

$$E_{out} = E_{sat} \ln \left[e^{\frac{E_T}{E_{sat}}} \left(e^{\frac{E_{in}}{E_{sat}}} - 1 \right) + 1 \right], \tag{4.2}$$

This fitting suggests that the maximum pump pulse energy injected into the cavity corresponds to $E_{in} = 0.22E_{sat}$ and the total energy, $E_T = 1.22E_{sat}$. Using this information it was possible to estimate the saturation energy, E_{sat}, by estimating E_{in}. The pump power before the QCL was measured to be 23 µW using a L:He cooled bolometer. This was then multiplied by several factors including the spectral overlap of the injected PC pulse with the lasing transition of the QCL (0.14), the confinement of the mode within the active region (see section 2.3.2)

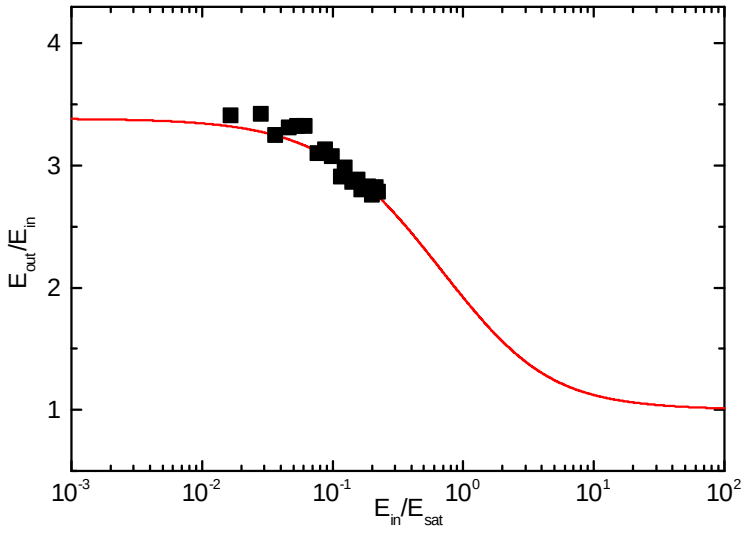

Figure 4.17: Shows the relationship between QCL gain (E_{out}/E_{in}) and injected pulse power (black squares). E_{out} and E_{in} have been measured from the FFT power at 2 THz and a fit based on the Frantz-Nodvik equation has also been plotted (red line). The x-axis has been scaled by the saturation energy, E_{sat}. This is graph was plotted by Dr. Joshua Freeman.

(0.3), and the facet transmission of the pulse (0.7). It was then divided by the laser repetition rate (80 MHz) to estimate a pump pulse energy of ~8.5 fJ coupled into the QCL. Using the relation found above, this gives $E_{sat} =\sim 38$ fJ.[2]

4.4.2 Gain Recovery time of THz-QCL

Having determined that the injected pump pulse can have a significant effect on the population inversion, the focus of the project was then to use a THz-pump-THz-probe experiment to determine the GRT of the QCL and thereby investigate how long it takes for the population inversion to restore to its steady state condition. However, prior to this it was important to determine the carrier lifetime of the materials used to fabricate the LoG emitter. For this the probe beam was unblocked and the QCL was completely removed from the setup. The amplitude of THz probe pulse was then measured as a function of PPD. Owing to the depletion of carriers due to the initial pump pulse, the THz probe signal was found to reduce for small PPDs [233]. The recovery of the emitter was found to be accurately described using two exponential components, and this is plotted in Figure 3.17. The initial shorter recovery, lasting ~2 ps can be assigned to recombination time of carriers in the LT-GaAs layer, whereas the longer component, lasting ~100 ps, can be assigned to the inadvertent excitation of carriers in

[2]This fitting was performed by Dr Joshua Freeman

the SI-GaAs substrate. In section 3.4.1, it was calculated that ~5 % of the optical beam is not absorption in the LT-GaAs layer and propagates through to the substrate. The recombination time of the carriers in the LT-GaAs was not expected to affect the following experiments since the smallest PPD used in this work was 2.5 ps. To account for the longer lifetime carriers in the SI-GaAs, the FFT data has been normalized to a low frequency peak.

To determine the GRT of the QCL, the laser was positioned back in the sample-space with both THz beams focused through the sample. With the QCL again cooled to 15 K inside the cryostat, the probe pulse was measured for different time-delays, with respect to the earlier pump pulse. To retrieve only the probe signal, the output from the first lock-in amplifier (referenced to the QCL) was connected to a second lock-in amplifier, which was referenced to an optical chopper positioned in the probe beam (shown in Figure 4.6) operating at 30 Hz. The modulation frequency for the second lock-in amplifier was limited by the need to be slow with respect to the time-constant of the first lock-in amplifier (which was set to 1 ms). In this way the second lock-in amplifier was used to discriminate between the THz pump and THz probe signals so that only signals from the THz probe were measured. For these measurements the QCL was again operated below threshold at 121 A cm^{-2}, while PC emitter was biased at 11 kV cm^{-1} and 900 mW pump power. These emitter bias conditions were a compromise between being able to generate a high enough seed energy to observe gain recovery, without damaging the device. The PC emitter was maintained at these bias conditions, unless otherwise stated. Figure 4.18 illustrates the probe signal for various PPD times, normalized to the peak of the incident THz probe pulse. As the PPD reduces, so does the relative gain at 2 THz, since the gain has less time to recover after the passage of the pump pulse. In the time-domain, this is indicated by the reduction in oscillation time and amplitude, while the spectra (Figure 4.19) reveal a reduced peak at 2 THz. To smooth the calculated FFT response shown here and reduce noise, the time-domain pulse were zero-padded. This is the case for the majority of spectra shown in this chapter and is clearly stated if not.

Figure 4.20 shows the peak spectral power at 2 THz as a function of PPD. This has been plotted for four separate bias conditions below threshold. It is clear from this graph that the closer the QCL is to its current threshold, the greater the gain and the higher the peak at 2 THz

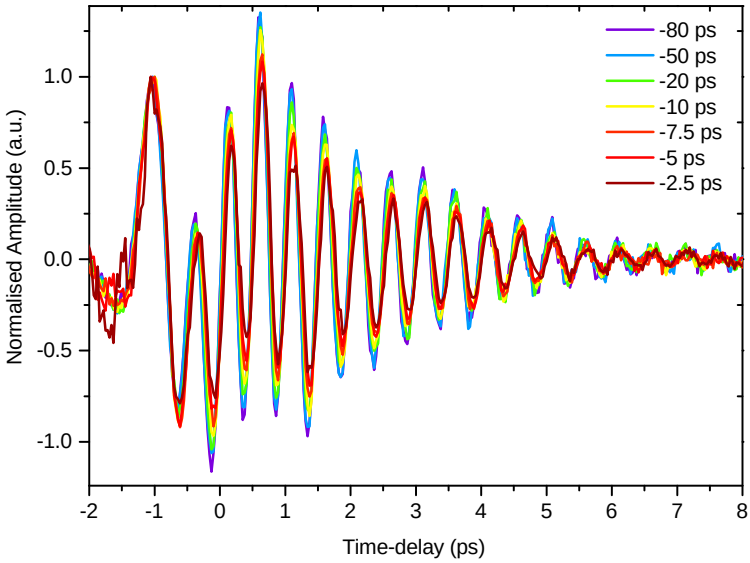

Figure 4.18: Time-domain plots of the THz probe pulse at various PPD positions. The trailing oscillations indicate the pulse has undergone relative amplification at the QCL's lasing frequency. The QCL was biased below threshold at a current density of 121 A cm^{-2}. Each pulse has been normalised to its original low frequency pulse at −1 ps. The seed pulse was generated by a PC LoG emitter, biased at 11 kV cm^{-1} and average pump power of 900 mW.

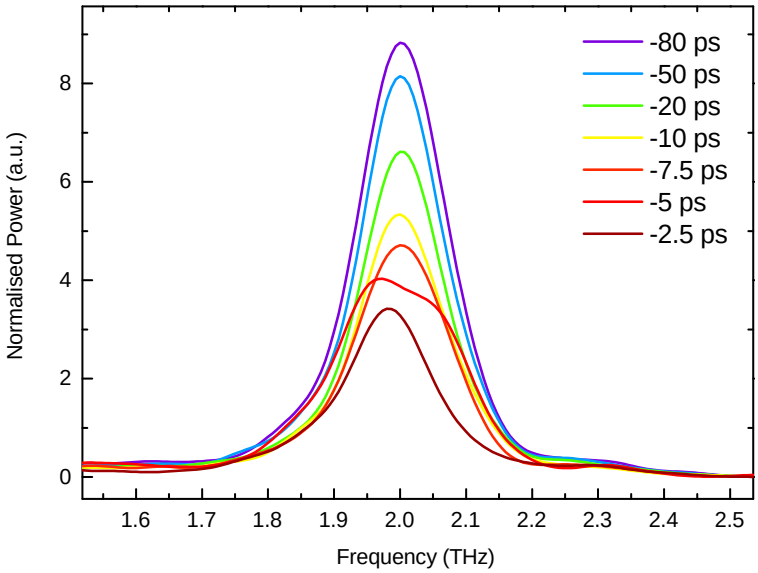

Figure 4.19: FFT data of the THz probe pulses plotted in Figure 4.18. Each spectra has been normalised to the same low frequency. Figures shows the evolution of the peak at 2 THz caused by the recovery of the gain, with at different PPD positions.

after its recovery. Exponential fits have been used to determine the recovery time for these values of current density and these are plotted together with the light-current-voltage characteristics for this device in figure 4.21. Errors bars extracted from the fitting have also been plotted. For cases where the probe pulse is weaker than the pump pulse, calculations based on the Frantz-Nodvik equation [232] show that the use of a long amplifier for these measurements can lead to a slight over-estimation of the GRT. This effect is partially offset, however, when the reflection of the pump pulse from the end facet of the cavity is taken into account, which acts to reduce the measured value of the GRT. For the present case (pump-probe power ratio of approximately five, and facet reflectivity of 0.3) it was determined that this measurement underestimates the underlying GRT by approximately 10 % when both of these effects are considered. This was calculated by dividing the cavity into sections and integrating along the length of the device, determining the effect of the reflected pump pulse on the measured probe pulse in each section. This underestimation is possibly due to further depletion of the gain by the reflected pump pulse. This estimated correction factor has been applied to the following results.

The data plotted in figure 4.21 reveals a significant decrease in the GRT from 27 ps to 17 ps as the laser approaches threshold. The reduction in error bars as the QCL is brought closer to threshold is caused by the increased gain (and therefore signal) as the structure becomes more aligned. The mechanisms for gain recovery in this case can be divided into two sources, carrier transport out of the lower laser level through the extractor mini-band and carrier transport into the upper laser, through the 'injection barrier' of the QCL (the thickest barrier in the active region period, immediately up-stream from the upper laser level). A labelled bandstructure for this device is given in section 4.5.2. Miniband extraction is known to be dominated by rapid electron-electron scattering [234] on sub-ps time-scales that we are not able to resolve in this experiment. It is therefore expected that the observed recovery time is dominated by carrier transport from the injector into the upper-lasing state. While quantitative calculations on carrier transfer rates have not been performed, simple bandstructure calculations, based on a Poisson-Schrodinger model, show that the injector-upper laser level coupling increases as the design is brought closer to full alignment.

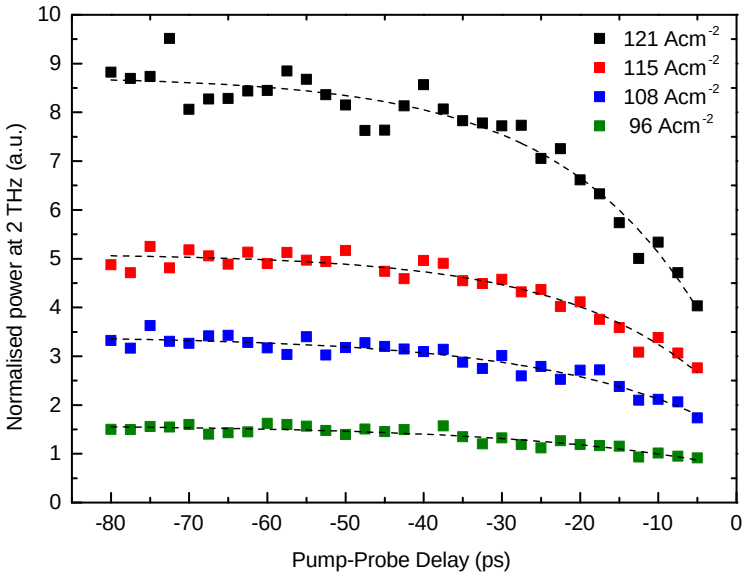

Figure 4.20: Peak power at 2 THz, extracted from the normalised spectra shown in figure 4.19, plotted as a function of PPD. This is been performed for four different bias values below lasing threshold.

As the QCL current is increased above threshold the mechanisms involved in gain recovery become more complex. The rise in the cavity photon density adds an additional mechanism for depopulation of the upper lasing level through stimulated emission. This mechanism is influenced by mirror losses, spectral hole burning and the precise photon distribution in the cavity. As such, an apparent decrease in the upper-lasing state lifetime is typically measured in pump-probe experiments above threshold [219]. Nevertheless for the purposes of rate equation calculations and modelocking considerations, only the 'bare cavity', purely electronic, recovery time is relevant. Here, when operating the QCL above threshold, an increased noise level and an increase in the extracted GRT values are observed. These have also been plotted in Figure 4.21. This additional noise above threshold may be due to spatial and temporal variations of the THz laser field inside the cavity, which are known to form coherent instabilities [217]. While the spatial averaged gain of the device is clamped, the cavity gain will not be temporally stable nor spatially uniform, and these variations would be sampled using our technique leading to increased noise in our measurements. One method to overcome these issues and obtain reliable measurements for the gain recovery time when the laser is biased for peak gain, is to apply ARC to the facets of the laser. By increasing the facet loses this works to suppress lasing and move the threshold to higher current density [223]. The advantages of using this technique are discussed in detail in section 4.5.

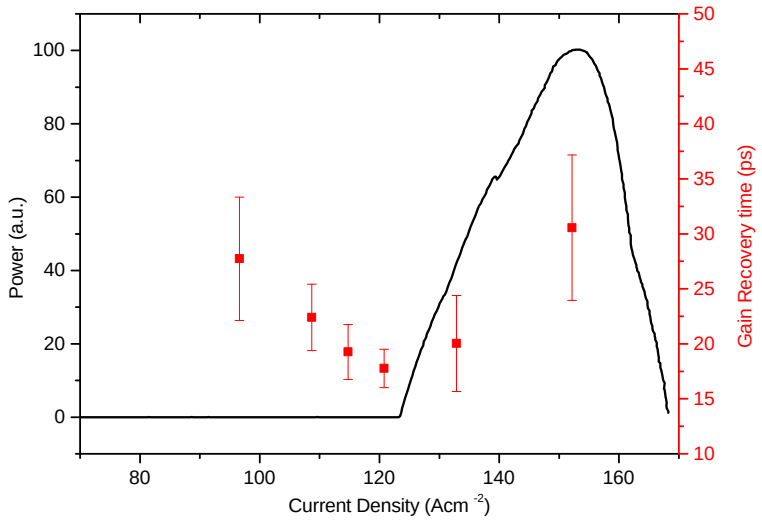

Figure 4.21: The extracted GRT + error bars (including the 10 % factor) plotted as a function of current density through the QCL. Also plotted (black) is the output power above threshold as a function of current density.

4.5 Anti-reflective coated QCL

For the measurements discussed in this section, two alterations have been made to the setup, which was originally discussed in section 4.3. Firstly a quartz-based PC emitter (LoQ emitter) was added to generate the broadband THz pulse used to deplete the gain in THz-QCL. The emitter was fabricated on a 350-µm-thick quartz substrate and was based on a slot electrode design with a 100-µm-wide gap patterned on top of the LT-GaAs. These emitters are presented in chapter 3 and are capable of significantly higher output fields compared to the previous LoG device, mainly owing to the higher dark resistance exhibited by the substrate. This increases the maximum bias field that can be applied to the PC emitter, from ~11 kV cm^{-1} with the LoG device to ~35 kV cm^{-1} when using the LoQ emitter. Another advantage of using this type of emitter is that the average carrier lifetime of the device is reduced to ~1 ps, as the SI-GaAs substrate with its longer carrier lifetime has been removed and replaced with z-cut quartz (see Figure 3.17). This allows the THz-pump-THz-probe technique to be used for smaller values of PPD. The second change to the setup is that the facets of the THz-QCL were both coated with an ARC. This has been shown to increase the facet losses of the cavity and push the threshold to a higher current density. This enables the pump-probe measurements to be performed at

higher bias conditions, giving excess to greater gain without the complications previously encountered. It also allows a higher proportion of the THz pulse to be coupled into the cavity, as less will be reflected at the laser facet. The laser facets were coated with parylene C (poly-monochoro-para-xylene), a material typically used in silicon passive optics [235, 236], as it possesses good thermal conductivity as well as having low absorption at THz frequencies. The QCL in question, which was the same device as previously used, was coated through chemical evaporation deposition which was performed by an external company (Curtiss-Wright). With this coating applied, the reflectivity of the QCL's facets can be reduced to zero if the following conditions are satisfied for n_{arc}, the refractive index of parylene C and d, its thickness;

$$n_{arc} = \sqrt{n} \tag{4.3}$$

$$d = \frac{m\lambda}{4n_{arc}} \tag{4.4}$$

In these expressions, n is the refractive index of the QCL, ~3.6, λ is the emission wavelength (~150 μm) and m is an odd integer. As the refractive index of parylene C is 1.62 [235] at THz frequencies and cannot be varied, it stands that the thickness of the coating is the main variable dictating the reflectivity of the facet. For the 2 THz laser used here, the coating thickness required was calculated to be 25.5 μm. Using this coating technique it has been shown that the reflectivity of each facet can be reduced from 0.32 [237] to <0.05 [235]. The LIV characteristics of the coated device are shown in Figure 4.22. For comparisons sake, the output power from the coated device has been scaled (x100) so that it is comparable to output signal from the uncoated device. To perform this measurement on the device, the cryostat was again cooled to 15 K using L:He and placed in the experimental setup shown in Figure 4.2. Unless otherwise stated, all of the following experiments were performed at this temperature. As the small detected power is a result of heating in the device, this confirms that coating the facets of the laser have prevented it from lasing.

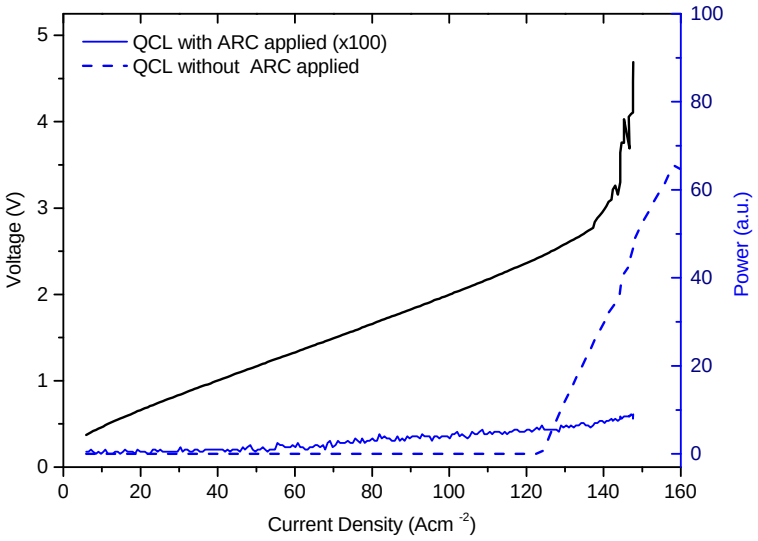

Figure 4.22: LIV plots taken with QCL after applying ARC to the both facets. The full blue line is the scaled power from the device with ARC (x100), while the dashed blue line shows the power from the QCL without coating, acting as a reference. For both scans the QCL was cooled to 15 K and driven in pulsed mode (2 % duty cycle).

4.5.1 Preliminary measurements on ARC THz-QCL

The transmissive properties of the coated device were measured using the setup shown in Figure 4.6 at a temperature of 15 K. Once again the THz pump and THz probe pulses were aligned to maximise their signal through the device. The QCL and the PC emitter were biased using the same synchronised pulse scheme as described in section 4.3. Initially the optical probe beam was blocked and the average optical power of the pump pulse was set to 500 mW. With the QCL current density set to 108 A cm^{-2}, the THz pump pulse was measured with the lock-in amplifier referenced at the QCL's modulation frequency. The black traces plotted Figure 4.23 represent the THz pulse, generated using the LoQ emitter, after having passed through the anti-reflective coated device. For comparison a THz pulse recorded with the uncoated device and a LoG PC emitter has also been plotted in red. For both these measurements the PC emitter was biased at its maximum applied field stated above. The data clearly shows that the significantly larger THz pulse injected into the ARC-QCL, which one would expect to result in a rise in stimulated emission at the lasing frequency. This is due to the increased THz power from the LoQ device together with the increased coupling efficiency of the THz pulses into and out of the cavity. To calculate the injected pump power and compare it with the uncoated device discussed in section 4.4.1, the pulse power from the LoQ emitter measured in front of the facet, as determined in section 3.5.4, was used. This measured value was again

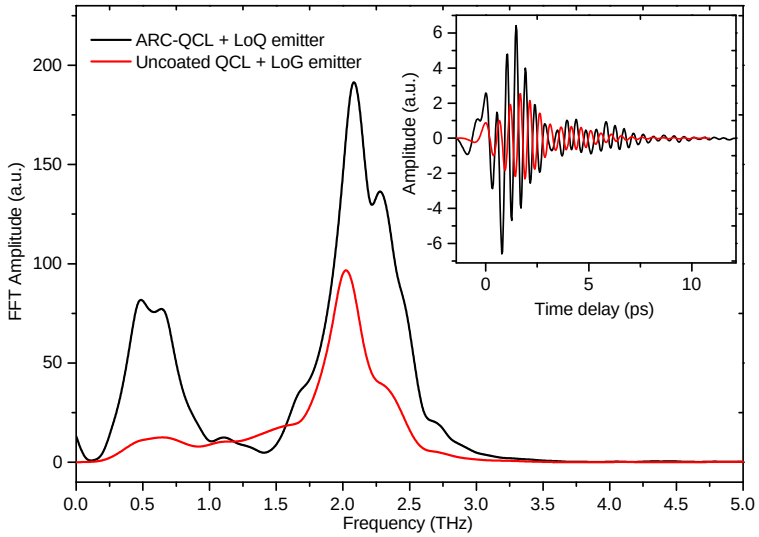

Figure 4.23: Inset: Time-domain traces of the THz-pump pulse after undergoing relative amplification within the cavity of the THz-QCL, biased at 108 A cm^{-2}, below threshold. The scan taken with the uncoated device and with a LoG emitter generating the seed pulse (900 mW/11 kV cm^{-1}) is shown in red, while the trace using the ARC device and using a LoQ emitter (500 mW/35 kV cm^{-1}) is shown in black. Main figure illustrates the corresponding FFT data.

multiplied by factors for the spectral overlap (0.14) and mode-matching (0.3), and divided by the laser repetition rate (80 MHz). For the coated device the facet transmission was assumed to be ~1 and so the pump pulse energy coupled into the QCL was estimated to be ~35 fJ, almost four times higher than for the uncoated device and LoG emitter.

Comparing the two spectra shown in Figure 4.23 reveals the interesting development of a second peak at ~2.3 THz, which is significantly more pronounced than in data obtained with the uncoated device. At 1.5 THz the detected signal in the black trace also appears to show a dip, where it drops below the previous measurement. This could only be an effect brought about by the ARC and its variation in transmission properties with frequency.

4.5.2 Measuring the gain recovery time of a ARC THz-QCL

To gather further insight into the gain dynamics at higher QCL bias conditions, the THz-pump-THz-probe experiment was repeated using the ARC device. Prior to this, however, it was important to investigate the spectral and dynamic properties of the THz probe pulse for an unperturbed system, i.e. in the absence of the THz pump-pulse. For this measurement the

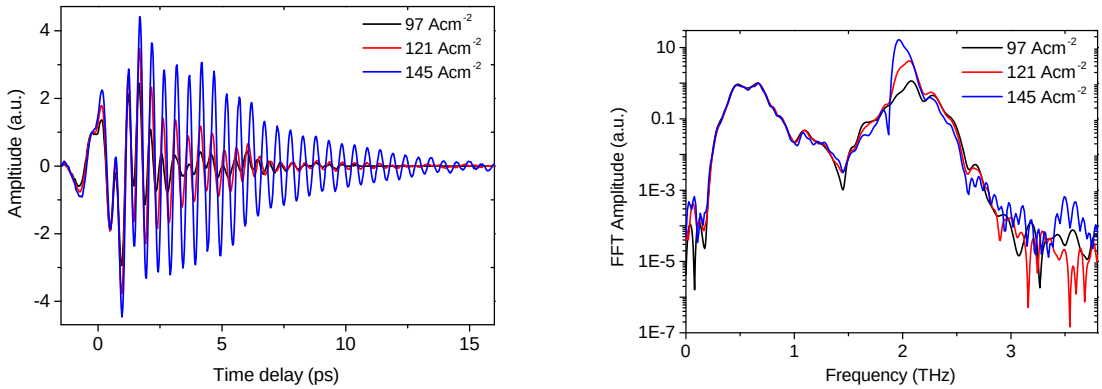

Figure 4.24: (left) Time-domain traces of the probe pulse (100 mW) taken at three QCL current densities, 97 (black), 121 (red) and 145 A cm^{-2} (blue). The pump pulse has been blocked and the LoQ PC emitter biased at 35 kV cm^{-1}. The corresponding FFT data are shown on the right and have been plotted on a logarithmic scale.

optical pump beam was blocked and the probe beam was unblocked and set to its maximum power of 100 mW. The PC emitter bias conditions were maintained from the previous data shown. With the lock-in amplifier referenced to the QCL modulation frequency, the THz probe pulse was measured over the full operating range of the coated device. The results are shown in Figure 4.24, with the time-domain data shown on the left and the corresponding spectra plotted on a logarithmic scale on the right. These time-domain pulse have been normalised to the incident THz pulse at 0 ps. As the bias across the QCL is increased the outputted time-domain trace can be seen to exhibit a trailing oscillation with increasing amplitude. This is assigned to a better alignment of states in the active region at higher bias, which produces a higher population inversion and gain. This increase in gain is exhibited as a greater peak at 2 THz in the FFT. Also apparent from the spectra is the red shift in the peak frequency as function of QCL bias. To investigate this further and gain a greater understanding of how the bandstructure varies with bias, the frequency spectrum of the probe pulse has been calculated for a range of QCL current densities and plotted on a linear scale in Figure 4.25. Each trace has been normalised to its gain peak at ~2 THz.

A closer look at the spectra reveals that there are three distinct peaks at ~1.96, 2.08 and 2.3 THz, the amplitude ratio between which is dependent on the bias applied to the laser. As this bias increases the spectral gain envelope shifts to lower frequencies and the size of the peak at 2.3 THz reduces. A bias sweep revealed that the peak output frequency shifts by ~120 GHz across the full operating range of the laser. For the time-domain trace taken at

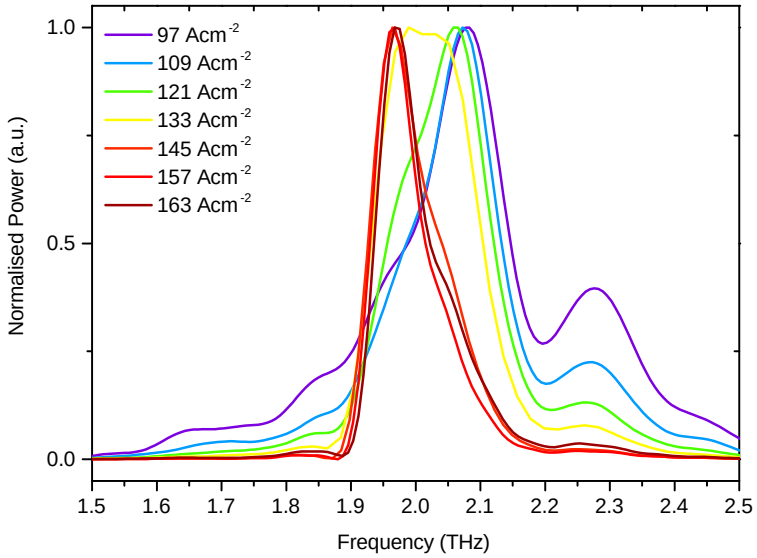

Figure 4.25: FFT's of probe pulses for a range of QCL bias conditions. Each trace has been normalised to its peak frequency and have been taken in the absence of the pump pulse. The field applied to the PC emitter was set to be 35 kV cm^{-1} and 100 mW optical power was used for the probe beam.

97 A cm^{-2} and plotted in black in Figure 4.24, the trailing oscillation of the pulse, which is due to the gain of the laser, appears to experience amplitude modulation. This is possibly the result of beating between the two frequencies (2.08 and 2.3 THz) within the active region. This conclusion is supported by the fact that the modulation effect appears to weaken as the bias across the QCL is increased, owing to a reduction in amplitude of the peak at 2.3 THz. The origin of these peaks are investigated in section 4.5.2. The advantage of using a broadband pump-probe technique in this respect is that the depletion and subsequent recovery of these individual gain peaks can be tracked over time. This provides a unique and interesting insight into the gain dynamics within the structure.

With the pump pulse unblocked and its optical power set to 500 mW, as used in section 4.5.1, the THz pump-probe measurements were repeated on the ARC-QCL. Figure 4.26 illustrates the THz probe pulse for various PPDs, with the laser current density set to 157 A cm^{-2}. This is greater than the threshold of the uncoated device. Once again, the THz pump pulse arrives first, depleting the gain in the system and the recovery is then measured using the later probe pulse. In the time-domain the depletion of gain within the system manifests itself as a reduction in the amplitude of the trailing oscillation. For small values of PPD, a comparison with the data taken with the uncoated device and plotted in Figure 4.18, suggests a

significantly reduced population inversion, relative to the gain when it is fully recovered. This suggests that the increased energy in the THz pump pulse, made possible from the changes to the setup, has resulted in enhanced depletion of carriers from the upper lasing levels. Compared to the probe pulses shown in Figure 4.18 taken at a lower current density, the elongated shape of the extracted time-domain pulses is assigned to the alignment of the injector state and upper-lasing state in the active region [238]. In the frequency domain (Figure 4.27) this corresponds to a narrowing of the gain spectrum, compared with equivalent data taken with the uncoated device and plotted in Figure 4.19.

To help show the recovery of the gain after the arrival of the pump pulse the spectra in Figure 4.27 have been normalised to a low frequency peak. Plotted on a linear scale, the transformation of the shape of the spectra clearly demonstrates the regeneration of the population inversion, on a time scale from 1 to 10 ps. Preliminary data in Figure 4.25 indicated a single mode at 1.96 THz for this current density (157 A cm^{-2}). However, the probe spectra measured 1 to 3 ps after the arrival of the pump pulse suggests the brief transient recovery of a second higher frequency transition at 2.08 THz. This peak has been shown to be prominent at lower bias conditions. After this short time period the high frequency peak appears to reduce, relative to the mode at 1.96 THz. For the PPD of 1 ps, the data plotted in both the time and frequency domain show that the oscillations and spectral peaks have almost completely disappeared. This is further evidence that this new arrangement, incorporating a LoQ PC emitter and ARC, has had a significant effect on the gain in the QCL.

As with data collected with the uncoated device in section 4.4.2, the spectral peaks from the FFT's have been extracted and plotted as a function of PPD, for a range of current densities. For the ARC sample these are plotted in Figure 4.28, where for clarity they have been normalised and offset based on their bias condition. From this figure it is apparent, even before performing an exponential fit on the data, that low bias conditions result in a shorter gain recovery time. This is implied from the gradient of the gain recovery. An interesting aspect of the data is the apparent oscillation in the recovery process, which is most prominent in the scans taken at 97 and 121 A cm^{-2}. The coherency of the oscillations suggests this is not noise but rather a modulation of the gain inside the cavity and could be an indication of coherent

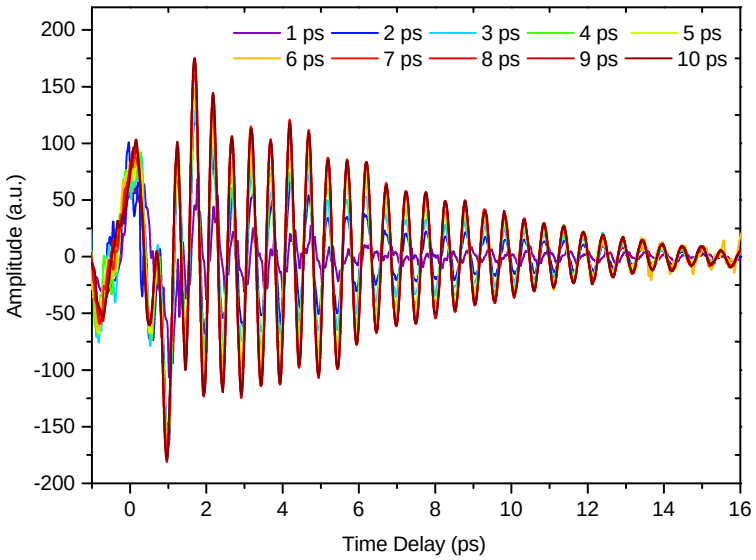

Figure 4.26: THz probe pulses plotted in the time-domain for multiple PPD, ranging from 1 to 10 ps. The QCL, which is cooled to 15 K, has been biased at 157 A cm^{-2} previously corresponding its maximum power. 500 and 100 mW used in the pump and probe optical beams respectively and the PC emitter was biased at 35 kV cm^{-1}.

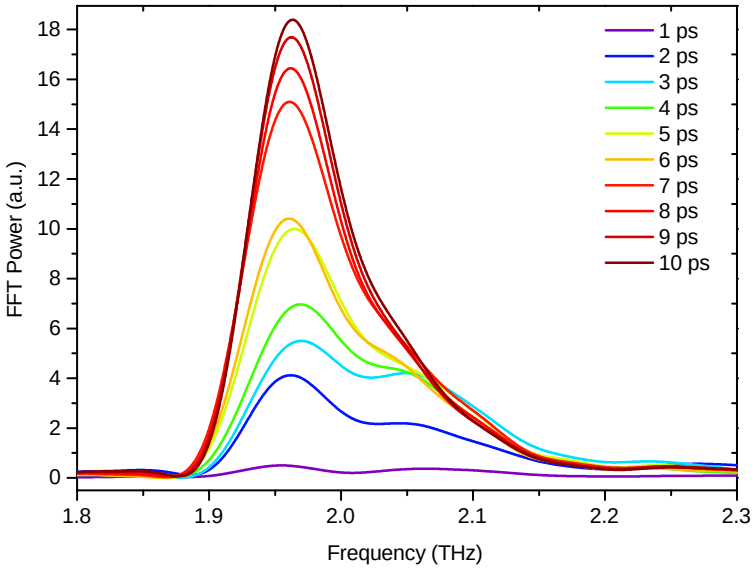

Figure 4.27: FFT of data plotted in figure 4.26. Each trace has been normalised to a low frequency point.

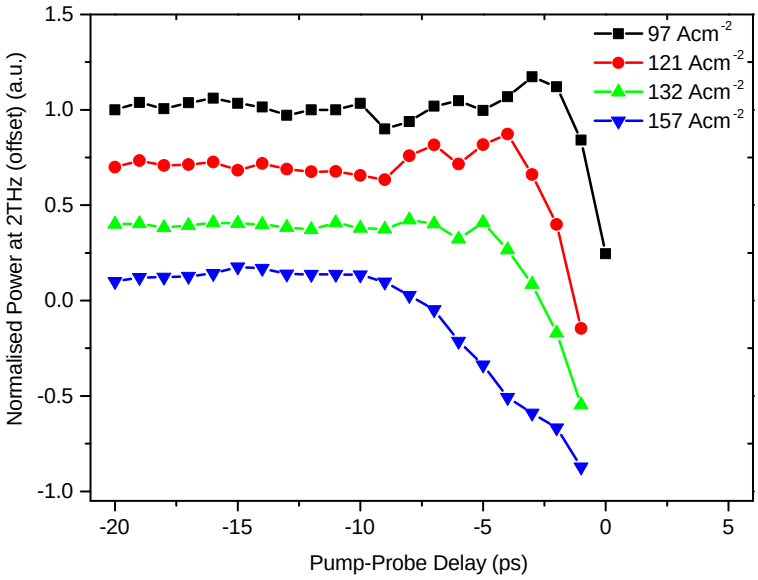

Figure 4.28: Peaks of the QCL gain spectra (figure 4.27) are plotted as a function of PPD. This has been plotted for four different QCL bias conditions. Each trace has been normalised and offset in the figure. The measurements were performed with the PC emitter bias at its maximum point.

resonant tunnelling between states in adjacent quantum wells [114]. Using expressions given in reference [111], for an anticrossing energy splitting of 1.6 meV [92], it has been calculated that τ_{coh}, the time period of coherent oscillation, should be ~2.5 ps. This agrees well with the oscillations seen at 121 A cm^{-2}. This hypothesis is reinforced by the apparent variation in dephasing time with QCL bias, i.e. how long the oscillations take to settle. The damping of these oscillations is believed to be heavily influenced by electron-phonon [239] and election-electron scattering, both of which are known to increase with bias [240]. Electron-impurity interactions and interface roughness are also thought to contribute to decoherence [241].

This phenomenon has been experimentally observed in MIR-QCLs [105], as well as in THz-QCLs [218]. The concept of coherent transport due to Rabi flopping has also been theorised as an important property for the gain recovery of THz-QCLs [108, 115]. However, unlike in the experiments performed on MIR-QCLs, where the current induced differential transmission of the optical pulse were measured as a function of PPD, here a time-resolved pulse from the output of the laser has been measured. To obtain the highest feasible frequency resolution, the FFT of each probe pulse for a given PPD is performed over a long time window, creating a rolling average of the time-domain data. As a result, it is possible that any oscillations occurring over a longer time-scale could undergo a filtering effect and be reduced or completed

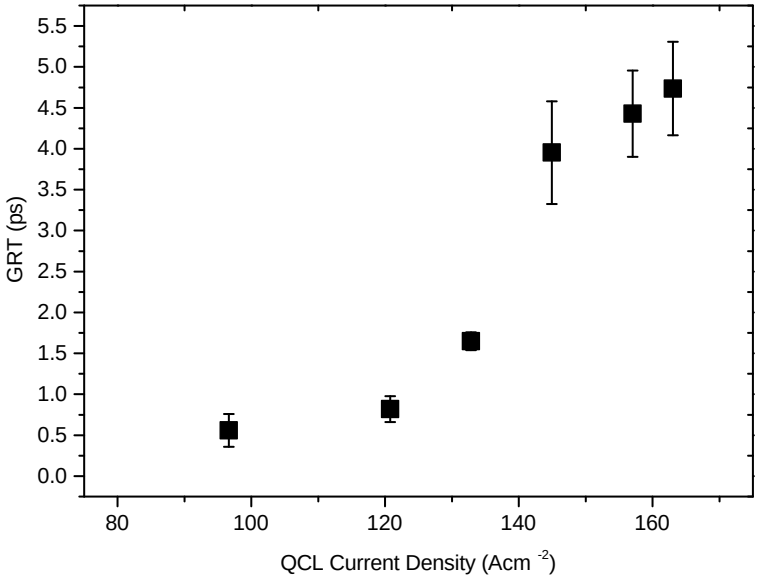

Figure 4.29: The first time-constant taken from exponential fittings performed on the traces in figure 4.28 are plotted against QCL current density. The error bars represent errors in the fitting.

removed from the spectral peaks. This limits the accuracy of any dephasing time extracted from the traces plotted in figure 4.28.

Values obtained for GRT have been plotted as a function of current density in Figure 4.29, along with error bars indicating the accuracy of the exponential fit. The increase in extracted GRT as a function of QCL bias agrees with the data found for the uncoated device, as well as that found by Green *et al* [218]. An inspection of the data suggests that it can be divided into two separate regimes. With the laser driven at low bias typical values of ~1 ps have been found. There appears a steep rise in the measured GRT as the laser is driven at higher current densities, with values of ~5 ps obtained. These values agree well with that found for MIR-QCLs [105]. One possible explanation for this rise could be due to the dephasing of the coherent carrier transport, induced by increasing scattering rates. This could also be affected by the separation of the upper lasing and injector states at higher bias.

It is also noted here that the values measured for the GRT and the error bars are both significantly smaller compared with the data obtained from the previous uncoated device. The more accurate curve fittings are most probably due to the increased SNR, owing to superior properties of the LoQ emitter. It is possible that the shorter GRT found here is related to the

oscillations shown in Figure 4.28. It has been proven that the loss of coherence in the resonant tunnelling process has a significant effect on the electron transport across the barriers [108]. If the dephasing time of the resonant tunnelling is very short, either due to high carrier scattering or other external influences, this could account for the lack of coherent oscillations in the data obtained from the uncoated device in section 4.4.2 [111]. This would also result in a longer GRT owing to the absence of resonant tunnelling-assisted transport across barriers [108, 242].

An equally plausible explanation for the short GRT found here could be that the high-power broadband pump-pulse is inadvertently exciting electrons into higher energy states, as well as depleting the gain of the lasing transition. As such, the recovery process would depend on the lifetime of these states, together with the tunnelling and scattering times of carriers drifting from adjacent lasing regions. If true, this suggests a limitation to using this broadband pump technique. To investigate this in more depth the GRT was measured as a function of injected pump power and the QCL operating temperature, and these results are discussed in section 4.5.3. Furthermore, to account for the frequency shift seen in Figure 4.25, simulations of the bandstructure of the device used here have been performed.

Investigation into the gain dynamics of a THz-QCL

The bandstucture shown here were simulated using a software package provided with Quantum Wells, Wires and Dots (QWWAD) [71]. As the THz-QCL used in this work was a regrowth of device presented in reference [224], the growth layer composition taken here acted as the input to the simulation. This simulation precedes by solving Poisson's equation to determine the effect of the external field on the structure, before solving Schroedinger equation to find the electron energy states contained within the quantum wells. As this structure was originally based on the device presented in reference [92], the operational properties are very similar. As such, the simulation results shown in Figure 4.30 were performed at a bias field of $1.5\,\mathrm{kV\,cm^{-1}}$, close to the optimal bias conditions for this structure. This is in good agreement with the field calculated across the device, multiplying the voltage drop per period, 22 meV [92], by the number of periods in the structure, 110. This is then divided by the sample thickness, 14.8 μm, to obtain the electric field. The value in brackets indicated a number assigned to each

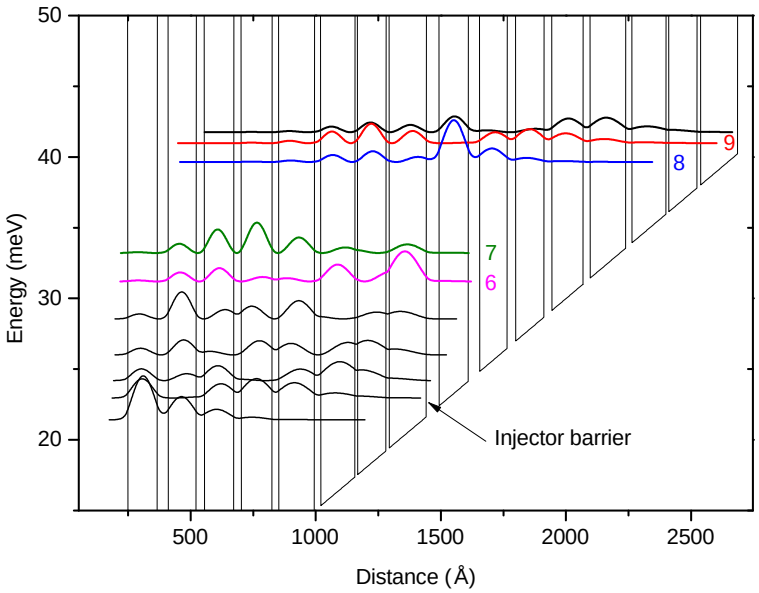

Figure 4.30: Bandstructure diagram of the 2 THz BTC THz-QCL used in this chapter. This was performed at an electric field of 1.5 kV cm^{-1}. The red and green states present the upper (9) and lower (7) lasing levels respectively. The blue wavefunction is the injector level (8) and the pink wavefunction is the second state in the miniband (6), which also has strong coupling with the upper lasing levels. The full growth procedure of the structure can be found in reference [224].

state, with the lowest energy state valued at 1 and the highest at 10. Several of these states are labelled in Figure 4.30, along with the injector barrier. The red and blue states represent the upper lasing (9) and the injector (8) levels respectively, while the green and pink states represent the lower lasing levels (7 and 6).

With data obtained from the simulated bandstructures it has been possible to calculate the transition frequency and dipole moment between different energy states. The three most important transitions involved in the lasing process have been identified and are plotted in Figure 4.31, with the transition frequency plotted on the left and the dipole moment on the right, both plotted as a function of field across the device. The transitions can be identified based on the values assigned in brackets to each state above. In regards to Figure 4.25 it is suggested that the peak at ~2.08 THz which is dominant at low current densities, 97 A cm^{-2}, is due to the strong dipole moment between states 8 and 6 (injector and miniband states). This is represented by the black curve in Figure 4.31. As the transition does not involve the upper lasing level (9), it is feasible that the recovery of this state occurs on a very short time-scale, which might account for the very short GRT (<1 ps) plotted in Figure 4.29. In this scenario the

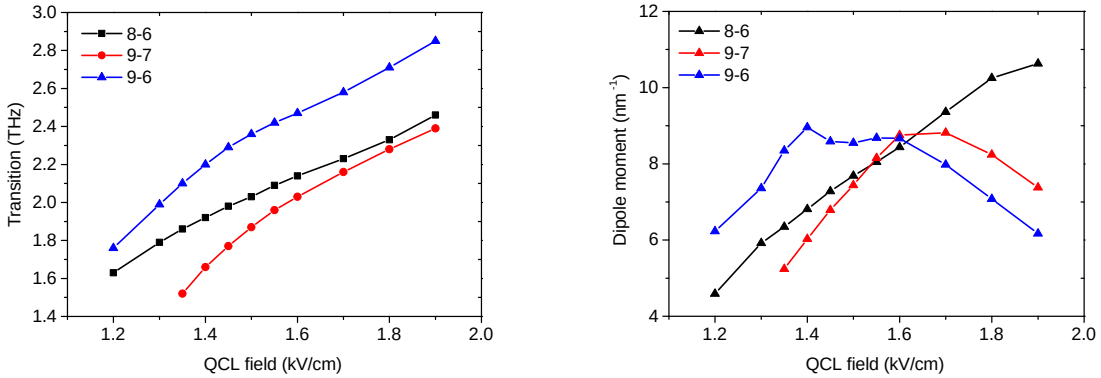

Figure 4.31: The difference frequency (left) and dipole moment (right) of three seperate lasing transitions are plotted as a function of electric field across the active region. The transitions occur between four separate wavefunctions. The upper and lower lasing levels are represented by 9 and 7 respectively. while 8 and 6 are the injector state and the second state in the extractor miniband.

recovery process may be limited by the time taken to tunnel through the thinner barrier, adjacent to the injector barrier, as well as being dependent on the alignment of the bandstructure. As previously mentioned, this process might also be facilitated by the excitation of electrons to high-energy states via the initial broadband THz pump-pulse. The smaller peak at 2.3 THz is accounted for by a higher frequency transition between states 9 and 6 (upper lasing and miniband states, shown in the blue curve).

As the field across the device is increased, the dipole moment between the upper and lower lasing level (9-7), plotted in red, rises until it exceeds that of state 8 and 6 (black) at ~ 1.5 kV cm^{-1}. Furthermore, the dipole moment between states 9 and 6 (blue) decreases, reducing the size of the peak at 2.3 THz. This leads to the frequency spectrum shown in Figure 4.25 for higher current densities (145 A cm^{-2}), where the main gain peak has shifted to a lower frequency transition at 1.96 THz (red).

These simulations also help to explain the change in the spectral shape of the probe over time, shown in Figure 4.27. With the arrival of the broad frequency pump pulse, both energy states 8 and 9, the injector and upper lasing levels, are partially depleted of carriers. As the population inversion is restored, carriers first repopulate the injector level (8) accounting for the peak at ~2.08 THz. Over time this reduces, relative to the main peak at 1.96 THz, as the carriers tunnel through the injector barrier (labelled) to the upper lasing level (9), eventually restoring the population inversion between the state 9 and 7. It should be noted that a

self-consistent solver was not used for these simulations, which could have an effect on the accuracy of the data.

4.5.3 Gain recovery time as a function of pump power and QCL temperature

To acquire a greater understanding of the GRT, two properties of the experimental setup were independently investigated. Firstly, with the THz-QCL bias kept constant at 145 A cm^{-2} and its temperature maintained at 25 K, the GRT was measured for a range of optical pump powers. The main trace in Figure 4.32 illustrates the spectral peak at ~2 THz as a function of PPD, taken using optical pump powers of 400 mW (black), 600 mW (red) and 800 mW (blue). These have been offset to help interpret the differences in the response of the device. The trace taken at 800 mW shows an overshoot of the recovering gain, peaking at ~10 ps before settling at a later PPD. This implies that for the 800 mW scan, the pump power injected into the cavity is powerful enough to stimulate so many carriers from the upper lasing level that it results in a surge of excess carriers through the injector barrier into the adjacent well. The steady state population inversion is then restored soon after. This overshoot is not observed in the data collected at 400 or 600 mW, as less powerful THz pulses are injected into the cavity and fewer carriers stimulated from the upper lasing levels. The GRT taken from the exponential fit performed on each data set has been plotted in the inset as a function of optical pump power. The data indicates that the extracted GRT is inversely proportional to the optical power used to generate the THz pump pulse. An explanation for this observed trend remains unclear, although these findings could provide an explanation of the reduced GRT found for the data taken with the ARC device.

Next the GRT was measured as a function of QCL operating temperature. For this the QCL current density was kept constant at 133 A cm^{-2} and the optical pump power was set to 800 mW. Once again, the power of the spectral peak at 2 THz has been plotted against PPD in the main trace in Figure 4.33, with the time-constants of the exponential fit plotted as a function of QCL operating temperature in the inset. Error bars have again been used to indicate the quality of the fit. These results indicate that a rise in temperature causes an increase in the measured GRT. As previously mentioned, the decoherence of resonant tun-

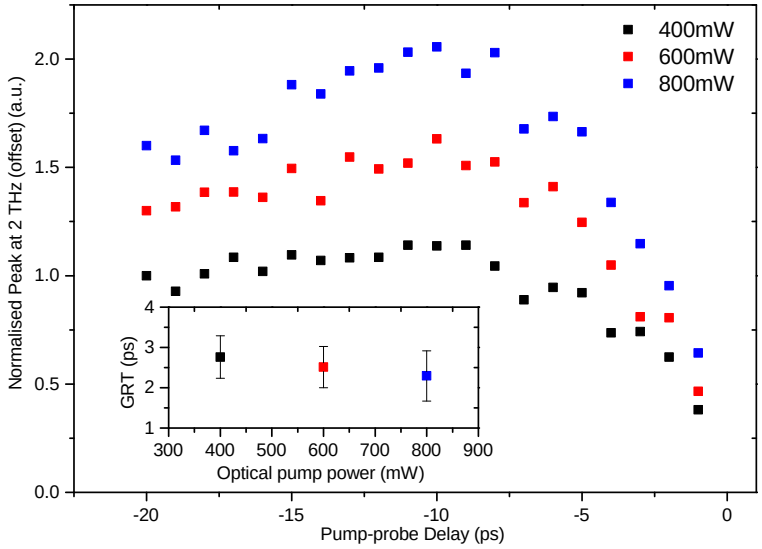

Figure 4.32: Main: The 2 THz spectral peak of the probe pulse, plotted as a function of PPD for three different optical pump powers, 400 (black), 600 (red) and 800 mW (blue). The bias field across the PC emitter was maintained at 35 kV cm^{-1}. Inset: GRT extracted from exponential fittings, plotted as a function of the pump power. The errors bars are extracted from the fittings. The QCL current density was maintained at 145 A cm^{-2}.

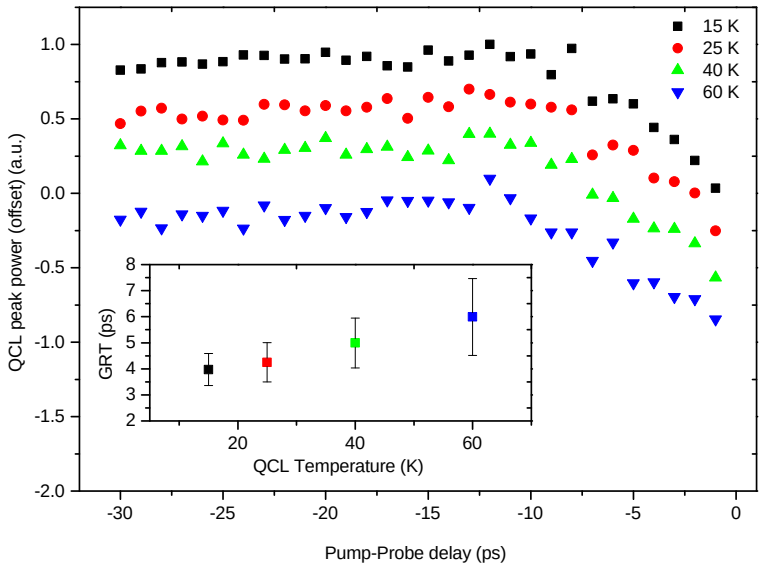

Figure 4.33: Main: The 2 THz spectral peak of the probe pulse, plotted as a function of PPD for a range of QCL operating temperatures. Inset: GRT extracted from exponential fittings, plotted as a function of the QCL temperature. The errors bars are extracted from the fittings. The QCL current density was maintained at 133 A cm^{-2}. The bias field across the PC emitter was maintained at 35 kV cm^{-1} and 800 mW optical pump power was used.

nelling is affected by carrier-carrier and carrier-phonon scattering, both of which are known to increase with temperature and could therefore have an effect on the measured GRT. The increase in the uncertainty of the exponential fit with temperature is due to the decreased gain at high temperatures, caused by thermal backfilling. The reduced carrier mobility at higher

temperatures, due to increased phonon scattering, could also be a factor [243].

4.6 Conclusion

The GRT of a THz-QCL with a BTC active region has been measured with and without ARC applied its the facets, using a THz-pump-THz-probe technique. Both scenarios have shown that the measured value is a function of bias applied across the device and increases as the QCL is driven at high bias conditions. The values measured range between 18 ps for the uncoated device to 5 ps for the coated device. It has been suggested that the discrepancy between these values is due to a variation in the resonant tunneling mechanisms, controlling the carrier transport rates between quantum wells. Furthermore, the GRT has been shown to be a function of the THz pump power and the QCL operating temperature. The use of a LoQ emitter in these experiments has provided the ability to probe specific features of the spectral output of the laser, and together with bandstructure simulations, have provided an interesting incite into its gain dynamics. However, the data presented in this chapter represents a small proportion of the interesting measurements that can be conducted using the THz-pump-THz-probe technique on QCLs.

Chapter 5

Investigation into the Gain Dynamics of a Terahertz Quantum Cascade Laser with Hybrid Active-Region

In this chapter THz-TDS is used to investigate a THz-QCL incorporating an ambipolar hybrid active-region design. After the device was fully characterising in both forward and reverse bias conditions, it was positioned in the sample-space of a THz-TDS transmission setup. Despite the device possessing a lasing frequency greater than the bandwidth of the TDS-setup used here, these tests revealed the existence of various other transitions. A THz-pump-THz-probe measurement was then performed on the device, and combined with bandstructure simulations, yielded interesting results that provides a unique insight into the carrier dynamics in this device.

5.1 Introduction

In chapter 4 it was demonstrated that the THz-pump-THz-probe technique can provide a unique incite into the gain recovery of the THz-QCL. Furthermore, by performing THz-TDS on the sample, multiple lasing modes have been distinguished and identified through band-

structure simulations. A BTC active region lasing at ~2 THz was used for that work, as it was predicted to have a relatively slow GRT compared with other designs and had a lasing transition within the frequency spectrum of the THz-TDS setup. However, theoretically the THz-pump-THz-probe technique could be used on any active region design, to help determine energy state lifetimes as well as the GRT. In this chapter a hydrid active region [96, 97] is investigated, employing a diagonal lasing transition exploited in BTC designs [92, 244], together with a resonant phonon extraction method [93]. This design combines the key advantages of two mechanisms discussed above. The reduced spatial overlap between the lasing states in the BTC design helps to maintain a population inversion and large gain [91], while a higher maximum operational temperature is achievable using a RP design [94, 245]. This is accomplished by engineering the spacing between the extraction energy states to be equal to the optical phonon energy (36 meV), which provides a significant energy barrier against thermal backfilling, as well as resulting in a short lower state lifetime [37]. The hybrid design also has the key advantage of reducing the parasitic current between the upper lasing level and the extracted state, as they are physically separated by the length of the lasing module [97].

To date, there has been several publications regarding the use of THz-TDS for the frequency-resolved detection of gain and loss in THz-QCL's [246]. Similar measurements have been performed on RP active regions [212] and BTC designs [247], both of which present an incite into the gain dynamics of the laser and consider improvements to the device. This could provide important feedback for the design and growth procedure. In this chapter the spectroscopy and pump-probe techniques that were introduced in chapter 4 are used on a THz-QCL with a hybrid active region device. As shown from the LIV curves presented in section 5.2, the device in question is ambipolar [248, 249], meaning it lases with both positive and negative voltage applied. Within this section a full characterisation of the device is performed in forward and reverse bias operation, before it is placed in a THz-TDS setup which is discussed in detail in section 4.3 and has been adapted for THz-pump-THz-probe measurements. Firstly, the gain and loss within the active region is investigated through the use of THz-TDS, before a pump-probe measurement is performed on the device and the results are discussed. These findings reveal the GRT of certain states involving in the lasing process and are validated through bandstructure simulations.

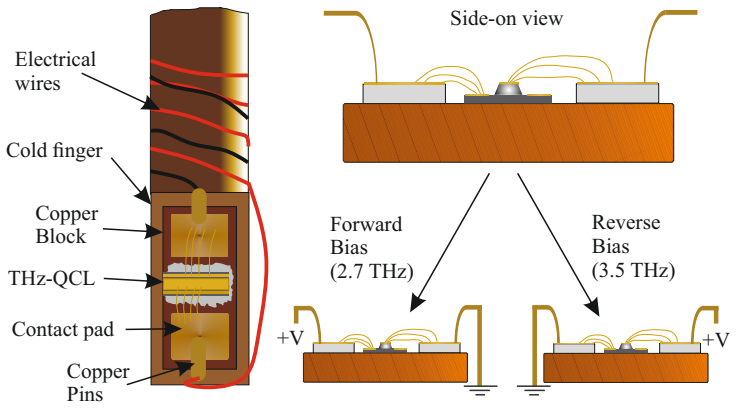

Figure 5.1: Diagram showing the electrical connections to the THz-QCL in forward and reverse bias. Left figure shows the device attached to the cold finger, while the right diagram shows how the output frequency is dependent on the electrical configuration.

5.2 THz-QCL Characterisation

The THz-QCL used in this investigation is based on the hybrid device discussed in reference [97], where each lasing module consists of four quantum wells formed from alternative layers of GaAs (wells) and AlGaAs (barriers). As with other hybrid designs [83], it possesses a diagonal lasing transition, as well as a separate quantum well to allow LO-phonon assisted extraction of carriers from the module. However, the design differs from that demonstrated by Amanti *et al.* [97], as it has been scaled to lase at lower frequencies, reducing from 2.9 THz to ~2.7 THz. This provided a better opportunity to observe the lasing transition through THz-TDS and was accomplished by strategically varying the width of the several of the quantum wells within the heterostructure. To realise this device, the original wafer was grown by Dr. Lianhe Li using MBE at The University of Leeds. The fabrication was performed by Dr. Iman Kundu who followed the same procedure as discussed in reference [225]. The lasing ridge was fabricated to be 150-µm-wide, 15-µm-high and was cleaved to be 3.5-mm-long. It was contained within a SI-SP waveguide [33]. Similar to that discussed in section 4.1.1, the device was indium soldered to a polished copper block. As before, two gold coated ceramic pads were glued at the two ends of the copper block to act as electrical contacts when mounted into the cyrostat. There were gold wire bonded to the device.

The device has been characterised using the experimental procedure discussed in section 4.2. For this the device was attached to the copper block which was mounted onto the

cold-finger of a continuous flow liquid helium Janis cryostat (ST-100). A thin-layer of thermal grease was applied between the device and the cold finger to ensure a good thermal contact. Two copper pins, labelled in Figure 5.1, were used to fix the device in place and apply voltage. With the heating shield and outer casing of the cyrostat attached, a vacuum pump was used to evacuate the chamber down to a pressure of 4×10^{-6} mbar. It is then cooled to ~10 K using L:He. To characterise the device firstly LIV measurements were performed by applying a known voltage across the sample and measuring the current drawn from the power supply, along with the outputted THz power collected. Following this, the output frequency spectrum was determined using an FTIR experimental setup. As this device was known to be ambipolar, each step of characterisation process was performed twice, as voltage was applied in both directions. A schematic diagram of the different configurations is shown in Figure 5.1. The left diagram shows the THz-QCL indium soldered to the copper block and attached to the cold finger. The image on the right depicts the laser from the side-on and shows that the direction the current flows through the device has an effect on its output frequency. To avoid confusion the bias direction used to obtain each piece of data has been highlighted in the caption of the figure.

5.2.1 LIV characteristics

An experimental setup similar to that shown in Figure 4.2 was used to determine the LIV characteristics of the device. The electrical connections required to perform this measurement have been extensively discussed in section 4.2. However there were several variations from the original setup. Firstly, for the LIV measurements a 3 kHz electrical pulse train was used to bias the THz-QCL, each pulse with a 20 % duty cycle. This was done as it echoes the QCL bias condition used in experiments discussed in section 5.4. Secondly, THz detection was achieved using a pyroelectric sensor. To allow lock-in detection of the pyroelectric output signal, the 3 kHz pulse train was electrical modulated with a 200 Hz signal. This is important as the sensor has a relatively slow response time.

The response of the laser has been plotted in Figure 5.2 and 5.3, for forward and reverse bias respectively. In both scenarios the device was tested and data plotted at three different operational temperatures, namely 10, 25 and 40 K. As output power and applied voltage have

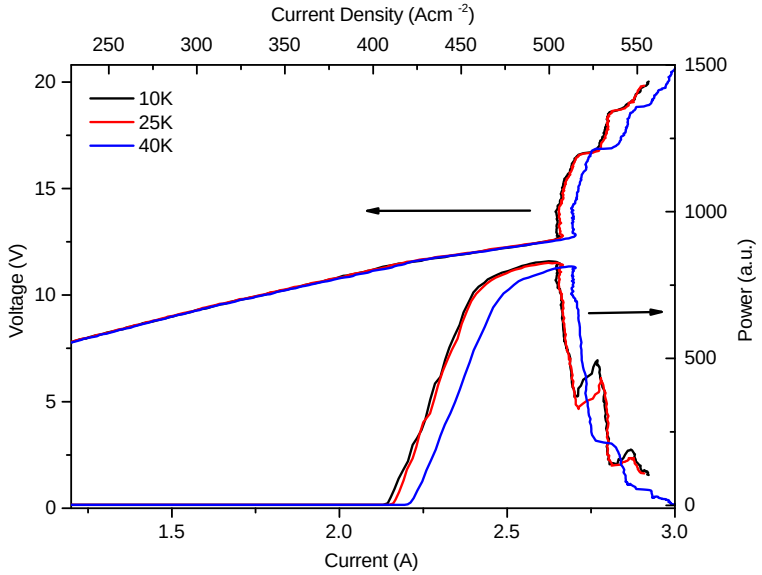

Figure 5.2: LIV data for a 3.5-mm-long THz-QCL with a hybrid active region. The device is **forward bias** with a duty cycle of 20 % and at an electrical modulation frequency of 3 kHz. Power (right) and voltage (left) have both been plotted against current (bottom) and current density (top). Data is shown for operational temperatures of 10, 25 and 40 K and are shown in black, red and blue respectively.

both been plotted as a function of current and current density, arrows are used to indicate the corresponding Y-axis. From this data, threshold current densities of ~400 A cm^{-2}(2.1 A) and 230 A cm^{-2}(1.2 A) have been found for forward and reverse bias respectively, at 10 K. The threshold increases as a function of QCL temperature, which is due to a reduction in gain and is attributed to increased carrier-phonon scattering rates and thermal backfilling at high temperatures [250]. These effects also contribute to the noticeable decrease in the measured output power with temperature, seen in reverse bias. As the bandstructure was not specifically designed to allow lasing in reverse bias, it is understandable that its overall output power is lower for a given temperature and is significantly affected at higher temperatures, compared with its forward bias operation. The I-V curves taken in reverse bias also show a sudden sharp rise in the voltage just below threshold, in which the current begins to oscillate. This is known to be caused by domain formation in the active region, where groups of lasing modules 'jump' to a higher bias to maintain a constant current through the device [93]. The maximum operating temperatures of this device were found to be 113 and 60 K for forward and reverse bias respectively. It was also found not to work in CW operation.

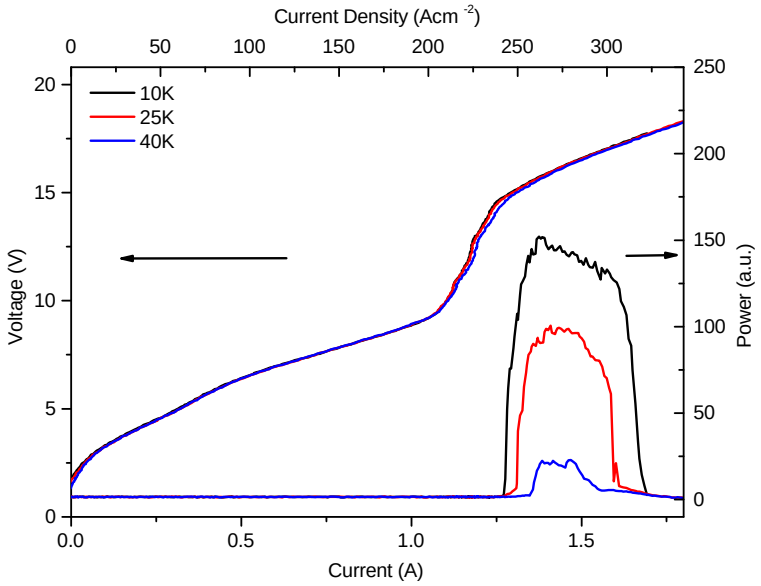

Figure 5.3: The corresponding data as that shown in Figure 5.2, for the **reverse bias** condition. This was again performed at multiple QCL operational temperatures and the colour coding remains consistent.

5.2.2 Spectra

To measure the frequency spectrum of the THz radiation outputted from the laser, the experimental setup shown in Figure 4.4 was used. This involved the use of an FTIR, previously described in section 4.2. The THz-QCL was electrically biased with a 10 kHz pulse train, each pulse with a 2 % duty cycle. To allow for the detection of the radiation using a liquid helium cooled bolometer, the pulse train was modulated by a 167 Hz gated signal, which acted as the reference for the lock-in amplifier. The spectra obtained for different driving currents has been plotted in Figure 5.4 for the device in forward bias and Figure 5.5 for reverse bias. Each spectra has been normalised to its maximum peak and been offset for clarify.

In forward bias (Figure 5.4) the data taken just above threshold (2.1 A) shows a single spectral peak at ~2.64 THz. An increase in current sees the emergence of other higher frequency peaks in the spectra. The difference in frequency between the modes is significantly greater than the longitudinal mode-spacing for this cavity, which was calculated to be ~11.9 GHz for a 3.5-mm-long device. It is feasible that these originate for different transitions in the active region, however further investigated is required to confirm this. The overall blue shift in the frequency spectrum observed with increased bias is most probably owing to the stark effect [227]. For the entire dynamic range of the device in forward bias, the emission frequency

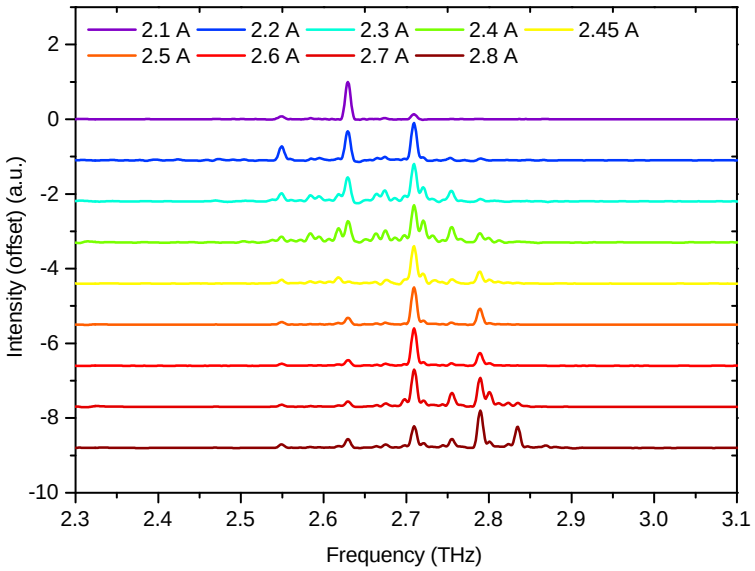

Figure 5.4: Frequency spectrum of the output of the laser for multiple driving currents. Each spectra is normalised to its highest peak and offset on the Y-axis. The laser is **forward bias**, with a 2 % duty cycle and was cooled to 10 K. These spectral measurements were performed by Dr. Iman Kundu.

is between 2.64 and 2.84 THz. However, in reverse bias the spectra plotted in Figure 5.5 reveal that the emission frequency span is broader then this, ranging from 3.38 THz just above threshold, to 3.77 THz at the maximum current density before lasing ceases. The broader spectrum could be an indication that multiple states are involved in the lasing process. This is investigated in section 5.3.3.

5.3 Spectroscopy of a hybrid device

THz-TDS has been proven to be a powerful technique for the inspection of THz-QCL's, as it can be used to determine the spectral gain profile of the laser [186,231]. As such both RP [212,246] and BTC active region designs [247] have been investigated to date. However, this technique has yet to be demonstrated with either a hybrid or an ambipolar active region. In this section, the hybrid device which was characterised in section 5.2, is placed in the sample-space of THz-pump-THz-probe setup shown in Figure 4.6. Broadband THz pulses generated by PC emission are coupled into the active region through the front facet of the laser. Having undergone relative amplification at the QCL's lasing frequency and left the cavity via the back facet, the amplitude and phase of the pulses are detected using EO-sampling with a 1-mm-thick ZnTe crystal. This was thinner than the crystal used in the initial measurements discussed in

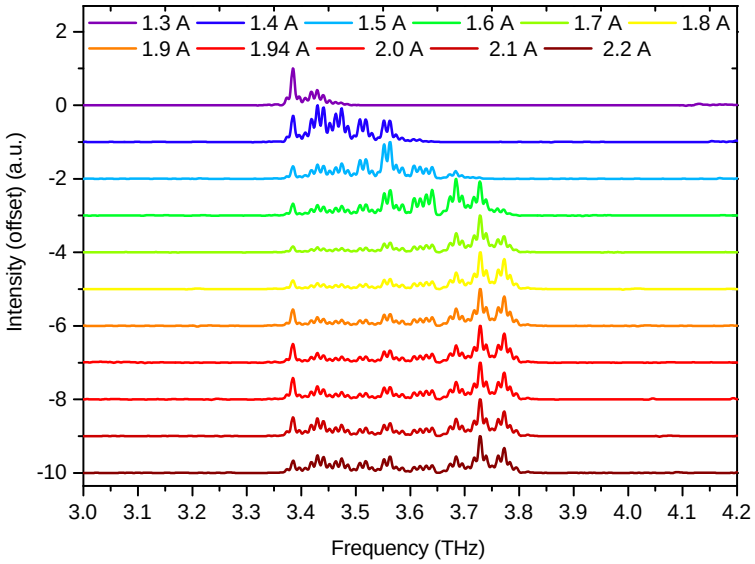

Figure 5.5: Frequency spectrum of the output of the laser for multiple driving currents. Each spectra is normalised to its highest peak and offset on the Y-axis. The laser is **reverse bias**, with a 2 % duty cycle and was cooled to 10 K. These spectral measurements were performed by Dr. Iman Kundu.

chapter 4, as the higher frequency output of the hybrid device meant that the system required a larger bandwidth. For more details regarding the experimental setup and the alignment procedure see sections 4.3 and 4.3.1 respectively. To perform spectroscopy on the laser the less powerful optical beam was blocked (the probe) while the pump beam was set at 500 mW and focused onto a LoQ PC emitter. This type of emitter was introduced in chapter 3. For this experiment a large-area slot electrode antenna with a 100-µm-wide gap was chosen and the device was fabricated on a 350-µm-thick z-cut quartz substrate. A hyper-hemispherical silicon lens was attached to the back of the emitter to increase the far-field signal and reduce the risk of substrate reflections.

5.3.1 Unbiased QCL

For this measurement the PC emitter was biased at 35 kV cm^{-1}, while the THz-QCL was left unbiased and cooled to 25 K inside the cyrostat. This meant that the THz pulse was coupled into and out of the cavity through the two PTFE windows. Both the PC emitter bias field and QCL temperature was maintained at these values, unless stated otherwise. To measure and record the THz pulse the lockin amplifier was connected to a computer and was referenced at the electrical modulation frequency of PC emitter (7 kHz). The main trace in Figure 5.6 depicts

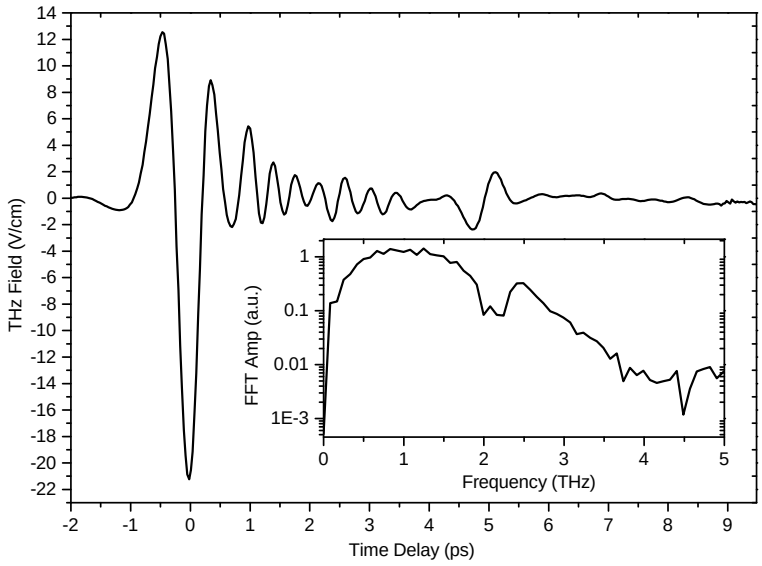

Figure 5.6: Main: Time-domain trace of the broadband seed pulse from the PC emitter having made a single pass through the **unbiased** cavity of the laser. The quartz-based PC emitter was bias at 35 kV cm^{-1} at with an electrical modulation frequency of 7 kHz and a duty cycle of 40 %. An optical pump power of 500 mW is used. Inset: FFT of the time-domain trace over a time window of 12 ps.

the broadband THz pulse after having passed through the cavity of the hybrid device. The FFT of the trace is shown in the inset. The oscillations trailing the main incident pulse are caused by the filtering and absorption of the pulse inside the cavity [186, 246]. A closer inspection of the time-domain trace reveals a second smaller pulse which arrives ~5 ps after the main pulse. Using equation 3.7 it has been calculated that the second pulse is owing to a reflection at the substrate-air interface. The addition of the trailing oscillation after this smaller pulse, which is only present when the QCL is biased, suggests that this also propagates through the cavity. The corresponding FFT data shows strong absorption between 2 and 2.5 THz. A comparison with other devices fabricated with SI-SP waveguides [247] suggests that the waveguide is not responsible for the spectral absorptions seen here.

To investigate the absorption in the pulse transmitted through the cavity, bandstructure simulations of the hybrid device have been performed. As with simulations on the BTC design discussed in section 4.5.2, all bandstructures shown here were calculated using the QWWAD software package [71]. The layer growth composition of the laser, taken from the active region design and is given in the caption in Figure 5.7, where the values in bold represent the AlGaAs barriers and the underlined value represents the doped layer. For more information

regarding the operation of the simulation package see section 4.5.2. This figure depicts the bandstructure simulated at 0 kV cm^{-1} (unbiased). This comprises of two lasing modules, each with four separate quantum wells. The wider right-hand well in each module labelled as 'LO-phonon', has been designed for phonon-assisted extracted of carriers. Each state in the diagram has been labelled from 1 to 10, with 1 having the lowest energy. It is expected that in the unbiased regime, the majority of carriers will reside in the lowest energy state of the quantum well at low temperatures. By calculating the dipole element between each state in the structure as a function of transitional frequency, it has been possible to identify 4 states (2 transitions) with a strong oscillation strength of 7 nm at frequencies between 2 to 2.5 THz. These correspond to the frequency of the absorption shown in the inset in Figure 5.6 and therefore may be responsible for this spectral features. The transitions are labelled as A and B in the bandstructure and are indicated with arrows to be between levels 3 and 5 (A) and 4 and 6 (B). Both have transitional frequencies of ~2 THz.

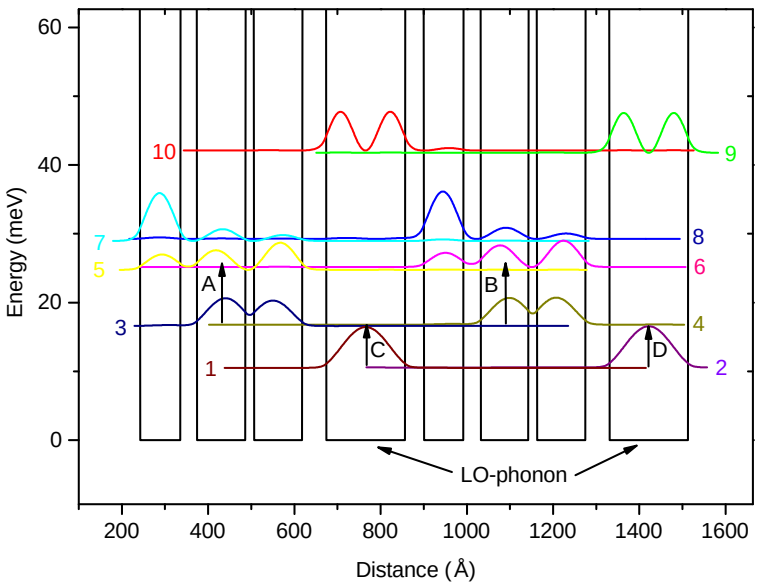

Figure 5.7: Simulated bandstructure of the hybrid active region with no external electrical field applied (**unbiased**). Electron states have been labelled from 1 to 10 with 10 being the highest energy. Transitions A and B represent relatively strong dipole moments (7 nm) calculated between levels 3-5 (A) and 4-6 (B). Transitions 1-3 (C) and 2-4 (D) are also labelled and could be responsible for the spectral features. The layer sequence of one period of structure, in nanometers, right to left as seen in the figure and starting from the LO-phonon well is **4.2**/9.4/**3.8**/11.3/**1.8**/11.3/**5.5**/<u>18.4</u> where the $Al_{0.15}Ga_{0.85}As$ barrier layers are in bold, and the doped layer of GaAs (3.5 x 10^{16} cm^{3}) is underlined.

It is predicted that as the broadband THz pulse passes through the unbiased QCL cavity, electrons residing in states 3 and 4 are optically pumped to levels 5 and 6. A value of 6 %

has been calculated for the thermal population of electrons in states 3 and 4 at 25 K, relative to the lowest energy levels (1 and 2). The frequency/dipole moment will vary slightly with the experimental data, as the bandstructure simulations are not self-consistent. Owing to the addition of dopants in the 'LO-phonon' quantum well and the low temperature of the experiment, the majority of carriers will reside in states 1 and 2. It is feasible that a self-consistent solution would show an increased dipole element between states 1 to 3, and states 2 to 4. These transitions are labelled as C and D respectively in Figure 5.7. These transitions correspond to a frequency of 1.5 THz and could account for the absorption seen in Figure 5.6.

5.3.2 Forward bias

In the section 4.4.1, THz-TDS is preformed on a BTC device, where the pulse train biasing the PC emitter is set to twice the frequency of that of the QCL. By referencing the lockin amplifier at the QCL's electrical modulation frequency, the amplifier is calculating and outputting the difference between the QCL on and the QCL off. However, in this instance the spectral absorption in the zero-bias pulse shown in the inset of Figure 5.6 prevents the use of this method, as the shape of the PC pulse varies between the QCL on and off conditions. This also prevents one from being able to accurately calculate the spectral gain of the laser, as the THz pulse passing through the unbiased QCL cavity can not be used as a reference.

To avoid these issues, in this instance the pulse train biasing the PC emitter and QCL are in phase and set to the same frequency (10 kHz) and duty cycle (20 %). The lock-in amplifier is referenced at this frequency and therefore receives information from both the THz-QCL and PC emitter (QCL on + PC emitter on). This measurement was conducted for three different forward bias conditions below threshold and the results are plotted in Figure 5.8. The pulses shown in the time-domain exhibit significantly larger oscillations than when unbiased, relative to the incident THz pulse at 0 ps. This is owing to the fact that the pulse is now undergoing relative amplification, or experiencing reduced attenuation inside the QCL cavity. The amplitude of the oscillations increase with rising driving current, as the alignment of states in the active region results in a higher population inversion. Judging from the L-I curve plotted in Figure 5.2, for the trace taken at 2.3 A the laser is believed to be above threshold, implying that the

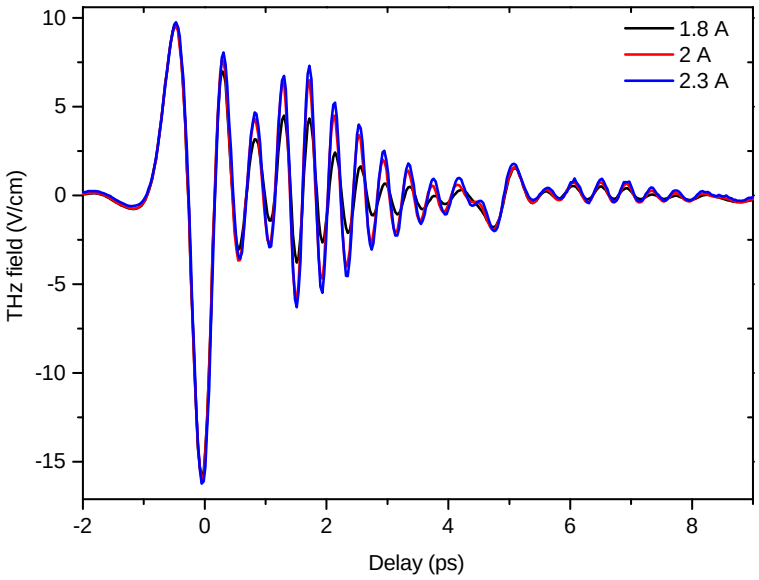

Figure 5.8: Plotted in the time-domain are multiple THz pump pulses after a single pass through the lasing cavity. The QCL is driven at 1.8 (black) and 2 A (red) below threshold and 2.3 A (black) above threshold. The laser is **forward bias** with a electrical modulation frequency of 10 kHz, applied with a 20 % duty cycle. The heatsink temperature was 25 K. The originally seed pulse is generated from a quartz-based PC emitter bias at 30 kV cm^{-1} at 10 kHz and 20 %. An optical pump power of 500 mW is used.

gain is clamped to the cavity losses. The equivalent Fourier transforms of the traces are plotted in Figure 5.9 and reveal an interesting property of the laser. Despite the FTIR measurements identifying a lasing transition at ~2.7 THz above threshold, the spectra shown here exhibits a broad peak centred at ~2.5 THz. The oscillations in the frequency domain are believed to be owing to a reflection in the time-domain and are not due to intersubband transitions. This is confirmed by the fact that the distinct peaks do not appear to vary in frequency with QCL bias. Furthermore, they can be seen throughout the frequency spectrum. The lack of an individual peak at 2.65 THz is most probably owing to the limited bandwidth of the TDS-setup.

To help understand the origin of the spectral peak displayed in Figure 5.9, bandstructure simulations were performed with the laser in forward bias. The calculated bandstructure is displayed in Figure 5.10, with an electric field of 6.45 kV cm^{-1} applied across the QCL. This is just below the anti-crossing energy of the injector state and the upper lasing level for this structure. As with the simulations shown for unbiased laser two lasing modules are displayed. These comprise of 10 separate energy states, labelled from the lowest energy state (1) to the highest energy state (10). Also labelled in this diagram is the diagonal lasing transition re-

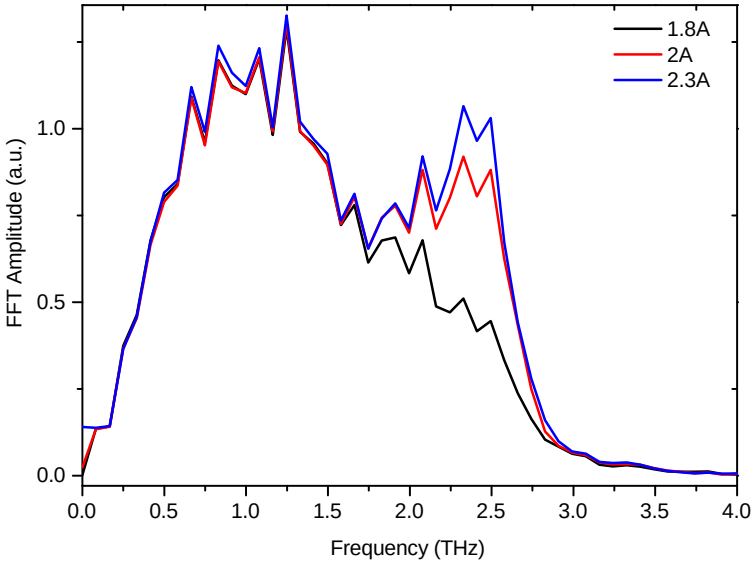

Figure 5.9: The FFT of the data plotted in Figure 5.8. The colour coding is kept consistent with the previous graph. This was performed over a 12 ps time window.

sponsible for the mode at 2.65 THz (A) and the transition at the LO-phonon energy (B). Dipole moment calculations have been used to determine that the lasing transition (A) occurs between the upper lasing level (9) and the second state in the miniband (6). The calculations also have revealed strong dipole moments between the upper lasing state (9) and the upper state in the miniband (7), as well as between the injector state (8) and the lower miniband level (6). While both transitions have been labelled collectively as C on the bandstructure, it is important to make a distinction between them. As such, the 9-7 transition is described as C-1 and 8-6 known as C-2. The calculated dipole moment and frequencies for these three possible transitions (A, C-1 and C-2) have been plotted against THz-QCL bias field in figure 5.11, in which the black curve represents the lasing transition (A).

From this data it can be suggested that the spectral peak in Figure 5.9, at ~2.5 THz, is owing to a combination of population inversions between the upper lasing/injector states (9-8) and the miniband states (7-6). The emergence of this feature as the QCL is biased close to threshold, together with the rise in dipole element of C-2, suggests that this transition is most likely responsible for the peak or reduced attenuation at ~2.5 THz. The relatively high oscillation strength found between the upper lasing state (9) and the second state of the miniband (6) is the reason for the device lasing at ~2.65 THz.

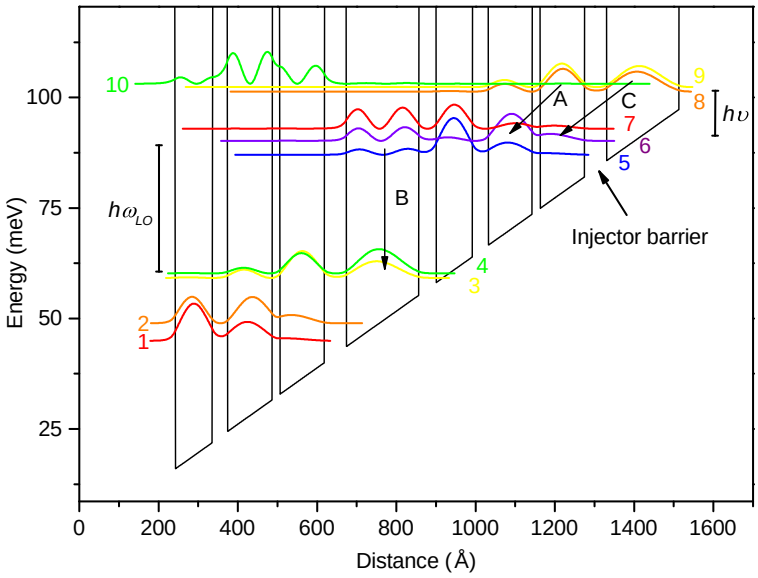

Figure 5.10: Simulated bandstructure of the hybrid active region used in these experiments, performed at 6.45 kV cm^{-1} in **forward bias**. Two lasing modules have been simulated and the states are labelled from 1 to 10, 1 being the lowest energy. State 9 and 8 represent the upper lasing and injector levels respectively, while states 7, 6 and 5 made up the miniband. The lasing transition at 2.65 THz is found to occur between states 9 and 6.

5.3.3 Reverse bias

The hybrid device under investigation is ambipolar and lases when in reverse bias, despite not being specifically designed with this property. Performing THz-TDS on the device in the reverse bias could therefore help to achieve a greater understanding of carrier dynamics in the laser. Furthermore, it could help to identify which states are responsible for the lasing transition. For this measurement the position of the THz-QCL and cryostat in the setup remained the same as in the forward bias, as does the means of biasing the QCL and PC emitter, with a synchronised pulse train at 10 kHz/20 % duty cycle. However, in this instance the current is driven the opposite direction through the QCL, as demonstrated in Figure 5.1. The resulting signals taken in reverse bias are plotted in the time domain in Figure 5.12, with the equivalent FFT data plotted in Figure 5.13.

As with the forward bias measurements, the scans have been performed for a range of reverse driving currents below threshold. Also plotted is data taken at 0 A, i.e. with the QCL off, which is the same as the information displayed in Figure 5.6 for the unbiased regime but on a linear scale on the Y-axis. In the time-domain, the incident THz pulse at 0 ps originates

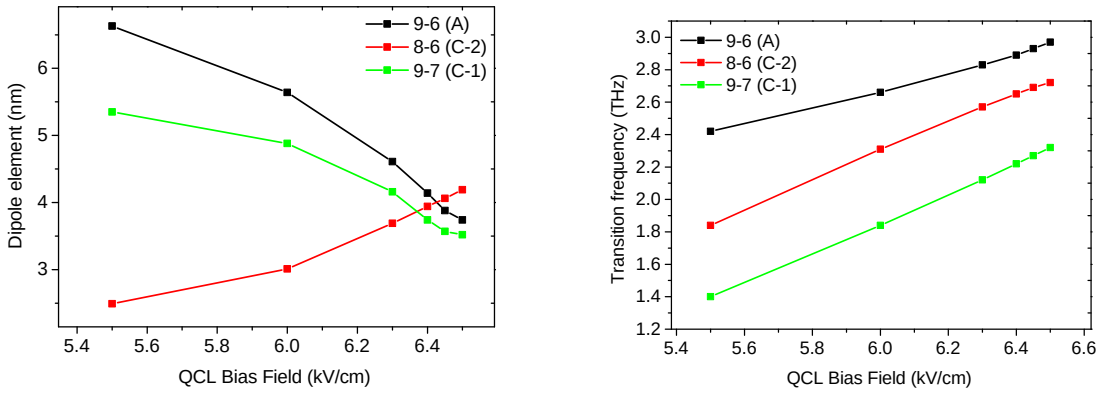

Figure 5.11: The calculated dipole elements (left) and transitional frequencies (right) for three possible transitions. There have both been plotted against the electic field applied to the THz-QCL. The transition used when the QCL is lasing is plotted in black (9-6).

from the PC emitter and does not vary with QCL bias. The spectra in Figure 5.13 shows several interesting properties. Despite being shown to lase in reverse bias between 3.38 to 3.77 THz (see Figure 5.5), the trace taken at the lowest reverse current, 0.1 A, displays a peak centred at 2.33 THz, together with an absorption at 1.89 THz. The progression of the spectra as a function of reverse bias brings about a decrease in magnitude of the peak as it moves to higher frequencies. The absorption also exhibits a blue shift as the reverse driving current is increased. This supports the argument that the absorption seen in unbiased spectra in figure 5.6 is due to the intersubband absorption. As the QCL is driven close to threshold (1.2 A) both the peak and absorption are not present in the spectra. The equivalent time-domain data exhibits a phase change in its trailing oscillation, relative to the other traces. This is an property typically associated with a shift from gain to strong absorption in the spectra [186, 212]. However, this could also be attributed to the change in spectral shape.

To determine which states in the active region are responsible for the spectral features seen in Figure 5.13, bandstructure simulations have been performed in reverse bias. The I-V response of the device in reverse bias, discussed in section 5.2, shows a sharp rise in the bias field just below threshold. It is therefore appropriate to consider the bandstructure in both a low bias (below threshold) and high bias (above threshold) regime.

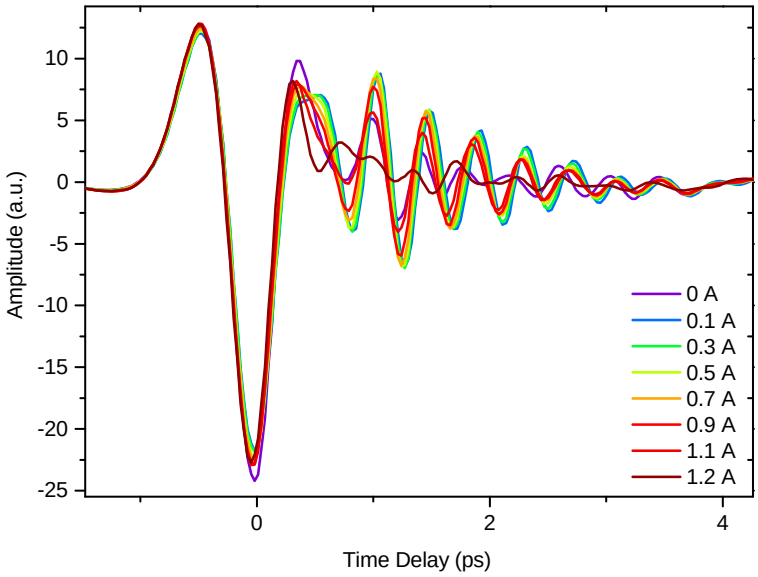

Figure 5.12: Spectroscopy performed with the THz-QCL **reverse bias**. An electrical modulation frequency of 10 kHz and duty cycle of 20 % was used for both the QCL and the PC emitter. Data plotted is collective information from the THz-QCL and the PC emitter (QCL-on + Emitter-on). The data taken at 0 A reveals just the information from just the emitter as it has passed through an unbiased cavity. The heatsink temperature was maintained at 25 K. The PC emitter was bias at 35 kV cm^{-1} and an optical pump power of 500 mW is used.

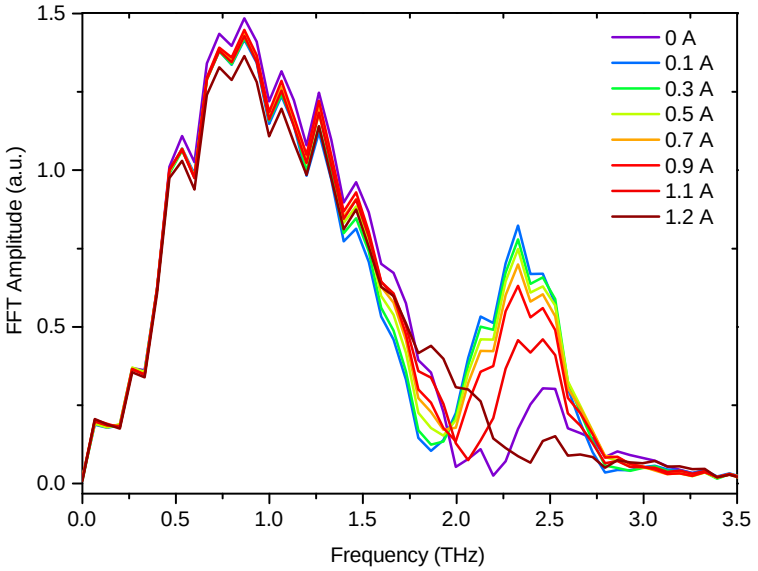

Figure 5.13: The FFT of the time-domain data plotted in Figure 5.12. The colour coding scheme is kept consistent for the two figures.

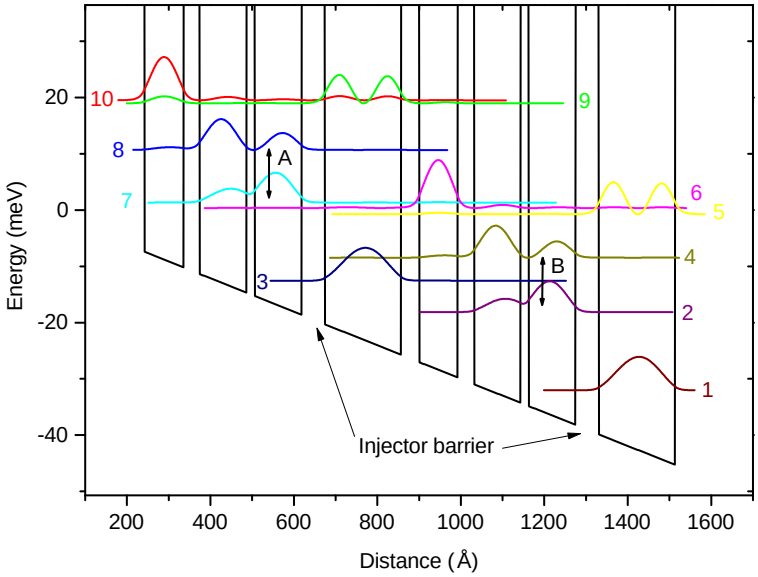

Figure 5.14: Simulated bandstructure of the hybrid active region used in these experiments, performed at 3 kV cm^{-1} in **reverse bias**. This is significantly lower than the lasing threshold. Two lasing modules have been simulated and the states are labelled from 1 to 10, 1 being the lowest energy. Strong dipole moments (~6.3 nm) have been found between states 8-7(A), and 4-2(B). Both of these have represented by black arrows.

Low QCL bias simulations

Firstly, a low bias scenario is considered, where the QCL bandstructure is simulated with a reverse applied field of 3 kV cm^{-1}. This lower field was chosen as the magnitude of the peaks in Figure 5.13 are inversely proportional to QCL bias. It is therefore logical that this would provide the best opportunity to identity the key states involved. The low field bandstructure is shown in Figure 5.14. Similar to before, the energy states have been labelled from 1 to 10, with 10 possessing the greatest energy. From this simulation dipole matrix elements have been calculated between all states. This has been plotted as a function of transition frequency on a scatter graph in Figure 5.15. Each symbol on the scatter graph represents a different energy level. Where two symbols overlap indicates the transition frequency and dipole element between the two corresponding states. The inset shows a small section of the main figure, enlarging the part of the frequency spectrum containing the spectral features in Figure 5.13. Shown in the inset are 5 possible transitions which have been identified between 7 different energy levels, based on their transitional frequency and strong dipole moments.

The strongest dipole moments are between energy levels 8 and 7, and 4 and 2. On the

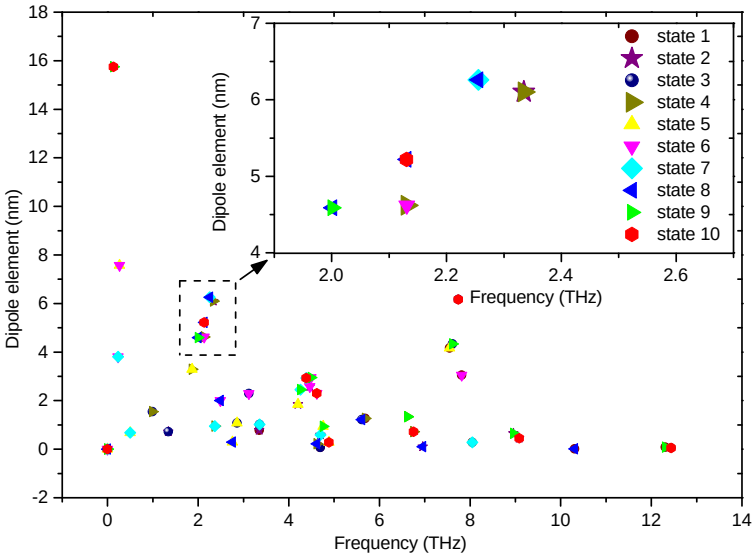

Figure 5.15: Main: A scatter graph showing the oscillation strength as a function transition frequency for all states in the bandstructure shown in Figure 5.14. Inset: A zoomed in section of the main figure presenting the transitions thought to be responsible for the spectral peaks seen in spectroscopy measurements.

bandstructure these have been represented by vertical black arrows labelled as A and B respectively. Based on the dipole moment graph in Figure 5.15 and the position of lower lasing levels of these transition (7 and 2) relative to the thick injector barrier (labelled), it is proposed that the lifetimes of the lower lasing states are longer than that of the upper states (8 and 4). The incident THz pulse optically pumps the electrons to the higher lasing levels, resulting in the spectral absorption seen in Figure 5.13 at 1.89 THz for 100 mA. This absorption undergoes a blue shift with a rise in reverse bias, owing to the separation of these states, otherwise known as the Stark effect. It is feasible that the peak at 2.33 THz is owing to reduced absorption at this frequency, as the magnitude of the peak is inversely proportional to the reverse QCL current and reduces with the increase in frequency of the previously mentioned absorption. However, further analysis would have to be completed to confirm this.

High QCL-bias simulations

To help understand how this bandstructure allows the device to lase at frequencies greater than 3.3 THz, the simulation have been repeated at a reverse bias field of 10 kV cm^{-1}. This field was chosen based on the reverse bias I-V response in Figure 5.3 above threshold and the resulting bandstructure is presents in Figure 5.16. Once again, the states are ordered and

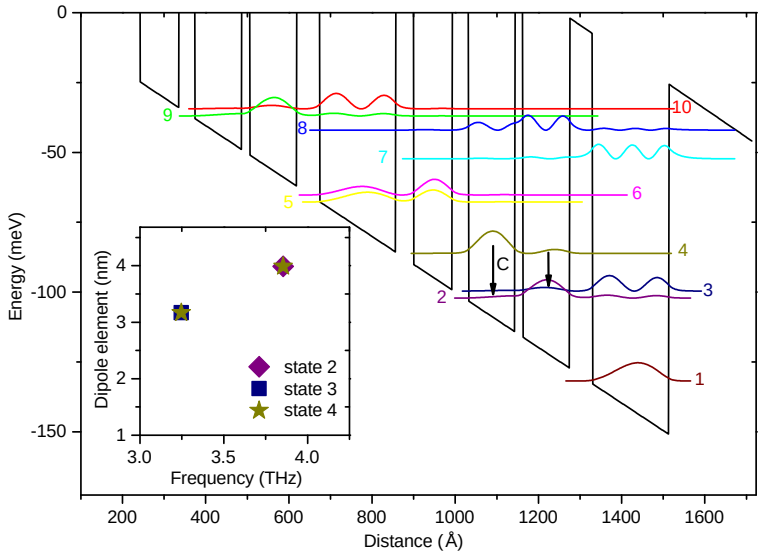

Figure 5.16: Main: Bandstructure diagram simulated in **reverse bias** at 10 kV cm^{-1}. The black arrows (C) indicates the probable lasing transitions at between 3.3 and 3.8 THz. Inset: Shows dipole elements against transitional frequency for multiple energy states in the active region. The 4-3 transition (bottom left) occurs at 3.25 THz, while the 4-2 transition (top right) is at 3.75 THz.

labelled on the diagram. The result of dipole calculations are shown in the inset and indicate two dipole moments between energy levels 4 and 3 at ~3.25 THz, and between 4 and 2 at ~3.75 THz. These have a strong oscillation strength, relative to other transitions on the scatter graph (not shown). These transitions are represented by black vertical arrows drawn on the band diagram (C) and are believed to be responsible for the lasing of the device in reverse bias, as they agree well with the spectra presented in Figure 5.5. The smaller dipole moment seen here, compared with when lasing in forward bias (Figure 5.11), could be partially responsible for the lower output power found in the reverse bias regime. However, other factors could also contribute to this, such as a reduced population inversion owing to increased parasitic current. The difference in energy between levels 2 and 1 could also be a contributing factor, as it is less than the 36 meV required for LO-phonon assisted carrier extraction [37]. This will also cause a reduction in output power at higher temperatures.

5.4 Preliminary THz-Pump-THz-probe measurements on a hybrid active region

To attempt to understand the mechanisms governing electron movement between lasing modules in more depth, the THz-pump-THz-probe technique discussed in section 4.4.2 was repeated using the hybrid device. The experimental setup was precisely the same as shown in Figure 4.6, which is discussed in detail in section 4.3. It was also very similar to the setup used for the spectroscopy measurements discussed in section 5.3 with minor alterations. Firstly, the optical probe arm was unblocked and used to excite the same PC emitter, generating a second THz pulse with optical power of 100 mW. Secondly, difference frequency and two lock-in amplifier detection techniques were reintroduced, having been originally discussed in section 4.3. The pulse train biasing the PC emitter was set to twice the frequency (7/3.5 kHz) and duty cycle (40/20 %) of that of the QCL. By referencing the first lock-in amplifier at the QCL's electrical modulation frequency, this subtracts data taken with the QCL off (i.e from the PC emitter), thereby becoming more sensitive to changes in the QCL output. The position and temperature of the cryostat with the THz-QCL inside were kept consistent with the previous experiment, as was the field applied to the PC emitter and the optical power used in the pump beam.

With the system aligned to maximise the THz pump and THz probe pulses through the QCL cavity, the pump pulse was initially configured to arrive at the QCL's facet 30 ps after the probe pulse. This was achieved using a second motorised delay stage on the pump arm. An optical chopper positioned in the probe beam was used as the reference frequency (30 Hz) for the second of the two lock-in amplifiers. These combined techniques allowed for the independent detection of the THz probe pulse having passed through the unperturbed laser cavity. This is plotted in the time and frequency-domain in Figure 5.17, for two different QCL driving currents in the forward bias regime below threshold. The general change in shape of the THz time-domain pulse, compared with previous measurements taken in forward bias in Figure 5.8, can be explained by the considering that in this instance a difference frequency measurement was performed and therefore the original PC pulse, shown in Figure 5.6, was removed. This partly explains the diminished oscillations trailing the incident pulse in the

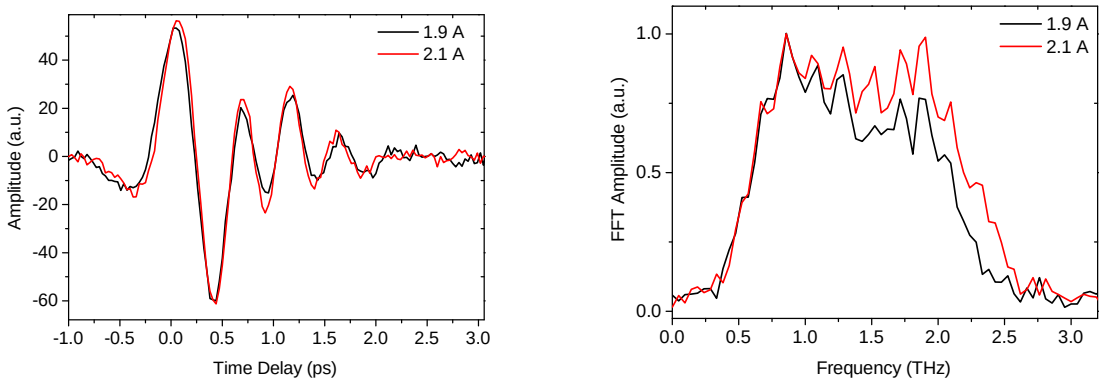

Figure 5.17: Left: Time-domain THz probe pulses having been amplified by the hybrid device in **forward bias**, at 1.9 and 2.1 A, both below threshold. The optical probe pulse is set to 100 mW and the pump pulse (500 mW) arrives 30 ps after the probe probe. The lock-in amplifier is referenced to the frequency of the electrical modulation of the THz-QCL (3.5 kHz), twice that of the PC emitter modulation frequency. Right: The equivalent FFT of the time-domain data shown on the left, normalised to a low frequency peak.

time-domain, and the smaller peak in the FFT data, relative to Figure 5.9. Furthermore, the use of an optical chopper in the probe beam results in a decrease in SNR and a reduction in the measured bandwidth. This means that the higher frequency transitions, identified in section 5.3.2, have less influence on the shape of the detected THz pulse. The FFTs in Figure 5.17 have been normalised to a lower frequency point to help illustrate the difference with increased QCL bias. The oscillations in the spectra are most probably owing to a reflection in the time-domain, outside the time window. These have also been previously observed in the data shown in Figure 5.9.

To perform the pump-probe experiment on the hybrid device, the THz pump pulse was repositioned to arrive prior to the probe pulse at QCL's facet. As the pump pulse arrives first in the laser cavity it stimulates carriers from the upper-lasing levels and the injector state into the miniband below. While the lasing transition itself is most probably unaffected as it occurs at 2.64 THz, greater than the bandwidth of the pump pulse, the population of the upper-lasing level may vary owing to strong dipole elements between it and other miniband states. By scanning the later arriving probe pulse at various PPD, the movement of carriers can be traced as a function of time, as the device works to restore the initial population inversion. The THz probe pulse has been measured for PPD's ranging from 1 to 5 ps. This was considerably shorter than when using the BTC device in section 4.4.2, as it was predicted that the recovery process of the upper-lasing/injector states would occur much faster in the hybrid device.

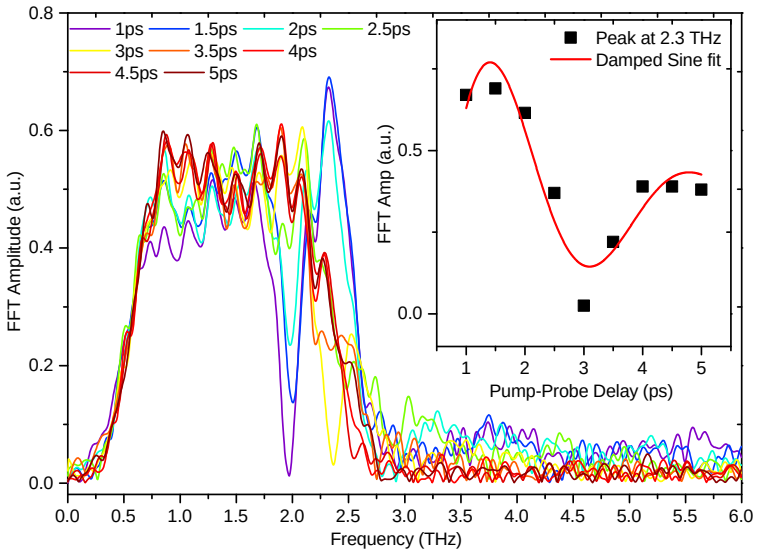

Figure 5.18: Main:FFT's of multiple THz-probe pulses at different pump-probe delays. The optical powers used for the pump/probe beams are 500 and 100 mW respectively, while the LoQ PC emitter was biased at 30 kV cm^{-1} at electrical modulation frequency of 7 kHz and 40 % duty cycle. The THz-QCL was in the **forward bias** regime at 2.1 A (3.5 kHz/20 %). The inset shows the peak at ~ 2.33 THz as a function of pump-probe delay (black scatter). Fit with a damped sine curve (red line).

This is owing to the LO-phonon assisted extraction of carrier from the miniband, as well as fewer quantum wells in each lasing module decreasing carrier transit time. For this measurement the QCL current was set to 2.1 A in forward bias. The zero-padded FFT's of the probe pulse for each PPD has been plotted in Figure 5.18. As the LT-GaAs in the LoQ PC emitter has a known carrier recombination time of ~1 ps, this presents a lower limit to the measurable PPD.

The trace taken at a pump-probe separation of 1 ps possesses two spectral artefacts, a dip at 2 THz and a peak at ~2.33 THz. An increase in PPD brings about a noticeable rise in this dip and a reduction in the peak. At a PPD of 2.5 ps the data reveals that the dip at 2 THz has been completely restored, as the spectral shape resembles that of the unperturbed system in Figure 5.17. In regards to the peak at 2.3 THz, the amplitude appears to reduce to almost zero, before settling at a steady state value after 4 ps and again resembling the unperturbed probe shape. The amplitude of the peak at 2.3 THz has been plotted as a function of PPD in the inset of Figure 5.18. This data is represented by black squares and has been plotted with a fitting performed using a damped sine function.

Bandstructure simulations and calculations discussed in section 5.3.2 have already estab-

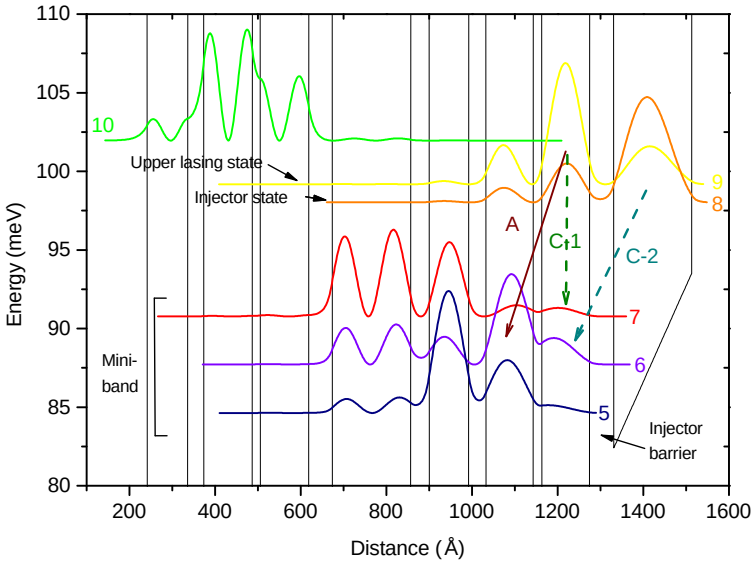

Figure 5.19: Simulated Bandstructure of hybrid device in **forward bias** at 6.2 kV cm^{-1}. A zoomed illustration of that shown in Figure 5.10. Transition A is responsible for the main lasing mode (9-6). C-1 (9-7) and C-2 (8-7) are also shown and are responsible for the spectral features shown in Figure 5.9. The injector barrier for the lasing module is labelled.

lished that the spectral features in forward bias (Figure 5.9) originates from two transitions, a lower frequency transition between the upper-lasing level (9) and an upper miniband state (7), named C-1, and a higher frequency transition from the injector state (8) to a lower miniband state (6), referred to as C-2. Figure 5.19 depicts a bandstructure simulated at 6.2 kV cm^{-1} in **forward bias**, on which both transitions are labelled. The lasing transition has also been labelled as A. This field is slightly lower than that used in figure 5.10 and was chosen simply as there is clear distinction between the injector and the upper-lasing level (8 and 9). This makes it easier to indicate the different transitions discussed in the text and would be more difficult at higher bias as the states begin to hybridise. Judging from the graph on the right-hand-side of the Figure 5.11, the transition frequency of C-1 is in good agreement with the spectral dip in Figure 5.18. This is also the case for C-2 and the spectral peak at ~2.3 THz. As both of these spectral artefacts have been tracked over time, this provides insight into the carrier dynamics and the relative population of states.

With the passage of the THz pump pulse at 0 ps, carriers are stimulated out of the upper lasing and injector states and drop into the miniband, where electron-electron scattering is the dominate transport mechanism. This process, combined with the LO-phonon assisted

extraction from the bottom of the miniband, are known to occur on a sub-picosecond timescale [101, 234]. Therefore, by the time the first measurement is performed at a PPD of 1 ps, carriers have already reoccupied the injector state (8) resulting in a prominent peak from C-2 at ~2.3 THz. The spectral dip at 2 THz is owing to the depletion of carrier from the upper lasing state. As the laser works to restore the initial population of states 9 and 8, electrons tunnel through the injection barrier (labelled in diagram 5.19) and repopulate the upper lasing level (9). The population inversion of transition C-1 and thus the carrier concentration of the upper lasing level is shown to be completely restored after <3 ps. The means by which this occurs however is disputable. It has been suggested that for an anti-crossing energy gap of <1 meV, as seen here, the strong dephasing caused by the various scattering mechanisms results in the incoherent transport across barriers [83, 106]. However, here the peak at 2.3 THz exhibits an oscillatory shape prior to it settling, implying that there is a coherent aspect to the carrier transport.

Both the recovery time of the upper lasing level and the coherent nature of the recovery process are similar to that demonstrated in MIR-QCLs [105, 219, 220]. Furthermore, by fitting the data in the inset of Figure 5.18 with a damped sine function (red line), an oscillation frequency of 590 GHz was obtained. This is in good agreement with calculated rabi-oscillation frequency (F_r) of 457 GHz calculated using expression $F_r = E_{89}/\hbar$ [108], where E_{ab} represents the anti-crossing energy between the injector and upper-lasing state. This was determined from the bandstructure simulations to be ~0.3 meV at threshold. As it has been suggested that resonant tunnelling is a function of barrier width [106], this might begin to explain why it is not as prominent in the data taken with the BTC active region, as the injector barrier for that device is 4.8-nm-thick, compared with 4.2-nm-thick in the hybrid device. Furthermore, it has been determined from bandstructure simulations in chapter 4, that the BTC device has an anti-crossing energy of ~0.18 meV, significantly lower than that of the hybrid device. The coherence of carrier transport across barriers is known to be affected by the anti-crossing energy gap, as dephasing mechanisms such as carrier-carrier and carrier-phonon scattering have a more significant effect with smaller gaps [108, 114]. It has been suggested that this is one reason why coherent tunnelling is not as dominate a transport mechanism in THz-QCL, relative to MIR-QCLs [108]. The QW barriers in MIR-QCLs are typically thinner, resulting

in anti-crossing energies in the region of 10 meV [105, 106]. Furthermore, this is possibly a reason for it not being fully investigated in THz-QCL.

5.5 Conclusion

THz-TDS has been performed on a THz-QCL fabricated with an ambipolar hybrid active region design. These results reveal that despite the device lasing in the forward bias at 2.7 THz and in reverse bias at 3.3 THz, interesting spectral features are present at lower frequencies, within the bandwidth of the TDS system. Furthermore it is revealed that the device behaves as a THz-bandstop filter when unbiased. To help answer some of these questions, bandstructure simulations and dipole moment calculations have been performed in the unbias, forward and reverse bias conditions. Conclusions have drawn based on these simulations. Lastly, THz-pump-THz-probe measurements have been performed on the device in forward bias which revealed some interesting results regarding the coherent transport of carriers across the injection barrier of each lasing module.

Chapter 6

Conclusions and further work

In chapter 1 a short introduction to THz radiation is provided. This discusses the various established techniques for the emission and detection of THz radiation, along with its industrial and academic applications. Following that, the motivation behind this project and the layout of the thesis are discussed. Chapter 2 contains a full literature review of THz-QCLs, beginning with basic laser theory and the background which led up to its invention to 2002. Carrier transport in THz-QCLs is also discussed, along with the advantages and disadvantages of the various active regions and waveguide designs.

In chapter 3 a new design of PC antenna is introduced, which uses epitaxial lift-off and van der Waals bonding techniques to transfer LT-GaAs active layers onto quartz substrates. This is shown to have three significant advantages over widely used PC emitters and detectors, which are fabricated directly onto an SI-GaAs growth substrate (LoG). Firstly, the reduction in dark current and parasitic photo-current in quartz-based devices leads to reduced heating and increased breakdown voltages. In the most significant comparison this has resulted in THz field amplitudes approximately eight-times larger than equivalent LoG devices. While these advantages have been demonstrated for several different electrode geometries, the benefits are most pronounced when using a large-area design. Secondly, when used in PC detection, the absence of an SI-GaAs substrate eliminates the long-lifetime carriers and increases the measured signal. Lastly, the ability to choose a thicker substrate allows system reflections to be delayed in time and their amplitude to be reduced without a loss of bandwidth, thereby increasing the available frequency resolution. To demonstrate this, data taken using devices

with quartz substrates ranging from 40 µm to 5-mm-thick has been presented. The addition of an optically transparent substrate also provides the option of performing back-side illumination, thus removing the attenuating effects of the substrate on the THz output pulse. Two examples of applications where LoQ devices have been used are presented in section 3.10.

In chapter 4 the GRT of a THz-QCL with a BTC active region has been measured with and without ARC applied its the facets, using a THz-pump-THz-probe technique. To collect the uncoated data a LoG emitter is used, while for the coated device, a significantly more powerful LoQ emitter is employed. Both scenarios have shown that the measured value is a function of bias applied across the device and increases as the QCL is driven at high bias conditions. Experimental evidence, combined with bandstructure simulations, suggest that this is due to the misalignment of the bandstructure and a shift in the lasing transition, brought about by a variation in dipole moment with bias. The values measured range between 18 ps for the uncoated device to 5 ps for the coated device. It has been suggested that the discrepancy between these values is owing to variation in the tunnelling mechanisms, controlling the carrier transport rates between quantum wells. Furthermore, the GRT measured here is shown to be a function of the THz pump power and the QCL operating temperature.

In chapter 5 THz-TDS has been used to investigate a THz-QCL, fabricated with an ambipolar hybrid active region. The results of these measurements reveal that despite the device lasing in the forward bias at 2.7 THz and in reverse bias at 3.3 THz, there appears to be interesting spectral features at lower frequencies within the bandwidth of the TDS system. Furthermore, these features appear to vary in both magnitude and frequency as a function laser bias. Based on these observations and combined with bandstructure simulations and dipole moment calculations for this device, it is possible to predict the relative population of states. This provides an interesting insight into the carrier dynamics of the device below threshold. Spectroscopy performed on the unbiased device revealed that it behaves as a THz bandstop filter, reducing the spectral amplitude between 2 to 2.5 THz. Lastly, THz-pump-THz-probe measurements performed with this device in forward bias have revealed some interesting preliminary results regarding the coherent transport of carriers across the injection barrier of each lasing module.

6.1 Further work

The invention of the LoQ device and its ability to withstand the high peak powers of amplified laser systems has opened up an interesting avenue for future research. Amplified femtosecond lasers are typically combined with non-linear crystals to generate THz fields in the order of several MV cm^{-1}. However, it is believed that with the use of a LoQ emitter, or a series of emitters fabricated into an array geometry, similar fields spread over a wider bandwidth can be reached. This would need to be designed with a microlens attached to focus the beam onto the individual emitters. A BSI technique could also be applied to increase the performance of the device. However, to attach a microlens without damaging the device, a protective layer of material would be required. A good option for this would be BCB, as it is transparent to THz radiation, provides good thermal and electrical insulation and can be spun into the surface of the device in micrometer-thick films. A powerful design of emitter would have many potential applications including the spectroscopy of highly absorbent materials such as biological samples, as well as helping to develop self-induced transparency in THz-QCLs.

It has been demonstrated in chapters 4 and 5 that the THz-pump-THz-probe technique is a very powerful tool for the investigation of carrier dynamics in THz-QCLs. However, section 5.4 only reveals preliminary results which require further investigation. It would be interesting to determine the dependence of coherent carrier transport on QCL temperature, bias conditions and the ratio between the pump and probe pulse power. It would also be interesting to use this technique on another hybrid/LO-phonon design QCL, preferable with the lasing transition within the bandwidth the TDS system.

Bibliography

[1] J. T. Keeley, *Self-Mixing in Terahertz Quantum Cascade Lasers*. PhD thesis, University of Leeds, 2016.

[2] J. F. Federici, B. Schulkin, F. Huang, D. Gary, R. Barat, F. Oliveira, and D. Zimdars, "THz imaging and sensing for security applications-explosives, weapons and drugs," *Semiconductor Science and Technology*, vol. 20, no. 7, p. 266, 2005.

[3] Q. Song, Y. Zhao, A. Redo-Sanchez, C. Zhang, and X. Liu, "Fast continuous terahertz wave imaging system for security," *Optics Communications*, vol. 282, no. 10, pp. 2019–2022, 2009.

[4] R. Appleby and H. B. Wallace, "Standoff detection of weapons and contraband in the 100 GHz to 1 THz region," *IEEE Transactions on Antennas and Propagation*, vol. 55, no. 11, pp. 2944–2956, 2007.

[5] K. Kawase, Y. Ogawa, Y. Watanabe, and H. Inoue, "Non-destructive terahertz imaging of illicit drugs using spectral fingerprints," *Optics Express*, vol. 11, no. 20, pp. 2549–2554, 2003.

[6] A. G. Davies, A. D. Burnett, W. Fan, E. H. Linfield, and J. E. Cunningham, "Terahertz spectroscopy of explosives and drugs," *Materials Today*, vol. 11, no. 3, pp. 18–26, 2008.

[7] C. Kagan, C. Murray, M. Nirmal, and M. Bawendi, "Electronic energy transfer in CdSe quantum dot solids," *Physical Review Letters*, vol. 76, no. 9, p. 1517, 1996.

[8] A. P. Alivisatos, "Semiconductor clusters, nanocrystals, and quantum dots," *Science*, vol. 271, no. 5251, p. 933, 1996.

[9] B. Cole, J. Williams, B. King, M. Sherwin, and C. Stanley, "Coherent manipulation of semiconductor quantum bits with terahertz radiation," *Nature*, vol. 410, no. 6824, pp. 60–63, 2001.

[10] R. M. Woodward, V. P. Wallace, R. J. Pye, B. E. Cole, D. D. Arnone, E. H. Linfield, and M. Pepper, "Terahertz pulse imaging of ex vivo basal cell carcinoma," *Journal of Investigative Dermatology*, vol. 120, no. 1, pp. 72–78, 2003.

[11] V. Wallace, A. Fitzgerald, S. Shankar, N. Flanagan, R. Pye, J. Cluff, and D. Arnone, "Terahertz pulsed imaging of basal cell carcinoma ex vivo and in vivo," *British Journal of Dermatology*, vol. 151, no. 2, pp. 424–432, 2004.

[12] A. J. Fitzgerald, V. P. Wallace, M. Jimenez-Linan, L. Bobrow, R. J. Pye, A. D. Purushotham, and D. D. Arnone, "Terahertz pulsed imaging of human breast tumors 1," *Radiology*, vol. 239, no. 2, pp. 533–540, 2006.

[13] F. Wahaia, G. Valusis, L. M. Bernardo, A. Almeida, J. A. Moreira, P. C. Lopes, J. Macutkevic, I. Kasalynas, D. Seliuta, R. Adomavicius, *et al.*, "Detection of colon cancer by terahertz techniques," *Journal of Molecular Structure*, vol. 1006, no. 1, pp. 77–82, 2011.

[14] P. H. Siegel, "Terahertz technology," *IEEE Transactions on Microwave Theory and Techniques*, vol. 50, no. 3, pp. 910–928, 2002.

[15] T. G. Phillips and J. Keene, "Submillimeter astronomy (heterodyne spectroscopy)," *Proceedings of the IEEE*, vol. 80, no. 11, pp. 1662–1678, 1992.

[16] G. J. Melnick, J. R. Stauffer, M. L. Ashby, E. A. Bergin, G. Chin, N. R. Erickson, P. F. Goldsmith, M. Harwit, J. E. Howe, S. C. Kleiner, *et al.*, "The submillimeter wave astronomy satellite: Science objectives and instrument description," *The Astrophysical Journal Letters*, vol. 539, no. 2, pp. L77–L85, 2000.

[17] R. W. Hoogeveen, P. A. Yagoubov, A. Maurellis, V. P. Koshelets, S. V. Shitov, U. Mair, M. Krocka, G. Wagner, M. Birk, H.-W. Huebers, *et al.*, "New cryogenic heterodyne techniques applied in TELIS: the balloon-borne THz and submillimeter limb sounder for atmospheric research," in *Optical Science and Technology, SPIE's 48th Annual Meeting*, pp. 347–355, International Society for Optics and Photonics, 2003.

[18] M. C. Gaidis, H. M. Pickett, C. Smith, S. C. Martin, R. P. Smith, and P. H. Siegel, "A 2.5-THz receiver front end for spaceborne applications," *IEEE Transactions on Microwave Theory and Techniques*, vol. 48, no. 4, pp. 733–739, 2000.

[19] S. Koenig, D. Lopez-Diaz, J. Antes, F. Boes, R. Henneberger, A. Leuther, A. Tessmann, R. Schmogrow, D. Hillerkuss, R. Palmer, *et al.*, "Wireless sub-THz communication system with high data rate," *Nature Photonics*, vol. 7, no. 12, pp. 977–981, 2013.

[20] T. Kleine-Ostmann and T. Nagatsuma, "A review on terahertz communications research," *Journal of Infrared, Millimeter, and Terahertz Waves*, vol. 32, no. 2, pp. 143–171, 2011.

[21] J. Ryu, Y. Jung, S. Baek, J. Lee, S. Kim, S. Kwon, and J. Kim, "Diagnosis of dental cavity and osteoporosis using terahertz transmission images," in *Ultrafast Phenomena XII*, pp. 265–267, Springer, 2001.

[22] J. Jackson, M. Mourou, J. Whitaker, I. N. Duling, S. Williamson, M. Menu, and G. Mourou, "Terahertz imaging for non-destructive evaluation of mural paintings," *Optics Communications*, vol. 281, no. 4, pp. 527–532, 2008.

[23] M. Tonouchi, "Cutting-edge terahertz technology," *Nature Photonics*, vol. 1, no. 2, pp. 97–105, 2007.

[24] P. Dean, A. Valavanis, J. Keeley, K. Bertling, Y. Lim, R. Alhathlool, A. Burnett, L. Li, S. Khanna, D. Indjin, *et al.*, "Terahertz imaging using quantum cascade lasers-a review of systems and applications," *Journal of Physics D: Applied Physics*, vol. 47, no. 37, p. 374008, 2014.

[25] Y.-S. Lee, *Principles of Terahertz Science and Technology*, vol. 170. Springer Science & Business Media, 2009.

[26] A. Maestrini, J. Ward, J. Gill, H. Javadi, E. Schlecht, G. Chattopadhyay, F. Maiwald, N. R. Erickson, and I. Mehdi, "A 1.7-1.9 THz local oscillator source," *IEEE Microwave and Wireless Components Letters*, vol. 14, no. 6, pp. 253–255, 2004.

[27] N. Orihashi, S. Suzuki, and M. Asada, "One THz harmonic oscillation of resonant tunneling diodes," *Applied Physics Letters*, vol. 87, no. 23, p. 233501, 2005.

[28] A. Davies, E. H. Linfield, and M. B. Johnston, "The development of terahertz sources and their applications," *Physics in Medicine and Biology*, vol. 47, no. 21, p. 3679, 2002.

[29] S. H. Gold and G. S. Nusinovich, "Review of high-power microwave source research," *Review of Scientific Instruments*, vol. 68, no. 11, pp. 3945–3974, 1997.

[30] W. He, C. Donaldson, L. Zhang, K. Ronald, P. McElhinney, and A. Cross, "High power wideband gyrotron backward wave oscillator operating towards the terahertz region," *Physical Review Letters*, vol. 110, no. 16, p. 165101, 2013.

[31] L.-P. Schmidt, S. Biber, G. Rehm, and K. Huber, "THz measurement technologies and applications," in *14th International Conference on Microwaves, Radar and Wireless Communications*, vol. 2, pp. 581–587, IEEE, 2002.

[32] G. Williams, "Far-IR/THz radiation from the jefferson laboratory, energy recovered linac, free electron laser," *Review of Scientific Instruments*, vol. 73, no. 3, pp. 1461–1463, 2002.

[33] R. Köhler, A. Tredicucci, F. Beltram, H. E. Beere, E. H. Linfield, A. G. Davies, D. A. Ritchie, R. C. Iotti, and F. Rossi, "Terahertz semiconductor-heterostructure laser," *Nature*, vol. 417, no. 6885, pp. 156–159, 2002.

[34] L. Li, L. Chen, J. Zhu, J. Freeman, P. Dean, A. Valavanis, A. Davies, and E. Linfield, "Terahertz quantum cascade lasers with > 1 W output powers," *Electronics Letters*, vol. 50, no. 4, pp. 309–311, 2014.

[35] M. Wienold, B. Röben, L. Schrottke, R. Sharma, A. Tahraoui, K. Biermann, and H. Grahn, "High-temperature, continuous-wave operation of terahertz quantum-cascade lasers with metal-metal waveguides and third-order distributed feedback," *Optics Express*, vol. 22, no. 3, pp. 3334–3348, 2014.

[36] G. Scalari, C. Walther, J. Faist, H. Beere, and D. Ritchie, "Laser emission at 830 and 960 GHz from quantum cascade structures," *ITQW2007, Ambleside, UK*, 2007.

[37] B. S. Williams, "Terahertz quantum-cascade lasers," *Nature Photonics*, vol. 1, no. 9, pp. 517–525, 2007.

[38] D. Auston, K. Cheung, and P. Smith, "Picosecond photoconducting hertzian dipoles," *Applied Physics Letters*, vol. 45, no. 3, pp. 284–286, 1984.

[39] A. Dreyhaupt, S. Winnerl, M. Helm, and T. Dekorsy, "Optimum excitation conditions for the generation of high-electric-field terahertz radiation from an oscillator-driven photoconductive device," *Optics Letters*, vol. 31, no. 10, pp. 1546–1548, 2006.

[40] G. Matthäus, S. Nolte, R. Hohmuth, M. Voitsch, W. Richter, B. Pradarutti, S. Riehemann, G. Notni, and A. Tünnermann, "Large-area microlens emitters for powerful THz emission," *Applied Physics B*, vol. 96, no. 2-3, pp. 233–235, 2009.

[41] C. W. Berry, M. R. Hashemi, and M. Jarrahi, "Generation of high power pulsed terahertz radiation using a plasmonic photoconductive emitter array with logarithmic spiral antennas," *Applied Physics Letters*, vol. 104, no. 8, p. 081122, 2014.

[42] E. Brown, F. Smith, and K. McIntosh, "Coherent millimeter-wave generation by heterodyne conversion in low-temperature-grown GaAs photoconductors," *Journal of Applied Physics*, vol. 73, no. 3, pp. 1480–1484, 1993.

[43] C. W. Berry, M. R. Hashemi, S. Preu, H. Lu, A. C. Gossard, and M. Jarrahi, "High power terahertz generation using 1550 nm plasmonic photomixers," *Applied Physics Letters*, vol. 105, no. 1, p. 011121, 2014.

[44] T. Kampfrath, K. Tanaka, and K. A. Nelson, "Resonant and nonresonant control over matter and light by intense terahertz transients," *Nature Photonics*, vol. 7, no. 9, pp. 680–690, 2013.

[45] W. Shi, Y. J. Ding, N. Fernelius, and K. Vodopyanov, "Efficient, tunable, and coherent 0.18–5.27-THz source based on GaSe crystal," *Optics Letters*, vol. 27, no. 16, pp. 1454–1456, 2002.

[46] Y.-S. Lee, T. Meade, V. Perlin, H. Winful, T. Norris, and A. Galvanauskas, "Generation of narrow-band terahertz radiation via optical rectification of femtosecond pulses in periodically poled lithium niobate," *Applied Physics Letters*, vol. 76, no. 18, pp. 2505–2507, 2000.

[47] K. Kawase, M. Sato, T. Taniuchi, and H. Ito, "Coherent tunable THz-wave generation from LiNbO3 with monolithic grating coupler," *Applied Physics Letters*, vol. 68, no. 18, pp. 2483–2485, 1996.

[48] J. E. Schaar, K. L. Vodopyanov, P. S. Kuo, M. M. Fejer, X. Yu, A. Lin, J. S. Harris, D. Bliss, C. Lynch, V. G. Kozlov, *et al.*, "Terahertz sources based on intracavity parametric down-conversion in quasi-phase-matched gallium arsenide," *IEEE Journal of Selected Topics in Quantum Electronics*, vol. 14, no. 2, pp. 354–362, 2008.

[49] Y.-S. Lee, T. Meade, T. B. Norris, and A. Galvanauskas, "Tunable narrow-band terahertz generation from periodically poled lithium niobate," in *Quantum Electronics and Laser Science Conference*, pp. 45–46, IEEE, 2001.

[50] K.-Y. Kim, A. Taylor, J. Glownia, and G. Rodriguez, "Coherent control of terahertz supercontinuum generation in ultrafast laser–gas interactions," *Nature Photonics*, vol. 2, no. 10, pp. 605–609, 2008.

[51] D. Saeedkia and S. Safavi-Naeini, "Terahertz photonics: Optoelectronic techniques for generation and detection of terahertz waves," *Journal of Lightwave Technology*, vol. 26, no. 15, pp. 2409–2423, 2008.

[52] D. Mittleman, *Sensing with terahertz radiation*, vol. 85. Springer, 2013.

[53] L. Fernandes, P. Kaufmann, R. Marcon, A. Kudaka, A. Marun, R. Godoy, E. Bortolucci, M. B. Zakia, and J. Diniz, "Photometry of thz radiation using golay cell detector," in *General Assembly and Scientific Symposium, 2011 XXXth URSI*, pp. 1–4, IEEE, 2011.

[54] A. J. Kreisler and A. Gaugue, "Recent progress in high-temperature superconductor bolometric detectors: from the mid-infrared to the far-infrared (THz) range," *Superconductor Science and Technology*, vol. 13, no. 8, p. 1235, 2000.

[55] A. J. Miller, A. Luukanen, and E. N. Grossman, "Micromachined antenna-coupled uncooled microbolometers for terahertz imaging arrays," in *Defense and Security*, pp. 18–24, International Society for Optics and Photonics, 2004.

[56] B. Ferguson and X.-C. Zhang, "Materials for terahertz science and technology," *Nature Materials*, vol. 1, no. 1, pp. 26–33, 2002.

[57] T. Yasui, A. Nishimura, T. Suzuki, K. Nakayama, and S. Okajima, "Detection system operating at up to 7 THz using quasioptics and schottky barrier diodes," *Review of Scientific Instruments*, vol. 77, no. 6, p. 066102, 2006.

[58] S. Ariyoshi, C. Otani, A. Dobroiu, H. Sato, K. Kawase, H. Shimizu, T. Taino, and H. Matsuo, "Terahertz imaging with a direct detector based on superconducting tunnel junctions," *Applied Physics Letters*, vol. 88, no. 20, p. 203503, 2006.

[59] S. Komiyama, O. Astafiev, V. Antonov, T. Kutsuwa, and H. Hirai, "A single-photon detector in the far-infrared range," *Nature*, vol. 403, no. 6768, pp. 405–407, 2000.

[60] Y. Shen, P. Upadhya, H. Beere, E. Linfield, A. Davies, I. Gregory, C. Baker, W. Tribe, and M. Evans, "Generation and detection of ultrabroadband terahertz radiation using photoconductive emitters and receivers," *Applied Physics Letters*, vol. 85, no. 2, pp. 164–166, 2004.

[61] C. Winnewisser, P. U. Jepsen, M. Schall, V. Schyja, and H. Helm, "Electro-optic detection of THz radiation in LiTaO3, LiNbO3 and ZnTe," *Applied Physics Letters*, vol. 70, no. 23, pp. 3069–3071, 1997.

[62] G. Gallot, J. Zhang, R. McGowan, T.-I. Jeon, and D. Grischkowsky, "Measurements of the Thz absorption and dispersion of ZnTe and their relevance to the electro-optic detection of THz radiation," *Applied Physics Letters*, vol. 74, no. 23, pp. 3450–3452, 1999.

[63] Y. Cai, I. Brener, J. Lopata, J. Wynn, L. Pfeiffer, J. Stark, Q. Wu, X. Zhang, and J. Federici, "Coherent terahertz radiation detection: Direct comparison between free-space electro-optic sampling and antenna detection," *Applied Physics Letters*, vol. 73, no. 4, pp. 444–446, 1998.

[64] T. H. Maiman, *Stimulated optical radiation in ruby*. 1960.

[65] R. N. Hall, G. E. Fenner, J. Kingsley, T. Soltys, and R. Carlson, "Coherent light emission from GaAs junctions," *Physical Review Letters*, vol. 9, no. 9, p. 366, 1962.

[66] M. I. Nathan, W. P. Dumke, G. Burns, F. H. Dill Jr, and G. Lasher, "Stimulated emission of radiation from GaAs p-n junctions," *Applied Physics Letters*, vol. 1, no. 3, pp. 62–64, 1962.

[67] Z. I. Alferov, V. Andreev, E. Portnoi, and M. Trukan, "AlAs-GaAs heterojunction injection lasers with a low room-temperature threshold," *Soviet Physics-Semiconductors*, vol. 3, no. 9, pp. 1107–1110, 1970.

[68] J. Van der Ziel, R. Dingle, R. C. Miller, W. Wiegmann, and W. Nordland Jr, "Laser oscillation from quantum states in very thin GaAs-Al0. 2Ga0. 8As multilayer structures," *Applied Physics Letters*, vol. 26, no. 8, pp. 463–465, 1975.

[69] H. Heard, "Ultra-violet gas laser at room temperature," *Nature*, vol. 200, no. 4907, pp. 667–667, 1963.

[70] Y. Arakawa and A. Yariv, "Quantum well lasers–gain, spectra, dynamics," *IEEE Journal of Quantum Electronics*, vol. 22, no. 9, pp. 1887–1899, 1986.

[71] P. Harrison and A. Valavanis, *Quantum wells, wires and dots: theoretical and computational physics of semiconductor nanostructures.* John Wiley & Sons, 2016.

[72] R. Kazarinov and R. Sui-is, "Possibility of the amplification of electromagnetic waves in a semiconductor with a superlattice," *Soviet Physics-Semiconductors*, vol. 5, 1971.

[73] J. Faist, F. Capasso, D. L. Sivco, C. Sirtori, A. L. Hutchinson, A. Y. Cho, *et al.*, "Quantum cascade laser," *Science*, vol. 264, no. 5158, pp. 553–556, 1994.

[74] F. Capasso, K. Mohammed, and A. Y. Cho, "Resonant tunneling through double barriers, perpendicular quantum transport phenomena in superlattices, and their device applications," in *Electronic Structure of Semiconductor Heterojunctions*, pp. 99–115, Springer, 1988.

[75] H. Liu, "A novel superlattice infrared source," *Journal of Applied Physics*, vol. 63, no. 8, pp. 2856–2858, 1988.

[76] J. Faist, F. Capasso, C. Sirtori, D. L. Sivco, A. L. Hutchinson, S.-N. G. Chu, and A. Y. Cho, "Continuous wave operation of quantum cascade lasers based on vertical transitions at λ= 4.6 μm," *Superlattices and Microstructures*, vol. 19, no. 4, pp. 337–345, 1996.

[77] C. Sirtori, J. Faist, F. Capasso, D. L. Sivco, A. L. Hutchinson, and A. Y. Cho, "Mid-infrared (8.5 μm) semiconductor lasers operating at room temperature," *IEEE Photonics Technology Letters*, vol. 9, no. 3, pp. 294–296, 1997.

[78] Y. Bai, S. Darvish, S. Slivken, W. Zhang, A. Evans, J. Nguyen, and M. Razeghi, "Room temperature continuous wave operation of quantum cascade lasers with watt-level optical power," *Applied Physics Letters*, vol. 92, no. 10, p. 101105, 2008.

[79] M. Woerner, K. Reimann, and T. Elsaesser, "Coherent charge transport in semiconductor quantum cascade structures," *Journal of Physics: Condensed Matter*, vol. 16, no. 4, p. R25, 2004.

[80] R. A. Kaindl, S. Lutgen, M. Woerner, T. Elsaesser, B. Nottelmann, V. M. Axt, T. Kuhn, A. Hase, and H. Künzel, "Ultrafast dephasing of coherent intersubband polarizations in a quasi-two-dimensional electron plasma," *Physical Review Letters*, vol. 80, no. 16, p. 3575, 1998.

[81] R. Köhler, A. Tredicucci, F. Beltram, H. E. Beere, E. H. Linfield, A. G. Davies, and D. A. Ritchie, "Low-threshold quantum-cascade lasers at 3.5 THz (λ= 85 μm)," *Optics Letters*, vol. 28, no. 10, pp. 810–812, 2003.

[82] B. Williams, S. Kumar, Q. Hu, and J. Reno, "Resonant-phonon terahertz quantum-cascade laser operating at 2.1 THz (λâĽČ 141 μm)," *Electronics Letters*, vol. 40, no. 7, pp. 431–433, 2004.

[83] S. Kumar, B. S. Williams, Q. Hu, and J. L. Reno, "1.9 THz quantum-cascade lasers with one-well injector," *Applied Physics Letters*, vol. 88, no. 12, p. 121123, 2006.

[84] J. Ulrich, R. Zobl, K. Unterrainer, G. Strasser, and E. Gornik, "Magnetic-field-enhanced quantum-cascade emission," *Applied Physics Letters*, vol. 76, no. 1, pp. 19–21, 2000.

[85] A. Wade, G. Fedorov, D. Smirnov, S. Kumar, B. Williams, Q. Hu, and J. Reno, "Magnetic-field-assisted terahertz quantum cascade laser operating up to 225 K," *Nature Photonics*, vol. 3, no. 1, pp. 41–45, 2009.

[86] S. Fathololoumi, E. Dupont, C. Chan, Z. Wasilewski, S. Laframboise, D. Ban, A. Mátyás, C. Jirauschek, Q. Hu, and H. Liu, "Terahertz quantum cascade lasers operating up to $\sim$ 200 K with optimized oscillator strength and improved injection tunneling," *Optics Express*, vol. 20, no. 4, pp. 3866–3876, 2012.

[87] B. S. Williams, S. Kumar, Q. Hu, and J. L. Reno, "High-power terahertz quantum-cascade lasers," *Electronics Letters*, vol. 42, no. 2, pp. 89–91, 2006.

[88] A. Tredicucci, F. Capasso, C. Gmachl, D. L. Sivco, A. L. Hutchinson, A. Y. Cho, J. Faist, and G. Scamarcio, "High-power inter-miniband lasing in intrinsic superlattices," *Applied Physics Letters*, vol. 72, no. 19, pp. 2388–2390, 1998.

[89] J. Faist, F. Capasso, C. Sirtori, D. L. Sivco, J. N. Baillargeon, A. L. Hutchinson, S.-N. G. Chu, and A. Y. Cho, "High power mid-infrared ($\lambda \sim 5$ μm) quantum cascade lasers operating above room temperature," *Applied Physics Letters*, vol. 68, no. 26, pp. 3680–3682, 1996.

[90] J. Faist, M. Beck, T. Aellen, and E. Gini, "Quantum-cascade lasers based on a bound-to-continuum transition," *Applied Physics Letters*, vol. 78, no. 2, pp. 147–149, 2001.

[91] S. Barbieri, J. Alton, H. E. Beere, J. Fowler, E. H. Linfield, and D. A. Ritchie, "2.9 THz quantum cascade lasers operating up to 70 K in continuous wave," *Applied Physics Letters*, vol. 85, no. 10, pp. 1674–1676, 2004.

[92] C. Worrall, J. Alton, M. Houghton, S. Barbieri, H. E. Beere, D. Ritchie, and C. Sirtori, "Continuous wave operation of a superlattic quantum cascade laser emitting at 2 THz," *Optics Express*, vol. 14, no. 1, pp. 171–181, 2006.

[93] B. S. Williams, S. Kumar, H. Callebaut, Q. Hu, and J. L. Reno, "Terahertz quantum-cascade laser operating up to 137 K," *Applied Physics Letters*, vol. 83, no. 25, pp. 5142–5144, 2003.

[94] B. S. Williams, S. Kumar, Q. Qin, Q. Hu, and J. L. Reno, "Terahertz quantum cascade lasers with double-resonant-phonon depopulation," *Applied Physics Letters*, vol. 88, no. 26, p. 261101, 2006.

[95] Y. Han, L. Li, A. Grier, L. Chen, A. Valavanis, J. Zhu, J. Freeman, N. Isac, R. Colombelli, P. Dean, *et al.*, "Extraction-controlled terahertz frequency quantum cascade lasers with a diagonal LO-phonon extraction and injection stage," *Optics Express*, vol. 24, no. 25, pp. 28583–28593, 2016.

[96] G. Scalari, N. Hoyler, M. Giovannini, and J. Faist, "Terahertz bound-to-continuum quantum-cascade lasers based on optical-phonon scattering extraction," *Applied Physics Letters*, vol. 86, no. 18, p. 181101, 2005.

[97] M. I. Amanti, G. Scalari, R. Terazzi, M. Fischer, M. Beck, J. Faist, A. Rudra, P. Gallo, and E. Kapon, "Bound-to-continuum terahertz quantum cascade laser with a single-quantum-well phonon extraction/injection stage," *New Journal of Physics*, vol. 11, no. 12, p. 125022, 2009.

[98] K. Ohtani and H. Ohno, "InAs/AlSb quantum cascade lasers operating at 10 μm," *Applied Physics Letters*, vol. 82, no. 7, pp. 1003–1005, 2003.

[99] C. Sirtori, P. Kruck, S. Barbieri, P. Collot, J. Nagle, M. Beck, J. Faist, and U. Oesterle, "GaAs/Al x Ga 1- x As quantum cascade lasers," *Applied Physics Letters*, vol. 73, no. 24, pp. 3486–3488, 1998.

[100] H. Beere, J. Fowler, J. Alton, E. Linfield, D. Ritchie, R. Köhler, A. Tredicucci, G. Scalari, L. Ajili, J. Faist, *et al.*, "MBE growth of terahertz quantum cascade lasers," *Journal of Crystal Growth*, vol. 278, no. 1, pp. 756–764, 2005.

[101] Q. Hu, B. S. Williams, S. Kumar, H. Callebaut, S. Kohen, and J. L. Reno, "Resonant-phonon-assisted thz quantum-cascade lasers with metal-metal waveguides," *Semiconductor Science and Technology*, vol. 20, no. 7, p. S228, 2005.

[102] M. A. Belkin, J. A. Fan, S. Hormoz, F. Capasso, S. P. Khanna, M. Lachab, A. G. Davies, and E. H. Linfield, "Terahertz quantum cascade lasers with copper metal-metal waveguides operating up to 178 K," *Optics Express*, vol. 16, no. 5, pp. 3242–3248, 2008.

[103] B. S. Williams, S. Kumar, Q. Hu, and J. L. Reno, "Distributed-feedback terahertz quantum-cascade lasers with laterally corrugated metal waveguides," *Optics Letters*, vol. 30, no. 21, pp. 2909–2911, 2005.

[104] M. S. Vitiello and A. Tredicucci, "Tunable emission in THz quantum cascade lasers," *IEEE Transactions on Terahertz Science and Technology*, vol. 1, no. 1, pp. 76–84, 2011.

[105] F. Eickemeyer, K. Reimann, M. Woerner, T. Elsaesser, S. Barbieri, C. Sirtori, G. Strasser, T. Müller, R. Bratschitsch, and K. Unterrainer, "Ultrafast coherent electron transport in semiconductor quantum cascade structures," *Physical Review Letters*, vol. 89, no. 4, p. 047402, 2002.

[106] C. Sirtori, F. Capasso, J. Faist, A. L. Hutchinson, D. L. Sivco, and A. Y. Cho, "Resonant tunneling in quantum cascade lasers," *IEEE Journal of Quantum Electronics*, vol. 34, no. 9, pp. 1722–1729, 1998.

[107] G. Scalari, R. Terazzi, M. Giovannini, N. Hoyler, and J. Faist, "Population inversion by resonant tunneling in quantum wells," *Applied Physics Letters*, vol. 91, no. 3, p. 032103, 2007.

[108] H. Callebaut and Q. Hu, "Importance of coherence for electron transport in terahertz quantum cascade lasers," *Journal of Applied Physics*, vol. 98, no. 10, p. 104505, 2005.

[109] R. Terazzi, T. Gresch, A. Wittmann, and J. Faist, "Sequential resonant tunneling in quantum cascade lasers," *Physical Review B*, vol. 78, no. 15, p. 155328, 2008.

[110] R. C. Iotti and F. Rossi, "Nature of charge transport in quantum-cascade lasers," *Physical Review Letters*, vol. 87, no. 14, p. 146603, 2001.

[111] H. Choi, T. B. Norris, T. Gresch, M. Giovannini, J. Faist, L. Diehl, and F. Capasso, "Femtosecond dynamics of resonant tunneling and superlattice relaxation in quantum cascade lasers," *Applied Physics Letters*, vol. 92, no. 12, p. 122114, 2008.

[112] J. Lü and J. Cao, "Coulomb scattering in the monte carlo simulation of terahertz quantum-cascade lasers," *Applied Physics Letters*, vol. 89, no. 21, p. 211115, 2006.

[113] E. Dupont, S. Fathololoumi, Z. Wasilewski, G. Aers, S. Laframboise, M. Lindskog, S. Razavipour, A. Wacker, D. Ban, and H. Liu, "A phonon scattering assisted injection and extraction based terahertz quantum cascade laser," *Journal of Applied Physics*, vol. 111, no. 7, p. 073111, 2012.

[114] S. Kumar and Q. Hu, "Coherence of resonant-tunneling transport in terahertz quantum-cascade lasers," *Physical Review B*, vol. 80, no. 24, p. 245316, 2009.

[115] F. Wang, X. Guo, and J. Cao, "Many-body interaction in resonant tunneling of terahertz quantum cascade lasers," *Journal of Applied Physics*, vol. 108, no. 8, p. 083714, 2010.

[116] J. Freeman, *Heterogeneous terahertz quantum cascade lasers*. PhD thesis, University of Cambridge, 2010.

[117] J. Faist, F. Capasso, C. Sirtori, D. Sivco, and A. Cho, "Intersubband transitions in quantum wells: physics and device applications ii," *Chap*, vol. 1, pp. 1–83, 2000.

[118] S. Lu, L. Schrottke, S. Teitsworth, R. Hey, and H. Grahn, "Formation of electric-field domains in Ga As/ Al x Ga 1- x As quantum cascade laser structures," *Physical Review B*, vol. 73, no. 3, p. 033311, 2006.

[119] L. L. Bonilla and H. T. Grahn, "Non-linear dynamics of semiconductor superlattices," *Reports on Progress in Physics*, vol. 68, no. 3, p. 577, 2005.

[120] M. Van Exter, C. Fattinger, and D. Grischkowsky, "Terahertz time-domain spectroscopy of water vapor," *Optics Letters*, vol. 14, no. 20, pp. 1128–1130, 1989.

[121] K. Cheung and D. Auston, "Excitation of coherent phonon polaritons with femtosecond optical pulses," *Physical Review Letters*, vol. 55, no. 20, p. 2152, 1985.

[122] D. Grischkowsky, S. Keiding, M. Van Exter, and C. Fattinger, "Far-infrared time-domain spectroscopy with terahertz beams of dielectrics and semiconductors," *Journal of the Optical Society of America B*, vol. 7, no. 10, pp. 2006–2015, 1990.

[123] P. F. Taday, "Applications of terahertz spectroscopy to pharmaceutical sciences," *Philosophical Transactions of the Royal Society of London A: Mathematical, Physical and Engineering Sciences*, vol. 362, no. 1815, pp. 351–364, 2004.

[124] C. J. Strachan, T. Rades, D. A. Newnham, K. C. Gordon, M. Pepper, and P. F. Taday, "Using terahertz pulsed spectroscopy to study crystallinity of pharmaceutical materials," *Chemical Physics Letters*, vol. 390, no. 1, pp. 20–24, 2004.

[125] B. M. Fischer, H. Helm, and P. U. Jepsen, "Chemical recognition with broadband THz spectroscopy," *Proceedings of the IEEE*, vol. 95, no. 8, pp. 1592–1604, 2007.

[126] M. Brucherseifer, M. Nagel, P. H. Bolivar, H. Kurz, A. Bosserhoff, and R. Büttner, "Label-free probing of the binding state of DNA by time-domain terahertz sensing," *Applied Physics Letters*, vol. 77, no. 24, pp. 4049–4051, 2000.

[127] A. Markelz, A. Roitberg, and E. J. Heilweil, "Pulsed terahertz spectroscopy of DNA, bovine serum albumin and collagen between 0.1 and 2.0 THz," *Chemical Physics Letters*, vol. 320, no. 1, pp. 42–48, 2000.

[128] M. Walther, B. M. Fischer, and P. U. Jepsen, "Noncovalent intermolecular forces in polycrystalline and amorphous saccharides in the far infrared," *Chemical Physics*, vol. 288, no. 2, pp. 261–268, 2003.

[129] B. Fischer, M. Hoffmann, H. Helm, G. Modjesch, and P. U. Jepsen, "Chemical recognition in terahertz time-domain spectroscopy and imaging," *Semiconductor Science and Technology*, vol. 20, no. 7, p. S246, 2005.

[130] P. U. Jepsen, H. Merbold, *et al.*, "Investigation of aqueous alcohol and sugar solutions with reflection terahertz time-domain spectroscopy," *Optics Express*, vol. 15, no. 22, pp. 14717–14737, 2007.

[131] J. Xu, K. W. Plaxco, S. J. Allen, J. E. Bjarnason, and E. R. Brown, "0.15–3.72 THz absorption of aqueous salts and saline solutions," *Applied Physics Letters*, vol. 90, no. 3, p. 031908, 2007.

[132] J. Xu, K. W. Plaxco, and S. J. Allen, "Probing the collective vibrational dynamics of a protein in liquid water by terahertz absorption spectroscopy," *Protein Science*, vol. 15, no. 5, pp. 1175–1181, 2006.

[133] Y. Yomogida, Y. Sato, R. Nozaki, T. Mishina, and J. Nakahara, "Comparative dielectric study of monohydric alcohols with terahertz time-domain spectroscopy," *Journal of Molecular Structure*, vol. 981, no. 1, pp. 173–178, 2010.

[134] K. D. Möller and W. G. Rothschild, *Far-infrared spectroscopy*. New York: Wiley, 1971.

[135] M. Tani, M. Herrmann, and K. Sakai, "Generation and detection of terahertz pulsed radiation with photoconductive antennas and its application to imaging," *Measurement Science and Technology*, vol. 13, no. 11, p. 1739, 2002.

[136] Y. Shen, P. Upadhya, E. Linfield, H. Beere, and A. Davies, "Ultrabroadband terahertz radiation from low-temperature-grown GaAs photoconductive emitters," *Applied Physics Letters*, vol. 83, no. 15, pp. 3117–3119, 2003.

[137] M. C. Nuss and J. Orenstein, "Terahertz time-domain spectroscopy," in *Millimeter and submillimeter wave spectroscopy of solids*, pp. 7–50, Springer, 1998.

[138] J. T. Darrow, X.-C. Zhang, D. H. Auston, and J. D. Morse, "Saturation properties of large-aperture photoconducting antennas," *IEEE Journal of Quantum Electronics*, vol. 28, no. 6, pp. 1607–1616, 1992.

[139] G. Klatt, F. Hilser, W. Qiao, M. Beck, R. Gebs, A. Bartels, K. Huska, U. Lemmer, G. Bastian, M. B. Johnston, *et al.*, "Terahertz emission from lateral photo-dember currents," *Optics Express*, vol. 18, no. 5, pp. 4939–4947, 2010.

[140] Q. Wu and X.-C. Zhang, "Free-space electro-optic sampling of terahertz beams," *Applied Physics Letters*, vol. 67, no. 24, pp. 3523–3525, 1995.

[141] D. Auston, A. Johnson, P. Smith, and J. Bean, "Picosecond optoelectronic detection, sampling, and correlation measurements in amorphous semiconductors," *Applied Physics Letters*, vol. 37, no. 4, pp. 371–373, 1980.

[142] A. Warren, N. Katzenellenbogen, D. Grischkowsky, J. Woodall, M. Melloch, and N. Otsuka, "Subpicosecond, freely propagating electromagnetic pulse generation and detection using GaAs: As epilayers," *Applied Physics Letters*, vol. 58, no. 14, pp. 1512–1514, 1991.

[143] E. Castro-Camus, J. Lloyd-Hughes, and M. Johnston, "Three-dimensional carrier-dynamics simulation of terahertz emission from photoconductive switches," *Physical Review B*, vol. 71, no. 19, p. 195301, 2005.

[144] M. Rogalla, R. Geppert, R. Göppert, M. Hornung, J. Ludwig, T. Schmid, R. Irsigler, K. Runge, and A. Söldner-Rembold, "Carrier lifetime under low and high electric field conditions in semi-insulating GaAs," *Nuclear Instruments and Methods in Physics Research Section A: Accelerators, Spectrometers, Detectors and Associated Equipment*, vol. 410, no. 1, pp. 74–78, 1998.

[145] X.-C. Zhang and D. Auston, "Optoelectronic measurement of semiconductor surfaces and interfaces with femtosecond optics," *Journal of Applied Physics*, vol. 71, no. 1, pp. 326–338, 1992.

[146] S. Winnerl, F. Peter, S. Nitsche, A. Dreyhaupt, B. Zimmermann, M. Wagner, H. Schneider, M. Helm, and K. Kohler, "Generation and detection of thz radiation with scalable antennas based on GaAs substrates with different carrier lifetimes," *IEEE Journal of Selected Topics in Quantum Electronics*, vol. 14, no. 2, pp. 449–457, 2008.

[147] L. Hou and W. Shi, "An LT-GaAs terahertz photoconductive antenna with high emission power, low noise, and good stability," *IEEE Transactions on Electron Devices*, vol. 60, no. 5, pp. 1619–1624, 2013.

[148] G. Segschneider, T. Dekorsy, H. Kurz, R. Hey, and K. Ploog, "Energy resolved ultrafast relaxation dynamics close to the band edge of low-temperature grown GaAs," *Applied Physics Letters*, vol. 71, no. 19, pp. 2779–2781, 1997.

[149] S. Gupta, J. F. Whitaker, G. Mourou, *et al.*, "Ultrafast carrier dynamics in iii-v semiconductors grown by molecular-beam epitaxy at very low substrate temperatures," *IEEE Journal of Quantum Electronics*, vol. 28, no. 10, pp. 2464–2472, 1992.

[150] M. Tani, S. Matsuura, K. Sakai, and S.-i. Nakashima, "Emission characteristics of photoconductive antennas based on low-temperature-grown GaAs and semi-insulating GaAs," *Applied Optics*, vol. 36, no. 30, pp. 7853–7859, 1997.

[151] M. Awad, M. Nagel, H. Kurz, J. Herfort, and K. Ploog, "Characterization of low temperature GaAs antenna array terahertz emitters," *Applied Physics Letters*, vol. 91, no. 18, p. 181124, 2007.

[152] I. S. Gregory, *The development of a continuous-wave terahertz imaging system.* PhD thesis, University of Cambridge, 2005.

[153] R. Höpfel, J. Shah, D. Block, and A. Gossard, "Picosecond time-of-flight measurements of minority electrons in GaAs/AlGaAs quantum well structures," *Applied Physics Letters*, vol. 48, no. 2, pp. 148–150, 1986.

[154] M. R. Stone, M. Naftaly, R. E. Miles, J. R. Fletcher, and D. P. Steenson, "Electrical and radiation characteristics of semilarge photoconductive terahertz emitters," *IEEE Transactions on Microwave Theory and Techniques*, vol. 52, no. 10, pp. 2420–2429, 2004.

[155] A. D. Burnett, *Analysis of Drugs and Explosives using Terahertz and Raman Spectroscopy.* PhD thesis, University of Leeds, 2008.

[156] P. Kirawanich, S. J. Yakura, and N. E. Islam, "Study of high-power wideband terahertz-pulse generation using integrated high-speed photoconductive semiconductor switches," *IEEE Transactions on Plasma Science*, vol. 37, no. 1, pp. 219–228, 2009.

[157] F. Miyamaru, Y. Saito, K. Yamamoto, T. Furuya, S. Nishizawa, and M. Tani, "Dependence of emission of terahertz radiation on geometrical parameters of dipole photoconductive antennas," *Applied Physics Letters*, vol. 96, no. 21, p. 211104, 2010.

[158] P. Benicewicz, J. Roberts, and A. Taylor, "Scaling of terahertz radiation from large-aperture biased photoconductors," *Journal of the Optical Society of America B*, vol. 11, no. 12, pp. 2533–2546, 1994.

[159] D. Dykaar, B. Greene, J. Federici, A. Levi, L. Pfeiffer, and R. Kopf, "Log-periodic antennas for pulsed terahertz radiation," *Applied Physics Letters*, vol. 59, no. 3, pp. 262–264, 1991.

[160] P. C. Upadhya, W. Fan, A. Burnett, J. Cunningham, A. G. Davies, E. H. Linfield, J. Lloyd-Hughes, E. Castro-Camus, M. B. Johnston, and H. Beere, "Excitation-density-dependent generation of broadband terahertz radiation in an asymmetrically excited photoconductive antenna," *Optics Letters*, vol. 32, no. 16, pp. 2297–2299, 2007.

[161] P. C. Upadhya, *Coherent generation and detection of Terahertz radiation: time domain Terahertz spectroscopy of molecular crystals.* PhD thesis, University of Cambridge, 2005.

[162] D. S. Kim and D. Citrin, "Dynamics of electric field screening in photoconductive THz sources with spatially patterned excitation," in *European Gallium Arsenide and Other Semiconductor Application Symposium, GaAs 2005*, pp. 417–420, IEEE, 2005.

[163] W. H. Knox, M. Downer, R. Fork, and C. V. Shank, "Amplified femtosecond optical pulses and continuum generation at 5-kHz repetition rate," *Optics Letters*, vol. 9, no. 12, pp. 552–554, 1984.

[164] V. Krylov, A. Rebane, A. G. Kalintsev, H. Schwoerer, and U. P. Wild, "Second-harmonic generation of amplified femtosecond ti: sapphire laser pulses," *Optics Letters*, vol. 20, no. 2, pp. 198–200, 1995.

[165] T. Hattori, K. Egawa, M. Sakamoto, S. Ookuma, R. Rungsawang, and T. Itatani, "Large-aperture THz emitter with interdigitated electrodes," in *2005 Joint 30th International Conference on Infrared and Millimeter Waves and 13th International Conference on Terahertz Electronics*, vol. 2, pp. 457–458, IEEE, 2005.

[166] G. Matthäus, S. Nolte, R. Hohmuth, M. Voitsch, W. Richter, B. Pradarutti, S. Riehemann, G. Notni, and A. Tünnermann, "Microlens coupled interdigital photoconductive switch," *Applied Physics Letters*, vol. 93, no. 9, p. 091110, 2008.

[167] A. Dreyhaupt, S. Winnerl, T. Dekorsy, and M. Helm, "High-intensity terahertz radiation from a microstructured large-area photoconductor," *Applied Physics Letters*, vol. 86, no. 12, p. 121114, 2005.

[168] C. W. Berry, N. Wang, M. R. Hashemi, M. Unlu, and M. Jarrahi, "Significant performance enhancement in photoconductive terahertz optoelectronics by incorporating plasmonic contact electrodes," *Nature Communications*, vol. 4, p. 1622, 2013.

[169] F. Sun, G. Wagoner, and X.-C. Zhang, "Measurement of free-space terahertz pulses via long-lifetime photoconductors," *Applied Physics Letters*, vol. 67, no. 12, pp. 1656–1658, 1995.

[170] M. Tani, K. Sakai, and H. Mimura, "Ultrafast photoconductive detectors based on semi-insulating GaAs and InP," *Japanese Journal of Applied Physics*, vol. 36, no. 9A, p. L1175, 1997.

[171] P. U. Jepsen, R. H. Jacobsen, and S. Keiding, "Generation and detection of terahertz pulses from biased semiconductor antennas," *JOSA B*, vol. 13, no. 11, pp. 2424–2436, 1996.

[172] N. C. van der Valk, T. Wenckebach, and P. C. Planken, "Full mathematical description of electro-optic detection in optically isotropic crystals," *Journal of the Optical Society of America B*, vol. 21, no. 3, pp. 622–631, 2004.

[173] C. Kübler, R. Huber, S. Tübel, and A. Leitenstorfer, "Ultrabroadband detection of multi-terahertz field transients with GaSe electro-optic sensors: Approaching the near infrared," *Applied Physics Letters*, vol. 85, 2004.

[174] P. C. Planken, H.-K. Nienhuys, H. J. Bakker, and T. Wenckebach, "Measurement and calculation of the orientation dependence of terahertz pulse detection in ZnTe," *Journal of the Optical Society of America B*, vol. 18, no. 3, pp. 313–317, 2001.

[175] Q. Wu, M. Litz, and X.-C. Zhang, "Broadband detection capability of ZnTe electro-optic field detectors," *Applied Physics Letters*, vol. 68, no. 21, pp. 2924–2926, 1996.

[176] Q. Wu and X.-C. Zhang, "7 terahertz broadband GaP electro-optic sensor," *Applied Physics Letters*, vol. 70, no. 14, pp. 1784–1786, 1997.

[177] R. Huber, A. Brodschelm, F. Tauser, and A. Leitenstorfer, "Generation and field-resolved detection of femtosecond electromagnetic pulses tunable up to 41 THz," *Applied Physics Letters*, vol. 76, no. 22, pp. 3191–3193, 2000.

[178] J. Kröll, J. Darmo, and K. Unterrainer, "High-performance terahertz electro-optic detector," *Electronics Letters*, vol. 40, no. 12, p. 1, 2004.

[179] J. Kröll, J. Darmo, and K. Unterrainer, "Metallic wave-impedance matching layers for broadband terahertz optical systems," *OpticsEexpress*, vol. 15, no. 11, pp. 6552–6560, 2007.

[180] A. Thoman, A. Kern, H. Helm, and M. Walther, "Nanostructured gold films as broadband terahertz antireflection coatings," *Physical Review B*, vol. 77, no. 19, p. 195405, 2008.

[181] L. Wang, Y. Liu, Y. Wang, and Z. Zhao, "A method for removing echoes in the terahertz time-domain spectroscopy system," in *Microwave and Millimeter Wave Technology (ICMMT), 2012 International Conference on*, vol. 2, pp. 1–4, IEEE, 2012.

[182] O. Hirsch, P. Alexander, and L. F. Gladden, "Techniques for cancellation of interfering multiple reflections in terahertz time-domain measurements," *Microelectronics Journal*, vol. 39, no. 5, pp. 841–848, 2008.

[183] M. Naftaly and R. Miles, "A method for removing etalon oscillations from THz time-domain spectra," *Optics Communications*, vol. 280, no. 2, pp. 291–295, 2007.

[184] C. Russell, C. D. Wood, A. D. Burnett, L. Li, E. H. Linfield, A. G. Davies, and J. E. Cunningham, "Spectroscopy of polycrystalline materials using thinned-substrate planar goubau line at cryogenic temperatures," *Lab on a Chip*, vol. 13, no. 20, pp. 4065–4070, 2013.

[185] J. Cunningham, C. Wood, A. Davies, I. Hunter, E. Linfield, and H. Beere, "Terahertz frequency range band-stop filters," *Applied Physics Letters*, vol. 86, no. 21, pp. 213503–213503, 2005.

[186] J. Kröll, J. Darmo, S. S. Dhillon, X. Marcadet, M. Calligaro, C. Sirtori, and K. Unterrainer, "Phase-resolved measurements of stimulated emission in a laser," *Nature*, vol. 449, no. 7163, pp. 698–701, 2007.

[187] X. Zheng, Y. Xu, R. Sobolewski, R. Adam, M. Mikulics, M. Siegel, and P. Kordoš, "Femtosecond response of a free-standing LT-GaAs photoconductive switch," *Applied Optics*, vol. 42, no. 9, pp. 1726–1731, 2003.

[188] H.-M. Heiliger, M. Vossebürger, H. Roskos, H. Kurz, R. Hey, and K. Ploog, "Application of liftoff low-temperature-grown GaAs on transparent substrates for THz signal generation," *Applied Physics Letters*, vol. 69, no. 19, pp. 2903–2905, 1996.

[189] R. D. V. Ríos, S. Bikorimana, M. A. Ummy, R. Dorsinville, and S.-W. Seo, "A bow-tie photoconductive antenna using a low-temperature-grown GaAs thin-film on a silicon substrate for terahertz wave generation and detection," *Journal of Optics*, vol. 17, no. 12, p. 125802, 2015.

[190] A. Halpern, *SchaumâĂŹs outlines beginning physics II*. New York, McGraw-Hill Companies Inc, 1998.

[191] C. Russell, *Broadband on-chip terahertz spectroscopy*. University of Leeds, 2013.

[192] M. Naftaly and R. E. Miles, "Terahertz time-domain spectroscopy for material characterization," *PROCEEDINGS-IEEE*, vol. 95, no. 8, p. 1658, 2007.

[193] J. Luo, H. Thomas, D. Morgan, D. Westwood, and R. Williams, "The electrical breakdown properties of GaAs layers grown by molecular beam epitaxy at low temperature," *Semiconductor Science and Technology*, vol. 9, no. 12, p. 2199, 1994.

[194] I. S. Gregory, C. Baker, W. Tribe, M. Evans, H. E. Beere, E. H. Linfield, A. Davies, and M. Missous, "High resistivity annealed low-temperature GaAs with 100 fs lifetimes," *Applied Physics Letters*, vol. 83, no. 20, pp. 4199–4201, 2003.

[195] E. Yablonovitch, D. Hwang, T. Gmitter, L. Florez, and J. Harbison, "Van der waals bonding of GaAs epitaxial liftoff films onto arbitrary substrates," *Applied Physics Letters*, vol. 56, no. 24, pp. 2419–2421, 1990.

[196] B. Hu, X.-C. Zhang, and D. Auston, "Temperature dependence of femtosecond electromagnetic radiation from semiconductor surfaces," *Applied Physics Letters*, vol. 57, no. 25, pp. 2629–2631, 1990.

[197] D. Aspnes and A. Studna, "Dielectric functions and optical parameters of Si, Ge, GaP, GaAs, GaSb, InP, InAs, and InSb from 1.5 to 6.0 eV," *Physical Review B*, vol. 27, no. 2, p. 985, 1983.

[198] M. V. Fischetti, "Monte carlo simulation of transport in technologically significant semiconductors of the diamond and zinc-blende structures. i. homogeneous transport," *IEEE Transactions on Electron Devices*, vol. 38, no. 3, pp. 634–649, 1991.

[199] Z.-S. Piao, M. Tani, and K. Sakai, "Carrier dynamics and THz radiation in biased semiconductor structures," in *SPIE Terahertz Spectroscopy and Applications Conference*, vol. 3617, pp. 49–56, 1999.

[200] R. Carlson, G. Slack, and S. Silverman, "Thermal conductivity of GaAs and GaAs1- xpx laser semiconductors," *Journal of Applied Physics*, vol. 36, no. 2, pp. 505–507, 1965.

[201] J. Blakemore, "Semiconducting and other major properties of gallium arsenide," *Journal of Applied Physics*, vol. 53, no. 10, pp. R123–R181, 1982.

[202] S. L. Teitel and J. Wilkins, "Ballistic transport and velocity overshoot in semiconductors: Part i- uniform field effects," *IEEE Transactions on Electron Devices*, vol. 30, no. 2, pp. 150–153, 1983.

[203] M. Khashan and A. Nassi, "Dispersion of the optical constants of quartz and polymethyl methacrylate glasses in a wide spectral range: 0.2âĂŞ3 μm," *Optics Communications*, vol. 188, no. 1âĂŞ4, pp. 129–139, 2001.

[204] M. Beck, I. Walmsley, and J. Kafka, "Group delay measurements of optical components near 800 nm," *IEEE Journal of Quantum Electronics*, vol. 27, no. 8, pp. 2074–2081, 1991.

[205] W. Boyle and P. Kisliuk, "Departure from paschen's law of breakdown in gases," *Physical Review*, vol. 97, no. 2, p. 255, 1955.

[206] J. Požela and A. Reklaitis, "Electron transport properties in GaAs at high electric fields," *Solid-State Electronics*, vol. 23, no. 9, pp. 927–933, 1980.

[207] M. Wellner, *Elements of physics*. Springer Science & Business Media, 2012.

[208] M. Radmilović-Radjenović, B. Radjenović, Š. Matejčik, and M. Klas, "The breakdown phenomena in micrometer scale direct-current gas discharges," *Plasma Chemistry and Plasma Processing*, vol. 34, no. 1, pp. 55–64, 2014.

[209] F. Sizov and A. Rogalski, "THz detectors," *Progress in Quantum Electronics*, vol. 34, no. 5, pp. 278–347, 2010.

[210] J. Ahn, A. Efimov, R. Averitt, and A. Taylor, "Terahertz waveform synthesis via optical rectification of shaped ultrafast laser pulses," *Optics Express*, vol. 11, no. 20, pp. 2486–2496, 2003.

[211] Z. Chen, X. Zhou, C. A. Werley, and K. A. Nelson, "Generation of high power tunable multicycle teraherz pulses," *Applied Physics Letters*, vol. 99, no. 7, p. 071102, 2011.

[212] N. Jukam, S. S. Dhillon, D. Oustinov, J. Madéo, C. Manquest, S. Barbieri, C. Sirtori, S. P. Khanna, E. H. Linfield, A. G. Davies, *et al.*, "Terahertz amplifier based on gain switching in a quantum cascade laser," *Nature Photonics*, vol. 3, no. 12, pp. 715–719, 2009.

[213] D. Oustinov, N. Jukam, R. Rungsawang, J. Madéo, S. Barbieri, P. Filloux, C. Sirtori, X. Marcadet, J. Tignon, and S. Dhillon, "Phase seeding of a terahertz quantum cascade laser," *Nature Communications*, vol. 1, p. 69, 2010.

[214] J. Maysonnave, N. Jukam, M. Ibrahim, K. Maussang, J. Madéo, P. Cavalie, P. Dean, S. P. Khanna, D. Steenson, E. H. Linfield, *et al.*, "Integrated injection seeded terahertz source and amplifier for time-domain spectroscopy," *Optics Letters*, vol. 37, no. 4, pp. 731–733, 2012.

[215] S. Barbieri, M. Ravaro, P. Gellie, G. Santarelli, C. Manquest, C. Sirtori, S. P. Khanna, E. H. Linfield, and A. G. Davies, "Coherent sampling of active mode-locked terahertz quantum cascade lasers and frequency synthesis," *Nature Photonics*, vol. 5, no. 5, pp. 306–313, 2011.

[216] J. R. Freeman, J. Maysonnave, N. Jukam, P. Cavalié, K. Maussang, H. E. Beere, D. A. Ritchie, J. Mangeney, S. S. Dhillon, and J. Tignon, "Direct intensity sampling of a modelocked terahertz quantum cascade laser," *Applied Physics Letters*, vol. 101, no. 18, p. 181115, 2012.

[217] A. Gordon, C. Y. Wang, L. Diehl, F. X. Kärtner, A. Belyanin, D. Bour, S. Corzine, G. Höfler, H. C. Liu, H. Schneider, T. Maier, M. Troccoli, J. Faist, and F. Capasso, "Multimode regimes in quantum cascade lasers: From coherent instabilities to spatial hole burning," *Physical Review A*, vol. 77, pp. 053804–, May 2008.

[218] R. P. Green, A. Tredicucci, N. Q. Vinh, B. Murdin, C. Pidgeon, H. E. Beere, and D. A. Ritchie, "Gain recovery dynamics of a terahertz quantum cascade laser," *Physical Review B*, vol. 80, no. 7, p. 075303, 2009.

[219] H. Choi, L. Diehl, Z.-K. Wu, M. Giovannini, J. Faist, F. Capasso, and T. B. Norris, "Gain recovery dynamics and photon-driven transport in quantum cascade lasers," *Physical Review Letters*, vol. 100, no. 16, p. 167401, 2008.

[220] W. Kuehn, W. Parz, P. Gaal, K. Reimann, M. Woerner, T. Elsaesser, T. Müller, J. Darmo, K. Unterrainer, M. Austerer, *et al.*, "Ultrafast phase-resolved pump-probe measurements on a quantum cascade laser," *Applied Physics Letters*, vol. 93, no. 15, p. 151106, 2008.

[221] J. R. Freeman, J. Maysonnave, S. Khanna, E. H. Linfield, A. G. Davies, S. S. Dhillon, and J. Tignon, "Laser-seeding dynamics with few-cycle pulses: Maxwell-bloch finite-difference time-domain simulations of terahertz quantum cascade lasers," *Physical Review A*, vol. 87, no. 6, p. 063817, 2013.

[222] D. R. Bacon, J. R. Freeman, R. A. Mohandas, L. Li, E. H. Linfield, A. G. Davies, and P. Dean, "Gain recovery time in a terahertz quantum cascade laser," *Applied Physics Letters*, vol. 108, no. 8, p. 081104, 2016.

[223] R. Rungsawang, N. Jukam, J. Maysonnave, P. Cavalié, J. Madéo, D. Oustinov, S. Dhillon, J. Tignon, P. Gellie, C. Sirtori, *et al.*, "Gain enhancement in a terahertz quantum cascade laser with parylene antireflection coatings," *Applied Physics Letters*, vol. 98, no. 10, p. 101102, 2011.

[224] J. R. Freeman, O. Marshall, H. E. Beere, and D. A. Ritchie, "Improved wall plug efficiency of a 1.9 THz quantum cascade laser by an automated design approach," *Applied Physics Letters*, vol. 93, no. 19, p. 1119, 2008.

[225] R. Anamari Mohandas, *Development of terahertz photomixer technology at telecommunications wavelength.* PhD thesis, University of Leeds, 2016.

[226] C. Walther, G. Scalari, J. Faist, H. Beere, and D. Ritchie, "Low frequency terahertz quantum cascade laser operating from 1.6 to 1.8 THz," *Applied Physics Letters*, vol. 89, no. 23, p. 231121, 2006.

[227] D. Miller, D. Chemla, T. Damen, A. Gossard, W. Wiegmann, T. Wood, and C. Burrus, "Band-edge electroabsorption in quantum well structures: the quantum-confined stark effect," *Physical Review Letters*, vol. 53, no. 22, p. 2173, 1984.

[228] D. R. Bacon, A. D. Burnett, M. Swithenbank, C. Russell, L. Li, C. D. Wood, J. Cunningham, E. H. Linfield, A. G. Davies, P. Dean, *et al.*, "Free-space terahertz radiation from a LT-GaAs-on-quartz large-area photoconductive emitter," *Optics Express*, vol. 24, no. 23, pp. 26986–26997, 2016.

[229] D. Bachmann, N. Leder, M. Rösch, G. Scalari, M. Beck, H. Arthaber, J. Faist, K. Unterrainer, and J. Darmo, "Broadband terahertz amplification in a heterogeneous quantum cascade laser," *Optics Express*, vol. 23, no. 3, pp. 3117–3125, 2015.

[230] A. W. M. Lee, Q. Qin, S. Kumar, B. S. Williams, Q. Hu, and J. L. Reno, "High-power and high-temperature THz quantum-cascade lasers based on lens-coupled metal-metal waveguides," *Optics Letters*, vol. 32, no. 19, pp. 2840–2842, 2007.

[231] N. Jukam, S. Dhillon, Z.-Y. Zhao, G. Duerr, J. Armijo, N. Sirmons, S. Hameau, S. Barbieri, P. Filloux, C. Sirtori, *et al.*, "Gain measurements of THz quantum cascade lasers using thz time-domain spectroscopy," *IEEE Journal of Selected Topics in Quantum Electronics*, vol. 14, no. 2, pp. 436–442, 2008.

[232] L. M. Frantz and J. S. Nodvik, "Theory of pulse propagation in a laser amplifier," *Journal of Applied Physics*, vol. 34, no. 8, pp. 2346–2349, 1963.

[233] M. Tonouchi, N. Kawasaki, T. Yoshimura, H. Wald, and P. Seidel, "Pump and probe terahertz generation study of ultrafast carrier dynamics in low-temperature grown-GaAs," *Japanese Journal of Applied Physics*, vol. 41, no. 6B, p. L706, 2002.

[234] R. Köhler, R. C. Iotti, A. Tredicucci, and F. Rossi, "Design and simulation of terahertz quantum cascade lasers," *Applied Physics Letters*, vol. 79, no. 24, pp. 3920–3922, 2001.

[235] A. Gatesman, J. Waldman, M. Ji, C. Musante, and S. Yagvesson, "An anti-reflection coating for silicon optics at terahertz frequencies," *IEEE Microwave and Guided Wave Letters*, vol. 10, no. 7, pp. 264–266, 2000.

[236] H.-W. Hübers, J. Schubert, A. Krabbe, M. Birk, G. Wagner, A. Semenov, G. GolâĂŹtsman, B. Voronov, and E. Gershenzon, "Parylene anti-reflection coating of a quasi-optical hot-electron-bolometric mixer at terahertz frequencies," *Infrared Physics & Technology*, vol. 42, no. 1, pp. 41–47, 2001.

[237] S. Kohen, B. S. Williams, and Q. Hu, "Electromagnetic modeling of terahertz quantum cascade laser waveguides and resonators," *Journal of Applied Physics*, vol. 97, no. 5, p. 053106, 2005.

[238] N. Jukam, S. Dhillon, D. Oustinov, Z.-Y. Zhao, S. Hameau, J. Tignon, S. Barbieri, A. Vasanelli, P. Filloux, C. Sirtori, *et al.*, "Investigation of spectral gain narrowing in quantum cascade lasers using terahertz time domain spectroscopy," *Applied Physics Letters*, vol. 93, no. 10, p. 101115, 2008.

[239] I. Waldmüller, J. Förstner, S.-C. Lee, A. Knorr, M. Woerner, K. Reimann, R. Kaindl, T. Elsaesser, R. Hey, and K. Ploog, "Optical dephasing of coherent intersubband transitions in a quasi-two-dimensional electron gas," *Physical Review B*, vol. 69, no. 20, p. 205307, 2004.

[240] R. Martini, G. Klose, H. Roskos, H. Kurz, H. Grahn, and R. Hey, "Superradiant emission from bloch oscillations in semiconductor superlattices," *Physical Review B*, vol. 54, no. 20, p. R14325, 1996.

[241] S.-C. Lee and A. Wacker, "Nonequilibrium greenâĂŹs function theory for transport and gain properties of quantum cascade structures," *Physical Review B*, vol. 66, no. 24, p. 245314, 2002.

[242] S. Luryi, "Frequency limit of double-barrier resonant-tunneling oscillators," *Applied Physics Letters*, vol. 47, no. 5, pp. 490–492, 1985.

[243] J. Palmier, H. Le Person, C. Minot, A. Chomette, A. Regreny, and D. Calecki, "Hopping mobility in semiconductor superlattices," *Superlattices and Microstructures*, vol. 1, no. 1, pp. 67–72, 1985.

[244] G. Scalari, L. Ajili, J. Faist, H. Beere, E. Linfield, D. Ritchie, and G. Davies, "Far-infrared (λ= 87 μ m) bound-to-continuum quantum-cascade lasers operating up to 90 K," *Applied Physics Letters*, vol. 82, no. 19, pp. 3165–3167, 2003.

[245] S. Kumar, Q. Hu, and J. L. Reno, "186 K operation of terahertz quantum-cascade lasers based on a diagonal design," *Applied Physics Letters*, vol. 94, no. 13, p. 131105, 2009.

[246] M. Martl, J. Darmo, C. Deutsch, M. Brandstetter, A. M. Andrews, P. Klang, G. Strasser, and K. Unterrainer, "Gain and losses in thz quantum cascade laser with metal-metal waveguide," *Optics Express*, vol. 19, no. 2, pp. 733–738, 2011.

[247] S. S. Dhillon, S. Sawallich, N. Jukam, D. Oustinov, J. Madéo, S. Barbieri, P. Filloux, C. Sirtori, X. Marcadet, and J. Tignon, "Integrated terahertz pulse generation and amplification in quantum cascade lasers," *Applied Physics Letters*, vol. 96, no. 6, p. 061107, 2010.

[248] L. Lever, N. Hinchcliffe, S. Khanna, P. Dean, Z. Ikonić, C. Evans, A. Davies, P. Harrison, E. Linfield, and R. Kelsall, "Terahertz ambipolar dual-wavelength quantum cascade laser," *Optics express*, vol. 17, no. 22, pp. 19926–19932, 2009.

[249] G. Beji, Z. Ikonić, C. Evans, D. Indjin, and P. Harrison, "Coherent transport description of the dual-wavelength ambipolar terahertz quantum cascade laser," *Journal of Applied Physics*, vol. 109, no. 1, p. 013111, 2011.

[250] C. Gmachl, F. Capasso, D. L. Sivco, and A. Y. Cho, "Recent progress in quantum cascade lasers and applications," *Reports on Progress in Physics*, vol. 64, no. 11, p. 1533, 2001.